High precision tests of QED : measurement of the alpha-particle and helion rms charge radius and the transition energies in highly-charged ions

Jorge Felizardo Dias Cunha Machado

Jorge Felizardo Dias Cunha Machado

M.Sc. in Physics Engineering

High precision tests of QED Measurement of the alpha-particle and helion rms charge radius and the transition energies in highly-charged ions

A co-tutelle Thesis at Universidade Nova de Lisboa and Université Pierre et Marie Curie submitted in partial fulfillment of the requirements for the degree of

Doctor of Philosophy in
Physics

Advisers: José Paulo Santos, Full Professor,
Faculdade de Ciências e Tecnologia
da Universidade Nova de Lisboa

Paul Indelicato, Full Professor,
Laboratoire Kastler Brossel, UPMC-Sorbonne Universités,
CNRS, ENS-PSL Research University, Collège de France,
Case 74; 4, place Jussieu, F-75005 Paris, France

Examination Committee

Chairperson:	Prof. Dr. Maria Adelaide de Jesus
Raporteurs:	Prof. Dr. Klaus Blaum
	Prof. Dr. José Pires Marques
Members:	Prof. Dr. Luisa Carvalho
	Dr. Paul Indelicato
	Prof. Dr. João Veloso
	Dr. Martino Trassinelli

FACULDADE DE CIÊNCIAS E TECNOLOGIA
UNIVERSIDADE NOVA DE LISBOA

February, 2018

High precision tests of QED
Measurement of the alpha-particle and helion rms charge radius and the transition energies in highly-charged ions

Jorge Felizardo Dias Cunha Machado

February 2018

High precision tests of QED
Measurement of the alpha-particle and helion rms charge radius and the transition energies in highly-charged ions

This document was created using the (pdf)LaTeX processor, based in the "novathesis" template[1], developed at the Dep. Informática of FCT-NOVA [2].
[1] https://github.com/joaomlourenco/novathesis [2] http://www.di.fct.unl.pt

To my beautiful butterfly!

Acknowledgements

This work could not have been carried out without the support of several people and institutions.

I would like first to express my deepest gratitude to my two supervisors, Prof. José Paulo Santos and Doctor Paul Indelicato, for their support and scientific guidance through all this journey. Thank you very much for everything.

During this journey, I had the opportunity of contacting with several scientific groups and collaborations which have always welcomed me. I would like first to acknowledge LKB and its people - starting with Doctor Csilla Szabo who has been the first person welcoming me in Paris and showing me all around, the lab and the University. To Jean-Michel Isac and all the mechanical workshop people, for their patience during the setup phase from the enormous number of requests.

To the INSP group who share the lab with us in Paris, for all the support and training in running SIMPA, specially to Doctor Martino Trassinelli and to Doctor Christophe Prigent, thank you.

I would like to express my gratitude to CREMA collaboration, not only for welcoming me and for all the scientific guidance and discussions, but also for all the fun moments I had the privilege to share with them during beamtime.

A todos os meus colegas na FCT-UNL, em especial aos Doutores Mauro Guerra e Pedro Amaro, pela ajuda e suporte ao longo deste caminho, pelas discussões ao almoço e fora dele. A todos os outros colegas, às Doutoras Sofia Pessanha e Marta Sampaio e ao meu colega de Doutoramento Luís Martins.

Last but not least, o meu obrigado a todos os meus amigos e famíla - à família de sempre, à família que se ganha e à família que se escolhe. Aos meus pais Ana e Fernando, aos meus tios e à minha Madrinha Manuela, que tanto me ajudaram durante toda a minha formação. À Marta e ao Maurício, ao Joel e à Emika, que mesmo estando fora estão sempre perto. À Mesquita, ao Tiago, à Catarina, à Sílvia e à Ariana. Aos meus sogros Fernanda e Zeca e à Madrinha Ana. Aos amigos de Paris, ao André, ao Marco, ao Danilo e ao João, o meu obrigado. Por fim, à minha irmã Inês e a ti Ana, principalmente a ti, por tudo o que já vivemos, pela felicidade partilhada em tê-lo vivido, e pela felicidade que o futuro nos trará.

Institutional Acknowledgements

The work reported in this Thesis was performed in collaboration with:

- Laboratório de Instrumentação, Engenharia Biomédica e Física das Radiações (LIBPhys) group from the Faculdade de Ciências e Tecnologia (FCT) of Universidade Nova de Lisboa (UNL);
- Métrologie des Systèmes Simples et tests Fondamentaux group of the Laboratoire Kastler Brossel (LKB). LKB is a unité mixte de recherche n° 8552 of the Université Pierre et Marie Curie (UPMC), École Normale Supérieure (ENS), Centre National de la Recherche Scientifique (CNRS), and Collège de France;
- Charge Radius Experiments with Muonic Atoms (CREMA) collaboration.

This work has been supported by:

- In part by the projects No. PEstOE/FIS/UI0303/2011, PTDC/FIS/117606/2010, and by the research centre grant No. UID/FIS/04559/2013 (LIB- Phys), from FCT/MCTES/PIDDAC, Portugal;
- "Testes de elevada precisão do QED - Medidas do raio de distribuição de carga das partículas alfa e do hélio e das energias de transição em iões altamente carregados", Acções Integradas Luso-Francesas, Acção ref TC-08_17, CRUP (Portugal) e pela CPU (France), April 2017 – December 2018;
- "Novos testes da electrodinâmica quântica em iões altamente carregados." Programa Pessoa 2017-2018, Proc. N. 441.00 France. FCT e pelo PHC, April 2017 - December 2018;
- Fundação para a Ciência e Tecnologia (FCT), contract SFRH/BD/52332/2013.

FCT
Fundação para a Ciência e a Tecnologia
MINISTÉRIO DA CIÊNCIA, TECNOLOGIA E ENSINO SUPERIOR

Abstract

This work aims to provide insight on Bound-State Quantum-Electrodynamics (BSQED) by experimental fundamentals high-precision tests in exotic states of matter. Although BSQED and the relativistic many-body problem have been undergoing important progress, there are still some issues that require the increase of the number and accuracy of experimental fundamental tests.

The first part of this work was done within the framework of the recent experiment in muonic helium ions ($\mu^4\mathrm{He}^+$ and $\mu^3\mathrm{He}^+$) by the CREMA collaboration. This experiment, aims to provide new accurate values for the root-mean-square (rms) charge radii of the helium isotopes nuclei that are extracted from the measurement of the *Lamb Shift*, *i.e.*, the measurement of the energy difference between the $2S - 2P$ states. With the goal of measuring the transition energies with an accuracy of at least 50 ppm, the rms charge radii of the helium isotopes will be determined with an uncertainty of 0.03%, a factor of ten more precise than previous results obtained from electron scattering.

The second part of this work aims the high-precision measurement of x-ray transitions in Highly-Charged Ions (HCI) using a Double-Crystal Spectrometer (DCS). These ions were produced in the plasma of an Electron-Cyclotron Resonance Ion Source (ECRIS). This kind of spectrometer is able not only to provide high-precision measurements but also reference-free measurements, without reference to any theoretical or experimental energy. Four transitions energies from $n = 2 \rightarrow n = 1$ have been measured in an argon plasma in three different charge states, He-, Be- and Li-like, with an accuracy of better than 3 ppm. Besides the energies, the natural width of each transition has also been experimentally obtained. The obtained results are in excellent agreement with the most recent theoretical calculations.

Keywords: Muonic atoms (ions), Lamb shift, Laser spectroscopy, Relativistic and QED effects, ECRIS, HCI, Reference-free x-ray spectroscopy

Resumo

Este trabalho tem como objetivo fornecer informação em eletrodinâmica quântica de estados ligados por testes experimentais fundamentais de alta precisão, em estados exóticos da matéria. Embora a electrodinâmica quântica de estados ligados e o problema relativista de muitos corpos tenham tido progressos importantes, existem ainda algumas questões que exigem o aumento do número e da precisão de testes experimentais fundamentais.

A primeira parte deste trabalho foi realizada no âmbito da recente experiência em iões de hélio muónico ($\mu^4\mathrm{He}^+$ e $\mu^3\mathrm{He}^+$) pela colaboração CREMA. Esta experiência tem como objectivo fornecer novos valores precisos para o valor quadrático médio dos raios da carga dos núcleos dos isótopos de hélio extraídos a partir da medição do *Lamb Shift*, ou seja, a partir da medição da diferença de energia entre os estados $2S - 2P$. Com o objetivo de medir as energias de transição com uma precisão de pelo menos 50 ppm, os raios da carga dos núcleos dos isótopos de hélio serão determinados com uma incerteza de 0,03%, um factor dez mais preciso do que os resultados anteriormente obtidos a partir da dispersão de electrões.

A segunda parte deste trabalho tem como objectivo a medida de alta precisão de transições de raios-x em iões altamente carregados, usando um espectrómetro de duplo cristal. Os iões foram produzidos num plasma de uma de fonte de iões de ressonância de electrões em ciclotrão (ECRIS). Este tipo de espectrómetro é capaz não só de fornecer medições de alta precisão, mas também de medições sem referência a qualquer energia teórica ou experimental. Quatro energias de transição de $n = 2 \rightarrow n = 1$ foram medidas num plasma de argon em três estados de carga diferentes, He-, Be- e Li-like, com uma precisão melhor que 3 ppm. Além das energias, a largura natural de cada transição foi também experimentalmente obtida. Os resultados obtidos estão em óptima concordância com os cálculos teóricos mais recentes.

Palavras-chave: Átomos (iões) muónicos, Lamb shift, Espectroscopia laser, Efeitos relativistas e de QED, ECRIS, HCI, Espectroscopia de raios-x sem uso de referência

Résumé

Ce travail vise à contribuer à l'amélioration de notre connaissance de l'électrodynamique quantique des états liés, par des mesures de haute précision dans des états exotiques de la matière. Bien que notre connaissance l'électrodynamique quantique des états liés et du problème relativiste à plusieurs corps aient fait des progrès importants ces dernières années, il reste des questions fondamentales dont la résolution nécessite d'augmenter le nombre et la précision des tests expérimentaux.

La première partie de ce travail a été réalisée dans le cadre de l'expérience récente sur les ions muoniques d'hélium ($\mu^4\mathrm{He}^+$ et $\mu^3\mathrm{He}^+$) conduite par la collaboration CREMA. Cette expérience vise à fournir de nouvelles valeurs précises pour les rayons de charge moyens des noyaux des isotopes stables de l'hélium. Ces valeurs sont extraites de la mesure du *déplacement de Lamb*, c'est-à-dire, de la mesure de la différence d'énergie entre les États $2S - 2P$. Une mesure des énergies de transition d'une précision d'au moins 50 ppm, permet de déterminer les rayons de charge des noyaux des isotopes d'hélium avec une incertitude de 0,03%, dix fois plus précise que les résultats précédents obtenu à partir de la diffusion d'électrons.

La deuxième partie de ce travail a été de réaliser des mesures de haute précision de transitions de rayons X dans des ions fortement chargés, à l'aide d'un spectromètre à double cristal plan. Ces ions étaient produits dans le plasma d'une source d'ions de type ECRIS (electron-cyclotron resonance ion source). Le spectromètre utilisé est non seulement capable de fournir des mesures de haute précision, mais aussi des mesures sans référence à des énergies de transition théorique ou expérimentales. Quatre énergies de transition de $n = 2 \rightarrow n = 1$ ont été mesurées pour des ions d'argon de trois états de charge différents, héliumoïde, lithiumoïde et berylliumoïde, avec une précision meilleure que 3 ppm. La largeur naturelle de chaque raie a également été obtenue expérimentalement. Les résultats trouvés sont en excellent accord avec les calculs théoriques les plus récents.

Mots-clés : Atomes muoniques (ions), Lamb shift, Spectroscopie laser, Effets relativistes et QED, ECRIS, HCI, Spectroscopie aux Rayons X sans référence

Contents

List of Figures

List of Tables

Acronyms

BSQED	Bound-State Quantum-Electrodynamics.
CREMA	Charge Radius Experiments with Muonic Atoms.
CT	Cyclotron Trap.
cw	continuous wave.
DAQ	Data Acquisition.
DCS	Double-Crystal Spectrometer.
EBIT	Electron Beam Ion Traps.
ECRIS	Electron-Cyclotron Resonance Ion Source.
ESR	Experimental Storage Ring.
EVG	event gate.
FWHM	Full Width at Half Maximum.
GDGD	GATE & DELAY GENERATOR DELAY.
HCI	Highly Charged Ions.
HIPA	High Intensity Proton Beam accelerator.

HV	High-Voltage.
LAAPD	Large Area Avalanche Photodiode.
LED	Light Emitted Diode.
LGS	Linear Gate and Stretcher.
LL	Lower Level.
MCA	MultiChannel Analyzer.
MCDF	Multiconfiguration Dirac-Fock.
MEC	Muon Extraction Channel.
NIST	National Institute of Standards and Technology.
PID	proportional-integral-differential.
PMT	Photomultiplier.
ppm	part per million.
PSC	Phase Space Compressor.
PSI	Paul Scherrer Institute.
QED	Quantum-Electrodynamics.
QI	Quantum Interference.
RCI	Relativistic Configuration Interaction.

rms	root mean square.
SCA	Single-Channel Analyzer.
SIMPA	Source D'Ions Multichargés de Paris.
TDC	Time-to-Digital Converter.
ToF	Time-of-Flight.
TPE	two-photon exchange.
UL	Upper Level.
WFD	WaveForm digitizer.

List of Symbols

Overall, throughout the document, symbols in bold font represents vectors, *e. g.*, **B** in pag. 23.

The following list describes the meaning of the most used variables and symbols in the text, sorted by order of appearance. The same symbol can have different meaning when defined in different contexts of the text.

Z	atomic number	pag. 1
μp	muonic hydrogen atom	pag. 1
μd	muonic deuterium atom	pag. 1
$\mu^3\mathrm{He}^+$	muonic helium-3 ion	pag. 2
$\mu^4\mathrm{He}^+$	muonic helium-4 ion	pag. 2
m_μ	muon mass	pag. 7
m_e	electron mass	pag. 7
m_p	proton mass	pag. 7
r_p	root-mean-square charge radius of the proton	pag. 7
r_d	root-mean-square charge radius of the deuteron	pag. 7
$\tilde{m}_\mu$	reduced mass of the muon	pag. 17
$\tilde{m}_e$	reduced mass of the electron	pag. 17
τ_{2S}	lifetime of the $2S$ state	pag. 18
e	elementary charge	pag. 50
$\hbar$	reduced Planck constant	pag. 50
c	light speed	pag. 50
u_B^u	muon magnetic moment	pag. 51
u_B^h	helion nucleus magnetic moment	pag. 51
λ	wavelength	pag. 69
d	lattice spacing	pag. 69
θ_{Bragg}	Bragg angle	pag. 69
Γ_L	transition natural width	pag. 98
Γ_G	Gaussian broadening FWHM value	pag. 98

Motivation

Bound-State Quantum-Electrodynamics (BSQED) and the relativistic many-body problem have been undergoing important progress in the past few years, being the high-precision tests provided by simple systems. In hydrogen, the $1S-2S$ transition have been measured with an stunning relative accuracy of a few times 10^{-15} [1, 2] while the $n = 2$ *Lamb shift* is known to a few ppm accuracy [3], from which was used to optimize the relative uncertainty of the Rydberg constant to a few times 10^{-12}. Besides Hydrogen, Helium has also been put to a meticulously research [4]. The reported disagreement between theory and experiment in the fine structure by means of microwave separated oscillatory fields [5], or by means of atomic beam and electro-optic laser techniques [6], has been solved [7] being the agreement between the reported experimental results and theory now very good. Nevertheless, there are still several issues which require increase number and higher accuracy experimental tests. High-precision measurements of transition energies on medium to high-Z elements [8–16], Landé g-Factors [17–23], hyperfine structure [24–36], just to name a few, are needed either to improve our understanding or to provide tests of higher-order Quantum-Electrodynamics (QED)-corrections, which calculations are very demanding.

Although being QED one of the most important foundation of modern physics and being intensively tested experimentally, recent results have triggered experimental and theoretical research regarding possible anomalies. The recent measurement of the *Lamb shift* in muonic hydrogen (μp) [37, 38], by the CREMA collaboration, produced a value for the proton charge radius that disagrees in 5σ from the the combined value from hydrogen spectroscopy and electron-proton scattering, the 2010 CODATA value [39]. This result and respective controversy became known as the *proton radius puzzle* and as for the time being has not yet been solved. Recent result from the same collaboration for the deuteron size in muonic deuterium (μd) [40], have also shown to be 3.5σ smaller than the value from electronic deuterium spectroscopy. This value, when combined with the electronic isotope shift, yields a small proton radius, similar to the one obtained

from muonic hydrogen that has amplified the proton radius puzzle. A very recent result from a $2S - 4S$ transition frequency in electronic hydrogen [41] has resulted in a value for the rms charge radius of the proton in agreement with the one extracted from the μp *Lamb Shift*. This measurement by means of a cryogenic H beam has been the first accurate measurement in electronic hydrogen providing a smaller rms charge radius of the proton than the one extracted from the μp. Another large discrepancy of 7σ has recently also been observed between the experiment suggested in [42] and the theoretical prediction in a specific difference between the hyperfine structures of hydrogen-like and lithium-like bismuth measured at the Experimental Storage Ring (ESR) at the GSI Helmholtzzentrum für Schwerionenforschung in Darmstadt [43].

This work, therefore, aims to provide insight on QED by experimental fundamentals high-precision tests. The first part of this work was done within the framework of the recent experiment in muonic helium ions (μ^4He^+ and μ^3He^+) by the CREMA collaboration at Paul Scherrer Institute (PSI), Villigen, Switzerland. The goal of the experiment is to improve the charge radii of ^{3}He and ^{4}He values by measuring the *Lamb shift*. Initially, the experiment will give insight on the *proton radius puzzle*. Together with the foreseen experiment of testing QED by measuring the $1s - 2s$ transition frequency in hydrogen-like helium [44], which requires a precise value of the charge radius of the helium nucleus, the μHe^+ *Lamb shift* experiment will ultimately test bound-state QED on a supplementary and more sensitive level than the corresponding hydrogen measurements. The second part of this work aims the high-precision measurement of x-ray transition in Highly Charged Ions (HCI) using a Bragg vacuum single-flat DCS produced in an ECRIS plasma. The experiment is located at the Laboratoire Kastler Brossel, UPMC-Sorbonne Universités, CNRS, ENS-PSL Research University, Collége de France, Paris, France. With the aim of part per million (ppm) accuracy, this method can be used to probe and test QED effects such as two-loop self-energy corrections and provide new, more reliable x-ray standards in the few keV energy region.

Part I

Measurement of the alpha-particle and helion rms charge radius

Chapter 1

Introduction

The extensive study of simple atomic systems, such as the simplest system of all, composed by a positively and negatively charged particle, throughout the years has improved both our understanding of the basic aspects of the laws of physics and has also been the system that has led to the major improvements in atomic physics. It was the extensive study of the hydrogen atom that led to the birth of quantum mechanics, having been Niels Bohr, in 1913, the first to incorporated quantum theory on his model in the effort to understand the hydrogen spectrum. His model of the atom, contained for the first time a quantum rule proposing that electrons orbiting the nucleus in ways that were consistent with Planck's quantum theory of radiation, being the electrons restrict to discrete energy levels without emitting radiation. The Bohr model of the hydrogen atom was the predecessor of wholly quantum mechanical models. Later, in 1926, Schrödinger took the Bohr atom model one step further. He succeed to explain the hydrogen spectrum by means of his wave equation, a more rigorous mathematical description of the atom which has set the theoretical foundations to quantum mechanics. Two years later, in 1928, Dirac proposed a relativistic formulation of quantum mechanics of the electron from which the spin emerged as a natural consequence of the relativistic treatment. From this relativistic formulation of quantum mechanics, Dirac was able to explain the fine and hyperfine structures in the hydrogen atom, consequences of the spin of the electron and nucleus, respectively.

Lamb and Retherford, by means of microwave techniques, have measured in 1947 the energy splitting between the $2S_{1/2}$ and $2P_{1/2}$ levels in the hydrogen

atom. They have experimentally shown that these two hydrogen levels are not degenerated as predicted by the Dirac equation, but shifted by 1.06 GHz [45], having become widely known as the *Lamb Shift*. This discovery together with the discovery of the anomalous magnetic moment of the electron [46] in the same year, has gave birth to QED. With the development of this relativistic quantum field theory of electrodynamics, the interaction of matter and light could be described for the first time where full agreement between quantum mechanics and special relativity has been achieved.

Since the development of QED, many H-like systems have been considered both experimentally and theoretically aiming to test this very successful and accurate theory. By achieving more and more precision in both experiments and calculations, theoretical predictions can be verified by experiments leading to a solid fundamental field of physics. This efforts in testing QED has improved the measurement of fundamental constants involved to unprecedented precision. One of this tests, the $1S - 2S$ transition in hydrogen have been measured with a stunning relative accuracy of a few times 10^{-15} [1, 2]. Yet, the agreement of BSQED and experiment was limited to a precision of a few ppm. This limitation from the theoretical prediction of this transition comes from the uncertainty in the measured values of the Rydberg constant and the root mean square (rms) value of the proton charge radius r_p. The rms proton charge radius r_p was only known to a 2% accuracy and the Rydberg constant is known with a relative uncertainty of few times 10^{-12}, being this last one differing in three orders of magnitude from the mentioned $1S - 2S$ transition uncertainty. This limitation in the theoretical prediction of the $1S - 2S$ transition in hydrogen can only be improved by improving the mentioned measured constants by better $2S - nl$ measurements or using an improved value of the proton charge radius obtained by different, more accurate technics.

The CREMA collaboration has proposed to measure the *Lamb Shift* in muonic hydrogen μH by means of laser spectroscopy, aiming to establish an independent method to access to these fundamental constants, the proton charge radius r_p and the Rydberg constant. The muon is about 200 times heavier than the electron, but being a lepton with the same charge as the electron, also interacts with the Coulomb potential. Having a larger mass implies that the negative muon moves around the nucleus with a atomic Bohr radius minor than in the corresponding electronic atom. Its radius is reduced by the ratio of the reduced muon mass to the reduced electron mass

$$\frac{m_\mu m_p}{m_\mu + m_p} \Big/ \frac{m_e m_p}{m_e m_p} \approx 186. \tag{1.1}$$

This reduced Bohr radius results in an increased overlap of the muon wavefunction with the nucleus. Whereas the 2S wavefunction has a large overlap with the nucleus, the probability of the 2P wavefunction be at the nucleus is very small, making the *Lamb Shift* measurement in muonic hydrogen an exceptional opportunity to obtain the proton charge radius. The measurement of the *Lamb Shift* in muonic hydrogen has been perform by the CREMA collaboration in 2010. The obtained derived value for the proton charge radius was [37, 38] $r_p = 0.84087(39)$ fm. Even though this value is 10 times more precise than the current value provided by CODATA least square analysis [39], from both electron scattering and hydrogen spectroscopy, it disagrees in 5σ. This controversy became known as the *proton radius puzzle* and gathered efforts from both theoretical and experimental sides to explain the discrepancy [47, 48]. As for the time being, the *proton radius puzzle* has not yet been solved [49]. Yet, very recently, a measurement of the $2S - 4S$ transition frequency in a cryogenic beam of electronic hydrogen [41] resulted in a value of 3.3 combined standard deviations smaller than the previous H world data. Even though this result is in agreement with the μp value, it is the only accurate measurement up to now to give a rms charge radius of the proton smaller than the one extracted from the μp *Lamb Shift*. Because of the inconsistent result, coming from the muonic atom, compared with most of both hydrogen spectroscopy and electron scattering and also because of the made assumption that both particles, muon and electron, interact with the proton exactly in the same way, CODATA has not yet included this value in the proton radius and Rydberg constant.

Recently the CREMA collaboration, from the measurement of the *Lamb Shift* in muonic deuterium μd, has also provided the value of the rms charge radius of the the deuteron [40] $r_d = 2.12562(78)$ fm. This value is once again more precise than the value from electronic deuterium spectroscopy, but again, the value from muonic atom spectroscopy has also shown to be 3.5σ smaller than the one from electronic spectroscopy. This value, when combined with the electronic isotope shift, yields a small proton radius, similar to the one obtained from muonic hydrogen which has amplified the *proton radius puzzle*.

After this successful campaigns, the CREMA collaboration has measured the *Lamb Shift* in muonic helium ions, $\mu^4\mathrm{He}^+$ and $\mu^3\mathrm{He}^+$, aiming the determination of the charge radii of the alpha particle and helion. With an estimated precision of 50 ppm [50] in the transition measurements, combined with the theoretical

predictions, will result in a relative uncertainty of 3×10^{-4} for the rms charge radii, in which the uncertainty is dominated by the uncertainty of the nuclear polarization contribution [51]. Two different *Lamb Shift* transitions have been measured in μ^4He^+ and three in μ^3He^+. In Fig. 1.1, the level schemes of both μ^4He^+ and μ^3He^+ are presented with the inclusion of the huge finite size effect, which is discussed further in the text on Section 1.1.

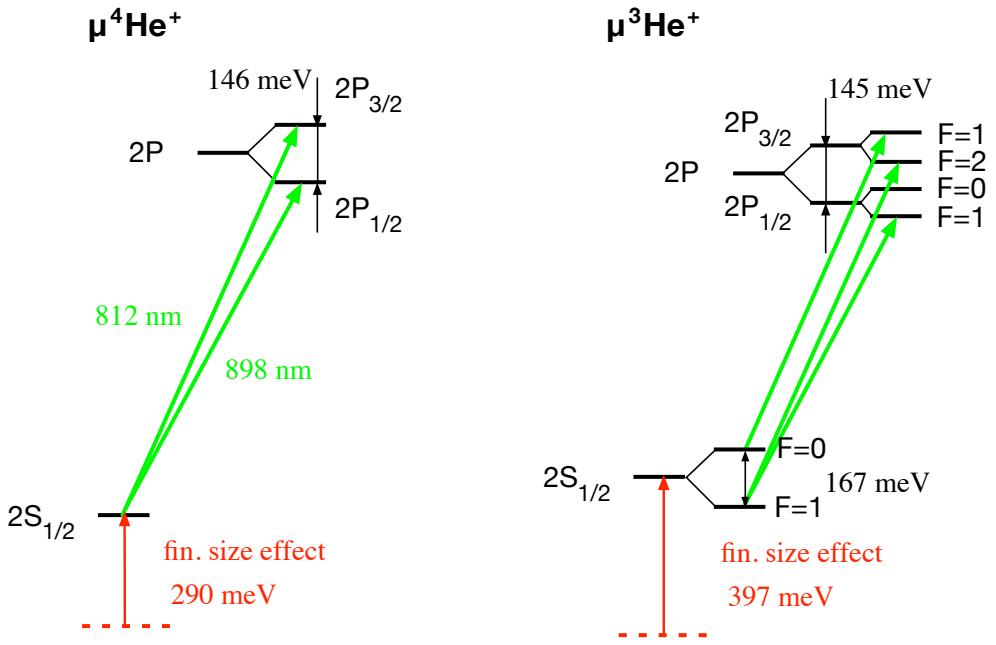

Figure 1.1 – Level schemes of μ^4He^+ and μ^3He^+ showing the huge finite size effect. The measured transitions are indicated by the green arrows. $2S - 2P$ transition properties for μ^4He^+ and μ^3He^+ are listed in Table A.1.

The CREMA collaboration involves currently (at the time of muonic helium *Lamb Shift* experiment) 40 people,

Marwan Abdou-Ahmed[6], Fernando D. Amaro[5], Pedro Amaro[8], Aldo Antognini[1,3], François Biraben[4], Tzu-Ling Chen[9], Daniel S. Covita[7], Andreas J. Dax[1], Marc Diepold[2], Beatrice Franke[2], Luis M.P. Fernandes[5], Sandrine Galtier[4], Andrea L. Gouvea[5], Johannes Götzfried[2], Thomas Graf[6], Theodor W. Hänsch[2], Malte Hildebrandt[1], Paul Indelicato[4], Lucile Julien[4], Klaus Kirch[1,3], Andreas Knecht[1], Franz Kottmann[3], Julian J. Krauth[2], Yi-Wei Liu[9], Jorge Machado[4,8], Cristina M. B. Monteiro[5], Françoise Mulhauser[2], Boris Naar[3], Tobias Nebel[2], François Nez[4], José Paulo Santos[8], Joaquim M. F. dos Santos[5], Karsten Schuhmann[1,3], Csilla I. Szabo[4], David Taqqu[3], Joao F.C.A. Veloso[7], Andreas Voss[6], Birgit Weichelt[6] and Randolf Pohl[2],

from 9 institutes of 5 different countries:

1. Paul Scherrer Institute, 5232 Villigen-PSI, Switzerland.
2. Max Planck Institute of Quantum Optics, 85748 Garching, Germany.
3. Institute for Particle Physics, ETH Zurich, 8093 Zurich, Switzerland.
4. Laboratoire Kastler Brossel, University P. et M. Curie, 75005 Paris, France.
5. Physics Department, University Coimbra, 3004-516 Coimbra, Portugal.
6. Institut für Strahlwerkzeuge, Universität Stuttgart, 70569 Stuttgart, Germany.
7. University Aveiro, Campus de Santiago, 3810-193 Aveiro, Portugal.
8. Physics Department, Nova School of Sciences and Technology, Nova University of Lisbon, 892-516 Caparica, Portugal.
9. Physics Department, National Tsing Hua University, Hsincho 300, Taiwan.

Our contribution (Lisbon group) has been mainly provided in the setup phase of the experiment, by helping preparing and installing all the needed hardware to perform the experiment. We have also participated in the data recording process during beam time as well as in the theoretical prediction of quantum interference effects in the experiments with muonic atoms and ions of CREMA collaboration and in the analysis of the output standard wave forms from the Large Area Avalanche Photodiode (LAAPD)s.

On this part of this document, the work performed within the framework of the recent experiment in muonic helium ions by the CREMA collaboration will be presented. Besides the description of the experimental method, the experimental setup, the systematics and the discussion of the preliminary results, the developed method in the analysis of LAAPDs signals is described in detail, being the topic in which I have been more involved. On the remainder of this Chapter, a discussion of the muonic helium ions and the various contributions to the energy shift of the *Lamb Shift* transition is presented.

On Chapter 2, the principle of the experiment is explained. A description of the experimental setup is given following the path of the high intensity proton beam provided in PSI, through the production and trapping of muons from the pion decay and the subsequent transport and detection of the muons until they reach the gas target, where they will form the muonic ions.

Chapter 3 is dedicated to the analysis of the LAAPD standard wave forms. The identification of different pulses from the LAAPD output, the explanation of the origin of the different forms is provided. The energy analysis calibration of

the signals and its importance is explained. A method developed by our group to distinguish between a electron signal from a x-ray signal with this detectors is presented.

The effects contributing to a shift or to an asymmetry of the line shape in the CREMA experiments are discussed on Chapter 4. The discussion on how these systematic effects will affect the measured *Lamb shift* transition frequency accuracy is presented.

Preliminary results from the data analysis of the experiment, for the 2 measured transition in μ^3He^+ and the 4 measured transitions in μ^3He^+ are shown on Chapter 5.

Final considerations and conclusions are presented on Chapter 6.

1.1 Muonic atoms and the Lamb shift

Dirac's theory predicted that the $2S_{1/2}$ and $2P_{1/2}$ states should be degenerated. Yet, Lamb and Retherford have experimentally shown that they are not [45]. They have shown that the $2P_{1/2}$ state in electronic hydrogen is slightly lower than the $2S_{1/2}$ state, resulting in a slight shift of the corresponding spectral line, known as the *Lamb Shift*. At the time, two contributions had been predicted for the energy difference between the $2S_{1/2}$ and $2P_{1/2}$, the finite size effect of the proton [52] and the *vacuum polarization* [53], also known as the Uehling term. Yet, these contribution were far too small to explain the *Lamb Shift*. In addition the Uehling term contribution had an opposite sign to the *Lamb Shift*.

After being extensively discussed, this result had been finally explained by Bethe calculations of the *self-energy* [54]. This contribution is explained by the absorption of a virtual photon by the bound electron from the interaction with the radiative field, *i.e*, is the energy contribution to the electron due to interactions between the particle and the system it is part of. Bethe calculation agreed very well with the measurement of Lamb and Retherford and set the foundations of QED.

In muonic atoms, due to the large muon mass, the vacuum polarization is much enhanced which makes it the QED leading term for the *Lamb Shift*. This is the opposite situation of ordinary hydrogen-like atoms where the self-energy is the leading QED contribution. Yet, nowadays, with the current level of few ppm accuracy [3] in the *Lamb Shift* measurement of electronic hydrogen, this effect can not longer be explained by pure QED. Several nuclear effects play an important

roll in the *Lamb Shift*. The approximation in considering the nucleus as a point-like particle is not suitable anymore, the so-called *finite size effect*. The spatial charge distribution affects the energy levels of the bound lepton. In the particular case of muonic atoms, the large mass of the muon strongly enhanced this effect from where S states are very sensitive to it (see Fig 1.1). Therefore, this special atomic systems are very well suited to measure the rms charge radii of the nuclei.

1.1.1 Contribution to the Lamb shift in μ^4He^+ and μ^3He^+

There are a number of different terms contributing to the theoretical Lamb shift in μ^4He^+ and μ^3He^+ that can be grouped as charge radius independent terms ($\Delta E_{LS}^{\text{indep.}}$) and charge radius dependent terms ($\Delta E_{LS}^{\text{dep.}}$). Yet, measuring the *Lamb Shift* means that we are measuring indeed a combination of the *Lamb Shift* (LS), the fine structure (FS), and the hyperfine structure (HFS). In order to extract the nucleus charge radii of the nuclei from the measurement of the $2S-2P$ transition, from an initial state i to a final state f the following parametrization is used [55]

$$\Delta E_{\text{total}}(i \to f) = \Delta E_{LS}^{\text{indep.}} + \Delta E_{LS}^{\text{dep.}}(\langle r^2 \rangle) + E_{2P}(f) + E_{2SHFS}(i), \tag{1.2}$$

where $\Delta E_{LS}^{\text{indep.}} + \Delta E_{LS}^{\text{dep.}}$ is the *Lamb Shift* energy, $E_{2P}(f)$ the energy difference between the final $2P$ state with the $2P_{1/2}$ state and $E_{2SHFS}(i)$ the energy difference between the initial $2S$ hyperfine state and the virtual $2S_{1/2}$ level. It depends on the splitting ΔE_{2SHFS} of the two $2S$ hyperfine levels. While μ^3He^+ have nuclear spin of $1/2$, resulting that the $2_{S1/2}$ and $2P_{1/2}$ states are indeed virtual states (the center of gravity of the hyperfine states), obliges to consider the hyperfine structure, the μ^4He^+ has zero nuclear spin which yields Eq. (1.2) as

$$\Delta E(2S_{1/2} \to 2P_j) = \Delta E_{LS}^{\text{indep.}} + \Delta E_{LS}^{\text{dep.}}(\langle r^2 \rangle) + \delta_{j,3/2}\Delta E_{FS}. \tag{1.3}$$

In the $2S_{1/2} - 2P3/2$ transition, the $2P$ fine structure interval of μ^4He^+ has to be added in order to account for spin-orbit coupling of the muon. The radius dependent part is parameterized with a constant times the charge radius squared.

A theory summary for the $n = 2$ levels in μ^3He^+ and μ^4He^+ with compiled radius dependent and independent terms are given in References [55] and [56], respectively. In these References, a summary of the works from Borie, and the groups of Martynenko, Jentschura, Karshenboim and Bacca [57–64] is compiled and compared, from where a average of the theoretical predictions is performed and the half of the spread of the values is used as uncertainty.

Independent of the muonic helium isotope, the largest term in the muonic atom and ions for the *Lamb Shift* comes from the first order contribution of

the electron vacuum polarization (eVP), the Uehling term, which scales with $\alpha(Z\alpha)^2 m$, being m the muon mass. This charge radius independent effect describes the creation of electron-positron pairs by the exchanged photon between the muon and nucleus on the propagation of the Coulomb force. The total energy contribution of this effect for the $\mu^4\mathrm{He}^+$ *Lamb Shift*, averaged from the mentioned calculations, is [56]

$$\Delta E^{\text{1-loop}}_{(2P-2S)} = 1666.2945(15)\ \text{meV}\cdot \tag{1.4}$$

The next largest term in the QED part of the muonic Lamb shift is given by the two-loop electron vacuum polarization in the one-photon interaction contribution (order $\alpha^2(Z\alpha)^2 m$), known as Källén-Sabry contribution. The third largest term is a combination of the contributions from muon self-energy and muon vacuum polarization (order $\alpha(Z\alpha)^4 m$). Including all the calculated QED terms up to the order of $(Z\alpha)^6$, the used radius independent contribution to the *Lamb Shift* for $\mu^4\mathrm{He}^+$ is [56]

$$\Delta E^{\text{indep.}}_{LS} = 1668.4867(134)\ \text{meV} \tag{1.5}$$

while for $\mu^3\mathrm{He}^+$ is [55]

$$\Delta E^{\text{indep.}}_{LS} = 1644.3466(146)\ \text{meV}, \tag{1.6}$$

being the one-loop eVP contributing in more than 99.5% in the total radius independent contribution of both isotopes.

The largest and leading order of the nuclear structure dependent contribution for the *Lamb Shift* ($\Delta E^{\text{dep.}}_{LS}$) is the already mentioned finite size effect. This effect leads to a decrease of the binding energy due to the lepton while inside the nucleus. It scales with $(Z\alpha)^4 m^3 r^2$ and with the square of lepton wave function at its origin. This dependence with the power of three of the muon mass for the finite size effect is what makes the muonic atoms so well suited to measure the rms charge radius of the establish muonic system. Only the S states are sensitive to this effect since they are the only non-zero states at the wavefunction origin. This contribution follows the Uehling term in the largest contributions to the *Lamb Shift*.

The two major contributions for the *Lamb Shift* prediction uncertainty comes from the nuclear structure dependent part, described by the polarizability of the nucleus. The contributions in question are the elastic and inelastic two-photon exchange (TPE) between muon and nucleus. This two TPE contributions, carrying the highest uncertainties to the *Lamb Shift*, limit the accuracy in the extraction

of the rms charge radii. The elastic part contribution of the TPE is given by the Friar-moment contribution ($\Delta E_{(\text{Friar})}$) which is proportional to the third Zemach moment and is the analog effect to the finite size effect in the two-photon interaction. The second term, the also called nuclear polarizability contribution, is the least known part in the muonic Lamb shift theory and the term that limits most the accuracy in the extraction of the charge radius of the nucleus.

Including high order corrections, the total contribution for $\mu^4\text{He}^+$ [56], including the independent and dependent radius terms gives:

$$\begin{aligned}\Delta E(2S_{1/2} \to 2P_{1/2}) &= \Delta E_{LS}^{\text{indep.}} + \Delta E_{(\text{finite size})} + \Delta E_{(\text{TPE elastic})} + \Delta E_{(\text{TPE inelastic})} \\ &= 1668.487(14)\ \text{meV} \\ &\quad - 106.358(7)\ \text{meV/fm}^2 \cdot \langle r^2 \rangle \\ &\quad + 6.761(77)\ \text{meV} \\ &\quad + 3.296(189)\ \text{meV}.\end{aligned} \tag{1.7}$$

For the $\mu^3\text{He}^+$ [55], the total contribution for the *Lamb Shift* is given by:

$$\begin{aligned}\Delta E(2S_{1/2} \to 2P_{1/2}) &= \Delta E_{LS}^{\text{indep.}} + \Delta E_{(\text{finite size})} + \Delta E_{(\text{TPE elastic + inelastic})} \\ &= 1644.346(15)\ \text{meV} \\ &\quad - 103.518(10)\ \text{meV/fm}^2 \cdot \langle r^2 \rangle + 0.1177(33)\ \text{meV} \\ &\quad + 5.300(520)\ \text{meV}.\end{aligned} \tag{1.8}$$

1.1.2 Fine and hyperfine structures

Only from one of the measured transitions in the muonic helium isotopes, the charge radius of the nucleus can be directly extracted from the total $\Delta E(2S_{1/2} \to 2P_{1/2})$ energy of Eqs. (1.7) and (1.8). That transition is of course the $2S_{1/2} \to 2P_{1/2}$ transition in $\mu^4\text{He}^+$, since there are no contributions from hyperfine structure (the $\mu^4\text{He}^+$ nuclear spin is zero) and the fine structure only has to be considered in the $2S_{1/2} \to 2P_{3/2}$ transition. For $\mu^3\text{He}^+$ the hyperfine and fine structure have to be taken in consideration when extracting the charge radius from all the measured transitions.

The $2P_{3/2} - 2P_{1/2}$ fine structure has to be considered when extracting the ^4He nucleus from the $2S_{1/2} - 2P_{3/2}$ transition. Using Dirac's theory and including additional contributions as the electron vacuum polarization, the muon anomalous

magnetic moment and recoil effects, the fine structure contribution can be calculated to a sufficient level of accuracy. The total fine structure for the $2P$ level in $\mu^4\mathrm{He}^+$ is given by [56]:

$$\Delta E_{FS} = 146.192(13)\ \mathrm{meV} \tag{1.9}$$

The nuclear spin of $\mu^3\mathrm{He}^+$ is 1/2, which obliges to consider the hyperfine structure of the $2S_{1/2}$, $2P_{1/2}$ and $2P_{3/2}$ and the $2P_{3/2} - 2P_{1/2}$ fine structure. Analogously to $\mu^4\mathrm{He}^+$ fine structure, including all higher order contributions, the total $2P$ fine structure of $\mu^3\mathrm{He}^+$ yields [55]

$$\Delta E_{FS} = 144.799(10)\ \mathrm{meV}\cdot \tag{1.10}$$

The hyperfine structure of the $\mu^3\mathrm{He}^+$ $2P$ state is given in Reference [55], where the final values are obtained by considering the spread of values from the different authors and a calculation following Pachucki [65] calculations for the μp atom. The final values, relative to the $2P_{1/2}$ state, are given by

$$\begin{aligned}
\Delta E(2P_{1/2}^{F=1}) &= -14.7979(102)\ \mathrm{meV} \\
\Delta E(2P_{1/2}^{F=0}) &= 43.8754(296)\ \mathrm{meV} \\
\Delta E(2P_{3/2}^{F=2}) &= 135.7554(27)(101)_{FS}\ \mathrm{meV} \\
\Delta E(2P_{3/2}^{F=1}) &= 160.0452(42)(101)_{FS}\ \mathrm{meV},
\end{aligned} \tag{1.11}$$

where uncertainties arise from differences between the published values and from the uncertainty in the fine structure value ΔE_{FS}.

The $2S$ hyperfine structure, similarly to the *Lamb Shift*, can be divided into a radius independent part and a radius dependent part which includes the nucleus polarizability. The leading therm contribution is the Fermy energy. By including all other higher order contributions, the $2S$ hyperfine structure is given by [55]

$$\Delta E_{\mathrm{2SHFS}} = -167.2(1.0)\ \mathrm{meV}\cdot \tag{1.12}$$

1.1.3 Summary of the $\mu^4\mathrm{He}^+$ and $\mu^3\mathrm{He}^+$ measured transitions

With the above discussed contributions for the *Lamb Shift* in $\mu^4\mathrm{He}^+$ and $\mu^3\mathrm{He}^+$ with the respective calculations of the fine and hyperfine structures, the measured transition energies in both muonic ions can be parametrized as a dependent charge radius square of the respective nucleus.

As mentioned, in $\mu^4\mathrm{He}^+$, the $2S_{1/2} \to 2P_{1/2}$ and the $2S_{1/2} \to 2P_{3/2}$ transitions have been measured. From Eqs. (1.7) and (1.9), these measured transition energies can be expressed with respect to the ^{4}He rms charge radius (in fm) as

$$\begin{aligned} \Delta E(2S_{1/2} \to 2P_{1/2})(\langle r^2 \rangle) &= 1678.544(287) - 106.358(7)\langle r^2 \rangle \text{ meV} \\ \Delta E(2S_{1/2} \to 2P_{3/2})(\langle r^2 \rangle) &= \Delta E(2S_{1/2} \to 2P_{1/2})(\langle r^2 \rangle) + 146.192(13) \text{ meV}\cdot \end{aligned} \tag{1.13}$$

In $\mu^3\mathrm{He}^+$, taking into account the fine and hyperfine structures, the transition are expressed with respect to the ^{3}He rms charge radius (in fm) as

$$\begin{aligned} \Delta E(2S_{1/2}^{F=1} \to 2P_{1/2}^{F=2})(\langle r^2 \rangle) &= \Delta E_{\mathrm{LS}}(\langle r^2 \rangle) - \frac{1}{4}\Delta E_{\mathrm{2SHFS}} + \Delta E(2P_{3/2}^{F=2}) \\ \Delta E(2S_{1/2}^{F=0} \to 2P_{3/2}^{F=1})(\langle r^2 \rangle) &= \Delta E_{\mathrm{LS}}(\langle r^2 \rangle) + \frac{3}{4}\Delta E_{\mathrm{2SHFS}} + \Delta E(2P_{3/2}^{F=1}) \\ \Delta E(2S_{1/2}^{F=1} \to 2P_{1/2}^{F=1})(\langle r^2 \rangle) &= \Delta E_{\mathrm{LS}}(\langle r^2 \rangle) - \frac{1}{4}\Delta E_{\mathrm{2SHFS}} + \Delta E(2P_{1/2}^{F=1}), \end{aligned} \tag{1.14}$$

from where ΔE_{LS} is the depended charge radius square of the *Lamb Shift* $\Delta E(2S_{1/2} \to 2P_{1/2})$ from Eq. (1.8), $\Delta E_{\mathrm{2SHFS}}$ is the hyperfine structure of the $2S$ state from Eq. (1.12) and the last term of each is given by Eq. (1.11).

Chapter 2

Experimental setup

The experiment described in this work has been performed at the High Intensity Proton Beam accelerator (HIPA) situated at Paul Scherrer Institute (PSI) in Villigen, Switzerland. This Chapter focuses in the principles of the experiment and on the description of the experimental apparatus in which the experiments with the muonic helium ions has been performed.

2.1 The experiment principle

The principle of the experiment is the creation of highly excited μHe^+ ions by stopping negative muons into a low pressure He gas target operated around 2 mBar. The injected muons in the gas environment undergo collisions with the surrounded ions of He. In these collisions, the muons kick out the electrons of the He ions and loses a minimum kinetic energy of 24.6 eV per collision, corresponding to the ionization energy of the He atom. The negative muons are injected into the gas target with a kinetic energy of roughly 15 keV which is translated in ≈200 muon collisions before remaining weakly bound to a He nucleus and form the highly excited μHe^+ ion. The μHe^+ is formed from initial state of $n \approx 14$ which is given by the maximum overlap between the electronic and muonic wavefunctions that can be estimated by the square root of the reduced mass ratio of the muonic and electronic systems [66]

$$\sqrt{\tilde{m}_\mu / \tilde{m}_e} \approx 14. \tag{2.1}$$

From the highly excited initial state, most of the μHe^+ ions deexcite quickly to the $1S$ ground state ($\approx$ 98%) emitting several *prompt* x-rays. Yet, $\approx$2% of them populate the long-lived $2S$ state [67]. After a certain time of the muonic atom formation, a shorter laser pulse with a tunable wavelength around $\lambda \in [800, 970]$ nm, corresponding to the ΔE_{2P-2S} energy shift, is sent to a mirror cavity surrounding the target gas volume in about 0.9 μs after the muon stops. When having the correct laser frequency, the ion is excited from the $2S$ to the $2P$ states from where is immediately ($\approx$0.5 ps) followed by the $2P - 1S$ deexcitation via emission of 8.2 keV K_α x-ray. Figure 2.1 schematically shows the principle of the experiment. A resonance curve is obtained by measuring at different laser wavelengths the number of 8.2 keV K_α x-ray which occur in time-coincidence with the laser pulse.

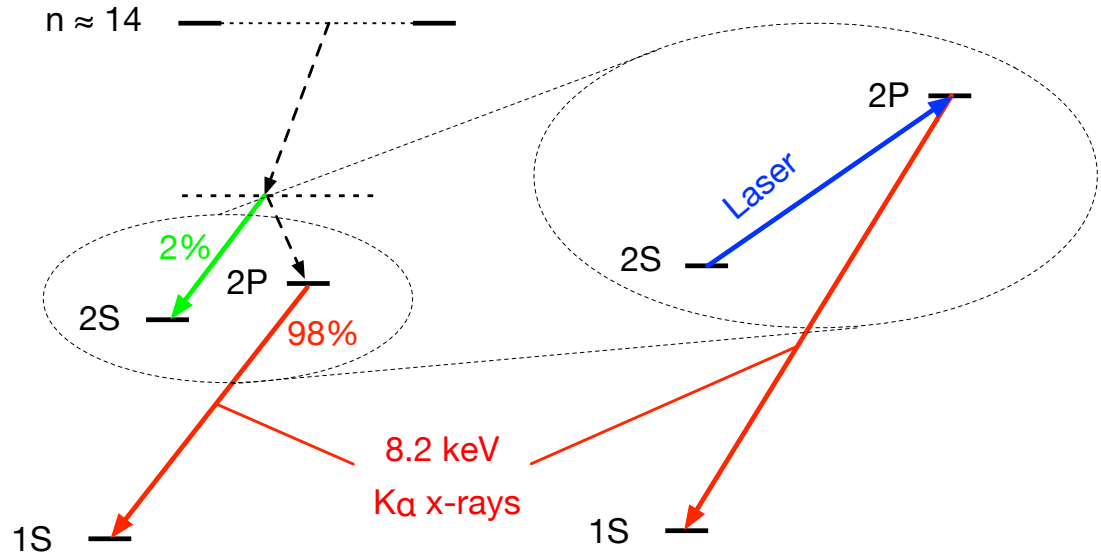

Figure 2.1 – Scheme of the atomic cascade taking place in muonic He ions. Muons are captured in highly excited states around $n \approx 14$. From there, they cascade towards the ground state emitting 8.2 keV *prompt* x-rays. Only roughly 2% of all initial ions end up in the $2S$ state. Muonic ions in the $2S$ are then excited to the $2P$ sate by the laser. From there they immediately decay to the ground state via emission of 8.2 keV K_α x-ray.

The lifetime τ_{2S} of the $2S$ state is crucial to the feasibility of the experiment. Induce the $1S - 2S$ transition directly is not possible via means of laser excitation in this case due to the very strong binding potential generated by the reduced Bohr radius in the muonic ions, being the $1S - 2S$ energy difference in the x-ray regime. The τ_{2S} of the $2S$ state is determined by

$$\tau_{2S}^{-1} = \tau_{\mu}^{-1} + \lambda_{xx} + \lambda_Q \tag{2.2}$$

being the $\tau_\mu = 2.2$ μs the muon lifetime and $\lambda_{xx} = 1.18 \times 10^5$ s^{-1} [68] the two-photon decay rate. The quenching rate λ_Q results from collisions with neighboring atoms and thus depends on the He pressure p_{He}. Experimentally it was found [67] that λ_Q is the sum of a linear and a quadratic term in the He pressure and to guarantee large enough surviving $2S$-populations for the delayed laser excitation, low gas pressures are needed, $\tau_{2S} = 1.71$ μs at $p_{\mathrm{He}} = 2$ mbar.

2.2 Muon beam

For the production of the negative low-energy muon beam, a high intensity proton beam is needed. The acceleration of the protons at PSI facility is done in a 3-stage process. At first, the protons are accelerated at 870 keV by a Cockcroft-Walton pre-injector [69]. The second and third stages are the two rings cyclotrons that accelerates the protons in succession up to 72 MeV and 590 MeV. The resulting proton beam has a current of 2.2 mA making it the most intense proton beam in the world. From the collision of the high intensity proton beam with a graphite target, pions are created from the interaction of the protons with the nucleons of the carbon atoms. Since for the *Lamb Shift* in muonic helium experiment we are interested in negative muons, only negative pions are needed. From the target, the low-momentum (40 - 120 MeV/c) negative pions are guided via the pion beamline to the entrance of low energy muon beamline into the cyclotron trap with a rate of 10^8 s^{-1}. The negative pions are obtained from a backward scattering angle of 175° to the proton beam. The pion beam is also composed by muons, electrons and neutrons.

To stop muons in the low pressure gas target, is mandatory to have a muon beam with low kinetic energy in the keV range. For that purpose, a specifically designed low-energy muon beam line has been developed at PSI [70]. The aim of this beam line is to slow down the original produced muons with kinetic energies of several MeV to energies in the keV range, within the muon lifetime. Besides reducing the muons energy the low-energy muon beam line was also designed to reduce the beam background. In Fig. 2.2 a illustration of the top view of the low energy muon beamline operated in the πE5 area at PSI is shown. The low-energy muon beam line can be divided in three major parts: the Cyclotron Trap (CT), the Muon Extraction Channel (MEC) and the Phase Space Compressor (PSC). These three major parts of the beam line are described in the following.

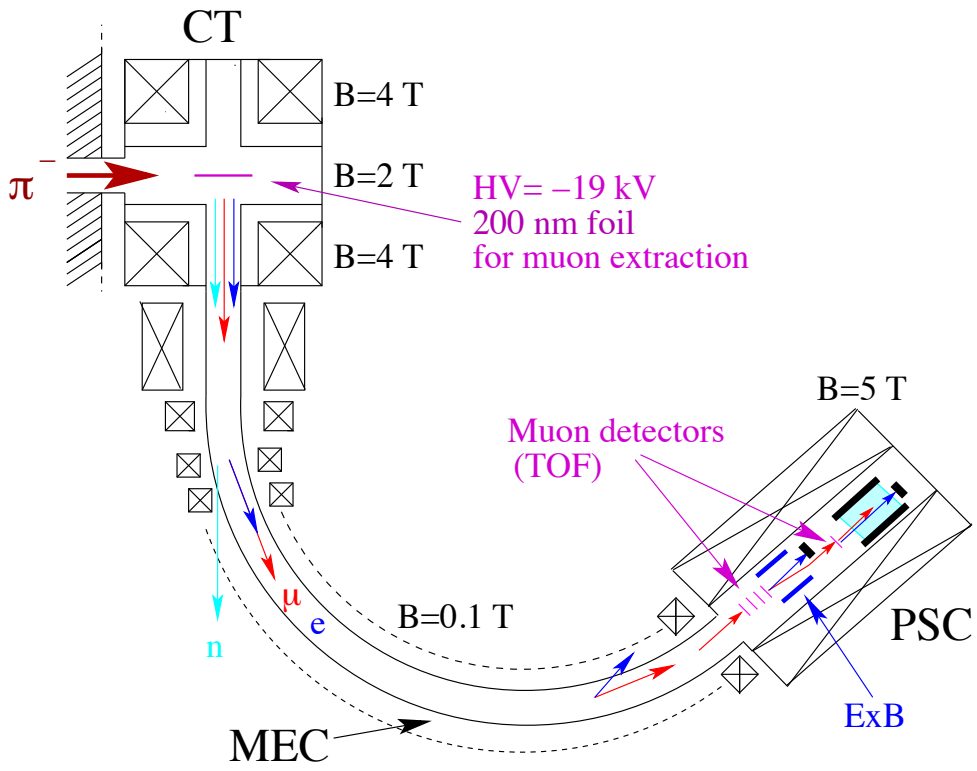

Figure 2.2 – Schematic drawing of the low-energy muon beam line. The low-energy muon beam line is placed in the πE5 area at PSI. The cyclotron trap (CT), the muon extraction channel (MEC) and the phase space compressor (PSC) target solenoid are shown.

2.2.1 Cyclotron trap

The main purpose of the CT [70] is to capture the incoming pions, decelerate them and produce low-energy muons which can be guided to the experimental region. The CT is composed by two 4 T superconducting coils that act as a magnetic bottle to confine the pions and the muons. The pion beamline supports pions with a momentum of ≈ 100 MeV/c with a momentum dispersion of 6% Full Width at Half Maximum (FWHM). These 100 MeV/c pions enter the CT tangentially where they are moderated by passing a degrader, the thickness of which is chosen such that they loose about half of their momentum. About 30% of the pions decays in flight to muons with a lifetime of 2.6×10^{-8} s via their leptonic decay channel

$$\pi^- = \mu^- + \bar{\nu}_\mu. \tag{2.3}$$

The remaining 70% of the pions are lost to the experiment either because they are

stopped in the moderator or because they hit the inner CT walls. The negative muons produced on flight are further decelerated by repeatedly passing a metalized 160 nm Formvar foil. Most of the muons have kinetic energies above the acceptance of the trap and are lost. The few percent that are radially and axially trapped in the magnetic bottle have kinetic energies below a few MeV. By repeatedly passing in the moderator with their spiral trajectory due to the magnetic bottle confinement, this few MeV muons are slowed down to kinetic energies of 20 – 50 keV. The moderator is kept at high-voltage (-18 kV) and mounted in the center plane of the CT. When the muons are decelerated to 20 – 50 keV, the electric potential dominates the magnetic confining and the muons leave axially the CT through the bottle neck and enter the MEC.

2.2.2 Muon extraction channel

The muons that escape the CT enter the MEC. The MEC acts as a momentum filter for muons in the energy range of 20 – 40 keV. It is assembled from 17 normal conducting magnetic coils mounted on a 130° segment of a circle with 1 m radius resulting in a magnetic field with a toroidal form of B = 0.15 T. The momentum filter is achieved due to the toroidal shape of the magnetic field, leading to a slight magnetic field gradient in the horizontal plane. Besides selecting the muon momentum with the help of the collimators at the end of the MEC (favoring muons of $\approx$ 20 keV), the MEC also separates the muons from unwanted background radiation and particles. The background radiation is mainly composed by high-energy electrons coming from the muon decay, electrons with keV energies being expelled from the Formvar foil in the CT and neutrons coming from the interaction of the pions with the apparatus walls. To further minimize the background induced by neutrons produced in the CT, a 1 m thick block of concrete is placed between the CT and the target solenoid. From the MEC, the muons are guided into the bore hole of a 5 Tesla superconducting PSC magnet, slightly above its axis.

2.2.3 Target

Muons accepted by the MEC are driven to the 5 Tesla superconducting 1 m length PSC solenoid that contains the gas target volume. This increase in magnetic field insures the decrease of the radius of spiraling muon motion to a few mm inside the gas target. This reduces drastically the size of gas target and consequently the volume that has to be illuminated by the laser. The solenoid bore hole

of 20 cm diameter requires that the entire detection setup (x rays and electrons) had to be done in a very compact manner. Figure 2.3 illustrates schematically the gas target and the nondestructive muon detection which is described in the following.

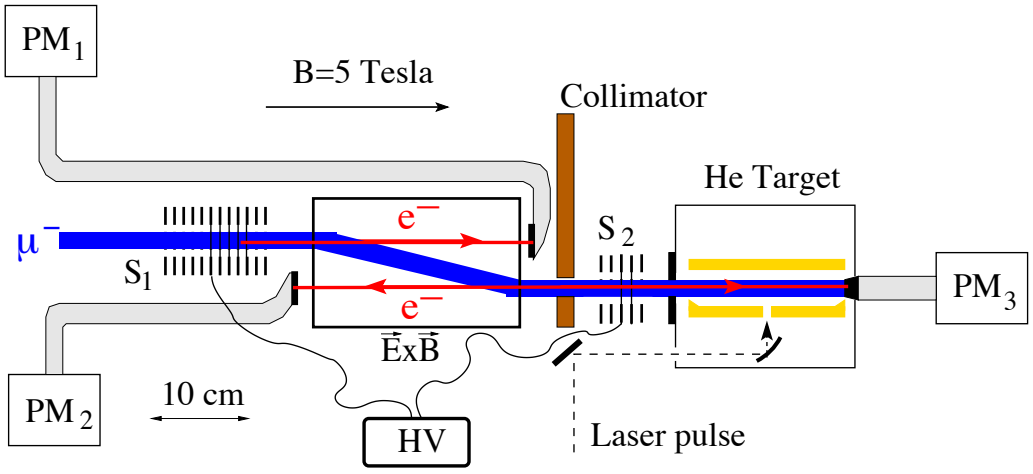

Figure 2.3 – Schematic drawing illustrating the nondestructive muon detection and the gas target. Muons arriving the target have to pass through 2 stacks of stainless steel rings (S_1 and S_2),which are kept on negative high voltage, and a $\mathbf{E} \times \mathbf{B}$ filter. The created secondary electrons kicked out from the carbon foils (present in the stacks) are detected in scintillators connected to the photomultipliers PM1, PM2 and PM3. Electrons created in the S_1 stack are detected by the scintillator connected to PM1 while the electrons created in the S_2 stack by the photomultipliers PM2 or PM3. The muons are separated from the electrons with the $\mathbf{E} \times \mathbf{B}$ filter. A coincidence of signals from S1 and S2 triggers the laser. After being detected nondestructively, the muons enter the gas target where they form muonic atoms.

2.2.3.1 Nondestructive muon detection

Usually, in experiments using particle beams, the experiment trigger is realized by a constant repetition rate that is synchronized with the particle source. Yet, in the case of CREMA experiments this is not possible. The muon beam results from the high intensity proton beam operated in a quasi-continuous regime (pulsed at 50 MHz), which is not suitable for laser synchronization. The arrival of muons at the gas target have a stochastic distribution which makes the individual detection of the muons entering the gas target in a nondestructive way, imperative to the experiment. The nondestructive muon detection has two different aims, on one hand it aims de muon detection entering the gas target and uses that signal

as the laser trigger, on the other hand it also serves to frictionally cool [71] more the muons to 5-8 keV. Muons arriving the gas target find in the way 2 stacks of stainless steel rings (S_1 and S_2, see Fig. 2.3) kept on negative high-voltage. The incoming muon will first pass through the S_1 stack. The S_1 stack contains 15 rings, where 4 of them (8 to 12 in the muon direction) contain ultra-thin ($d = 4\mu$g cm^{-2}) carbon foils. S_2 only contains 5 rings with the third ring carrying a carbon foil. Each muon passing through the carbon foils releases a few electrons which are separated from the much slower muons in an $\mathbf{E} \times \mathbf{B}$ separator field. The electrons are detected by scintillators connected to photomultipliers, PM1 for the electrons created in the first stack S_1 and PM2 and PM3 for the electrons created in the second stack S_2. The coincidence signal between the electrons of S_1 and the electrons of S_2 together with the ToF of 5 keV muons are used as trigger system for the DAQ and the Laser.

2.3 The gas target

Finally, after being detected by the nondestructive muon detection system, the muons reach the gas target. Inside the low pressure He gas target, the they suffer several collisions (≈ 200) before its energy is below the ionization energy of He and gets weakly bound to a He nucleus. The gas target with a shape volume of $5 \times 12 \times 194$ mm is mounted inside the solenoid bore hole of 20 cm length and is surrounded by a multipass cavity and below and above with several x-ray detectors. Outside the target area there are plastic scintillator paddles arranged in an X shape around the muon beam for the electrons detection. The gas target is enclosed horizontally by the multipass cavity and vertically by thin, aluminum coated foils which protect the LAAPDs placed on top and bottom of the gas target from laser light. In order to keep the He gas as pure as possible, the gas in the target is continuously exchanged by a circulation system that has been built and which also contains a He purification mechanism.

2.3.1 The multipass cavity

The multipass cavity has been specially designed and built for the CREMA experiments [72]. In Fig. 2.4 the cavity is schematically shown and its principle is demonstrated. It has been designed to be robust, to illuminate the whole gas volume reasonably homogeneously and to have long term stability. It is composed by two elongated mirrors that enclose the gas target horizontally. Both mirrors have a reflectivity of 99.98% in the 800 to 1000 nm range and have silica as

subtract material. The coated surface has the dimensions of 190×12 mm^2. One of the mirrors is flat (M_1) and has at its center a 0.6 mm diameter hole from where the laser pulse enters the cavity. The cylindrical mirror M_2 (110 mm radius) confines the light in the vertical direction. Horizontal confinement is accomplished by cylindrical "ears" mounted at the ends of the flat mirror substrate such that the mirror surfaces merge continuously.

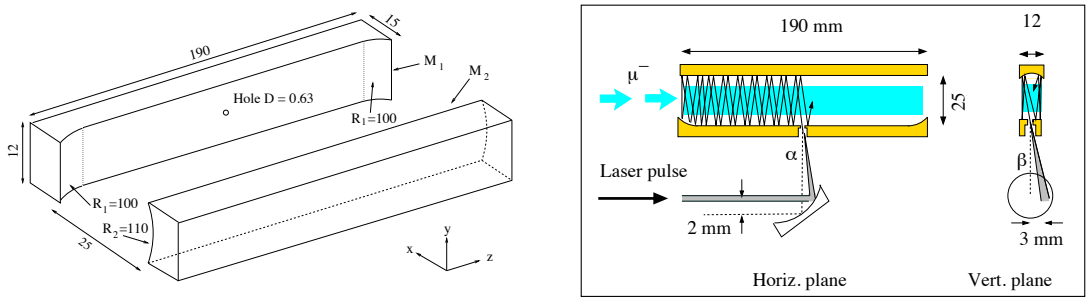

Figure 2.4 – The multipass cavity. The multipass cavity consists of two 190 mm long mirrors. A focusing optical element is used to inject the light through the 0.63 mm large hole in the flat mirror (M_1). The light confinement is created vertically by the cylindrical mirror (M_2) and horizontally by the end caps of the flat mirror (M_1). Injection under a slightly tilted angle in horizontal and vertical direction (α and β) is used in order to illuminate all volume almost homogeneously.

The light enters the cavity with slightly tilted vertical α and horizontal β angles (see Fig. 2.4) in order to illuminate all volume. This is achieved by using a paraboloid and hitting it of-center with the laser, causing the beam to be injected in an angle other than perpendicular. The laser light is focused through the injection hole. The total coupling efficiency through the injection hole was measured to be 95%. The lifetime of the light inside the cavity is $\sigma_c \approx 110$ s that corresponds to ≈ 1300 total number of reflections. This lifetime is constrained by the size of the injection hole, the reflectivity of the mirrors coating and by the gaps between the flat mirror and the cylindrical end caps. The laser fluence F in the cavity can be parametrized as

$$F = f_t f_c \frac{n_{\text{ref}}}{A} \cdot E_{\text{laser}}, \tag{2.4}$$

being f_t the transfer efficiency of the light from the laser output to the target cavity entrance, f_c the coupling efficiency through the $\phi = 0.6$ mm diameter hole, $A = 8.8$ cm^2 is the illuminated mirror surface, n_{ref} the number of reflections and E_{laser} the pulse energy from the laser. This fluence can be compared to the *saturation* fluence for each transition. To avoid power broadening of the resonance

lines we have to work at, or below half of the saturation fluence. Table A.1 gives the saturation fluence for all possible $2S-2P$ in μ^4He^+ and μ^3He^+. With an average output energy between 3 mJ and 10 mJ depending on the wavelength, it results in a fluence in the cavity between 0.4 J/cm^2 and 1.4 J/cm^2 which is therefore considered enough to measure all intended transitions.

2.3.2 Electron and x-rays detection

The deexcitation of the recently produced muonic helium ion from $n \approx 14$ to the $1S$ state is followed by emission of *prompt* x-rays. The deexcitation from the laser induced $2P$ sate to the ground state is followed by immediate emission of 8.1 keV x-ray. Being the muons unstable elementary particles, it will finally decay to an electron antineutrino and a muon neutrino

$$\mu^- = e^- + \bar{\nu}_e + \nu_\mu. \tag{2.5}$$

All these events have to be detected in order to determine the *Lamb Shift* transition energy. A compact dedicated detector system has been developed for this purpose. Figure 2.5 schematically illustrates the arrangement of the detector system present around the gas target.

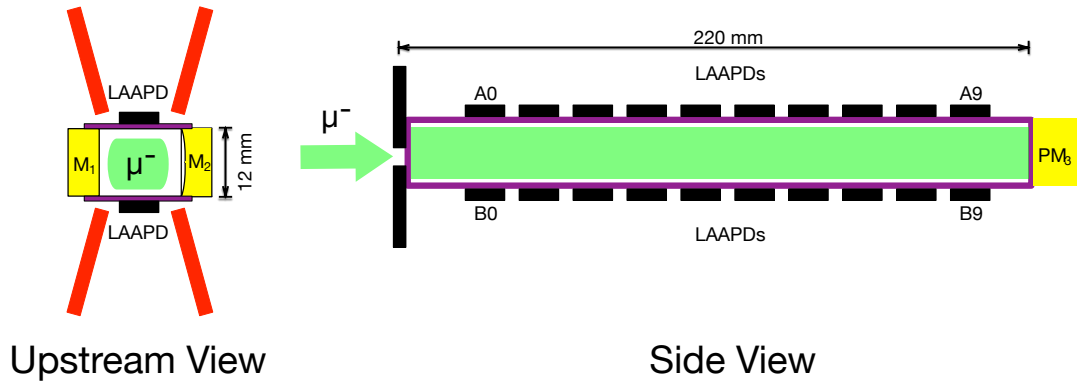

Figure 2.5 – Illustration of the x-ray and electron detectors in a sectional view. (Left) Upstream view showing the four plastic scintillator plates placed outside the gas target in X shape. Each pair of scintillator paddles (left or right) are read out by a photomultiplier. M_1 and M_2 are the mirrors from the multipass cavity. (Right) Side view of the muon beam entering the target system. On the top and below there are two arrays of APDs, each with 10 detectors labelled from $A_0 - A_9$ (the top array) and $B_0 - B_9$ (the below array).

For the x-rays detection in the experiment, it is required that the detectors are relatively compact, with large active area and good energy resolution, fast time

response and able to work in a 5 Tesla magnetic field. Considering these requirements and the previous experience in the μp experiment, Large Area Avalanche Photodiodes (LAAPDs, or short APDs) [73], have been used in the *Lamb Shift* experiment of μHe. They are biased with a high reverse voltage of 1600-1690 V resulting in a gain of 200. Two arrays of 10 APDs are used. They are located face-to-face above and below the gas target at 8 mm from the muon beam center covering roughly 30% of solid angle in which the x-ray are emitted. The individual APDs have an active surface of 14×14 mm^2 and are installed very close to each other reducing the size of the gap between them. In the above array the single APDs are labeled as $A_0 - A_9$ and $B_0 - B_9$ in the array below the gas target (see Fig. 2.5). Each APD has a pre-amplifier right next to it, a low noise charge sensitive pre-amplifier designed by ETH and responsible for the first amplification stage by a factor of about 100. Post-amplifiers outside the vacuum of the PSC further amplify the signal (4×) to a final signal amplitude of about 200 mV. A closed ethanol circuit is used to cool down the APDs to −30 C° and stabilize to temperature variations of less than 0.1 C°. Under all these conditions, an energy efficiency of 50% and a 15% energy resolution for 8.1 keV x-rays is achieved. The signal of each APD is recorded on a circular memory buffer of a WaveForm digitizer (WFD) and a Time-to-Digital Converter (TDC). A complete description and characterization of the APDs used in the muonic helium isotopes *Lamb Shift* experiment can be found in [74].

The electrons from the muon decay have energies in the MeV range and are detected by four plastic scintillator paddles with dimensions of $250 \times 60 \times 5$ mm^3 placed outside the gas target in a X shape (see Fig. 2.5). The electrons created in the muon decay close to the muon beam axis, due to the strong 5 Tesla magnetic field, spiral out from the gas target and hit the plastic scintillator plates. The paddles are connected to two photomultipliers (PMT) which reads out the two paddles on the left and on the right, being the signals only distinguishable from left to right. Before being recorded to a TDC the signal from each (PMT) is discriminated into signals of four different amplitudes. Besides being detected in the scintillator paddles, the electrons might also deposit energy (10-20 keV) in the APDs originating signals with high amplitudes. The electron detection by plastic scintillators or APDs in coincidence with x-ray detection in an APD is used to reduce the background of the experiment - the detection of an electron in the scintillator paddles after an x-ray signal from the APDs insures that the signal from the APD has not been created by the electron from the muon decay.

2.4 Laser system

As discussed, the nondestructive muon detection system provides the stochastic trigger to the laser system and Data Acquisition (DAQ). With an average rate of muons of $\approx 500\ s^{-1}$, the laser has to deliver pulses of 4.5 mJ (in average) and has to be stochastically triggered with an average rate of $\approx 500\ s^{-1}$. Being the lifetime of the $2S$ state, $\tau_{2S} = 1.71\ \mu s$, the laser has to be fast enough to insure that the delay between the trigger to arrival of the pulse inside the cavity is $< \tau_{2S} = 1.71\ \mu s$. In order to be able to record the resonance, the laser has to be tunable for 2 THz (5 nm) around each predicted line (see Table A.1 for all predicted line values) and to have a bandwidth < 10 GHz to scan and search for the resonance. A scheme illustrating the complexity of the laser system is shown in Fig. 2.6.

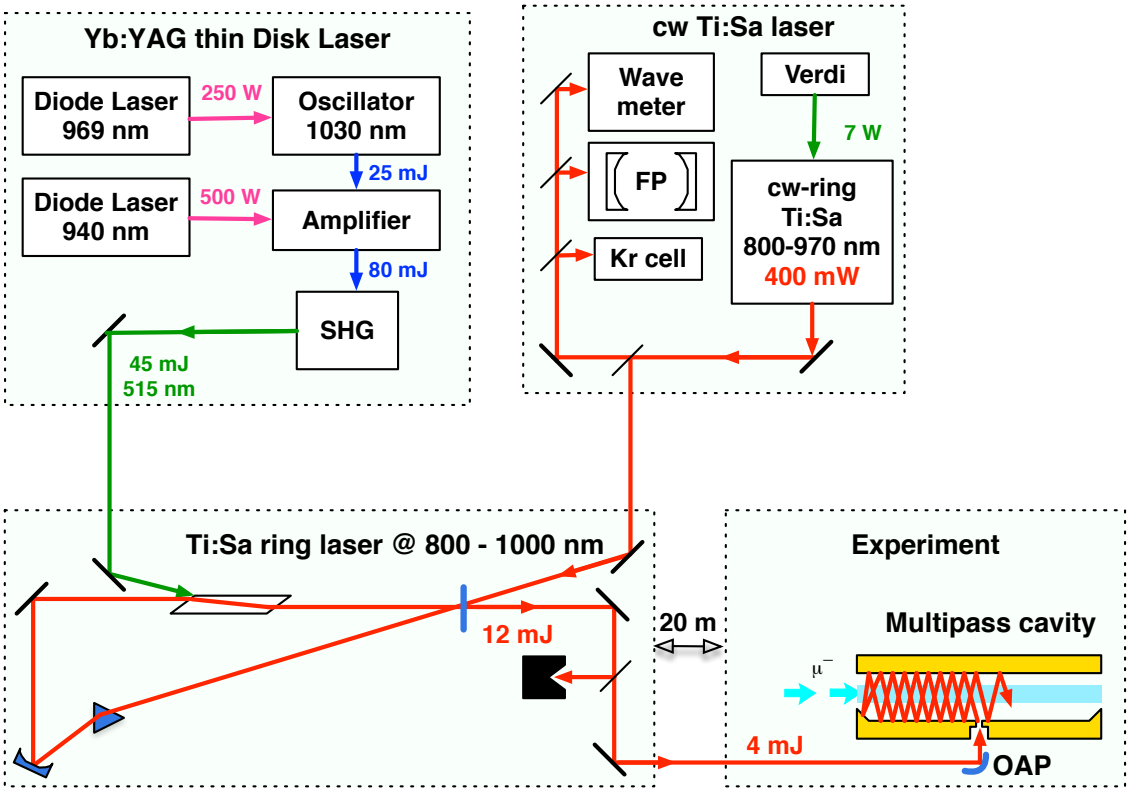

Figure 2.6 – Schematic drawing of the laser system used in the experiment. The main components are a pulsed thin-disk laser with frequency doubling, a tunable cw Ti:Sa laser, a pulsed oscillator-amplifier Ti:Sa laser, and a multipass mirror cavity with its diagnostic system. FP: Fabry–Perot, Kr cell: Krypton absorption cell.

As for the other described systems of the experiment, another requirement for

the laser system is the very good long term stability and reliability for continuous months of active operation. The laser system is composed by three main distinct parts. A pulsed amplifier Titanium-Sapphire Ti:Sa oscillator tunable in the required range of 800-1000 nm (see Table A.1 for all *Lamb Shift* transitions), pumped by a frequency-doubled Ytterbium-YAG (Yb:YAG) thin disk laser [75, 76] and injection seeded by a frequency controlled continuous wave (cw) Ti:Sa ring laser. Although it has been aimed and possible to have a laser with roughly at one third of the saturation intensity of the intended measurements of the *Lamb Shift* transitions, the laser has been mostly operated at lower values in order to avoid damage on the cavity mirrors.

The laser system used in the $\mu^4\mathrm{He}^+$ and $\mu^3\mathrm{He}^+$ experiments is very similar with the one used in the μp and μd experiments [77]. The description of the laser system is presentes in more detailed in the following.

2.4.1 Thin disk laser

The signal from the muons entrance nondestructive detector system triggers two parallel Yb:YAG thin disk laser systems. Each disk laser system consists out of a Q-switched oscillator followed by a 8-pass thin disk amplifier. The disk of the oscillator is cw pumped by a diode laser (969 nm) with 250-W. To achieve a minimal intrinsic delay of the laser pulse buildup, the Yb:YAG oscillators have been operated in "cw-prelasing" mode.

After a muon trigger, the Q-switched oscillator cavities are closed by switching one of the two High-Voltage (HV) electrodes of their Pockels cells (PC) within a few nanoseconds. Fast intra-cavity pulse build-up follows. After a delay of about 200 ns the cavities are opened by switching the second electrode of the PC. The circulating power is thus released and the emitted pulse enters the multipass amplifier. The 8 pass thin disk amplifier is pumped by a second diode laser (940nm) with 500 W. The gain depends on several parameters as the pump power density, temperature, thickness of the disk. Pulses exiting the disk amplifier have energies of 80 mJ at 1030 nm.

A second harmonic generation (SHG) stage based on LBO crystals (Lithium triborate LiB_3O_5) is used to convert the two disk-laser pulses from 1030 nm to 515 nm. These pulses, with an energy of 45 mJ at 515 nm have now a suitable wavelength and are used for pumping the Ti:Sa laser.

2.4.2 Ti:Sa laser

The Titanium-Sapphire Ti:Sa oscillator is an injection seeded ring laser by a frequency controlled cw Ti:Sa ring laser, meaning that the frequency of the Ti:Sa laser is controlled by injection seeding the Ti:Sa oscillator with a single-mode cw Ti:Sa laser. Therefore, tuning the wavelength of the cw Ti:Sa laser leads to a tuning of the frequency of the Ti:Sa pulses. The seed Ti:Sa laser is tunable in the interval of 800-1000 nm, which covers most of the $\mu^4\mathrm{He}^+$ and $\mu^3\mathrm{He}^+$ *Lamb Shift* transitions (see Table A.1), and is pumped continuously with 7 W at 532-nm provided by a frequency-doubled Nd:YVO_4 diode laser.

The stability of the cwTi:Sa laser is guaranteed by locking it to an external reference Fabry-Perot cavity. This Fabry-Perot cavity is temperature stabilized and low expansion cavity and has been calibrated by means of two-photon spectroscopy of well-known Rb and Cs lines. The resulting free spectral range was measured to be 1497.33(4) MHz in the 812 nm region. The frequency of the cw Ti:Sa laser is thus absolutely known with a precision of 30 MHz.

The frequency of the pulsed Ti:Sa laser equals the frequency of the cw Ti:Sa. In order to avoid uncertainties related with any chirping effects in the Ti:Sa laser, the pulses Ti:Sa oscillator are also calibrated by means of Cs one- and two-photon spectroscopy. In such a way, the frequency of the pulses used to drive the $2S - 2P$ resonance is known over all scanning range with an accuracy better than 200 MHz.

The final pulses, with energies in the range of 4 mJ, exiting the Ti:Sa oscillator are sent to the non-resonant multipass cavity (Section 2.3.1) which is located roughly at 20 m distance.

Chapter 3

LAAPDs data analysis

The recorded data from the experiment is organized by *runs*. Each *run* has about one hour of data taking and is recorded in a single file. Between *runs*, the frequency of the laser can be changed and, if necessary, one can enter inside the safety zone in order to fix some parameters that could have changed during the last *run*.

The structure of the recorded data is based on event-structure. It is defined by the detection of a muon in the nondestructive muon detection system by the coincidence of the signals from the electrons released in two stacks of carbon foils with the muon Time-of-Flight (ToF). As mentioned this event triggers the laser but it also triggers the start of an event gate (EVG). An EVG is 20 μs long and it only starts if the frontend (FE) computer is ready. The single hits on the detectors detected in this time interval are written on a ring buffer of the VME modules (TDC, WFD).

The formation of a muon ion is confirmed by a x-ray hit in the APDs. If this occurs, besides knowing that a muon has formed a bound state with a nucleus of the gas in the target, the APD gate opens. The electrons from the muon decay are detected by the plastic scintillator paddles as explained in Section 2.3.2 and sorted by their amplitude in four categories. After the EVG of 20μs, the (EEVG) signal closes the event gate. A STROBE signal is created whenever the EEVG signal and the APD gate are active. This STROBE signal stops the data recording of the WFDs and TDCs. After being stopped, the data can be readout and sent to a memory of the frontend (FE). From there the data is sent to a backend (BE) computer and recorded in a hard drive. After being sent, the FE is once again

ready for a new event. This data event-structure has the advantage of saving hard drive space without losing any important information and facilitates the data analysis afterwards. The software used for the DAQ system has been MIDAS [78, 79] and ROOT [80–82] has been used for the data analysis and the online-analysis.

The online-analysis is based on the data monitoring in real time. Energy and time spectra are stored and checked without performing a very detailed data analysis. No rigorous energy or time calibration is performed and no significant cuts or coincidences are performed.

The data analysis is performed with the main purpose of finding good events in the enormous amount of data. The coincidence in a time window of the signal of the muon entering the target (the laser is triggered and the pulse is sent to the multipass cavity) followed by the detection of a delayed kα x ray of 8.2 keV by the APDs and the subsequent detection of the electron from the muon decay by the APDs and the scintillator paddles is the so-called good event. The discrimination of these events in the overall data, significantly reduces the background together with time and energy calibrations for all detectors and applying electron and muon energy cuts.

The energy of the *Lamb Shift* transition is then determined by fitting a Lorentzian to a plot of the delayed kα x-rays versus the laser frequency normalized with the prompt x-rays.

3.1 LAAPD's waveform analysis

The hits in the APDs during an EVG are recorded by wave form digitizers (WFD). The current signal is converted in a negative voltage signal and subsequently digitized by the WFD. The amplitude of the recorded waveforms depends on the energy deposit by the particles in the APD. As mentioned, besides the prompt x-rays from the muonic ion deexcitation cascade and the delayed $2P-2S$ kα x-rays, the electrons resulting from the muon decay also deposits energy in the APDs. Figure 3.1 shows pulses from APD_A6 directly from the WFD. As it can be seen, there are two signals present in the Figure. One at ≈ 960 time bins with lower amplitude and another signal at ≈ 2450 time bins with higher amplitude. Each time bin corresponds to 4 ns and the amplitude voltage has 4096 channels corresponding to 1 V. The first signal corresponds to an 8.2 keV x-ray event from either the *prompt* x-rays from the muon cascade towards the ground state or from the delayed $2S-1S$ transition x-ray of the $\mu^4\mathrm{He}^+$. The second signal is originated by an electron which has been probably originated from muon decay

that is depositing energy in the APD.

In order to obtain useful time and energy information, a complete and careful characterization of the waveforms from the APDs is needed. The analysis of the waveform from the APDs is performed by the following steps:

- Find the edge time bin, *i.e.*, the time where the pulse begins;
- Guess a standard wave form (SWF) for the pulses;
- Fit a set of hand-selected "known-good" waveforms with the SWF;
- Get a fitted amplitude for the pulse;
- Average all fits and try to fit the pulses evaluating the reduced χ^2 of each guessed SWF as goodness-of-a-fit parameter.

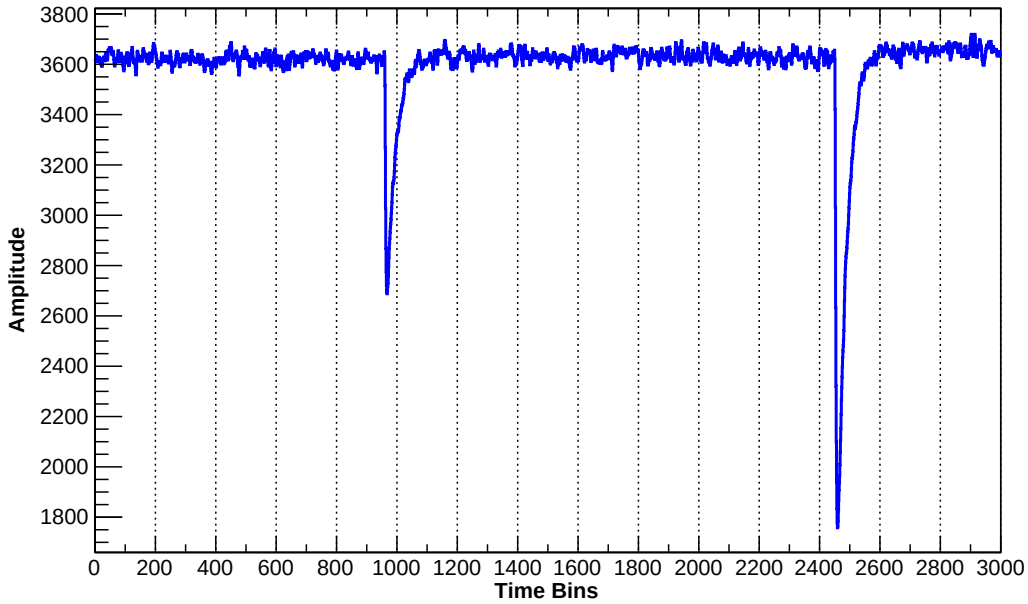

Figure 3.1 – Pulses from the APD_A6 directly from the WFD in the μ^4He^+ experiment. Two different distinct signals are shown. One at $\approx$ 960 time bins with lower amplitude and another signal at $\approx$ 2450 time bins with higher amplitude. Each time bin corresponds to 4 ns and the amplitude voltage has 4096 channels corresponding to 1 V.

In the setup phase of the experiment, two different pulses for the same x-ray energy from a radioactive source has been observed in a test setup. Also, as it can be seen in Fig. 3.2, for the 8.2 kα x-rays from the μ^4He^+ experiment, two different waveform shapes with different rise times of the pulses has been

observed. Figure 3.2 shows a set of hand-selected "known-good" signals from a single APD (APD_A6). By finding the edge time bin,*i. e.*, the time where the pulse begins, the pulses where shifted so they start all at the same bin. As it can be seen, two different waveforms are clearly noticeable with two different shapes, amplitudes and rise times for the same x-rays energy. This effect had been already reported [83] for beveled edge APDs and 14.4 keV x-rays.

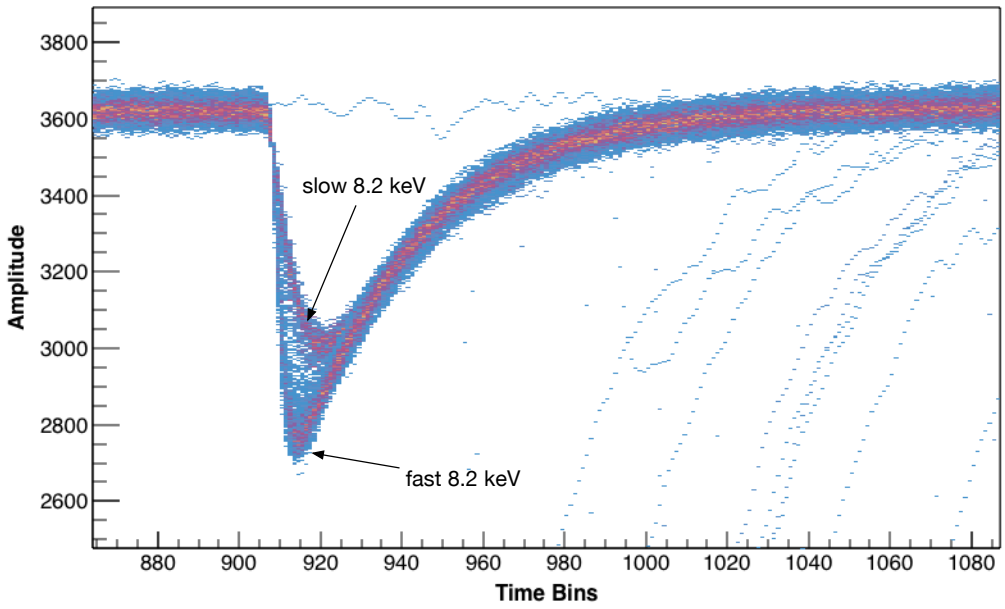

Figure 3.2 – Set of hand-selected "known-good" response pulses to 8.2 keV x-rays from a single APD (APD_A6). The data has been recorded in the μ^4He^+ experiment. Two distinct responses from the monoenergetic x-rays can be seen, labeled as slow and fast 8.2 keV x-rays since they clearly show two different rise times.

The origin of this effect in our experiment comes from the different region where the 8.2 kev x-ray is absorbed in the APD [84]. Figure 3.3 illustrates the working principle of the APD used in the muonic helium *Lamb Shift* experiment and explains the different possibilities from where this effect comes from. The calculated absorption length for 8.2 keV x-rays is 70 μm from National Institute of Standards and Technology (NIST) database. Yet, an effective 1.6 times longer average path inside the APDs from the x-rays happens in the setup due to the extended size of the x-ray source. This makes the absorption length of the 8.2 keV x-ray similar to the APD layer thicknesses leading to an APD output which depends on the region where the photon is absorbed. The detector energy acceptance depends on the thickness of the conversion region (II) of the APD. It is in this region that the primary photoelectrons are created by the absorption of

incoming photons. On the back side of this layer, an avalanche region is created by placing a p-n junction (III). Inside this region, electron impact ionization at the high field p-n junction leads to a multiplication of free charge carriers providing gain for the initially converted primary photoelectrons. Figure 3.3 exemplifies the three possibilities of effects in the APD depending on the region where the x-ray is absorbed. The 8.2 keV can be absorbed in the 3 different regions of the APD. Yet, most of them are absorbed in the conversion region and follows the normal APD working principle that provides high charge collection efficiency and fast amplification which corresponds to the fast 8.2 keV x-rays signals identified in Fig. 3.2. The x-rays absorbed in the amplification region undergo only partial amplification resulting in low amplitudes down to zero [83]. If the incoming x-rays are absorbed in the drift region, they generate electrons which are only slowly transferred to the following region (avalanche region) due to the lower field strengths of the drift region. This region may hold electrons for non-negligible times which slows down the pulse and reduces its amplitude, being the identified slow 8.2 keV x-rays signals in Fig. 3.2 the pulses from x-rays absorbed in the drift region.

This APD behavior strongly affect the energy resolution of the APDs when calculating a simple integral over the recorded pulses. This results in a double-peak structure for the same x-ray energy, being the calculated integral from the slow rise time 8.2 keV pulses giving a less energy value than the fast rise time 8.2 keV [84].

In an effort to try to correct this effect, mainly to improve the energy resolution of the APDs and to reduce the background, the characterization of the APDs waveform response has been tried by fitting the waveforms using two different functions based on probability distributions: a log-normal distribution and a exponentially modified gaussian distribution. These two distributions have been chosen by their fast growth to the maximum probability value and their slow exponential decay. Moreover, in both distributions the width and the slow exponentially decay can be parametrized.

The lognormal distribution is given by

$$f(x;m,s) = \frac{1}{xs\sqrt{2\pi}}\, e^{-\frac{(\ln(x)-m)^2}{2s^2}}, \tag{3.1}$$

from where the mean μ, variance σ^2, skewness γ_1, and kurtosis γ_2 are given from the distribution m and s parameters as

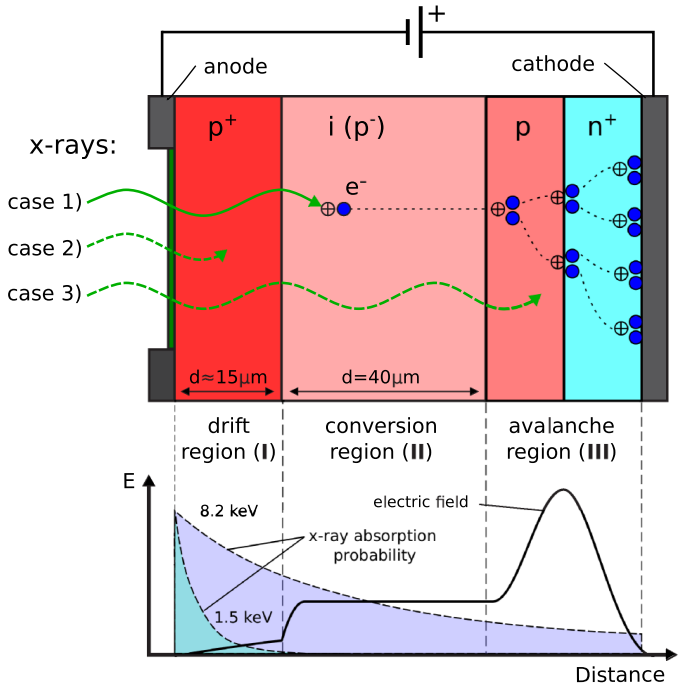

Figure 3.3 – Working principle of avalanche photodiodes based on a p^+-i-p-n^+ doping profile. The weakly doped intrinsic part (II) serves as conversion region for most incoming x-rays (case 1). Photoelectrons created are transferred towards the avalanche region. In this high field area, secondary electrons are generated through impact ionization providing charge gain. Low energy x-rays have a high probability of being stopped in the initial drift region (I) (case 2). These experience additional signal delay and reduced gain. Some photons convert in the multiplication region (III), also leading to reduced signal amplitudes (case 3). The bottom figure shows the electric field profile in the several regions of the APD together with the x-ray absorption profile for 1.5 keV and 8.2 keV x-rays. Figure and caption taken from Reference [84].

$$
\begin{aligned}
\mu &= e^{m+s^2/2} \\
\sigma^2 &= e^{s^2+2m}(e^{s^2}-1) \\
\gamma_1 &= \sqrt{e^{s^2}-1}(2+e^{s^2}) \\
\gamma_2 &= e^{4s^2}+2e^{3s^2}+3e^{2s^2}-6\cdot
\end{aligned}
\tag{3.2}
$$

The exponentially modified gaussian distribution is derived via convolution of the normal and exponential probability density functions and is given by

$$
f(x;\mu_g,\sigma_g,\lambda) = \frac{\lambda}{2} e^{\frac{\lambda}{2}(2\mu_g+\lambda\sigma_g^2-2x)} \operatorname{erfc}\left(\frac{\mu_g+\lambda\sigma_g^2-x}{\sqrt{2}\sigma_g}\right), \tag{3.3}
$$

where μ_g is the mean of the gaussian component, σ_g^2 is the variance of gaussian

component and λ is the rate of the exponential component. The erfc component is the complementary error function defined as

$$\mathrm{erfc}(x) = 1 - \mathrm{erf}(x) = \frac{2}{\sqrt{\pi}} \int_x^\infty e^{-t^2} dt\cdot \tag{3.4}$$

The mean μ, variance σ^2, skewness γ_1, and kurtosis γ_2 for the modified gaussian distribution are given by

$$\begin{aligned}
\mu &= \mu_g + 1/\lambda \\
\sigma^2 &= \sigma_g^2 + 1/\lambda^2 \\
\gamma_1 &= \frac{2}{\sigma_g^3 + \lambda^3}\left(1 + \frac{1}{\sigma_g^2 + \lambda^2}\right)^{-3/2} \\
\gamma_2 &= \frac{3(1 + \frac{2}{\sigma_g^2\lambda^2} + \frac{3}{\sigma_g^4\lambda^4})}{\left(1 + \frac{1}{\sigma_g^2\lambda^2}\right)^2} - 3\cdot
\end{aligned} \tag{3.5}$$

To obtain a standard wave form (SWF) for each of the identified pulses (slow and fast 8.2 keV x-rays), two histograms have been constructed by the set of hand-selected "known-good" pulses of Fig. 3.2 in which the slow and fast rise times of the 8.2 keV x-rays have been separated, *i.e.*, one histogram has been constructed with the slow 8.2 keV x-rays and the other with the fast 8.2 keV x-rays. These histograms have been filled in the following way: at each time bin i, the amplitude $A(i)$ is calculated as the mean value of the amplitude from the n hand-selected pulses with similar rise times

$$A(i) = \frac{1}{n} \sum_{i=0}^{i=n} A_i. \tag{3.6}$$

At each bin, the corresponding bin error δA is calculated as the standard error of the mean

$$\delta A(i) = \frac{\sqrt{\frac{1}{n} \sum_{i=0}^{i=n} (A_i - A(i))^2}}{\sqrt{n}}. \tag{3.7}$$

Two functions, LogN and ExpG, based in the above described probability distributions with adjustable parameters, have been fitted by χ^2 minimization to the constructed histograms. These functions have been defined as

$$\begin{aligned} \text{LogN} &= b - A\frac{1}{(x-x_0)s\sqrt{2\pi}}\, e^{-\frac{(\ln(x-x_0)-m)^2}{2s^2}} \\ \text{ExpG} &= b - A\frac{\lambda}{2}\, e^{\frac{\lambda}{2}(2\mu_g+\lambda\sigma_g^2-2(x-x_0)}\, \text{erfc}\Big(\frac{\mu_g+\lambda\sigma_g^2-(x-x_0)}{\sqrt{2}\sigma_g}\Big), \end{aligned} \tag{3.8}$$

where b is the baseline coefficient, x_0 the time bin edge, A the amplitude and s, m, λ, μ_g and σ_g are the probability distribution parameters that have been also considered as adjustable coefficients of the fit functions. Figure 3.4 shows the previously described histograms and the functions from Eq. (3.8) fitted to each histogram. The full black line corresponds to the constructed histograms with the respective bin errors, the dashed red line corresponds to the best fit with the LogN function and the full green line corresponds to the ExpG function.

As it can be seen, the pulses can be reasonably parametrized by using the functions of Eq. (3.8) as SWF of the APD pulses. Yet, the averaged histogram of the fast 8.2 keV x-rays is better parametrized with the ExpG function than with the LogN function, being the obtained reduced χ_r^2 value of 8.60 for the ExpG function and 12.29 for the LogN function. For the averaged histogram of the slow 8.2 keV x-rays the situation has been the opposite: the histogram is better parametrized with the LogN function with a $\chi_r^2 = 4.27$ against a $\chi_r^2 = 19.96$ for the ExpG.

Since the χ_r^2 values from the best fits with the two functions are very different, we have found two different SWF for the two distinct APD pulses. From the best fit coefficients, we can now construct two SWF with the timing of the trace as the only free parameter and fit each signal to decide whether the fitted signal appears as a slow or a fast x-ray. The amplitude can be parametrized from the integral of the signal and the baseline as a average of the amplitude when in the absence of a pulse. After being identified, the different APD pulses can be calibrated individually to the 8.2 keV energy and improve the APD energy resolution.

With the obtained two SWF for the two distinct signals, the signals from the APD are then fitted with the SWF in order to be characterized. This works as follows: the edge of the pulse beginning is found by an algorithm that scans the histogram, 5 bins at a time. From the amplitude value of each bin the algorithm calculates a slope of a straight line passing on these points. If the slope is negative and above a certain threshold (to avoid incorrect edges calculation from the baseline noise) an edge is founded and recorded with the time of the first bin from the set of 5 bins. The baseline b is calculated by the same algorithm. Every time the edge finder is scanning the histogram out of the signal range, an average

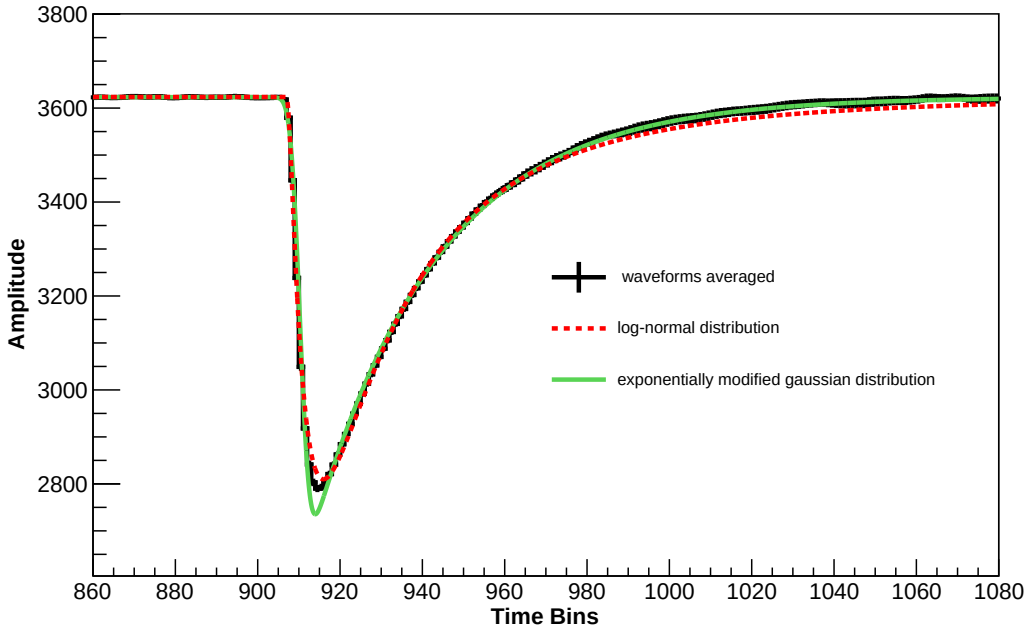

a) Fast 8.2 keV x-rays.

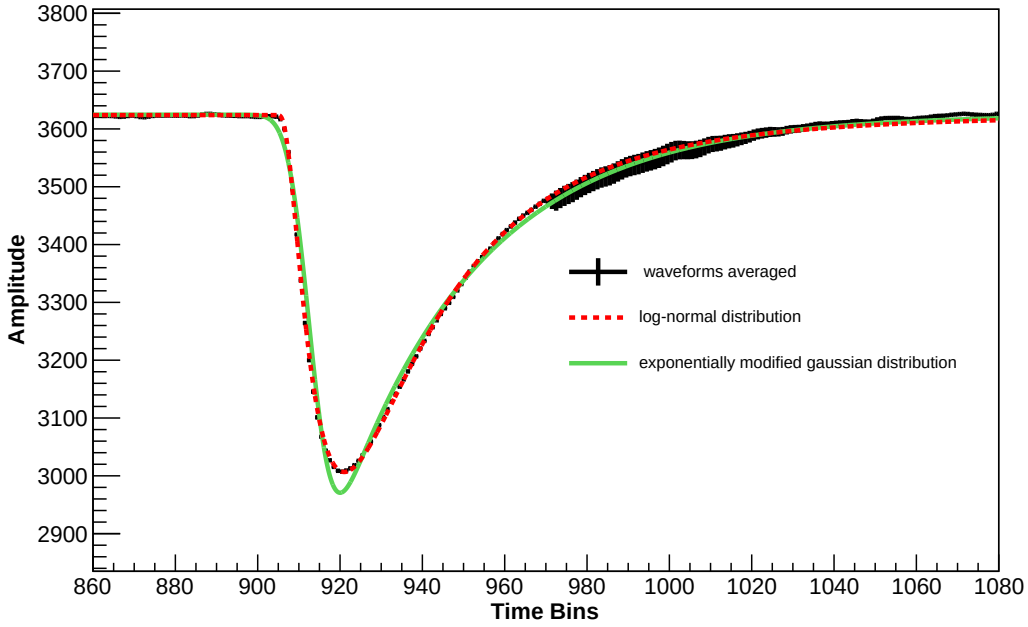

b) Slow 8.2 keV x-rays.

Figure 3.4 – Histograms constructed by averaging a set of hand-selected "known-good" pulses from Fig. 3.2 and separated by they distinct rise time. The full black line corresponds to the constructed histograms with the respective bin errors (see text), the dashed red line corresponds to the best fit with the LogN function and the full green line corresponds to the ExpG function. Both functions are defined in Eq. 3.8. The fits have been performed by χ^2 minimization and the best fit coefficients obtained for the best fit functions in each histogram.

amplitude is calculated and used as the baseline parameter of the functions of Eq. (3.8). The amplitude is parametrized from the amplitude coefficients A of Eq. (3.8) obtained from the fits to the averaged constructed histograms of Fig. 3.4 and the integral value of the signal. All the remaining adjustable coefficients of the two SWF functions of Eq. (3.8) are then fixed from the best optimized values from the fits performed by χ^2 minimization to the averaged histograms.

When a edge is found, the reduced χ^2_r is calculated for the two SWF functions (with all the adjustable coefficients fixed) by

$$\chi^2_r = \frac{1}{\nu}\sum_{i=1}^{n}\frac{(A(i)-\mathrm{SWF}(i))^2}{\mathrm{SWF}(i)}, \tag{3.9}$$

being n the number of bins, $A(i)$ the amplitude of the pulse, $\mathrm{SWF}(i)$ the calculated amplitude with the SWF function and $\nu = n-m$ the number of degrees of freedom, being 0 in this case the number of adjustable parameters m. Finally, from the best χ^2_r value from the two SWF is decided whether the fitted signal in the analysis appears as a slow or a fast x-ray.

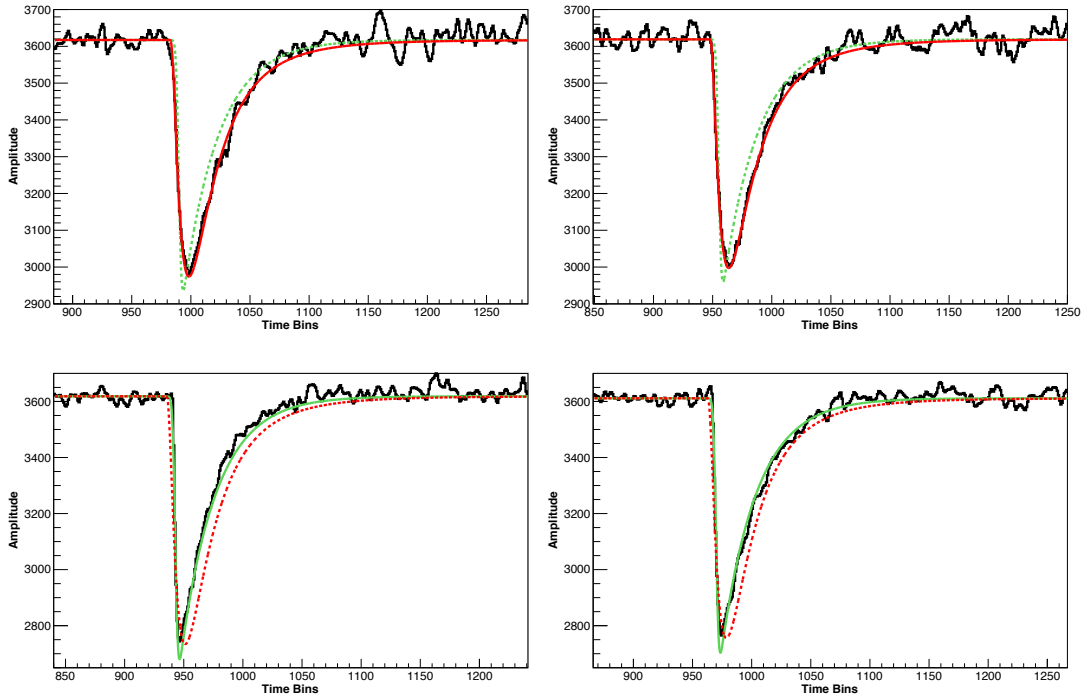

Figure 3.5 – Example of 4 different APD pulses fitted with the 2 parametrized standard waveforms. The red line represents the function LogN and the green line the ExpG defined on Eq. (3.8). Full lines represent the chosen best fit by a χ^2_r calculation and the dashed lines the rejected fit. In the two upper APD signals the LogN fit function is selected (slow x-ray) while in the lower APD signals the ExpG fit function is selected (fast x-ray).

Figure 3.5 shows 4 examples of APD pulses in which the explained procedure is exemplified. The red line represents the function LogN and the green line the ExpG of Eq. (3.8). Both SWF functions are fitted to each signal presented on Fig 3.5. By the best χ^2_r value ,the SWF is selected and is represented in the Figure by the full line while the rejected SWF is represented by the dashed line. The two different APD behavior output is clearly noticeable which we have been able to identify and characterize by this procedure.

3.2 Particle identification with LAAPDs

While performing the characterization of the different pulses from the APDs, another different behavior has been observed. As mentioned, electrons resulting from the muon decay often deposit energy in the APDs. Figure 3.6 shows two pulses in a event from one of the APDs. As in Fig 3.1, the first pulse results from a x ray absorbed in the APD and the second pulse, with higher amplitude, comes from an electron which has deposit some energy in the APD, probably originated by the muon decay.

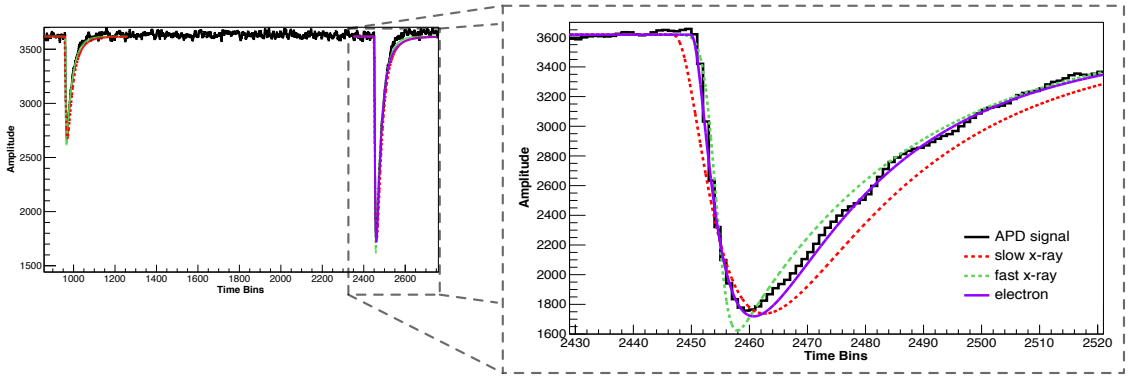

Figure 3.6 – (Left) Pulses from one APD directly from the WFD in the μ^4He^+ experiment. First pulse results from a x ray absorbed in the APD and the second pulse, with higher amplitude, comes from an high energy electron which has deposit energy in the APD. Both signals had been found by the edge finder algorithm and the fast and slow SWF have been fitted to both signals. Dashed lines correspond to rejected SWF and full lines represent the SWF with smaller χ^2_r value. The smaller signal is better fitted with the ExpG SWF. (Right) Zoom in of the signal with higher amplitude. Both constructed SWF do not fit the signal well, being its rise time in between the SWFs. Another SWF has been constructed ($LogN_{Elec}$) using the LogN function of Eq. (3.8) by fitting a set of hand-selected "known-good" electron pulses.

By executing the explained procedure to characterize the APD waveforms, it has been found that the signals coming from the detection of electrons on the

APD had another SWF, different from the parameterized slow and fast 8.2 keV x-rays. Whereas the pulse generated by the x-ray is accurately fitted by the fast SWF, the rise time of the electron is between both parametrized SWF, being the latter not well fitted by neither of the constructed standard waveforms. Having the electrons in the experiment energies up to 50 MeV, they deposit up to 50 keV in the APD due to their passage through all the APD layers, showing a waveform with a different shape. Another SWF ($\mathrm{LogN_{Elec}}$) has been constructed using the same procedure that has been used to parametrize the fast and slows x-rays SWF. From fitting the functions of Eq. (3.8) to a set of hand-selected "known-good" electron pulses, the function based on the log-normal probability distribution has shown a better χ^2_r. With the optimized coefficients from the fit and parametrizing the amplitude as a function of the integral of the pulse, a distinct SWF for the electrons $\mathrm{LogN_{Elec}}$ has been constructed. By fitting all signals with the selected SWFs, we are able not only to improve the energy resolution of the APDs by calibrating individually the fast and slow x-rays to 8.2 keV, but also to reduce background by identifying the signals resulting from an energy deposition by an electron and removing them from the energy spectra of the APDs.

For the final data analysis of the experiment, it has been decided to use SWFs constructed by a numerically averaging pulses from a collection of selected APD signals for the electrons and for the slow and fast 8.2 keV [84], after shifting each signal to correct for the variation of the beginning of the signal edge, in a similar way as it has been done for Fig. 3.2. In order to select the different waveform classes for the numerical average, the rise time as a function of the integral has been plotted for roughly 2.5×10^4 APD signals. Figure 3.7 shows a example of such a plot. Four different contributions can be identified. With slightly different integral values, the two most prominent peaks result from the two different rise times of the 8.2 keV, the slow and fast 8.2 keV. For the integral value < 200, the low energy 1.5 keV Lα x-rays from the muonic helium deexcitation can be identified, showing predominantly a slow rise time. The last contribution that can be identified for integrals roughly > 700 results from the signals of the high energy electrons that deposits energy in the APDs. As previously discussed, the rise time of these signals are in between the fast and slow 8.2 keV x-rays.

The analysis routine to find the edge and the calculation of the rise time slope has been also changed in the analysis. The edge is located by scanning a square weighting function with a width of 200 ns over the signal and the slope leading edge is fitted with a linear function which is optimized by varying the start time of the pulse within 20 ns while keeping the fitting window fixed. The slope is then selected using a χ^2 criterium.

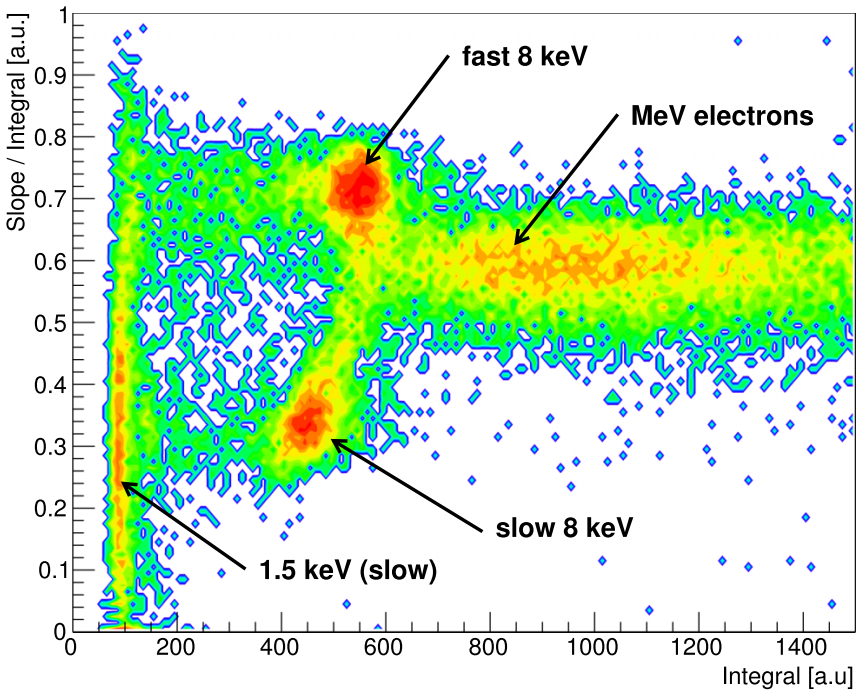

Figure 3.7 – Normalized slope of the rising edge plotted versus the integral of the pulse. The z-axis (color scale) is logarithmic. Integrals are roughly proportional to the deposited energy of the registered x-rays. Four contributions are visible: low energy 1.5 keV x-rays show integrals below 200. The recorded 8.2 keV x-rays create two different responses in the APD, one with slow rise time (slope ≈ 0.3) and one with significantly faster rise time (slope ≈ 0.7). The last contribution with an integral above 700 arises from MeV electrons depositing keV energy in the APD active region. Figure and caption taken from Reference [84].

By applying adequate cuts to the peaks of Fig. 3.7 plot, the numerical average of each different SWF (electrons and slow and fast x-rays) is performed. Then, by fitting each signal coming from the APDs with the 3 SWF they are separated in three different classes. The timing, amplitude and integral values of the recorded signal is obtained by the best fitting class. The obtained x-ray energy spectrum, after calibrating the two different 8.2 keV x-ray integral values (slow and fast 8.2 keV) by matching the peaks to the respective energy of 8.2 keV, is shown in Fig. 3.8 in which the different contribution of each distinct SWF classes is identified, labeled as Tr_{slow}, Tr_{fast} and Tr_{elec} corresponding to slow and fast 8.2 keV and to electrons, respectively. As discussed and expected, the major contribution for the 8.2 keV peak results from the fast 8.2 keV x-rays that are absorbed in the APD conversion region. The observed ratio between the slow and fast 8.2 keV x-rays of 1/1.7 roughly agrees with the expected absorption ration of 1/1.5 estimated from the thickness of the APD layers corresponding to the conversion and drifting regions, where the x-rays are absorbed and produce both distinct APD

outputs.

This waveform analysis for the APD output signals has ultimately improved the energy resolution of the APDs by a factor of 2. While the different classes of SWF have been founded in all the 20 APDs present in the experiment setup, only in 6 of them, the double-peak structure by a simple integral resulting from the different amplitudes of the slow and fast 8.2 keV x-rays have been found. Besides the improved energy resolution, the characterization of the electrons SWF has allowed a significant background reduction in the muonic helium experiments. An effectiveness of 86% for the correct electron identification has been achieved by this method while only 14% of the 8 keV x-rays were wrongly identified as electrons.

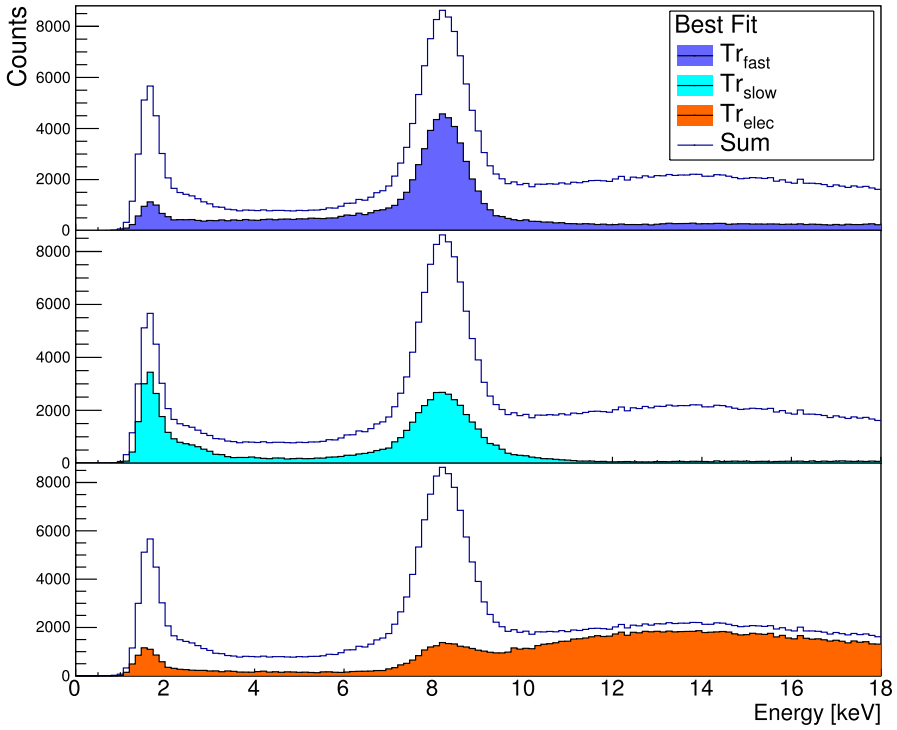

Figure 3.8 – Energy spectra of recorded x-ray and electrons in the muonic helium *Lamb Shift* experiment categorized by the standard waveform which provides the lowest χ^2 in a range of 200 ns after the leading edge of the pulse. All spectra show two prominent peaks at 1.5 keV and 8.2 keV. The fast rising component provided by Tr_{fast} in dark blue enfolds signals converted in or behind the conversion region (II). It consists mostly out of 8.2 keV x-rays and the visible low energy tail is created by the loss of gain for x-rays converted in the avalanche region (III). The light blue distribution stands for all SWF that were best described by the slow rising pulse shape Tr_{slow} and consists mostly out of 1.5 keV x-rays and some 8.2 keV x-rays mixed in. Signals best matching the electron SWF Tr_{elec} are shown in the orange division. These signals are formed by a continuous electron background and a contribution of wrongly identified x-rays. Figure and caption taken from Reference [84].

Chapter 4

Error budget and contributions to the resonance line shape

In muonic systems, the high enhancement of the finite size effect together with the strong binding energies results in a high insensitivity of the experiment to systematic effects, when compared with the electronic atom and ion spectroscopy. Yet, a complete study in order to estimate and provide upper limits for possible systematic effects had to be performed. The study of the systematic effects in measurement of the *Lamb Shift* in muonic atoms systems have already been described for μ^4He^+ in [85] and for μ^3He^+ in [86]. Most of the systematic effects are similar in both systems and are estimated in the same way. Yet, as mentioned, the non-zero nuclear spin in the μ^3He^+ case originates the hyperfine splitting of the energy levels given rise to very close energy levels which enhances an effect that can change the resonant line shape, the so-called Quantum Interference (QI). For sake of completeness, the possible systematic effects in the *Lamb Shift* experiments with muonic ions are briefly discussed here in a summarized manner.

With the exception of QI effects which have only be considered very recently in atomic laser spectroscopy, the contributions of several possible systematic effects have been considered through the years and can be found in literature (see *e.g.*, from μp experiment, Reference [77]). In Section 4.1 the contribution of the QI effects to the final result of the resonant transitions in μ^3He^+ is discussed. In Section 4.2 the contribution from the laser to the line center uncertainty are presented. The remaining contributions to the total error budget are summarized and briefly discussed in Section 4.3 and the total budget is presented on Section 4.4.

4.1 Quantum interference

QI effects (often referred as nonresonant corrections) have been recently theoretically investigated in [87] for the CREMA experiments, following Reference [88]. In that work, the muonic systems in which the *Lamb Shift* has been measured by the CREMA collaboration that have non-zero nuclear spin (given rise to very close energy states, the hyperfine structure) have been investigated. QI effects play an important role in the Lorentzian line shape when two or more resonances are separated by the order of a natural line width that arises the possibility of interference. This correction leads to a systematic effect resulting in an asymmetry of the line profile, which is no longer a simple sum of Lorentzians. Therefore, fitting Doppler-free spectroscopic spectra with Lorentzians profiles becomes ambiguous.

The calculations have been performed independently by two different groups (Lisbon and MPQ Munich) giving very similar results. The calculations have been performed considering a point-like detector or the detection system geometry of the CREMA experiments. Motivated by the experiment configuration it has been also considered incident photons to have linear polarization and non-observation of scattered photon's polarization.

When considering the experiment's geometry, the results of the effect when fitting a purely Lorentzian line shape have been obtained to the calculated distorted line. For the transitions mentioned in this work, it has been concluded that the shifts were to small to be significant for the $\mu^3\mathrm{He}^+$ transitions, being the larger shift obtained for the $2S_{1/2}^{F=0} - 2P_{3/2}^{F=1}$ transition of 0.05% of the transition linewidth [87]. Yet, a conservative value of 0.2 GHz has been considered for the contribution in the shift of the line, coming from QI effect, in the $\mu^3\mathrm{He}^+$ measured transitions.

4.2 Laser systematics

The characterization and evaluation of the systematics coming from the laser performance has been done in detail in Reference [85]. The largest contribution coming from the laser, which results in the broadening of the transition line, is its bandwidth whose FWHM is

$$\Delta\nu_{\mathrm{FWHM}} = 0.84(10)\ \mathrm{GHz}. \tag{4.1}$$

Yet, when compared with the linewidth of ≈ 318 GHz makes this effect completely negligible to the line shape being ≈ 400 times smaller than the linewidth.

Another contribution from the laser comes from its frequency calibration. The frequency calibration is done using a commercial wavemeter calibrated using transitions measured in saturated Kr and Cs spectroscopy being its total accuracy of 60 MHz. Another contribution to the frequency shift comes from the laser chirp. The laser chirp has been measured and a conservative contribution of 100 MHz has been accounted to the final uncertainty coming from the laser. By combining quadratically both contributions from the frequency shift, the final value accounted for the total budget coming from the laser uncertainty is

$$\Delta\nu_{\text{laser}} = 0.12 \text{ GHz}. \tag{4.2}$$

4.3 Other systematics

The effects which are mentioned below are possible shifts due to the Zeeman effect, Doppler broadening and collisional effects. These effects have been extensively described for μp [77] for $\mu^4\text{He}^+$ [85] and for $\mu^3\text{He}^+$ [86]. The AC and DC Stark effects have been evaluated in detail for μp in Reference [77] and is several orders of magnitude below the required precision. The AC Stark effect is related to the shift of atomic energy levels when the atom is subjected to a laser field. Yet, this effect has been considered negligibly small in the CREMA experiments because of the very short (0.5 ps) lifetime of the $2P$ state which imposes an overdamping on the Rabi oscillations that vanishes the AC Stark shift on resonance. The DC Stark effect on the energy levels results from static electric fields interacting with the atom. In the experiment, although the target being at ground potential, the movement of the muonic ions inside the 5 Tesla magnetic field can lead the ion to experience an electric potential. It has been also considered negligible mainly due to the 200 times smaller Bohr radius.

In addition to QI effects, there are different experimental parameters that can lead to asymmetries in the measured resonances which may shift the line center. One possible effect that could lead to an asymmetry in the line could be related to the different data recording times at different laser frequencies. This possible effect is accounted by normalizing the delayed $K\alpha$ x-rays by the prompt $K\alpha$ x-rays (see Chapter 5).

Other parameters in the experiment that could lead to asymmetries in the line shape are related with the laser which intrinsic properties and fluctuations of its pulse energy can arise asymmetries in the line shape. The laser is tuned under an interval of several hundreds of GHz and is operated for periods from days

to weeks. The temperatures fluctuation during the resonance measurement can lead to misalignments resulting in shifts during the long period of data taking. In order to avoid this asymmetries, the laser frequency tuning is done randomly switching from the two sides of a particular line and its pulse energy is measured and recorded in a pulse-per-pulse basis with photodiodes and calibrated after each run. Overall, the measured pulse energy as a function of the laser frequency does not change much, yet, the fluctuations in the laser pulse energy are accounted by the fitting procedure of the resonant lines in which each bin (corresponding to a specific laser frequency) is fitted with a different amplitude depending on the laser pulse energy at the respective laser frequency (see Chapter 5).

4.3.1 Zeeman effect

As mentioned in the description of the instrumental setup, the muon target is located inside a 5 Tesla superconducting solenoid to insure the decrease of the radius of spiraling muon motion to fit in the small stop volume delimited horizontally by the multipass cavity. The presence of this strong magnetic field, changes the energy level structure of the ion due to the coupling with the magnetic field. The contribution of the Zeeman effect has been evaluated in [85, 86] for the muonic helium isotopes and in [77, 89] for the muonic hydrogen experiment. The interaction between the muonic ion and the external magnetic field **B** can be described according the Hamiltonian defined by

$$\mathcal{H}_B = \frac{e\hbar}{2mc}(L_z + 2S_z)B, \tag{4.3}$$

where e and m are respectively the charge and mass of a charged particle in a constant magnetic field B, being L_z and S_z respectively the angular and spin operators. Considering the Hamilton operator of Eq. (4.3) applied to both particles forming the atomic system, the atomic interaction with an external field **B** is given by [89]

$$\begin{aligned}\mathcal{H}_B &= (g_L^u u_B^u \mathbf{L} + g_L^h u_B^h \mathbf{L} + g_S^u u_B^u \mathbf{S} + g_I u_B^h \mathbf{I}) \cdot \frac{\mathbf{B}}{\hbar} \\ &= \left(g_L^u L_z + g_L^h \frac{u_B^h}{u_B^u} L_Z + g_S^u S_z + g_I \frac{u_B^h}{u_B^u} I_Z\right) u_B^u B\end{aligned} \tag{4.4}$$

where g_L^u, g_L^h, g_S^u and g_I are respectively the muon orbital, the nuclear orbital, the muon spin and nuclear Landé g-factors. **L** stands for the orbital momentum of the orbiting particle which is the same as the orbital momentum of the nucleus, **S** the muon spin and **I** the nucleus spin. The muon magnetic moment is given

by $u_B^u = e\hbar/2mc$ where m is the muon mass and u_B^h is the helion nucleus magnetic moment which is given by $u_B^h = e\hbar/2Mc$ where M is the nucleus mass.

Despite the magnetic field being strong (5 T), the Zeeman energy in a muonic atom is still best described in the IJ-coupling scheme where the induced Zeeman shift is small compared to the fine and hyperfine splitting (weak field approximation) [89]. Therefore, **J** (**J** = **L**+**S**) is a good quantum number and the Hamiltonian can be written as

$$\mathcal{H}_B = \left(g_J J_z + g_I \frac{u_B^h}{u_B^u} I_z\right) u_B^u B, \tag{4.5}$$

where

$$g_J = g_L \frac{J(J+1) - S(S+1) + L(L+1)}{2J(J+1)} + g_S \frac{J(J+1) + S(S+1) - L(L+1)}{2J(J+1)}. \tag{4.6}$$

Similarly, if the energy shift due to the external magnetic field is small compared to the hyperfine splitting, then **F** (**F** = **J** + **I**) is a good quantum number and the interaction Hamiltonian $\mathcal{H}_B$ becomes

$$\mathcal{H}_B = g_F u_B^u B \frac{F_z}{\hbar}, \tag{4.7}$$

where the hyperfine Landé g-factor is given by

$$g_F = g_J \frac{F(F+1) - I(I+1) + J(J+1)}{2F(F+1)} + g_I \frac{u_B^h}{u_B^u} \frac{F(F+1) + I(I+1) - J(J+1)}{2F(F+1)}. \tag{4.8}$$

The shift of different energy levels by the Zeeman effect in this regimes, can be written in first order as

$$\Delta E_B = g_{F/J} u_B^u m_{F/J} B \tag{4.9}$$

where $m_{F/J}$ the projection of the total angular momentum F/J and $g_{F/J}$ are the above defined Landé g-factors in fine and hyperfine structure basis. The g-factors are $g_S = 2.002$, $g_L^{4He} = 0.97$, $g_L^{3He} = 0.96$ and $g_I^{3He} = 4.26$ and the ratio of the helion nuclear magneton to muon Bohr magneton ratio is $u_B^h/u_B^u = 0.038$.

All initial $m_{F/J}$ sub-states in the muonic helium isotopes are equally populated in the $2S$ state. Since the laser light inducing the transition is linearly polarized this results in a broadening effect from the presence of the magnetic field, yet no shift happens because of the cancelation of the effect between the different Zeeman sub-levels. The considered line broadening due to the shifts of individual

$m_{J/F}$ sub-levels has been 100 MHz in the two $\mu^4\mathrm{He}^+$ measured lines [85] and 500 MHz in the $\mu^3\mathrm{He}^+$ transitions [86], being however, completely negligible when compared with the transition linewidth ($\approx 0.2\%$ of the linewith).

4.3.2 Doppler broadening and shift

When particles have a velocity **v** component parallel to the laser propagation **k** the Doppler effect leads to a shift in the effective frequency w' seen by the particle

$$w' = w + \mathbf{vk}, \tag{4.10}$$

where w is the transition frequency of the ion at rest. Yet, in the experiment, muons arriving to the gas target with few keV are stopped in the gas where they lose most of its kinetic energy by inelastic collisions with the surrounding atoms, before forming a bound state with a atom nucleus. The laser pulse arrives with a delay of roughly 1 μs after the muonic ion formation. After this time, the muonic ion is thermalized at 293 K. The target is temperature stabilized and therefore the muonic ions are assumed to have the same temperature. Since the muonic ion is thermalized at the time the laser pulse arrives, its velocity distribution is given by a Maxwell distribution and leads to a broadening effect that follows a Gaussian profile with a FWHM that is given by

$$\delta\nu = \sqrt{\frac{8kT\ln 2}{mc^2}}\nu_0, \tag{4.11}$$

where k is the Boltzmann constant, T the temperature and m the mass of the emitting particle. Considering the lines with the largest transition frequencies in both $\mu^3\mathrm{He}^+$ and $\mu^4\mathrm{He}^+$, this has leaded to consider an upper limit for the broadening effect of $\delta\nu = 2.4$ GHz and $\delta\nu = 2.3$ GHz, respectively. This effect corresponds roughly to 0.8% of the linewidth and is therefore negligible.

4.3.3 Collisional effects

Collisions between the muonic ion and the surrounding atoms (at ≈ 2 mbar pressure) from the interaction of the electromagnetic field of the laser can lead to a broadening and shift effect in the transitions. In Reference [90], the effect of the collisions of the muonic ion with the surrounding gas has been calculated for a gas target pressure of 100 mbar. Their calculation at this pressure yields a shift of 50 MHz and a broadening effect of 13.6 MHz for $\mu^3\mathrm{He}^+$ ions. Yet, at the pressure of 100 mbar the collision rate is enhanced. At the experiment gas pressure of

2 mbar, this effect is expected to be much lower (two orders of magnitude) and negligible.

4.4 Total budget

In Table 4.1, the considered contributions to final error budget in the measured *Lamb Shift* transitions (shift) and possible broadening effects, for the preliminary results that have been given by References [85, 86], are listed with the exception of the AC and DC Stark effects being their contribution much lower than the collisional effects. The largest contribution to the final uncertainty in the measured transitions is, in the case of the μ^3He^+, coming from QI effects, in which a conservative upper limit has been considered. Frequency shifts coming from the laser are also contributing to the uncertainty of all the measured transitions. Yet, considering the aiming accuracy of 50 ppm, the overall systematic frequency shifts are negligible. Moreover, the final uncertainty is dominated by statistics, being almost a factor of roughly 100 larger than the systematics for all transitions. All the broadening contributions from the experimental environment, also listed on Table 4.1, are negligible due to the width of the measured transitions.

Table 4.1 – Systematic effects in the μ^3He^+ and μ^4He^+ experiments. This table shows the shifts and the broadenings due to effects presented in this section. The AC and DC Stark effects are not listed because of their small contribution. The given uncertainty for the quantum interference (QI) is a conservative upper limit. The total final uncertainty value considered is the quadratic sum off all different contributions and considered as systematic uncertainty in the preliminary analysis of References [85, 86].

	μ^4He^+		μ^3He^+	
Source	Shift (GHz)	Broadening (GHz)	Shift (GHz)	Broadening (GHz)
QI	0	0	0.2	
Laser	0.12	0.84	0.12	0.84
Zeeman effect	0	0.5	0	0.5
Doppler	0	2.3	0	2.4
Collisional effects	0	$\leq 1\times10^{-3}$	$\leq 5\times10^{-4}$	$\leq 2\times10^{-4}$

Chapter 5

Preliminary results on μ^4He$^+$ and μ^3He$^+$ Lamb Shift transitions

A preliminary data analysis has been performed by *Diepold* [85] for μ^4He$^+$ and by *Krauth* [86] for μ^3He$^+$ in their Thesis. In these References, the energy cuts in the analysis as well as the systematics in the measurement of the transition lines are discussed.

To obtain the resonance, binned $K\alpha$ x-ray spectra are constructed. As already mentioned, most of the times the formed muonic ion deexcite quickly to the $1S$ ground state emitting several prompt x-rays. Yet, when the $2S$ state is populated, the sent laser pulse of about 1 μs, delayed in respect to the muon detection, may excite the the ion to the $2P$ state which is followed by a delayed x-ray emission. When plotting the 8.2 keV x-ray events as function of time, being the starting time t_0 the muon detection time (see Section 2.2.3), a peak will appear originated from the prompt x-rays at a certain time after the muon being detected. When resonant with the laser, another peak, later in time, appears. This peak results from the laser stimulated excitation of the $2S$ to $2P$ state and respective delayed emission of a x ray (see Fig 5.1). By selecting the delayed x-rays events during the laser time window, normalizing them with the prompt x-ray events and plot it as a function of the laser frequency, the resonance plot is created. The normalization is performed due to a different statistics coming from different recording times and proton beam fluctuations at each laser frequency. Figure 5.1 shows a time spectrum of the $2S_{1/2}^{F=1} \rightarrow 2P_{3/2}^{F=2}$ transition where the delayed x-rays are clearly visible when in resonance with the laser. The grey shaded area represents the

selected time window for the prompt x-rays and the blue shaded area is the laser time window in which the laser may drive a transition to the $2P$ state followed by the delayed 8.2 keV $K\alpha$ x-ray emission.

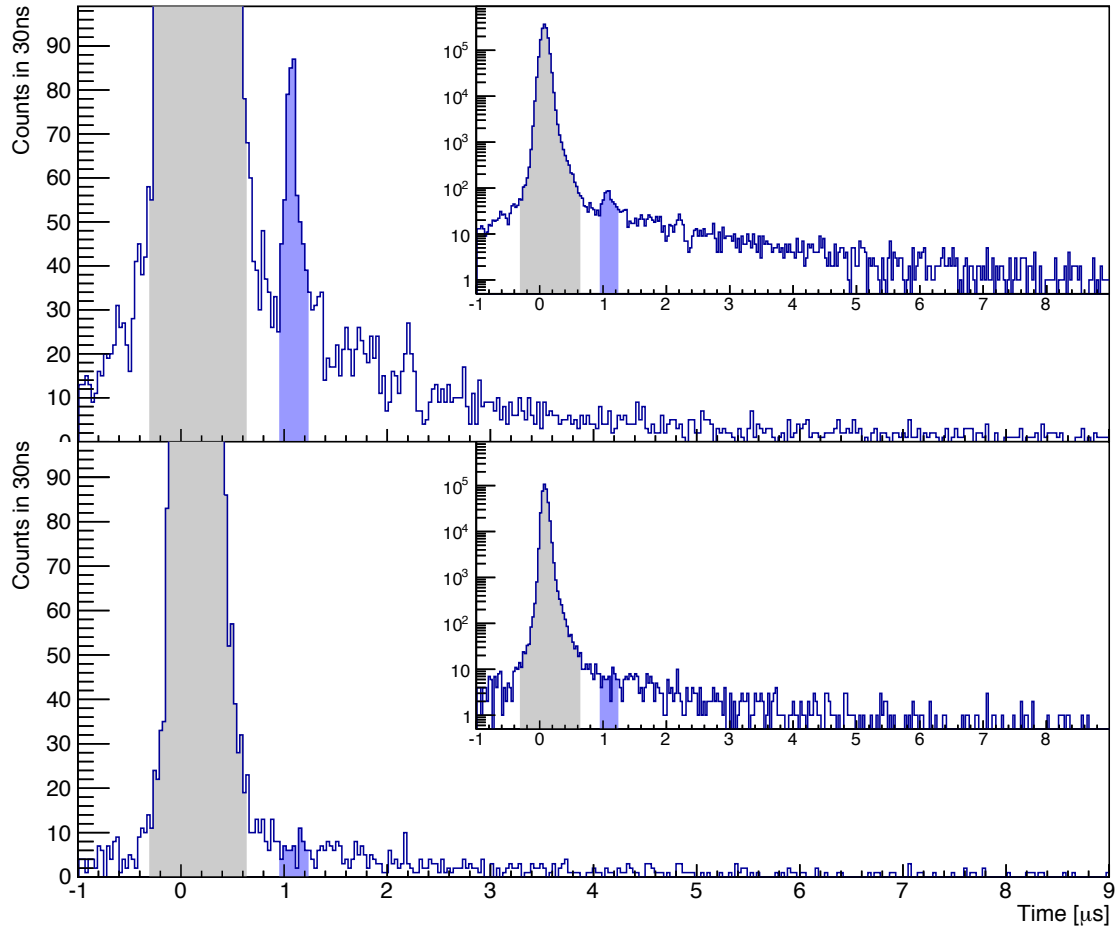

Figure 5.1 – Time spectrum of 8.2 keV x-ray events for the $2S^{F=1}_{1/2} \rightarrow 2P^{F=2}_{3/2}$ transition in μ^3He$^+$. The grey shaded area represents the prompt x-rays time interval and the blue shaded area represents the laser time window. The top plot shows the $K\alpha$ x-ray time spectrum with the laser in resonance while the bottom plot shows the spectrum with laser off resonance where no delayed x-ray peak exists.

5.1 μ^4He$^+$ and μ^3He$^+$ measured resonances

The natural transition line from an atomic transition is characterized by a Lorentzian function. The Lorentzian function can be derived by the Fourier transform of the power spectral density time function to the amplitude as a function of frequency [91]. The Lorentzian function is given by

$$L(\nu) = \frac{1}{\pi} \frac{(\frac{1}{2}\Gamma)^2}{(\nu - \nu_0)^2 + (\frac{1}{2}\Gamma)^2)}, \tag{5.1}$$

where ν_0 is the center and Γ is a parameter specifying the width of the function. The transition width is dominated by the $2P$ state lifetime ≈ 0.50 ps that can be obtained by *Fermi's Golden Rule* in the first order time-dependent perturbation theory [91].

Although a Voigt profile (convolution of a Gaussian and a Lorentzian) is usually used to fit the data from transitions in atomic systems, in the CREMA experiments only the Lorentzian shape is considered in the fits to the resonances. As described in Chapter 4, the largest contribution for the line broadening is given by the laser bandwidth which is ≈ 400 times smaller than the natural linewidth of ≈ 318 GHz, resulting in a negligible Gaussian broadening of the lines. The constructed function to fit the data, based in the Lorentzian function given by Eq. (5.1), is given by:

$$N_{\text{prompt}}(\nu) \cdot \left(\frac{P_{\text{laser}}(\nu)}{\langle P_{\text{laser}} \rangle} \cdot \frac{A \cdot (W/2)^2}{(\nu - \nu_0)^2 + (W/2)^2} + B \right), \tag{5.2}$$

where A, B, W and ν_0 are the adjustable fit parameters. The parameter A accounts for the signal amplitude, W the resonance width, B the background level and ν_0 the center frequency. The amplitude of the fit is scaled with the laser pulse energy by the fraction of the laser pulse energy per frequency by its global average pulse energy ($P_{\text{laser}}(\nu)/\langle P_{\text{laser}} \rangle$). The background level parameter accounts for the fake signals in the APDs which have been wrongly considered as x rays. For an accurate description of the data, the total fit function is scaled with the number of recorded prompt x-rays per frequency. All adjustable coefficients are appropriately scaled to avoid numerical problems in the minimization process.

Two data sets are considered in the final analysis in order to determine the background with higher precision. These data sets are the laser-on and laser-off data. Laser-on data is the data recorded containing the actual information for the resonance determination which corresponds to the data when the laser is fired in the laser time window after being triggered by the incoming muon. The laser-off data corresponds to the events recorded when no laser pulse is sent to the cavity. The laser-off data is summed and used as additional points to obtain the background level far off the resonance. The fit is a maximum log-likelihood fit optimized by the MINUIT package implemented in CERN ROOT[80–82].

In Figs. 5.2, 5.3 and Figs. 5.4, 5.5 preliminary plots of the measured resonances are shown with the respective described fit to the data in μ^4He$^+$ and μ^3He$^+$, respectively. Full circles represent the laser-on data and empty circles the laser-off data. All plots are presented with the x-axis representing the offset frequency when taken the fitted resonance center as reference ("0").

As mentioned, the final data analysis has been performed in [85] and [86] for the μ^4He$^+$ and μ^3He$^+$, respectively. Their preliminary results on the measured *Lamb Shift* transition frequencies and the respective extracted nuclear charge radii are listed on Table 5.1. From their preliminary data analysis, the muonic values of the extracted nuclear charge radii of the helium isotopes seem to agree with the most recent results from electron scattering of ^{4}He$^+$ [92] and ^{3}He$^+$ [93]. Yet, the large uncertainty of the charge radii value extracted from electron scattering experiments does not exclude a possible frequency shift comparable in size to the offset that created the proton radius puzzle in muonic hydrogen. The final data analysis is still ongoing for all measured resonances. The final results for the extracted nuclear charge radii obtained from the *Lamb Shift* transitions in μ^4He$^+$ and μ^3He$^+$ and its respective publications are expected soon.

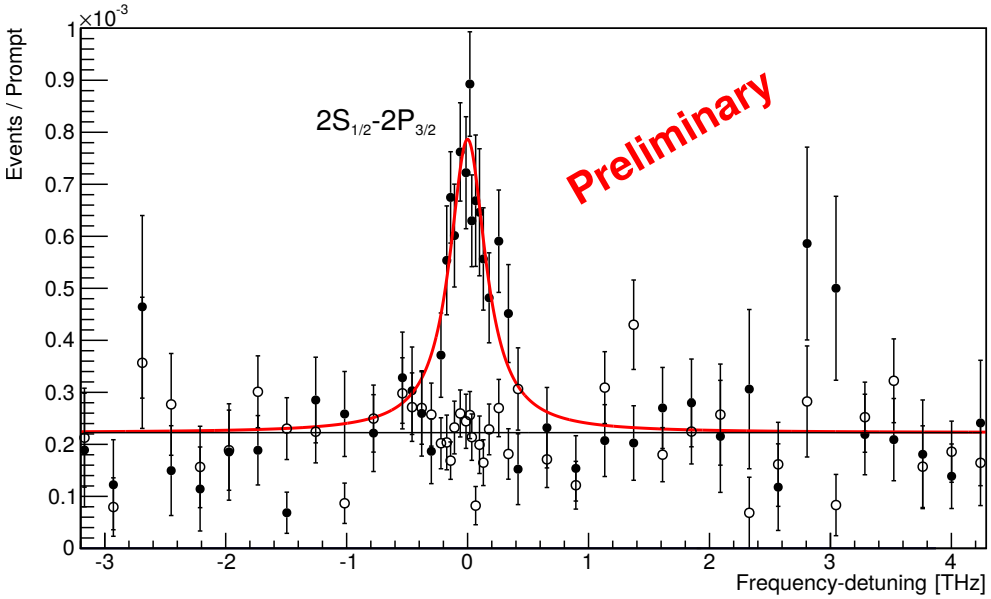

Figure 5.2 – The μ^4He$^+$ $2S_{1/2} - 2P_{3/2}$ resonance. Fit of the experimental data used to determine the position of the resonance. Two data sets are shown. The data sets for laser-on data (full circles) and laser-off data (empty circles) are shown. Laser-off points are extracted using a fit of the time dependent x-ray background and serve only as verification for the laser-on data. The x-axis is presented as an offset frequency to the line fitted position frequency.

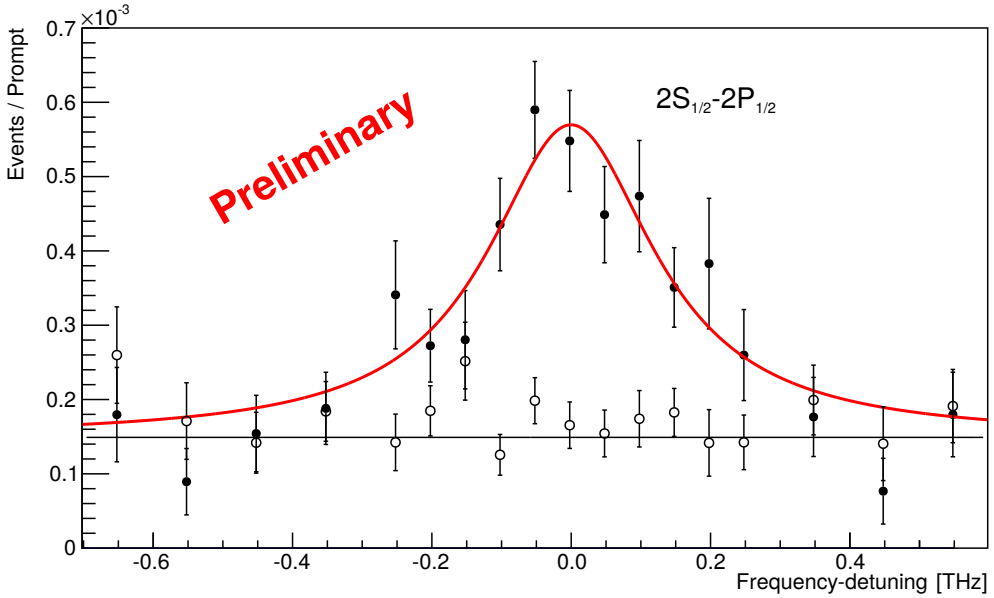

Figure 5.3 – The μ^4He$^+$ $2S_{1/2} - 2P_{1/2}$ resonance. Fit of the experimental data used to determine the position of the resonance. Two data sets are shown. The data sets for laser-on data (full circles) and laser-off data (empty circles) are shown. Laser-off points are extracted using a fit of the time dependent x-ray background and serve only as verification for the laser-on data. The x-axis is presented as an offset frequency to the line fitted position frequency.

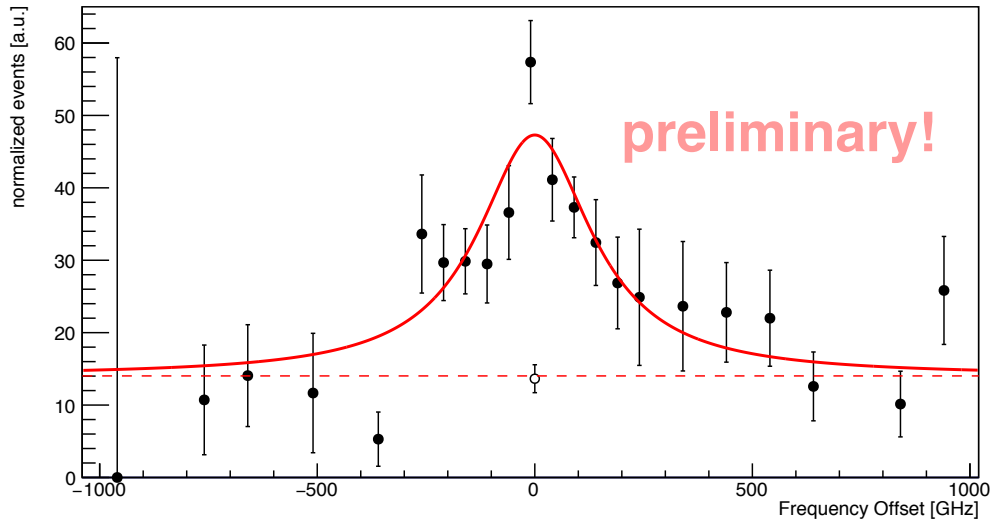

Figure 5.4 – The μ^3He$^+$ $2S_{1/2}^{F=1} - 2P_{3/2}^{F=2}$ resonance. Fit of the experimental data used to determine the position of the resonance. Two data sets are shown. The data sets for laser-on data (full circles) and laser-off data (empty circles) are shown. Laser-off points are extracted using a fit of the time dependent x-ray background and serve only as verification for the laser-on data. The x-axis is presented as an offset frequency to the line fitted position frequency.

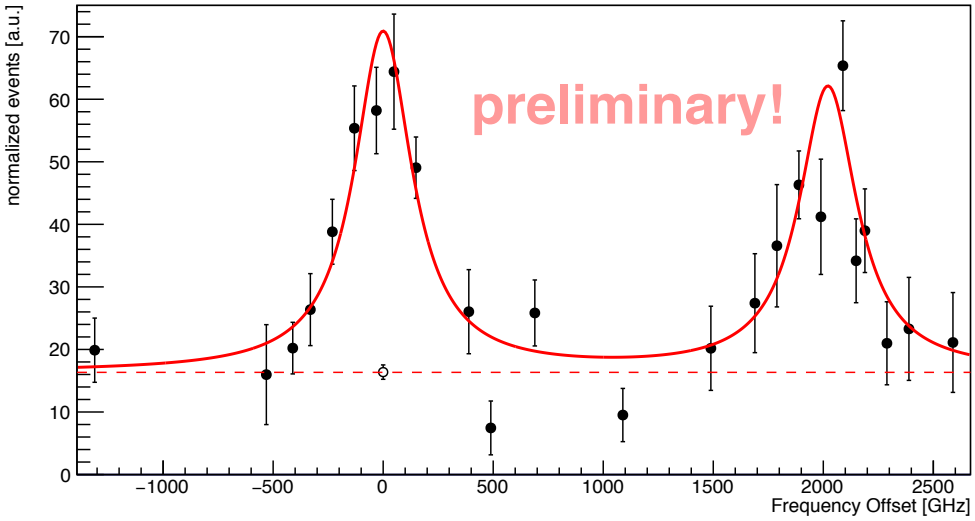

Figure 5.5 – The μ^3He$^+$ $2S^{F=0}_{1/2} - 2P^{F=1}_{3/2}$ and $2S^{F=1}_{1/2} - 2P^{F=1}_{1/2}$ resonances. Fit of the experimental data used to determine the position of the resonance. Two data sets are shown. The data sets for laser-on data (full circles) and laser-off data (empty circles) are shown. Laser-off points are extracted using a fit of the time dependent x-ray background and serve only as verification for the laser-on data. The x-axis is presented as an offset frequency to the line fitted position frequency.

Table 5.1 – Preliminary results from the CREMA *Lamb Shift* experiment in μ^3He$^+$ and μ^4He$^+$. The measured transitions positions (in THz) with the respective total uncertainty is shown. The rms charge radii extracted from the measured transition is also shown by considering the summary of Lamb shift QED contributions given in [55, 56] described in Section 1.1. The preliminary experimental results have been taken from [85, 86].

Transition	Position [THz]	rms charge radius [fm]	Reference
	μ^4He$^+$		
$2S_{1/2} - 2P_{1/2}$	333.352(16)	1.67829(54)	Diepold (2015) [85]
$2S_{1/2} - 2P_{3/2}$	368.660(17)		
	μ^3He$^+$		
$2S^{F=1}_{1/2} - 2P^{F=2}_{3/2}$	347.211(20)	1.96861(129)	Krauth (2017) [86]
$2S^{F=0}_{1/2} - 2P^{F=1}_{3/2}$	312.829(21)		
$2S^{F=1}_{1/2} - 2P^{F=1}_{1/2}$	310.814(20)		

Chapter 6

Conclusion

The performed experiments in the muonic helium isotopes campaign has been very successful. Five *Lamb Shift* transitions have been measured in total, two in $\mu^4\mathrm{He}^+$ and three in $\mu^3\mathrm{He}^+$.

By performing the LAAPD's waveform analysis, we have been able to identify signals coming from the electrons energy deposition in the x-ray detectors. This has improved the signal to noise ratio in the experiments and the energy resolution of the detectors by a factor of 2. An effectiveness of 86% for the correct electron identification as been achieved in the analysis.

From the preliminary results, the transitions have been measured with a precision better than 70 ppm being the final accuracy completely dominated by statistics. With the preliminary values of the measured transitions, the rms charge radius for the helion particle has been extracted with a relative uncertainty of 7×10^{-4} while for the alpha particle the rms charge radius has been extracted with a relative uncertainty of 3×10^{-4}, being both uncertainties limited by the uncertainty in the polarizability of the nucleus. Both preliminary values are in agreement with electron scattering measurements, yet, the very large uncertainties (more than 10 times the value from muon ions spectroscopy value) in the available values does not exclude a possible shift in the order of the offset from the proton radius puzzle.

Part II

High-precision measurements of transition energies in highly-charged ions

Chapter 1

Introduction

1.1 Goals and motivation

Neutral elements with a K vacancy created by electron bombardment or photoionization have been used for a century to provide information on atomic and solid state structure, and as x-ray standards. Although, even with the given high precision close to 1 ppm in some lines [94], does not necessarily mean that these standards, because of the complex nature of inner-shell transitions in multielectron systems, can be used to such accuracy. The shape and peak positions of those lines depends on many factors like the excitation energy [95–97], the chemical composition and the surface contamination of the sample. Moreover, shake-off processes, Auger Coster-Kronig effects lead to numerous satellite transitions very close in energy to the line, which cannot be resolved and produce asymmetric line shapes [98–100]. Another inherent problem associated with the use of this x-ray standard lines is their broad natural width, typically 10 times larger than the resolution of the best of x-ray spectrometers, being thus this lines not suitable to characterize the response function of a x-ray spectrometer [101, 102]. Relativistic correlation effects and QED contributions have been also subject of numerous work and together with all experimental values since 1920s and advanced atomic calculations lead to the publication of a complete tabulation of all available x-ray standards [94]. Yet, since the center of gravity of this experimental measured lines cannot be attributed unambiguously to a physical transition, all this considerable work does not allow for precise-enough tests of QED and relativistic effects. It

was shown therefore, that, to provide reliable, reproducible, narrow, x-ray standard lines which can be used to test and probe QED, either exotic atoms [101] or combination of exotic atoms and relatively cold, highly charged ions, produced in an ECRIS [103] can be used.

The first observed x rays coming from HCI argon up to He-like from an ECRIS plasma has been done in 2000 [104]. Since then, several experiments have been performed at PSI [102, 105–107] using an ECRIS which had allowed an improvement in the understanding of the ECRIS plasmas for sulfur, chlorine and argon [108–111].

The study of few-electrons HCI of medium-Z systems, such as argon ions, which are the subject of this work, is one of the main methods to test and probe BSQED. Although the strong dependence with Z of BSQED contributions (the retardation correction to the electron-electron interaction contribution scales as Z^3, and the one-electron corrections, self-energy and vacuum polarization, scale as Z^4), at high-Z, the strong enhancement of the nuclear size contribution and associated uncertainty limits the degree to which available experimental measurements can be used to test QED [112–116]. At very low-Z, experiments can be much more accurate, but tests of QED can be limited as well, even for very accurate measurements of transitions to the ground state of He [117–119]. For few-electron atoms and ions, they are limited by the large size of electron-electron correlation and by the evaluation of the needed higher-order QED screening corrections, in the non-relativistic QED formalism (NRQED) [120–124]. It can also be limited by the slow convergence of all-order QED contributions at low-Z, which may be required for comparison, and because of the insufficient knowledge of some nuclear parameters, namely the form factors and polarization [37, 38, 40, 125]. In medium-Z elements like argon or iron, the nuclear mean spherical radii are sufficiently well known (*e.g.*, [126]) and nuclear polarization is very small. So uncertainties related to the nucleus are small compared to experimental and theoretical accuracy. This can be seen in the theoretical uncertainties claimed in [125].

HCI can be produced, *e.g.*, using high-energy accelerators, Electron Beam Ion Traps (EBIT), or ECRIS. They have been first studied in laser-produced plasmas [127]. Beam-foil spectroscopy has also been applied to several ions in systems of one and two electrons [128, 129] and by using the interaction of fast ion beams with gas targets in heavy-ion accelerators. Ion storage rings have also been used [130–132]. Yet, high-accuracy spectroscopy in this measurements is limited due to Doppler effects, which affects energy measurements and requires a precise determination of the ions speed and angle of observation of the x rays emitted in flight to be corrected, and the Doppler broadening, which affects any possible

width measurement. In order to solve this problem, x-ray recoil ions spectrometry spectroscopy [133] and "accel–decel" method [134] have also been tried.

Recently, high-precision measurements using medium-Z HCI produced in EBITs or ECRIS have been reported. Measurements of transition energies in H- and He-like systems have been divulged by the Livermore group [15], Heidelberg group [8, 11, 16, 135] and the Melbourne and NIST collaboration [10, 12, 13]. Measurements in EBIT are also known, as in vanadium [136] and iron [137], for terrestrial and astrophysics plasma applications. There have also been relative measurements in ECRIS for sulfur, chlorine and argon [138], using the relativistic M1 transition $1s\,2s\,^3S_1 \rightarrow 1s^2\,^1S_0$ as a reference. The present collaboration has reported values [9] using an ECRIS with the same setup in which this work has been performed. In both types of sources, EBIT and ECRIS, the ions have only thermal motion which does not require correction for Doppler shifts.

The Heidelberg group reported the measurement of the $1s\,2p\,^1P_1 \rightarrow 1s^2\,^1S_0$ He-like argon line with an accuracy of 1.5 ppm without the use of a theoretical or experimental reference line [135]. The spectrometer used in that work is made of a single Bragg crystal coupled to a CCD camera, which can be positioned very accurately with a laser beam reflected by the same crystal as the x rays. Recently, the Livermore group reported a measurement of all $n = 2 \rightarrow n = 1$ lines in helium-like copper [15], using hydrogen-like lines in argon as calibration. It has also been reported measurements of all 4 lines in He-like xenon, using a micro-calorimeter and calibration with x-ray standards [139]. The Melbourne-NIST collaboration reported the measurement of all the $n = 2 \rightarrow n = 1$ transitions in He-like titanium with a relative accuracy of 15 ppm, using a calibration based on neutral x-ray lines emitted from an electron fluorescence x-ray source [10, 12, 13]. The technique described in Reference [135] that uses just single flat crystal, is well adapted to the EBITs, which provides a very narrow, but rather weak x-ray source. ECRIS plasmas however, are very intense sources of x rays. At low energies, cylindrically or spherically bent crystal spectrometers and DCS can be used. A single flat-crystal spectrometer as used in Heidelberg [135], and the DCS [140, 141] are the only two methods that can provide high-accuracy, reference-free measurements in the x-ray domain (transition energies in the 2–15 keV range).

Chantler and co-workers [10, 12, 112] have claimed that available experimental data shows the evidence of a discrepancy between the most advanced BSQED calculation [125] and measurements in the He-like isoelectronic sequence, leading to a deviation with $\simeq Z^3$ dependence. They speculated [10] that this systematic discrepancy could provide insight into the *Proton Size Puzzle*, the Rydberg and fine-structure constants, or missing three-body BSQED terms.

In addition to the fundamental aspect and motivation, high-precision x-ray standards are important to a variety of fields: spectroscopy [142], plasma physics [108], biological studies [143], material sciences [144], environmental sciences [145] and astrophysics. For example, an unidentified line was recently detected at 3.55 keV - 3.57(3) keV in an XMM-Newton space x-ray telescope spectrum of 73 galaxy clusters [146] and at 3.52(3) keV for another XMM spectrum in the Andromeda galaxy and the Perseus galaxy cluster [147]. One year later, a line at 3.539(11) keV was observed in the deep exposure data set of the Galactic center region with the same instrument. A possible connection with a dark matter decay line has been put forward, yet measurements performed with an EBIT seems to show that it could be a set of lines in highly charged sulfur ions, induced by charge exchange [148].

In this work, the measurement of transition energies from $n = 2 \rightarrow n = 1$, the $1s\,2p\,^1P_1 \rightarrow 1s^2\,^1S_0$ in He-like argon, the $1s\,2s^2\,2p\,^1P_1 \rightarrow 1s^2\,2s^2\,^1S_0$ Be-like argon and the $1s\,2s\,2p\,^2P_J \rightarrow 1s^2\,2s\,^2S_{1/2}$ Li-like argon doublet, with an accuracy better than 3 ppm and respective natural widths using a DCS connected to an ECRIS, is presented.

The Part II of this work is organized as follows. On the remainder of this chapter a brief historical introduction to the DCS (section 1.2), an overview of the technical aspects of the experimental setup (section 1.3), the ECRIS (section 1.3.1) and the work principle of the DCS among the description of its components (section 1.3.1) and the procedure for the spectrometer alignment (section 1.4) will be presented. Chapter 2 discusses the data analysis procedure where we apply the method developed to measure the energy and line-width of the $1s\,2s\,^3S_1 \rightarrow 1s^2\,^1S_0$ M1 transition reported in Ref. [9] and the Montecarlo code developed by *Amaro* [149]. On Chapter 3, the study of systematic errors and the total error budget of the measurements using the DCS will be discussed. The results, its discussion and the comparison with the most advanced calculations will be shown on Chapter 4. A systematic and very detailed study of He-like isoelectronic sequence of available experimental data compared with the most accurate BSQED theory of Ref. [125], which covers $12 \leq Z \leq 92$, for evaluation of a possible discrepancy between experiment and theory will also be presented. Final considerations and conclusion are provided on Chapter 5.

1.2 DCS - A historical introduction

It was while working with a cathode ray tube in his laboratory, late in 1897, that the German physicist *W. C. Roentgen* has made an accidental discovery, the x rays [150]. Labeled at the time as a medical miracle, *Roentgen* was the first Nobel Prize laureate in physics, in 1901. His discovery was revolutionary and would ultimately benefit a variety of fields, having at the time specially benefited medicine. In physics, this discovery has quickly triggered research with x rays, fact that can be easily confirmed since half of the Nobel Prizes in Physics between 1914 and 1924 were given to the development in x-rays.

Even before the x-ray diffraction on crystals had been discovered, some fundamentals properties of x-rays were empirical revealed by systematic studies carried out by using the fluorescence method with an ordinary x-ray tube as primary source. This systematic studies has formed the basis for a more quantitive and detailed studies from diffraction of the x-ray radiation. These early researches on x-ray fundamentals were specially conducted by *Charles G. Barkla* which, in 1909, has found a relation between x-rays radiating from a sample and the atomic weight of the sample [151]. He has also been the first to identify two series of homogeneous x-ray radiation coming from a x ray irradiated sample from different elements, which he called K- and L-fluorescent radiations [152]. Seventeen years after the discovery of x rays, *Max von Laue* and co-workers had the idea of sending a x-ray beam through a copper sulfate crystal and record the results on photographic plates [153]. The results showed diffraction spots surrounding the central spot of the primary beam which has strengthening the old controversy regarding the nature of this radiation favoring the hypothesis of being electromagnetic waves. The confirmation has come in the same year by *W.H. Bragg* and *W.L. Bragg* [154]. Those experiments add a common conclusion: a distinct diffraction pattern was clearly noticeable with a simple explanation - the crystal structure is made by a periodic ordered arrangement of the atoms which, being x rays electromagnetic waves, they would be scattered if its wavelength is in the same order as of the crystal interatomic distance. This diffraction pattern led to Bragg law [155]

$$n\lambda = 2d \sin\theta_{\text{Bragg}}, \tag{1.1}$$

where n is the diffraction order, d is the lattice spacing of the crystal, λ the wavelength and θ_{Bragg} the Bragg angle related to the wavelength. Bragg law states that an incident monochromatic x ray on a crystal will be reflected only at certain specific incident angles, the so-called Bragg angles θ_{Bragg}.

These discoveries gave birth to two new fields, x-ray spectroscopy and x-ray crystallography for which precision x-ray spectroscopy using a DCS was first conceived independently by *Compton* in 1917 [156], *Bragg* and co-workers in 1921 [157] and *Wagner* and *Kulenkampff* in 1922 [158] with the purpose of measuring absolute integrated reflections of crystals. On the same field, *Davis* and *Stempel* [159] used the DCS with the purpose of experimentally characterize the reflectivity profiles of crystals. With the works of *Davis* and *Purks* [160, 161] in which they found the high-resolution capability of the DCS dispersive mode, lead the way to use the instrument in the x-ray spectroscopy. First with the measurement of K-line widths of some elements by *Allison* and co-workers [162, 163] and later, with the improvement of the accuracy for energy measurements by the correction of the vertical divergence [164], absolute measurements of x-ray wavelength by *Bearden* [165, 166] with the deduction of a value for the calcite lattice spacing [167]. Detailed technical description of the instrument can be found in [168, 169], given respectively by *Compton* and by *Williams* and *Allison* while a theoretical description of the instrument provided by *Schwarzschild* can be found in [170]. More detailed information of the instrument description an theory can also be found in the following text book [171].

The DCS has been used through the years to measure x-ray energies. Although, without knowing accurately the lattice spacing of the crystals in use, most of energy measurements were relative to standard lines until very recently. With the arising of high-purity germanium and silicon single-crystals, new interferometric methods were developed to the direct measurement of the lattice spacing in terms of laser wavelength with accuracies below 10^{-8} [172–176]. With this accuracies of the lattice spacing together with the development of high-precision encoders for the angle measurements, the DCS became a tool to make absolute measurements of x-ray energies, being the reference the well-measured lattice spacing of the crystals. With the design and development of vacuum DCS to absolute measurements of soft x-rays by *Deslattes* [140], x-ray standards started to be measured with the DCS. Some examples of absolute energy measurements of K lines in light and heavy elements can be found in [98, 177, 178].

More recently, *Amaro* and co-workers [9] had for the first time measured the absolute energy of a x-ray line from a HCI transition using a DCS. They had measured with a 2.5 ppm accuracy the absolute energy of the $1s\,2s\,^3S_1 \rightarrow 1s^2\,^1S_0$ magnetic dipole transition in Ar^{16+} emitted by the plasma of an ECRIS. The experimental setup on which this measurement has been performed is the same experimental apparatus on which this work is based on. This experimental setup will be described in section 1.3.

1.3 Experimental setup

A DCS connected to an ECRIS was used in this work to measure absolute energies of core excited transitions, with a precision better than 3 ppm, on a few electrons ions of argon. Through the years, as already mentioned, it has been shown that ECRIS plasmas can be very intense sources of x rays, but have diameters of a few cm. Although, being them massive, vacuum complicated devices, built with several components that can weight tons, they are better adjusted to be connected to spectrometers that can be used to an extended source.

In this section, a description of the experimental setup is given, starting by the description of the used ECRIS, the Source D'Ions Multichargés de Paris (Source D'Ions Multichargés de Paris (SIMPA)), followed by the description of the DCS with all its instruments, working principle and its fundamental features.

1.3.1 The SIMPA ECRIS

The Electron Cyclotron Resonant Ion Source (ECRIS) provides medium to HCI and were originally developed for high energy physics applications, used as injectors in linear accelerators or cyclotrons to further increase the ion energy. Nowadays they are widely used in diverse fields and applications such as high energy physics, ion traps, x-ray spectroscopy or the interaction dynamics of ions with matter. The ECRIS was first proposed in 1969 by *Geller* [179] and by *Potsma* and co-workers [180] in 1970. The first operational ECRIS has been reported in 1971 by *Geller* and co-workers [181]. From the first operational ECRIS up to nowadays a great technological improvement has been rapidly put forward and several reviews on the technique, on the history of the ECRIS development and on the current status of development can be found in the literature [182–186].

The ECRIS are plasma ion sources. To be sustained, the plasma needs to be constantly heated and confined. In an ECRIS, this is done by a structure of minimum magnetic field designed to trap hot electrons, in which the constant heating is performed by the injection of microwaves in resonance with the cyclotronic movement of the trapped electrons. The magnetic field design needs to match the injected microwaves frequency. The working principle, upon which the ECRIS is based, is schematically shown on Fig. 1.1. A metallic vessel serves both as a multi-mode cavity and as a plasma chamber. The dimension of the plasma chamber must be larger than the wavelength of the injected microwaves. In the case of SIMPA, an all permanent-magnets SUPERNANOGAN [187] type ECRIS, which uses 400 W microwaves of 14.5 GHz frequency, the wavelength is $\lambda = 2$

cm. SIMPA has been jointly operated by Laboratoire Kastler Brossel (LKB) and the Institut des NanoSciences de Paris (INSP) since 2004. Several projects with different motivations using both the extracted beam or the x-ray radiation have been started in atomic, plasma and surface physics [9, 149, 188–197].

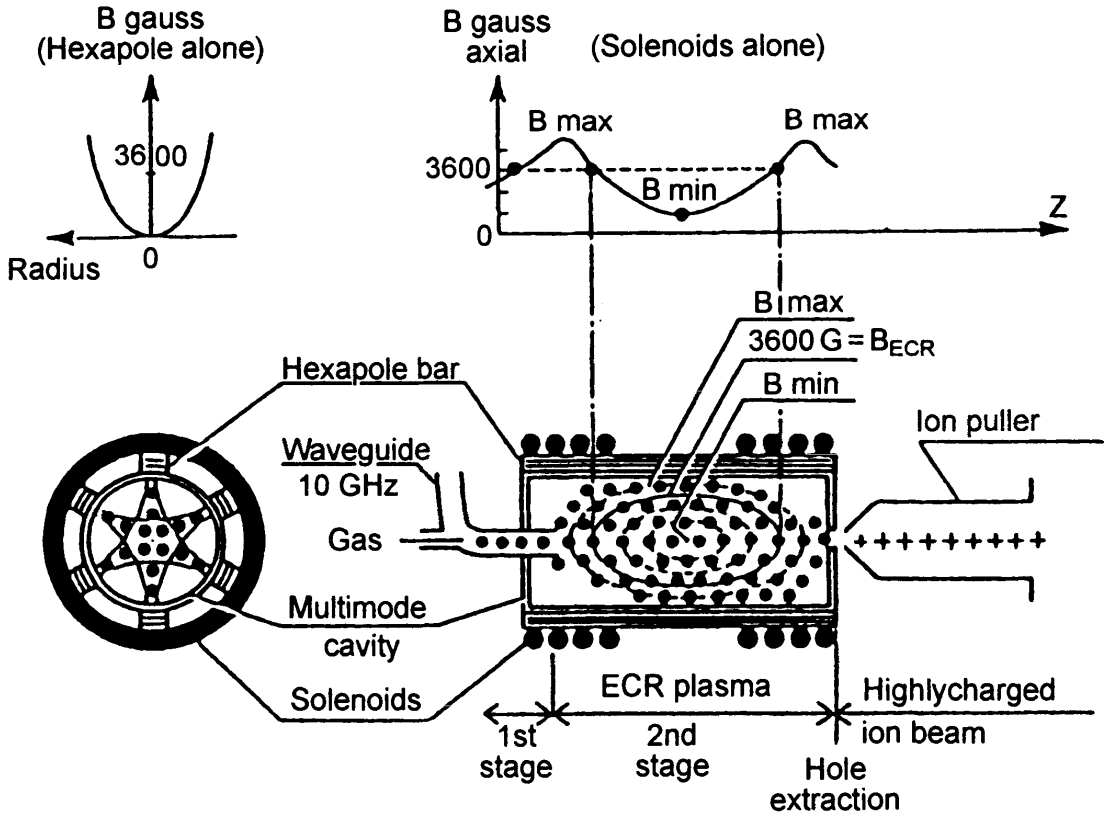

Figure 1.1 – Principle of a 10 GHz ECR ion source. The plasma electrons are trapped in a B_{min} structure and are energized at the magnetic surface where the magnetic field is B_{ECR}. Picture and caption taken from [198] ©1991 Springer.

In SIMPA ECRIS, the microwaves are powered by a 2 KW klystron couple to the cavity through a single ridge waveguide. A reservoir of electrons, in a first stage, are provided by a copper biased polarization electrode emerged in a strong magnetic field produced by a permanent magnet of 1.3 T. This magnetic field has a configuration of a magnetic bottle with a presence of an hexapole that traps the electrons in the beam axis and along the perpendicular direction, the so-called *minimum-B structure*. This structure is illustrated in Fig. 1.1. The steam of electrons provided by the polarization electrode diffuse into the main second stage where the cold plasma is finally ignited.

To maximize the field of HCI in the plasma through step-by-step ionization its mandatory to maximize the product of electron density, electron velocity and ion confinement $n_e v_e \tau_c$ keeping at same time a low neutral density to avoid ion

charge reduction through charge exchange. To effectively produce HCI like Ar^{16+} is estimated from theory [199] that a minimum time of 10 ms of ion confinement is required. This long ion lifetime can be achieved with the described magnetic field bottle like structure illustrated by Fig. 1.1. The B_{min} and B_{max} values of the axial field and the ellipsoidal electron-cyclotron-resonance surface fulfilling the resonance condition for a 10 GHz microwave field is also illustrated by Fig 1.1. Although, as mentioned, this *minimum-B structure* is achieved by the use of an all permanent magnets at SIMPA, this structure can be constructed by the use of normal coils or in some cases superconducting coils. Two examples of ECRIS facilities using superconducting coils can be found in the references [200, 201]. Different devices, such the ECR ion trap (ECRIT) hybrid magnetic system, constructed combining superconducting coils magnetic bottle and a permanent magnet hexapole can be found in [202].

The electrons, which happen to be on phase with the microwaves electric field component, are accelerated by the transfer of electromagnetic energy perpendicular to the magnetic field at the ECRIS surface. The electrons arriving out of phase are decelerated. Through many passes by ECRIS surface, the energetic electrons ionize by inelastic collisions the gas in the magnetic structure, being the resulting ions trapped in the space charge of the electrons. The resulting plasma has a ion-speed distribution of a few eV per charge while the electrons can reach several tens of keV. With this electron kinetic energies, ionization by electron-impact can occur creating holes in the inner-shells of the present elements in the plasma. The detection of radiation produced by the transitions to the created inner-shell holes in the plasma can be used to plasma diagnostics [203]. From x-ray high-precision spectroscopy, the measurement of the charge distribution in a ECRIS plasma has been performed in [204] by a complete analysis of the spectra, identifying all excitation and ionization processes that lead to the excited states of the different ionic species, whose decay will yield into the detected lines. Some examples on the investigating of ion creation and excited level population mechanisms in an ECRIS plasma can be found in [109, 111, 205–207].

In the commercial all permanent-magnets SUPERNANOGAN 14.5 GHz, the electronic temperature has been measured through the use of electron Bremsstrahlung spectra [188] and through high-precision x-ray spectroscopy the charge state distribution and electronic density has been characterized [208].

Figure 1.2 shows a schematic drawing of the SIMPA ECRIS. On the left side, a portion of the plasma can be extracted through the use of electrostatic lenses and focused with a solenoid. A specific charge state of an element present in the plasma can be further selected with the Dipole Magnet to perform experiments or

to monitor the stability of the source during its operation. On the left side, a high-precision single-flat Double-Crystal Spectrometer (DCS) is connected through a beryllium window capable to isolate the vacuum from the source to the primary vacuum of the DCS ($\simeq 100N/m^2$). The window is semi-transparent to the soft x-rays coming from the source having a transmission of about 50% for soft x-rays with energy of 3 keV. In the zoomed part of Fig. 1.2, the position of the plasma and the beryllium window to the DCS is illustrated. The position of the polarization electrode can be changed by moving the cross where it is fixed in order to maximize the trapped electron density at the first stage. This movement is allowed by the use of a belly tube which connects the cross where the beryllium window is installed to the copper cube where the polarization electrode goes inside the plasma chamber.

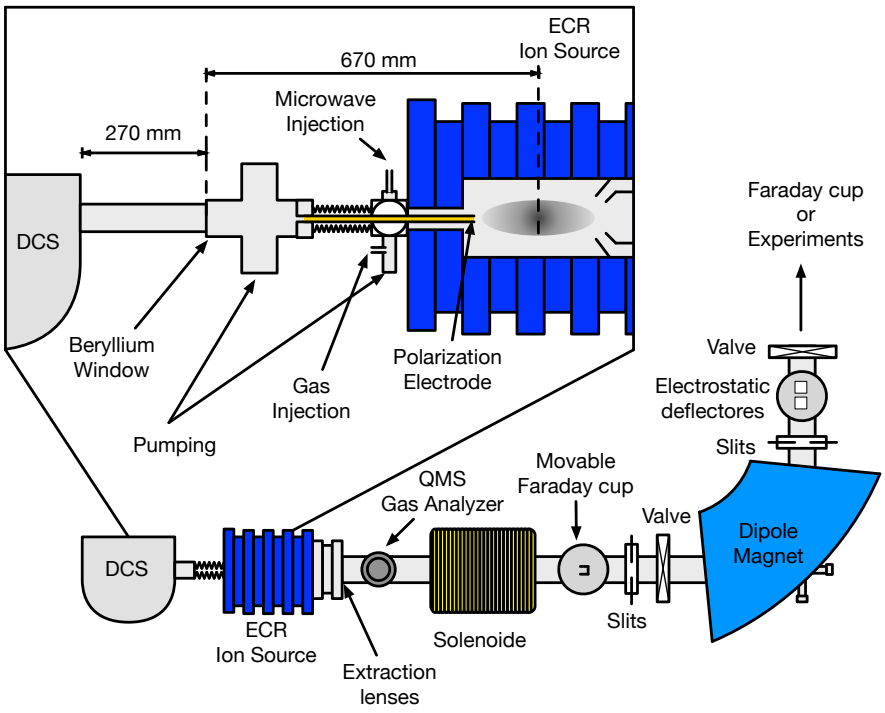

Figure 1.2 – Global view of the SIMPA ECRIS with the DCS installed on the left side to perform x-ray spectroscopy. On the right side, a portion of the plasma can be extracted and a specific charge state can be selected to perform experiments or to analyze the presence of a specific charge state in the plasma. In the zoomed part, the distance from the DCS to the plasma and to the Beryllium window can be seen.

1.3.2 The Double-Crystal Spectrometer (DCS)

Single-flat double-crystal spectrometers are Bragg type spectrometers in which two crystals are arranged in such way that there are two different positions of the crystals that satisfies the Bragg condition (Eq. (1.1)).

Figure 1.3 illustrates the two measurement positions of the DCS. In a DCS, the first crystal is kept fixed for both operation positions illustrated in Fig.1.3. The first crystal can be thought as a collimator or a wavelength filter, the accepted wavelengths from the first crystal at a certain position only depends on its width. The second crystal sees the reflected x rays whose direction is defined by the first crystal according to the Bragg law (Eq. (1.1)). As mentioned, there are two different positions for the second crystal which satisfies the Bragg condition of reflection: one position where the two crystals are parallel (non-dispersive mode) and another position where the crystals deflect the x rays in the same direction (also called antiparallel mode). To perform a measurement, the first is kept fix while the second crystal does a angular scan around the Bragg angle θ_{Bragg} for a given wavelength in both non-dispersive and dispersive modes. An angular spectra for each operation mode will be acquired. In the non-dispersive mode, a peak (parallel peak) is obtained, whose shape only depends on the response function of the instrument. A second peak is obtained in dispersive mode (antiparallel peak) which shape in this mode depends on the line shape and on the response function of the instrument. The difference of the angular position of the second crystal in both modes corresponds to $2\theta_{\text{Bragg}}$, which, taken into account the DCS geometry, is directly related by

$$\theta_{\text{Bragg}} = 180 - (\theta_{\text{disp}} - \theta_{\text{non-disp}})/2, \tag{1.2}$$

being θ_{disp} and $\theta_{\text{non-disp}}$ the angular settings of the second crystal in the dispersive and non-dispersive modes, respectively. Being both peak dependents on the response function of the instrument, some corrections are needed to correctly obtain both θ_{disp} and $\theta_{\text{non-disp}}$ angles from the spectra, *e.g.*, the index of refraction of the crystals, the vertical misalignment, the temperature of the crystals have to be corrected. This subject will be discussed further in the text.

The DCS used in this work, whose top schematic view is illustrated in Fig. 1.4, has a particular characteristic when compared to the existing double-crystal spectrometers. Both crystals are mounted in a single horizontal table of 6 cm thick and weighing $\simeq$ 200 Kg that rotates around the first crystal axis. Usually, in other DCSs, the crystals are mounted in a steady platform taking advantage on the fact that the x-ray source can be placed at different positions. In this work, the DCS

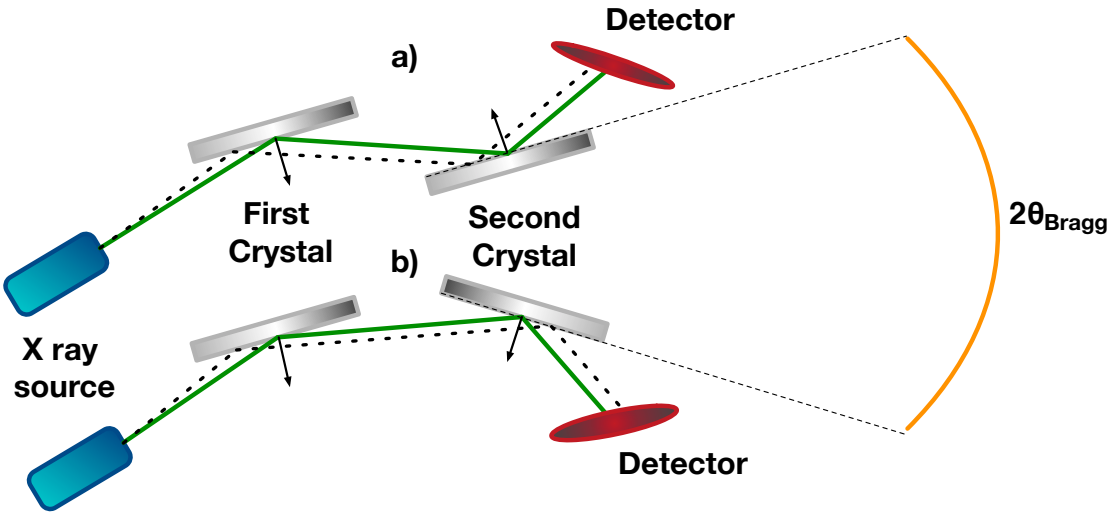

Figure 1.3 – Illustration of the two measuring modes of the DCS. The non-dispersive mode (a) where the crystals are geometrically parallel (also called parallel mode) and the dispersive mode (b), where the crystals deflect the x rays in the same direction (also called antiparallel mode).

is connected to SIMPA which is a massive, complicated vacuum system build with many components which makes the task of moving it for each different measurement arduous or even impossible, being this DCS thought in is development process to be connected to a not movable x-ray source.

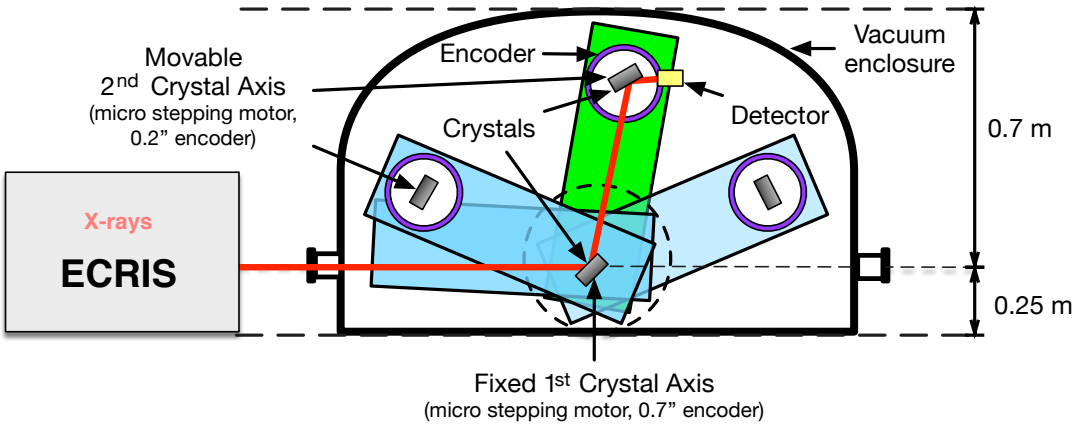

Figure 1.4 – Schematic of the top view of the DCS. Both crystals are installed in a single table that rotates around the 1st crystal axis. The detector is mounted also in the table and is with a rotation trajectory is concentric with the 2nd crystal axis.

The general setup of the DCS used in this work with all its components is illustrated on Fig. 1.5. The single horizontal table and the crystals supports are made of a special alloy, nitrated stainless steel LK3 (0.4% C, 1.8% Cr, 1% Al, 0.25% Mo)

since it provides long-term stability. The material was thermally treated at 900 °C after machining to avoid residual constraints in the material. The parts were finally finished by grinding the different surfaces to 2 μm accuracy. To enable the table rotation to an arbitrary angle, it is mounted in a heavy-duty indexing table rotating around the first crystal vertical axis. In order to rotate, the table is mounted in a pair of canonical wheels ground to have perfect contact. The wheels are driven through a special metallic track equipped with a system of adjustment screws. Both track and wheels have been hardened. The chamber itself is mounted on a support table with anti-vibration feet. Between the spectrometer chamber and the support table, four translation stages are placed to allow the translation of the spectrometer for alignment purposes together with four screws for translation movement of the chamber. Together, the translation stages, the four feet of the chamber and the four feet of the supporting platform allows the movement of the entire chamber in all the spatial degrees of freedom to a precise alignment. The vacuum chamber weights more than 1000 Kg and a primary vacuum pressure of 2×10^{-2} mbar can be applied to reduce the absorption of soft x-rays and allows to apply HV to bias the detector below the Paschen breakdown voltage for air, avoiding discharges (1800 V - 2000 V).

Besides the table, there are three more rotation stages present in the DCS: the first and second crystals and the detector. The rotation of the crystals is performed by precision micro stepping motors powered and controlled by a three-axis Newport ESP301-3G controller able to perform small steps of 0.017". A Huber goniometer 410/410A motor is used for the first crystal, a Newport RV80 for the second crystal and a RV240 for the rotation stage of the detector. The angles are measured using optical rotary encoder which have built-in transparent glasses with two high quality graduated scales concentric to the axis rotation. A projected-light from Light Emitted Diode (LED) is mounted in one side of the graduated scales while a photocell is mounted in the opposite side to detect the light intensity. The two graduations with equal grating periods are moved relatively to each other. When they move relative to each other, the incident light is modulated being almost perfectly sinusoidal. This allows a very precise system to measure the angle. One of the grading scales has a single reference mark to allow to perform absolute measurements; each time the system is rebooted a full turn of the encoder is needed to find the reference mark. The angle of the first crystal is measured with an Heidenhain ROD800 encoder with a precision of 0.07" read by a Heidenhain IK 220 PC card, while the second crystal angle is measured up to a precision of 0.2" with an Heindenhain RON905 encoder, controlled by an Heidenhain AWE1024. Descriptions of technical aspects of this particular DCS

can also be found in Amaro's [149], Guerra's [190] and Schlesser's [209] Thesis and in Ref. [141].

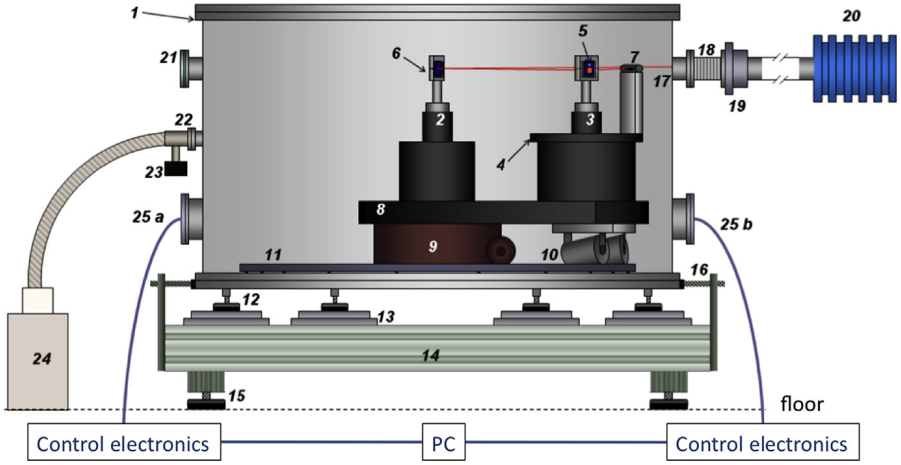

Figure 1.5 – Spectrometer setup: (1) vacuum chamber; (2) axis #1 (first crystal support with rotation stage and angular encoder); (3) axis #2 (second crystal support, rotation stage, encoder); (4) x-ray detector rotation stage ; (5) crystal on second axis; (6) first axis crystal holder; (7) x-ray detector; (8) spectrometer table; (9) spectrometer table rotation stage; (10) conic wheels; (11) tracks for wheels; (12) vacuum chamber anti-vibration feet with vertical positioning; 13) translation stages; (14) spectrometer support table; (15) anti-vibration feet with vertical positioning; (16) positioning screws; (17) x-ray entrance; (18) bellows; (19) Be window; (20) SIMPA ECRIS; (21) optical window; (22) bellows connection to vacuum pump; (23) pressure gauge and valve; (24) primary vacuum pump; (25) a and b flanges equipped with feedthroughs for cables and cooling water. Picture and caption taken from [141].

1.3.3 Crystal diffraction

As mentioned, the allowance of high-precision absolute measurements using a DCS is possible only by knowing with high accuracy the lattice spacing of the crystals in use. For the measurements, we have available two pairs of 6×4 cm^2, 6 mm-thick silicon crystals, two with *Miller* indices (111) (Si_{111}), which are the ones used in the measurements performed in this work, and two (220) (Si_{220}). The crystals were cut from a single bundle of silicon to ensure a perfect crystal without defects and manufactured at NIST for the Paris DCS. In the manufacturing process, the crystals were oriented using a x-ray spectrometer while being polished using a colloidal slurry. The crystals polishing was done so that the angle between crystal planes and crystal surface is smaller than 10" at a temperature of 22.5°. The crystals were then etched in a bath of hydrofluoric acid to remove strains, surface damages and minimize lattice spacing dispersion. The lattice spacing of both

orientation of the same Si bundle was also measured at NIST using as a standard reference a crystal, cut from a bundle grown by Wacker–Siltronic (WASO04) as nearly perfect single crystal natural silicon material, specifically grown for the *International Avogadro Project* [39, 210–214]. The lattice spacing of the reference crystal was determined in Ref. [214]. The measured lattice spacing of $Si_{(220)}$ for the Paris DCS, from the difference of the lattice spacing of the reference crystal and the DCS crystals of $(d_{\text{reference}} - d_{\text{DCS}})/d_{\text{DCS}}) = (-2.3 \pm 1.1) \times 10^{-8}$, is in vacuum at 22.5 °C, $d_{(220)} = 1.920155651\,(23)$ Å, corresponding to a lattice spacing of $d_{(111)} = 3.135601047(38)$ Å for the $Si_{(111)}$. Being the relative uncertainty of the Paris DCS of 0.012 ppm, using this lattice spacing our measurements provides wavelengths directly tied to the definition of the meter. The lattice spacing of the reference crystal was measured in vacuum at 20 °C. When using the crystals at different conditions of those in which the reference crystal lattice spacing has been measured, its value has to be corrected for the laboratory temperature and pressure conditions. For a different temperature, it can be corrected using

$$\frac{\Delta d}{d} = \eta_0(T - 20) + \eta_1(T - 20)^2, \tag{1.3}$$

where T is the laboratory temperature in °C, $\eta_0 = 2.5554 \times 10^{-6}\,°C^{-1}$ and $\eta_1 = 4.58 \times 10^{-9}\,°C^{-1}$ [215]. The compressibility correction is

$$\frac{\delta d}{d} = -\epsilon p, \tag{1.4}$$

where p is the laboratory pressure in atm and $\epsilon = 3.452 \times 10^{-7}\,\text{atm}^{-1}$ [216].

As mentioned, the result spectra from the dispersive and non-dispersive mode scans are dependent of the spectrometer response function. The main contribution for the response function is the crystals reflectivity profile. Accurate calculation of the reflectivity profiles (rocking curve) for the DCS crystals are calculated using the Xcrystal package included in x-ray oriented program XOP [217–219], which uses dynamical diffraction theory from Ref. [220]. Figure 1.6 shows the $Si_{(111)}$ crystals reflectivity profiles calculated from XOP for the $1s\,2p\,^1P_1 \rightarrow 1s^2\,^1S_0$ transition energy of 3139.5821 eV taken from *Artemyev et al.* (2005) [125], as a function of the angle θ centered at the Bragg angle of the transition $\theta - \theta_{\text{Bragg}}$. The blue dashed line corresponds to the σ polarization profile, the green dotted line corresponds to the π polarization profile and the red full line corresponds to the unpolarized profile obtained by sum of the $\sigma + \pi$ profiles. The σ and π components are referent to the polarization vector perpendicular and parallel to the surface, respectively.

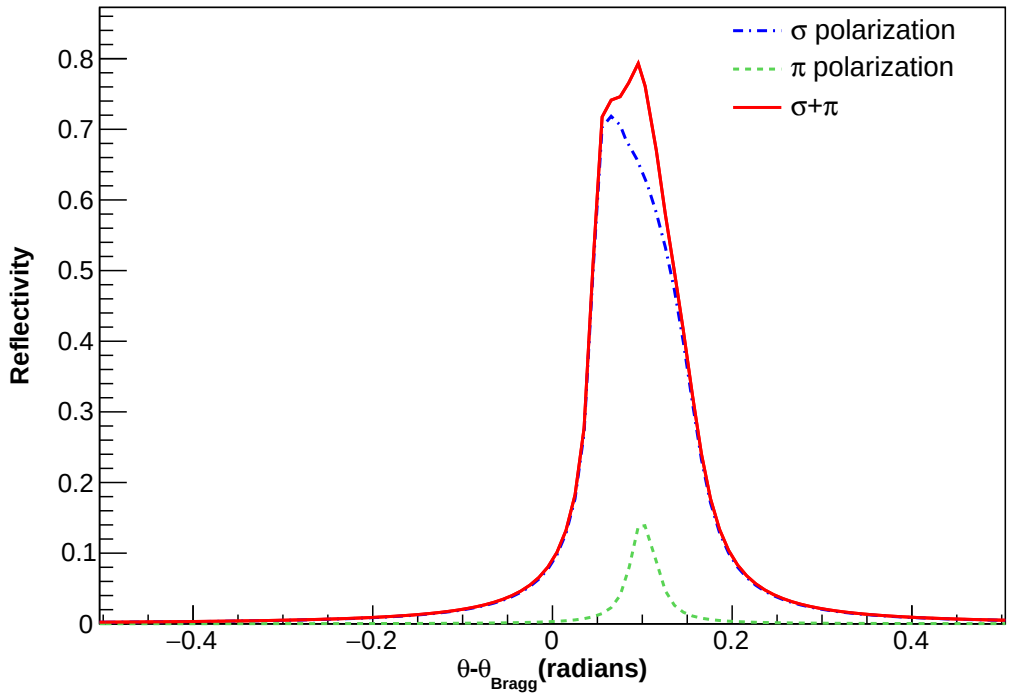

Figure 1.6 – Reflectivity curve (diffraction profile) of Si(111) crystals calculate with Xcrystal from the XOP [217–219] for the $1s\,2p\,^1P_1 \rightarrow 1s^2\,^1S_0$ transition energy of 3139.5821 eV taken from *Artemyev et al.* (2005) [125]. The σ (blue dashed line) and π (green dotted line) polarizations profiles and the unpolarized profile (red full line), obtained by the sum of $\sigma + \pi$ profiles, are shown.

As it can be seen from Fig. 1.6, the unpolarized profile is slightly asymmetric. This asymmetry results from the inclusion of absorption on the calculation of the reflectivity profiles which causes a slight asymmetry on the σ component. This asymmetry for the non-dispersive mode is cancelled since the peak is the convolution of the reflectivity profile with its mirror image. As for the dispersive mode, this effect results in a slightly asymmetry since the reflectivity profile is convolved with itself, which enhances the asymmetry.

In order to overcome this effect, for the analysis and for finding a specific line at a given spectrometer position, a ray-tracing Monte-Carlo simulation code has been developed by *Amaro* which uses as input the reflectivity profiles from XOP and contains the source and the spectrometer geometry [141, 149] (a more detailed description of the code will be given on section 2.1). As discussed by *Guerra* [190], several simulations have been performed and compared to experimental spectra in order to evaluate the polarization contribution to the spectra. It has been concluded that the effect in energy of considering the unpolarized reflectivity profile or the σ polarized reflectivity profile in the simulations is

1 meV. It has also been concluded that the best agreement between simulations and experiment was achieved when considered for the simulations the unpolarized reflectivity profile.

1.3.4 Detector system and electronics

The detector is mounted on a Newport RV 240PP rotation stage with a rotation axis concentric with the second crystal rotation axis. Two different detectors were used in different parts of this work, a Saint-Gobain proportional counter filled with xenon (90%) and methane (10%) gas and a non-cooled LAAPD from Advanced Photonix.

The proportional counter has a 50 μm beryllium window and an 12×25 mm^2 active area. It is operated at HV ($\simeq$ 2000 V) thought an external ORTEC 659 (5 kV) Bias Supply and its charge signal integration by an ORTEC 142PC low noise charge-sensitive preamplifier. The LAAPD is also operated at HV ($\simeq$ 1800 V) but its signal is processed by an ORTEC 142HI preamplifier. The ORTEC 142HI has similar performance and characteristics than the ORTEC 142PC, being the major difference the possibility to operate the ORTEC 142HI under vacuum. The low energy noise of the LAAPD increases with the cable length connection to the preamplifier which forces the preamp installation inside the vacuum chamber. Very detailed operation principles of this device can be found in literature, see *e.g.* [83, 221, 222]. Although the major disadvantages of using an LAAPD being its high sensitivity to external light and temperature and its low-energy noise tail, which depends on each device itself, can limit the minimum detectable x-ray energy, is windowless characteristic can be crucial for detection of soft x-rays, and in this specific application an improvement of event rate. A study of the LAAPD performance for soft x-rays applications at room temperature and a comparison to proportional counters is given in [223], in which its applicability to detect the minimum x-ray energy of 1 keV (depending on the device) and its comparable energy resolution to proportional counters is presented.

Despite the utilization of two different detectors in this application, the overall electronics, with the exception of the preamplifier, is the same. The signal coming from the preamplifier is processed by ORTEC 572 spectroscopy amplifier. The signal from the amplifier is used as input to a ORTEC 551 TIMING Single-Channel Analyzer (SCA) in window mode operation, which generates a TTL pulse when the signal amplitude is between two preselected thresholds, Lower Level (LL) and Upper Level (UL). The selectable range of the LL is from 0 V to 10 V and from 0 V to 1 V above the LL for the UL, being 1 V the maximum range for the

signal amplitude gate window. This allows the selection of a x-ray energy range of interest and the suppression of the high-energy background coming from the bremsstrahlung radiation produced by the high-energy electrons in the source, and the suppression of the low-energy noise tail in the case of the LAAPD. The TTL pulses coming from the TIMING SCA are accumulated by 6602 PC card from National Instruments. The control of the micro-stepping motor control unit for both crystals and detector rotation stages, the angles and the x-ray acquisition are controlled by a Labview^{T} M program. The program reads the first crystal encoder throught a Heidenhain IK 220 PC card and the second crystal encoder through a GPIB bus from the Heidenhain AWE1024 controller. The program monitors the first crystal angle in order kept it steady with a feedback algorithm while the second crystal perform scans at roughly constant speed in a predefined angular range. The range is divided into a predefined number of bins of equal size. The number of pulses are accumulated in a bin while the read angle of the second crystal encoder is contained in between each bin interval. The time spent at each bin is also recorded to insure proper normalization, by dividing the counts per time spend at each bin. When the first crystal angle drifts too far away from the selected angle, the counts and time spent are discarded from the histogram until the first crystal gets to the set position by the feedback algorithm.

During a DCS scan, a MultiChannel Analyzer (MCA) spectrum is also acquired to check for possible problems or detector drifts. To perform the MCA energy calibration, the radioactive sources ^{55}Fe and ^{109}Cd have been used. The 5.9 keV Mn Kα x-rays from the ^{55}Fe source, and the 3.2 KeV and 22 keV from, respectively, the Lα and Kα Ag x-ray transitions have been used for the energy calibration at the same detector applied bias and amplifier conditions. Gaussian fits have been made to the peaks and a linear regression of the energy as a function of the MCA channels has been performed. In Fig. 1.7 an acquired spectrum of the ^{55}Fe with the MCA using the LAAPD is shown, where the 5.9 keV Mn Kα and the low-energy noise tail limit of the LAAPD are clearly noticeable. Since the LAAPD noise tail limit is around 2.2 keV, it allows the utilization of the detector for measuring the core excited radiative transitions in He-, Be-, Li- and B-like Argon.

The 3.2 KeV Ag Lα from the ^{109}Cd source has been also used to correctly select the gate window in the ORTEC 551 TIMING SCA for the required x-ray energy range, especially to suppress the LAAPD noise tail. Coincidences between the analog signal from the amplifier and the TTL signal from the TIMING SCA can be done to check if the correct signal amplitude thresholds have been selected. Figure 1.8 schematically illustrates the electronics modules used to perform the coincidences. Two identical ORTEC 572 Amplifiers at the same gain and shaping

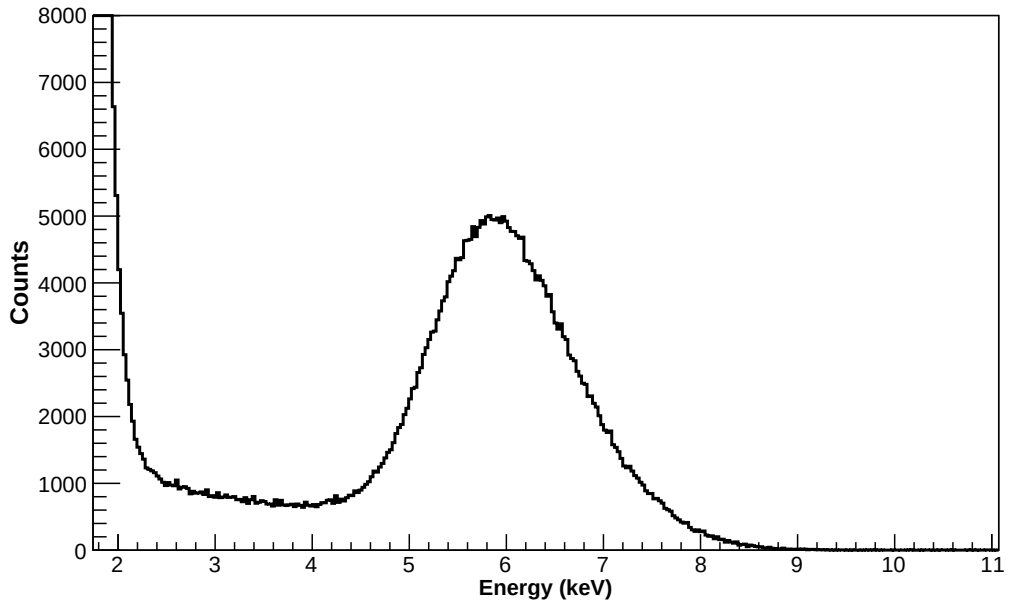

Figure 1.7 – Calibrated energy spectrum acquired by the MCA using the LAAPD. The 5.9 keV Mn Kα and the low-energy noise tail limit of the LAAPD are clearly noticeable. The noise tail limit is at around 2.2 keV which allows the utilization of the LAAPD for measuring the core excited radiative transitions in He-, Be-, Li- and B-like Argon, around 3 keV.

time are used to process the signal from the preamplifier with similar output. In one of the amplifiers, amplifier 2, the output signal is delayed in respect to the output signal from amplifier 1. From amplifier 1, the signal is injected in the TIMING SCA in window mode of operation being its output, as already mentioned, a +5 V 500 ns wide TTL signal happening when the input pulse exceeds the adjusted LL but by an amount that is less than the UL. In coincidence mode, the TTL is used as a gate input pulse in the ORTEC 542 LGS while the delay output from the amplifier 2 is used as its linear input. The gate input signal must occur before the peak amplitude from the amplifier 2 and last longer. To optimize the gate input width, an ORTEC 416 GATE & DELAY GENERATOR DELAY (GDGD) is used to increase the signal width since the output from the amplifier 2 has a width equal to its integration time shape of 500 ns, therefore equal to the TTL width from the TIMING SCA output, however, delayed. The output from the LGS in coincidences mode has the same amplitude and width as its linear input and occurs each time a valid gate is in coincidence. The LGS output is then fed to the MCA and a spectrum from the ^{109}Cd source is taken varying the TIMING SCA LL and UL to optimize the energy range of interest.

In Figure 1.9, a ^{109}Cd spectra from the energy range selection process is shown.

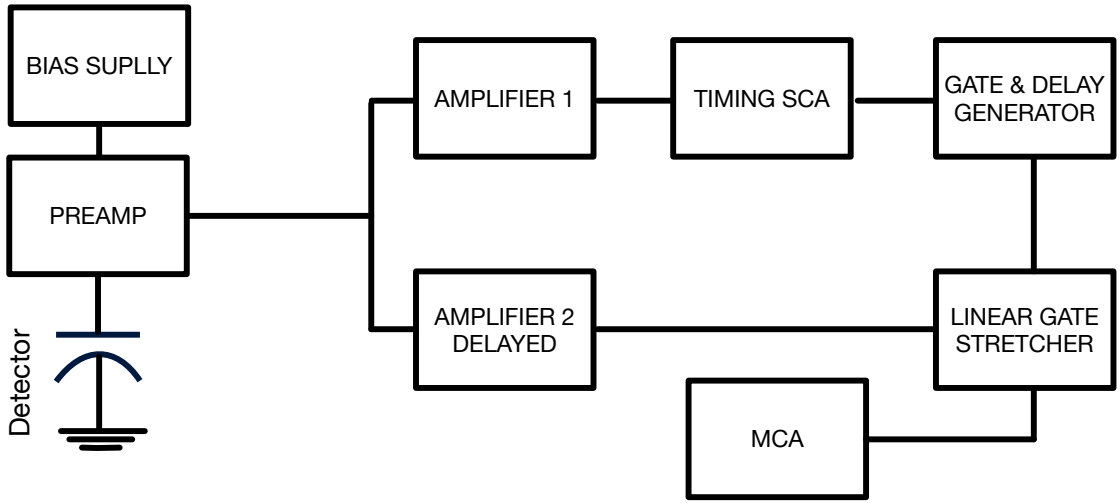

Figure 1.8 – Scheme of the detection electronic modules and connections to the amplitude gate window selection, *i.e.*, to tune the TIMING SCA LL and UL for the energy range of interest.

The black line corresponds to the full spectrum taken directly from the amplifier 2 output (without coincidences to the gate window), the red line corresponds to the LAAPD low-energy noise tail without the radioactive source and the green line corresponds to the spectrum acquired from the LGS in coincidences with the gate during the TIMING SCA LL and UL optimization for the 3.2 KeV Ag Lα x-ray peak. As it can be seen from the same picture, the LAAPD noise tail is completely suppressed, being the LL optimized for the measurement. It can also be seen that the UL is not fully optimized, lasting longer than the 3.2 peak. This UL optimization was performed during the data acquisition from the experiment itself.

1.3.5 Temperature stabilization

While in vacuum performing an experiment, the stepping motors of the crystals rotation stages heat, which, without air convection inside the chamber, makes the task of stabilizing the temperature inside the spectrometer chamber very hard to perform, on the one hand, and mandatory on the other hand, in order to keep the crystals at the same temperature while performing a scan.

The importance of stabilizing the crystals temperature is easily understood from Bragg law (Eq. (1.1)). The performed measurements with the DCS provide us the Bragg angle of a given transition from Eq. (1.2) that can be traced back to the respective energy using the high accurate measurement of the crystals lattice. Yet, being the lattice spacing the average interatomic distance of the Si atoms

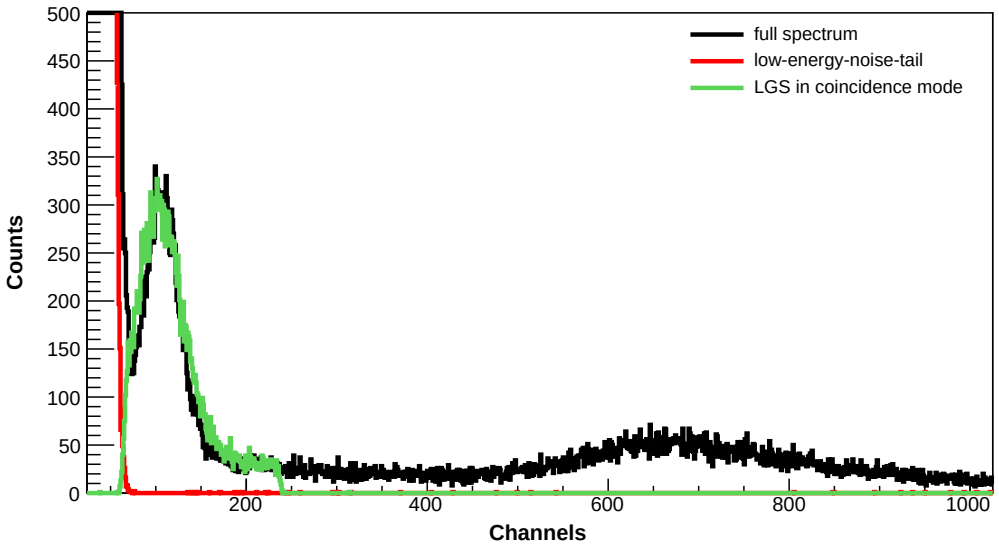

Figure 1.9 – ^{109}Cd spectra from the energy range selection process taken with the LAAPD. The black line corresponds to the full spectrum taken directly from the amplifier 2 output, the red line corresponds to the LAAPD low-energy noise tail without the radioactive source and the green line corresponds to the spectrum acquired from the LGS in coincidences with the gate.

correlated with their kinetic energy, a correct measurement of a x-ray transition energy is dependent on the crystal temperature. As mentioned in section 1.3.3, the lattice space correction for the laboratory temperature can be performed from Eq. 1.3 together with the provided measured difference of the lattice spacing between the DCS crystals and the reference crystal. Even though this correction can be done, the crystals have to be at a fixed temperature to avoid drifts during the experiment. To overcome this, a heating element is pressed between two thin copper plates pressed against the back of the crystals and a 0.1 °C accurately calibrated Pt100 thermistor is used to measure the crystals temperature. A 100 μm thick soft graphite foil assures a good thermal contact between the crystal and the copper plate in vacuum. Figure 1.10 shows a picture of the support with the crystal where the copper plate on the back of the crystal can be seen. The temperature sensor and the heater are connected through a proportional-integral-differential (PID) controller, Jumo Dicon 500 with parameter self-optimization, to set the crystals temperature at 22.5 °C. A feedback loop controls the power in the heating element through the PID controller by calculating continuously the difference of the read temperature and the set value of 22.5 °C. At each experimental run, the temperature is recorded being the maximum allowed fluctuation while measuring 0.2 °C. Water-cooling is also applied to the rotary stages stepping motors in

order to provide sufficient heat loss when the spectrometer is under vacuum.

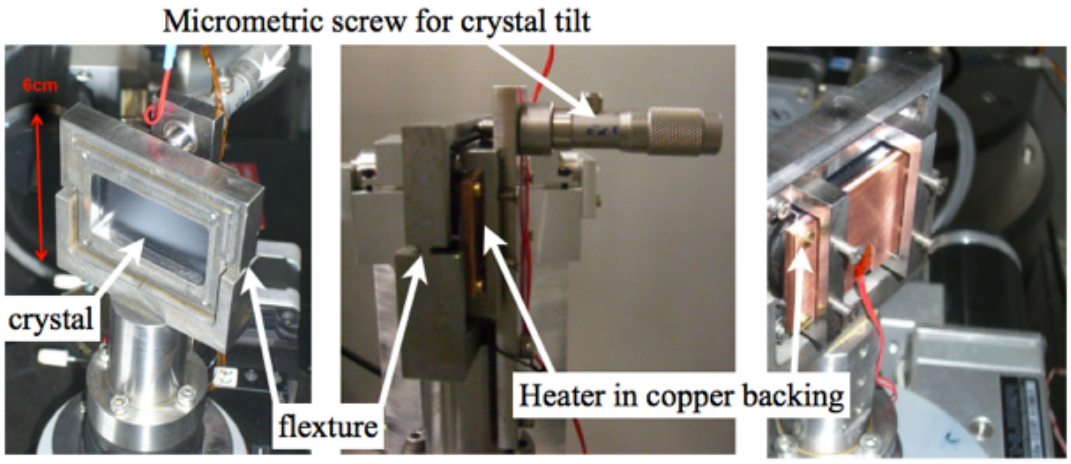

Figure 1.10 – Picture of the crystal supports. Details of the supports are shown: micrometric screw and flexure for the crystal verticality correction and the copper heater plate on the back of the crystal to insure temperature stability during the experiment. The Pt100 thermistor is placed between the copper plate and the crystal.

Several tests have been performed to the temperature measurements. Figure 1.11 shows the record of the temperature of crystal 1 thermistor in thermal contact with crystal 2 thermistor, at atmospheric pressure and laboratory temperature during almost 6 days recording. As it can be seen, the temperature curves of both sensors are almost overlapped for the entire time of the measurement. The calculated average difference of the two temperatures of 6 days recording is 0.0005 °C with a standard deviation of 0.0346 °C, being both, average and standard deviation smaller than the accuracy of the Pt100 thermistor. This allows to confirm that both sensors are calibrated and given the same reading values for the temperature. Furthermore, this gives a measurement of the variation of the laboratory temperature. The laboratory is air-conditioned in order to provide heat loss from all the powered devices in the laboratory, especially the vacuum pumps and klystron. From the 6 days recorded time, an average value of 21.07 °C with a standard deviation of 0.14 °C has been measured allowing the conclusion that the temperature in the laboratory is reasonably stable.

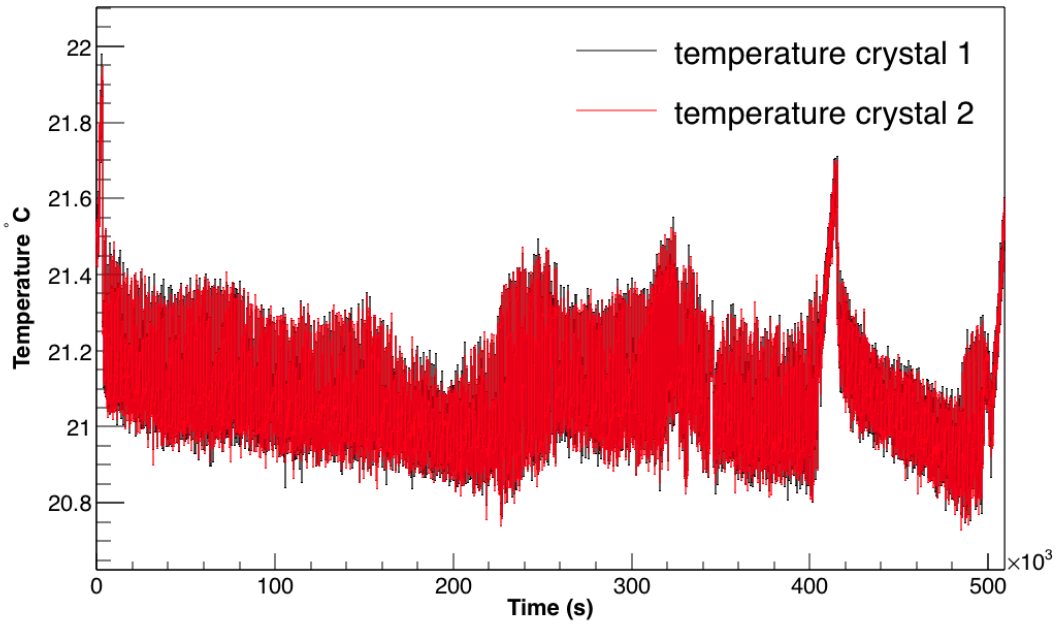

Figure 1.11 – Record of the temperature of crystal 1 thermistor in thermal contact with crystal 2 thermistor, at atmospheric pressure and laboratory temperature during almost 6 days recording. Black line corresponds to the crystal 1 thermistor and red line corresponds to the crystal 2 thermistor.

1.4 Alignment

Before starting a measurement, a correct and careful alignment of the DCS with respect to the SIMPA axis is fundamental to maximize the x ray intensity that reaches the spectrometer and to favor the locating of a specific x-ray line. A correct vertical alignment is crucial to reduce systematic errors, a more detailed discussion about its importance will be given further in the text on Section 3.1.

The alignment is performed with the help of a theodolite equipped with angular encoders of arcsecond accuracy and a tilt-meter, a laser bench, a few machined cylindrical pieces with crosshairs and two plastic targets with a small hole at the very center which area is the full accepted area by the crystals supports. The laser bench is equipped with two high quality mirrors which allows the alignment of the laser beam with the source axis (one for translation and the other rotation), a beam splitter, a cross that works as a reference to the source axis and two cameras, one to monitor the beam spot at the reference cross and the other to match the outgoing beam with the reflective beam which allows the correction of the absolute

angle position of both crystal axes and the correction of the vertical alignment. In Fig. 1.12(a) a picture with a legend of the laser system components can be seen.

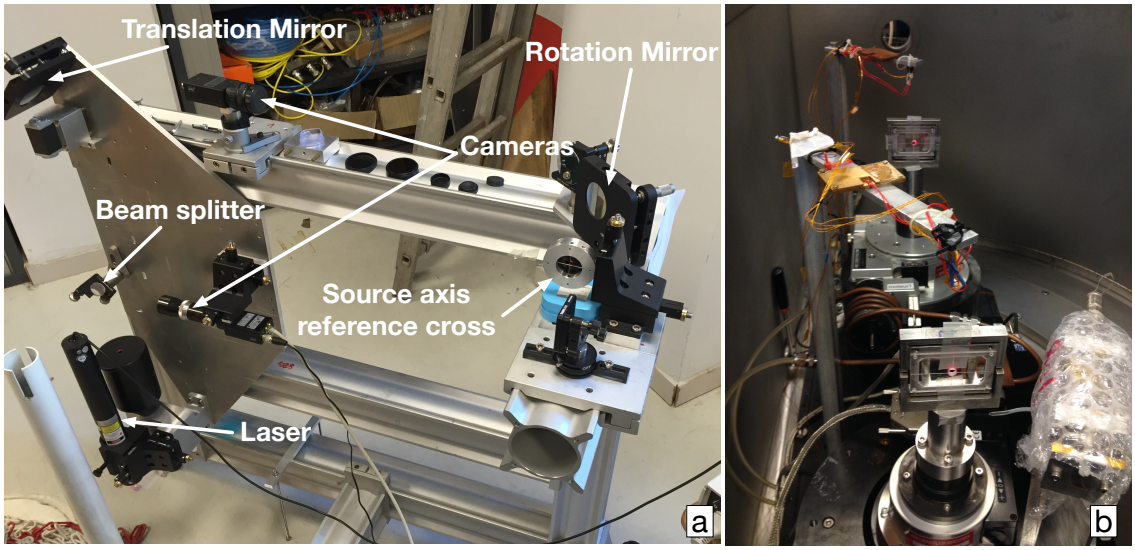

Figure 1.12 – (a) Picture of the alignment laser system with legend. (b) Table in the zero position with the laser passing through the plastic targets. Both crystal axis are positioned at the absolute angle of 180°.

The alignment is performed in the following way:

- SIMPA is opened and putted it on air. Two of the cylindrical pieces with crosshairs are placed, one in the copper cube flange where the polarization electrode goes (see Fig. 1.13(a)) and the other one at the end of the beam line, on the alignment port of the dipole magnet. Both flanges are assumed to be aligned since they were aligned before with the source axis;

- The theodolite is positioned after the end flange of the spectrometer in a way so that is on a straight line that passes through the center of two cylindrical crosshairs;

- The two plastic targets are placed in the crystal supports and two more cylindrical crosshairs are installed at the spectrometer entrance and end flanges. Both targets in the crystal supports are positioned perpendicularly to the straight line formed by the two crosshairs at each source end by rotating the table to the zero position (in a parallel position in respect to the source axis with the two targets facing the source axis perpendicularly) and both crystal goniometers. The vertical and horizontal position of the spectrometer is then corrected so that the straight line formed by the source crosshairs

passes through the spectrometer crosshairs and at the very center of the targets placed in the crystal supports;

- The laser is aligned with the source axis with the help of the two mirrors placed in the laser bench. The beam is aligned so that the beam spot is centered at each crosshair placed at the spectrometer and at the source and passing through the holes present in the plastic targets (see Fig. 1.12). Figures 1.13(b) and 1.13(c) shows the beam spot centered at the crosshair placed at the copper tube flange and at the end of the beam line.

- The plastic targets are then removed and a high quality mirror is placed in the first crystal support. The mirror is rotated to the absolute angle of 180° in order to be in a perpendicular position in respect to the incoming laser beam. The laser beam enters the spectrometer chamber at its end flange in opposite direction of the x rays coming from the source. With the help of the camera, the absolute angle of the first axis encoder is corrected by rotating the axis until horizontal match is achieved of the outgoing laser beam with the reflective beam. The angle of the axis in this position is set as 180°. At this point, the verticality of the support is also corrected by matching vertically the beams in a similar way as the horizontality correction. The verticality of the crystals axes can be adjusted. The crystal supports uses a system of flexure hinges and a micrometric screw to adjust the verticality of the support [224] (see Fig. 1.10). Since the crystals supports rotates on a axis that goes through the front surface of the mirror and its surface is grounded to 2 μm accuracy, the mirror can be substituted by the crystal without losing the vertical alignment;

- After the first axis being aligned, the procedure is repeated to the second crystal support. With both supports aligned horizontally and vertically, the crystal axis are parallel and the spectrometer is ready to be positioned to preform the measurements.

1.4.1 Setting up the spectrometer for a measurement

With the spectrometer aligned with respect to the SIMPA axis we can now set the DCS to measure a given transition. To position the table and the crystal axis for a measurement we make use once again of the alignment system (Fig. 1.12(a)). For a given Bragg angle θ_{Bragg} corresponding to a transition energy, the DCS is positioned performing the following steps:

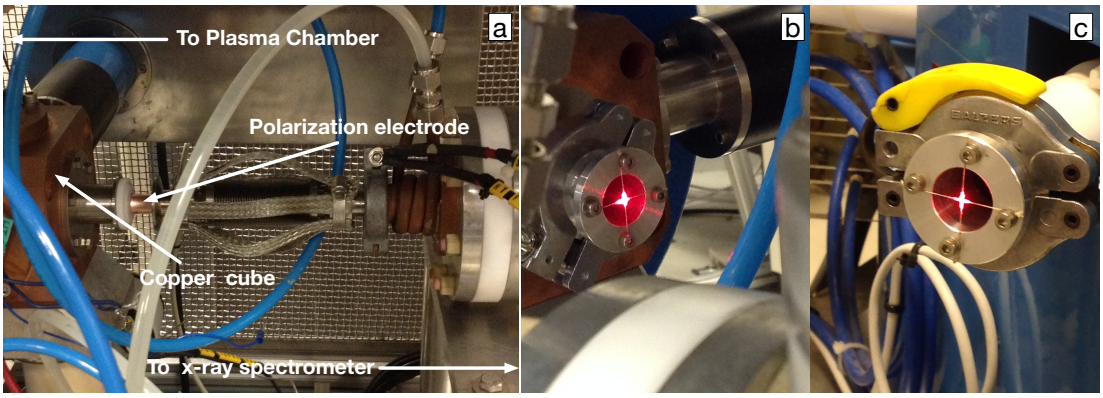

Figure 1.13 – (a) The connection from the SIMPA ECRIS to the DCS where the polarization electrode and the copper tube are visible; (b) the laser aligned with the cross placed in the copper tube flange; (c) the laser beam aligned with the cross placed at the end of the beam line.

- The table is not equipped with an accurate encoder. To rotate the table accurately we make use of the first crystal axis equipped with the mirror. With the table parallel to the source axis (see Fig. 1.14(a)) the first mirror is rotated by $2\theta_{\text{Bragg}}$ or to the absolute angle of $(-180 + 2\theta_{\text{Bragg}})$. The reflected beam is no longer being seen by the camera in the alignment system, as it can be seen in the schematic drawing of Fig. 1.14(b), the reflected laser beam spot is hitting the inner vacuum enclosure wall chamber;

- Rotating the table in the opposite direction in which the first mirror was rotated, the beam spot position is recovered, *i.e*, the reflected beam is again seen by the camera and the rotation of the table will be stopped at the position where the reflected and the outgoing laser beam matches again. At this position, the table has been rotated by $-2\theta_{\text{Bragg}}$. Figure 1.14(c) shows a drawing of the DCS at this position;

- The first mirror is rotated by $-\theta_{\text{Bragg}}$ in order to get the beam spot hitting the center of the second support. Positioning the detector at 0° (with the detector in a perpendicular position with respect to the table), and with the second support empty, the detector encoder read angle can be corrected. The laser spot should hit the detector at its center at this position. The detector encoder angle is set at 0° by correcting the possible existing angle offset;

- The second mirror is installed in the second support. With the beam spot hitting the center of the second mirror, the verticality of the axis is checked again by comparing the reflected with the outgoing laser beam position seen by the camera;

- At this point, the mirrors are replaced by the crystals and the temperature sensors and the copper plate heaters are installed on the back of both crystals. The crystals are carefully pushed against the reference frame of the supports, to which the verticality of these were corrected using the mirrors, using four nylon screws in each support. By the use of nylon screws the constrains in the crystals are avoided and the crystal surface is maintained flat during the measurements;

- To place the DCS in the parallel measuring position, the first axis is rotated to the absolute angle of $90 + \theta_{\text{Bragg}}$. With this rotation which is represented by the Fig. 1.14(d), the angle between the source axis and the first crystal surface will correspond to the θ_{Bragg} of the transition as well as the angle between the first crystal surface and the straight line passing through the center of both crystals when both placed at 0°. In Figure 1.14(e) is schematically shown the rotation of the second crystal and the detector. The crystal is rotated to the absolute position of $-(90 - \theta_{\text{Bragg}})$ and the detector to the absolute position of $2\theta_{\text{Bragg}}$. By these rotations, the angle between the surface and the x rays reflected by the first crystal corresponds to the θ_{Bragg} and the reflected x rays from the second crystal arriving to the detector makes a θ_{Bragg} in respect to the surface of the second crystal;

- To position the spectrometer in the dispersive position of measurement, the second crystal is rotated by $90 - \theta_{\text{Bragg}}$ and the detector by $-2\theta_{\text{Bragg}}$. Figure 1.14(f) shows a drawing of the spectrometer on this measurement mode;

- At both dispersive and non-dispersive mode the vertical alignment of the crystals are measured. For the measurement of the verticality of the crystals the Wyler Zerotronic sensor connected to the Wyler Clino 2000 tilt-meter with a precision of a few seconds of arc is used.

1.4.2 Alignment check with x-ray photostimulable plates

To confirm the alignment, *i.e.*, that we are at the center of the transition in which the spectrometer was positioned to measure, and to check the uniformity of the x rays, the SIMPA is started with a photostimulable image plate ($BaFBr:Eu^{2+}$) inside the chamber in one of three different positions.

The x rays produced in the ECRIS ionizes the Eu^{2+} present in the photostimulable plates to Eu^{3+}, liberating the released electrons to the conducting band of

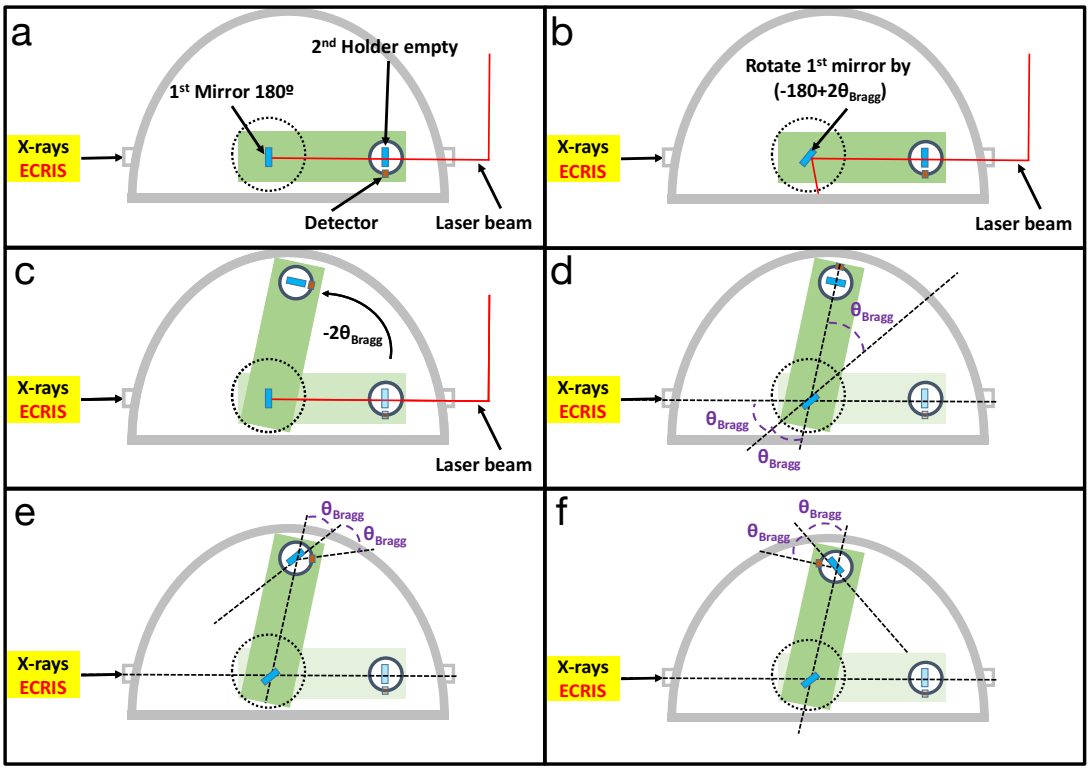

Figure 1.14 – Schematic drawing of the positioning of the DCS to perform a measurement. The steps in the procedure are performed sequentially from (a) to (d), being (e) the non-dispersive mode and (f) the dispersive mode of acquisition.

the phosphor crystals. These electrons are trapped inside the Bromine vacancies produced during the manufacturing process of the plates. By the exposure of a laser light of 633 nm, photons of about 390 nm are released and further detected by a high quantum efficiency Photomultiplier (PMT). Both the laser and PMT are installed in the plates reading system, the Perkin-Elmer Image Plate Scanner (Cyclone). This system allows us to measure the spatial distribution and intensity of the x rays that hit the plates.

The plates are placed in one of three different positions at turn:

- The first crystal is rotated to an angle in which is positioned perpendicularly to the incoming x rays from the source. The plate is placed in front of the first crystal with a lead tape frame marking the lower and upper border of the crystal;

- The first crystal is rotated to again to the θ_{Bragg} of the transition with the second crystal positioned perpendicularly with respect to the table. The image plate is placed in front of the second crystal;

- The image plate is placed in front of the detector with the spectrometer positioned in the non-dispersive mode.

At each different position, the plate is measured by the Perkin-Elmer Image Plate Scanner (Cyclone) and erased by an uniform UV light source before the next measurement. An example of the pictures acquired in the above described different positions, with the DCS positioned to measure the Be-like Argon $1s\,2s^2\,2p\,^1P_1 \rightarrow 1s^2\,2s^2\,^1S_0$ transition, is presented in Fig. 1.15.

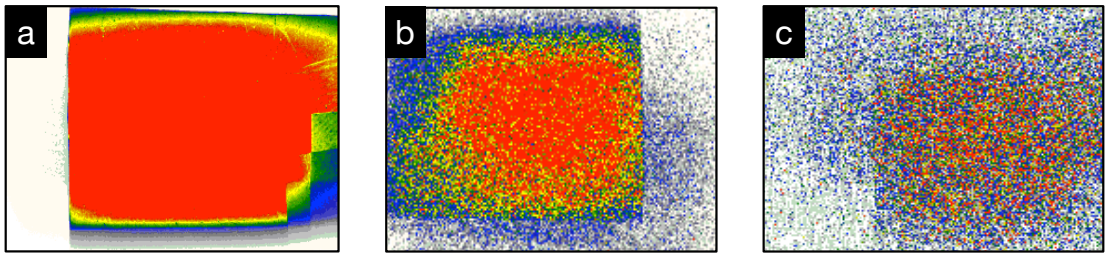

Figure 1.15 – Photostimulable image plate read by the Perkin-Elmer Image Plate Scanner (Cyclone) stimulated by the ECRIS x rays. The plates are placed in the spectrometer chamber at three different positions to check the alignment and the uniformity of the incoming x rays. The spectrometer was aligned to measure the Be-like Argon $1s\,2s^2\,2p\,^1P_1 \rightarrow 1s^2\,2s^2\,^1S_0$ transition. The three positions corresponds to the plate placed in front of the first crystal (a), in front of the second crystal (b) and in front of the detector (c).

The acquisition time at each position of Fig. 1.15 was approximately 30 minutes. As it can be seen, the intensity of the x rays decreases for each position since we lose x rays by each diffraction process at each crystal. Although, it's clearly noticeable in the plate the position of highest x ray intensity. This method is very useful to check qualitatively the horizontal alignment of the spectrometer. Nonetheless, to have a better method using this system, a more accurate procedure of positioning the plates would be necessary to know precisely the area of the plate that is in front of the crystal or the detector.

1.4.3 Measurement method description

The measurements are performed by acquiring angular spectra from a series of scans of the second crystal around the Bragg angle of the transition, for both dispersive and non-dispersive modes. The crystal is rotated continuously back and forth by the stepping motor between two previously defined angles corresponding to the angular range of the spectrum. The first crystal is maintained

at a fixed position while the second crystal rotates. Both crystal angles are continuously measured by the Heidenhain high-precision encoders during the scans. X-rays are recorded in a histogram continuously while the rotation of the second crystal. The angular range is divided by a preselected number of bins. The time that the second crystal spends at each bin is also recorded in order to normalize the spectra. At the end, for each position we get a angular histogram of counts/s. The temperature of each crystal is monitored and also recorded. For a reference-free energy measurement using the double-flat crystal x ray spectrometer, the acquisition of the pair of dispersive and non-dispersive spectra is needed since is the angular difference of the peaks that can be traced back to the energy of the measured transition. The experiment is performed by taken first a non-dispersive spectrum of usually 30 minutes, equivalent at three 10 minutes run, being a run the scan of the second crystal between the preselected range in one direction. This measurement is followed by the recording of a dispersive spectrum which, due to a low counting rate, usually is performed by twenty to twenty five, 20 minutes runs. After the dispersive spectrum being recorded, another non-dispersive spectra is taken in the same way as the first one. This sequence of three recorded spectra takes one full day to acquire due to the already mentioned low counting rate.

This sequence of three recorded spectrum allows us to compensate possible time-dependent drifts in the experiment. For each one-day sequence we will get two values for the Bragg angle, one value from the first non-dispersive spectrum against the dispersive spectrum and the another value from the same dispersive spectrum against to the non-dispersive spectrum obtained immediately after. In order to obtain enough statistics, this one-day sequence is usually repeated typically 7 to 15 times.

Chapter 2

Data Analysis

In previous measurements, the data analysis has been performed by fitting a Voigt profile to the experimental spectra to obtain the angle position of the parallel and antiparallel peaks. With the peaks position, from Eq. (1.2), the uncorrected Bragg angle of the transition is obtained while the energy is deduced with the previous obtained uncorrected Bragg angle and corrected it with the corrections of the refraction index and vertical divergence using

$$E(T,\theta) = \frac{Cn}{2d(1+\alpha(T-T_0))} \cdot \frac{1}{\sin(\theta+\chi\tan\theta)\left(1-\frac{\delta}{(\sin\theta)^2}\right)}, \tag{2.1}$$

where n is the order of refraction, δ is the refraction index, $C = hc$ is the wavelength to energy conversion factor equal to 12,398.41875(31) eV Å [39]. The coefficient χ is the vertical divergence correction [225]

$$\chi = \frac{a^2+b^2}{24L^2}, \tag{2.2}$$

where a and b are the vertical and horizontal dimensions of the x-ray beam size, which are defined by the polarization electrode and the detector window, and L the distance from the polarization electrode to the detector window.

Yet, as mentioned in sec. 1.3.3, the asymmetry of the crystals rocking curve (see Fig. 1.6) results on an asymmetric dispersive peak. Obtaining the energy by fit the antiparallel spectra with a Voigt profile may lead to deviations on the measured line because the center of gravity of the dispersive peak cannot be attributed unambiguously to the peak position. A deviation of 1.86×10^{-3} degrees

between the peak positions obtained from the simulation and the Voigt fit has been observed in the dispersive side [141], which is translated into 19 times the angular encoder error.

To overcome this problem, a Monte-Carlo ray-trace simulation code has been developed [141, 149] for the data analysis. With a complete simulation of the apparatus, the problem of the not-well defined peak in the dispersive spectra is solved. By including the reflectivity profile of the crystals in the simulations, which produces the asymmetry, and fit the experimental data with the simulations, the energy of the simulated line can be used to match both scenarios, experimental and simulation.

Besides the data analysis, the simulation code is also used to find the angle settings of both crystals in a scan of a given transition. As mentioned, the first crystal acts as a wavelength filter in the apparatus. The accepted wavelengths by the first crystal in a fixed position, *i.e.*, the x-ray distribution reaching the first crystal with a given angle, depends on the first crystal width, on the polarization electrode distance and diameter and on shape of the geometrical slits. Varying the angle of the first crystal is thus the same as varying the accepted x-rays energy range by it. Hence, the simulation code is used to optimize the crystals angle settings when we want to measure a transition with the spectrometer centered at a transition energy different from the one we would like to measure.

On this Chapter, a description of the DCS simulation code is given on section 2.1. The data analysis method based on simulations is described on section 2.2 for obtaining the transition natural widths (section 2.2.1) and the energies (section 2.2.2).

2.1 The DCS Monte Carlo simulation code

The Monte-Carlo ray-trace simulation code has been developed within the group by *Amaro* [141, 149] in which all relevant geometric components from the plasma until the detector are implemented. As output, the simulation provides a full simulated spectrum for both dispersive and non-dispersive modes.

Several quantities are used to approach the simulations as much as possible to reality. One of its features is the implementation of specific distribution functions around a given x-ray energy. As mentioned, the dispersive spectra is a convolution between the transition natural width, the Gaussian broadening due to the plasma temperature and the crystals reflectivity profile. To take all this into account, a Lorentzian and Gaussian distributions are implemented around a given

x-ray energy by the generation of a Lorentzian and Gaussian random numbers, being in this way, the generated wavelength λ distribution correspondent to a Voigt profile (the convolution between a Lorentz and a Gaussian distributions). The reflection on the crystals is described by dynamical diffraction theory. The crystals reflectivity curve is calculated using the Xcrystal package included in x-ray oriented program XOP [217–219] assuming an unpolarized X-ray source, taking into account the reflections of both σ and π polarizations. The reflectivity curves from XOP are used as input from the simulation code as a probability distribution for the reflection of an x ray in the crystals, being interpolated in the code using cubic splines. The reflectivity curves calculated with XOP are checked with X0h [226]. An example of the reflectivity curves calculate with XOP are shown in Fig 1.6 on Section 1.3.3. The curves are evaluated at the Bragg angle θ_{Bragg} corresponding to the wavelength λ and the angle θ, which is the angle between the incoming ray and the crystallographic plane of the crystal. The curve depends on the refraction index and absorption coefficients which are dependent on the energy and evaluated by XOP. At each crystal, the position of the random generated x ray is evaluated and the angle between the incoming ray and the normal vector to the crystallographic plane calculated. In order to introduce a crystal vertical angle, to take into account a possible vertical misalignment, an angle is introduced in the simulation between the normal plane vector of the crystal surface and the horizontal plane. This angle follows a $\sin(\theta)$ function along the horizontal rotation angle (θ) of the crystal. A more detailed description of the dependency of the crystal tilt angle with the horizontal angle of rotation of the crystals will be given in Section 3.1. In that Section, a study of the influence of a tilt angle in the energy measurement based on simulations and measurements of the crystal supports verticality is also shown.

The lattice space dependence with temperature $d(T)$ is also implemented in the code. The dependence is given by

$$d(T) = d_{22.5}(1 + (T - 22.5)\eta(T)), \tag{2.3}$$

where $\eta(T)$ is the coefficient of thermal expansion, $d_{22.5}$ the lattice at 22.5 °C and the temperature given in degree Celsius. The quantities $\eta(T)$ and $d_{22.5}$ are deduced from Eq. 1.3 on Section 1.3.3. Since we are dealing with small temperature variations, the dependence of $\eta(T)$ with temperature is neglected in the code.

With all this implemented in the code, the simulations are thus capable to provide a line-width and energy analysis from the experimental spectra. The method used for data analysis is described in the remain of this Chapter. A more

detailed description of the DCS Monte-Carlo simulation code can be founded on Ref. [141, 149].

2.2 The analysis procedure

The data analysis is preformed in three steps. First we obtain a value for the transition natural width. In order to obtain it, a set of simulations is performed for different Lorentzian widths, using as Gaussian broadening the value obtained in Ref. [9], using an approximate energy (*e.g.*, the theoretical value). A weighted average is performed to all values from each dispersive mode recorded and the value of the natural width and respective error is obtained. With the derived natural width, another set of simulations are performed using different, but approximate, energies and second crystal temperatures. These simulation are then use to fit each pair of dispersive and non-dispersive experimental spectrum to obtain the line energy. A more detailed description of the method follows on the text.

2.2.1 Line Widths

From Ref. [9], a value for the ions temperature inside the plasma, which is necessary to calculate the Gaussian broadening, was obtained. In that work, which has been performed in the same experimental apparatus of this work, the M1 Relativistic Magnetic Dipole $1s\,2s\,^3S_1 \rightarrow 1s^2\,^1S_0$ transition in He-like argon has been measured. The natural transition of this line is $\approx 1 \times 10^{-7}$ eV, being thus completely negligible compared to the inherent energy resolution of the DCS and the Gaussian Broadening. From that work, a Gaussian broadening FWHM value of $\Gamma_G^{\text{Exp.}} = 80.5\,(46)$ meV has been obtained. With the knowledge of the Gaussian width, all needed simulations for the analysis of the lines under study can be performed, since all lines of this work have been measured on argon. For the description of the method, the example of the measured He-like $1s\,2s\,^1P_1 \rightarrow 1s^2\,^1S_0$ transition is going to be used. The analysis procedure to obtain the experimental width is the following:

- Perform simulations for the dispersive spectra for a set of natural width values Γ_L^i using as energy the theoretical energy E_0, using the already known $\Gamma_G^{\text{Exp.}}$, and as crystal temperature $T_{\text{ref.}} = 22.5\,^\circ C$;
- Each different simulation is interpolated by spline functions in order to obtain a set of continuous and parametrized functions $S_{[E_0,\Gamma_L^i,\Gamma_G^{\text{Exp.}},T]}(\theta - \theta_0)$,

where $(\theta - \theta_0)$ corresponds to the angle at which the simulation reaches its maximum value and $T = T_{\text{ref.}}$;

- Normalize the $S_{[E_0,\Gamma_L^i,\Gamma_G^{\text{Exp.}},T]}(\theta - \theta_0)$ functions in order to have the same maximum. The $\Gamma_L = 0$ function has been taken as reference;

- Fit each experimental dispersive spectrum with the set of parametrized functions obtained above

$$I(\theta - \theta_0, I_{\max}, a, b) = I_{\max} S_{[E_0,\Gamma_L^i,\Gamma_G^{\text{Exp.}},T]}(\theta - \theta_0) + a + b\theta, \tag{2.4}$$

  where $I_{\max}$ is the peak intensity, θ_0 the crystal angle, a the background intensity and b the background slope. The θ_0 coefficient allows the function to shift in θ in the fit. The angle settings or temperature chosen for the simulation may not be exactly the same as the experiment, resulting in a shift between the two peaks. Yet, the shape of the peak is independent of the angle settings and temperature, unless the x rays are been diffracted at near the second crystal edge, in which other dynamical effects may play an important role. The fits are done by the minimization of the $\chi^2(\Gamma_L^i)$, being $I_{\max}$, θ_0, a and b adjustable coefficients. The $\chi^2(\Gamma_L^i)$ minimization is performed using the nonlinear least-squares Levenberg–Marquardt algorithm implemented from [227]. The algorithm is implemented in ROOT CERN data analysis framework [80–82] through the MathMore library which uses the GSL-GNU implementation [228]. A typical dispersive spectra from the He-like $1s\,2s\,^1P_1 \rightarrow 1s^2\,^1S_0$ transition and the fitted simulated functions, for all the Γ_L^i ranging from $\Gamma_L = 0$ meV to $\Gamma_L = 300$ meV are shown on Fig. 2.1;

- At each performed fit to the dispersive spectrum, evaluate the minimum of the square deviation, the χ^2 given by

$$\chi^2 = \sum_{i=1}^{i=n} \frac{(O_i - I_i)^2}{I_i}, \tag{2.5}$$

  where O_i is the measured point and I_i is the calculated point from the optimized fit function from the χ^2 minimization.

  The reduced χ_r^2 is also evaluated at each performed fit as a goodness-of-a-fit criterium and is given by

$$\chi_r^2 = \frac{\chi^2}{\nu}, \tag{2.6}$$

where number of degrees of freedom, $\nu = n - m$, is given by the number of points n minus the number of fitted adjustable coefficients m;

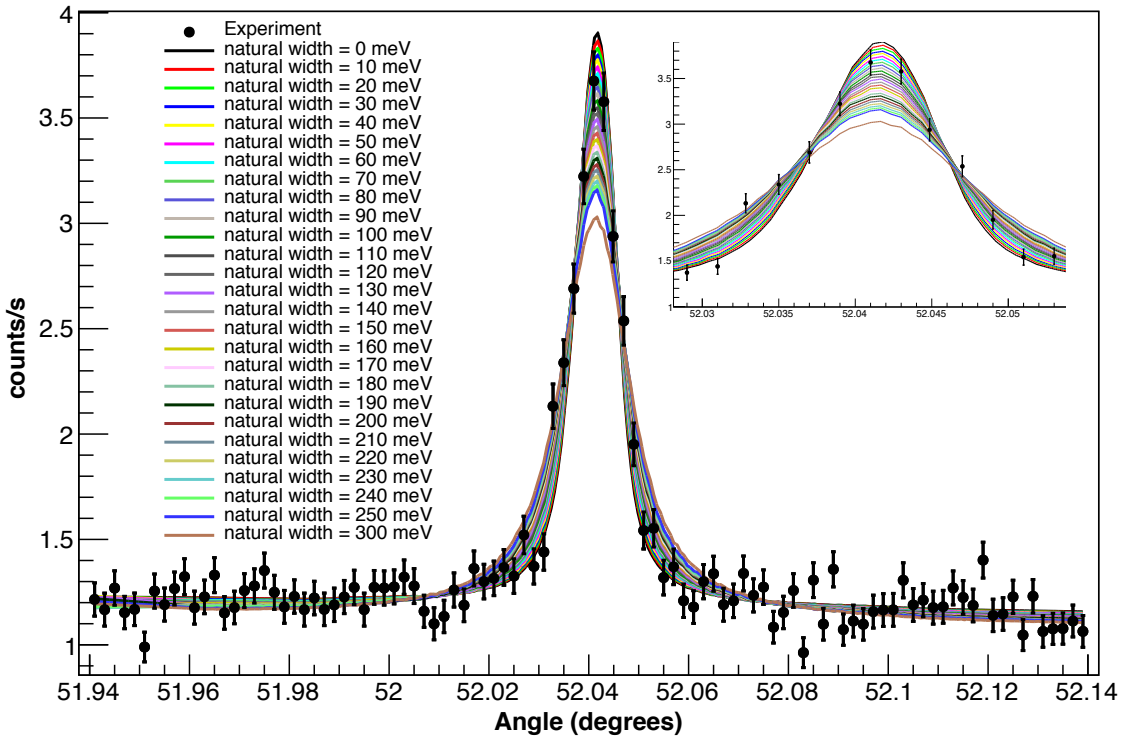

Figure 2.1 – Example of fit to the dispersive spectrum of the $1s\,2s\,^1P_1 \rightarrow 1s^2\,^1S_0$ transition by interpolated simulations spectra for a set of Lorentzian widths. In the legend, the color and Lorentzian width of each fit is shown ranging from $\Gamma_L = 0$ mev to $\Gamma_L = 300$ mev. The error bar in each point is the $\sqrt{n}/t$, being n the number of counts and t the time spent in the bin.

- Fit a third degree polynomial to the set of points $\left[\chi^2(\Gamma_L^i), \chi^2\right]$;
- From the third degree polynomial fit, obtain the minimum corresponding the optimum Lorentzian width $\Gamma_{L\text{opt.}}^{n_r}$, n_r being the run number of the specific spectrum. Figure 2.2 shows an example of the third degree polynomial fit to the set of points $\left[\chi^2(\Gamma_L^i), \chi^2\right]$ obtained from the fits corresponding to Fig. 2.1;
- Get the 68% (1σ) error bar $\delta\Gamma_{L\text{opt.}}^{n_r}$ by finding the values for the width for which [229]

$$\chi^2\left(\Gamma_{L\text{opt.}}^{n_r} \pm \delta\Gamma_{L\text{opt.}}^{n_r}\right) = \chi^2\left(\Gamma_{L\text{opt.}}^{n_r}\right) + 1; \tag{2.7}$$

- A weighted average from all the recorded spectra optimum widths set of data $\Gamma_{L\text{opt.}}^{n_r}$ to obtain the experimental value $\Gamma_L^{\text{Exp.}}$ and respective error bar:

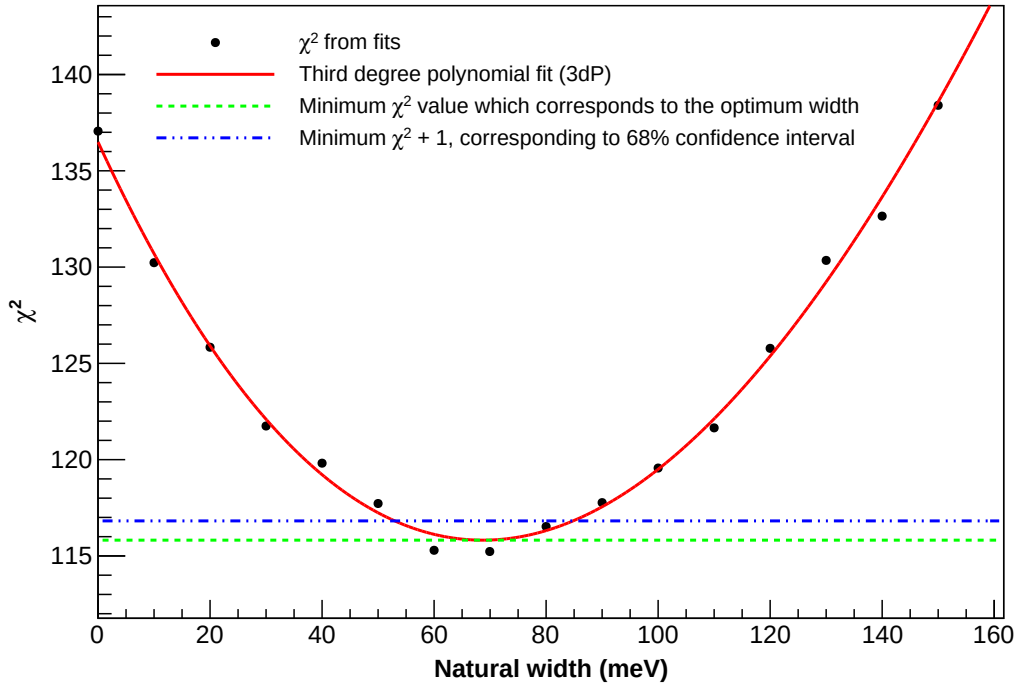

Figure 2.2 – Third degree polynomial (red full curve) fitted to the $[\chi^2(\Gamma_L^i), \chi^2]$ set of points (black dots), for the He-like Ar $1s\,2s\,^1P_1 \rightarrow 1s^2\,^1S_0$ transition. The values χ^2 were obtained from the fits represented in Fig. 2.1 with the different values of Γ_L presented on the figure. The dashed green line represents the minimum χ^2 value corresponding to the optimum width $\Gamma^i_{L\,\mathrm{opt.}}$. The dashed blue line represents the minimum $\chi^2 + 1$ interval for the evaluation of the 68% confidence interval.

$$\frac{1}{\left(\delta\Gamma^{n_r}_{L\,\mathrm{opt.}}\right)^2} = \sum_{n_r} \frac{1}{\left(\delta\Gamma^{n_r}_{L\,\mathrm{opt.}}\right)^2},$$
$$\Gamma_L^{\mathrm{Exp.}} = \left(\delta\Gamma_L^{\mathrm{Exp.}}\right)^2 \sum_{n_r} \frac{\Gamma^{n_r}_{L\,\mathrm{opt.}}}{\left(\delta\Gamma^{n_r}_{L\,\mathrm{opt.}}\right)^2}. \tag{2.8}$$

The results of the line widths under study are presented on Chapter 4. The data analysis has been performed using the data analysis framework ROOT from CERN, version 6.08 [80–82]. In some cases, the Wolfram MATHEMATICA program, version 11 [230], has also been used, given both programs similar results within the respective error bar.

2.2.2 Transition Energies

After obtained the experimental Lorentzian width of a measured line $\Gamma_L^{\text{Exp.}}$, the data analysis method to obtain the correspondent experimental transition energy $E_{\text{exp.}}$ is the following:

- With the derived experimental natural width $\Gamma_L^{\text{Exp.}}$, perform a new set of simulations in the dispersive and non-dispersive modes of transition energy values $E_k = E_{\text{theo.}} + k\Delta E$, where $E_k = E_{\text{theo.}}$ is the theoretical energy value, ΔE an energy increment and k an integer that can take positive or negative values. The simulations are performed with the experimental natural width $\Gamma_L^{\text{Exp.}}$ and Gaussian broadening $\Gamma_G^{\text{Exp.}}$. The simulations are done at several crystal temperature values T_l for each simulated energy E_k;

- As for the case of obtain the natural width, interpolate each simulation spectra from both dispersive and non-dispersive modes, to obtain a set of continuous and parametrized functions depending on the temperature and energy $[E_k, Tl]$;

- Fit each dispersive and non-dispersive spectra using Eq. (2.4) with $E_0 = E_k$ and $T = T_l$. From the fits obtain the angle offset coefficient θ_0 between experimental and simulation, from both dispersive and non-dispersive spectra. Figure 2.3 shows an example of 5 different temperatures T_l at 6 different energies E_k simulated spectra fitted to both experimental non-dispersive (Fig. 2.3(a)) and dispersive (Fig. 2.3(b)) spectrum. Each simulated spectrum has the same natural width $\Gamma_L^{\text{Exp.}}$ and Gaussian broadening $\Gamma_G^{\text{Exp.}}$, being all fits in Fig. 2.3 to both spectra overlapped, yet in the zoomed peak of each spectrum is clearly noticeable all the colored lines correspondent of each interpolated fit function from the simulation. The energy increment ΔE and the different T_l have no contribution for the width of the spectra. For different energies E_k for the same T_l, the difference of the simulation output is a shift of the simulated non-dispersive peak, the parallel peak position does not change, being, as mentioned, its position independent of the energy. For the same energy E_k, a change in temperature T_l has the same effect as a small increment in the energy, since it changes the crystal lattice spacing which is effectively the same as a small difference in energy;

- For each pair of dispersive (DM) and non-dispersive (NDM) modes experimental spectra, calculate the offsets between simulated spectra

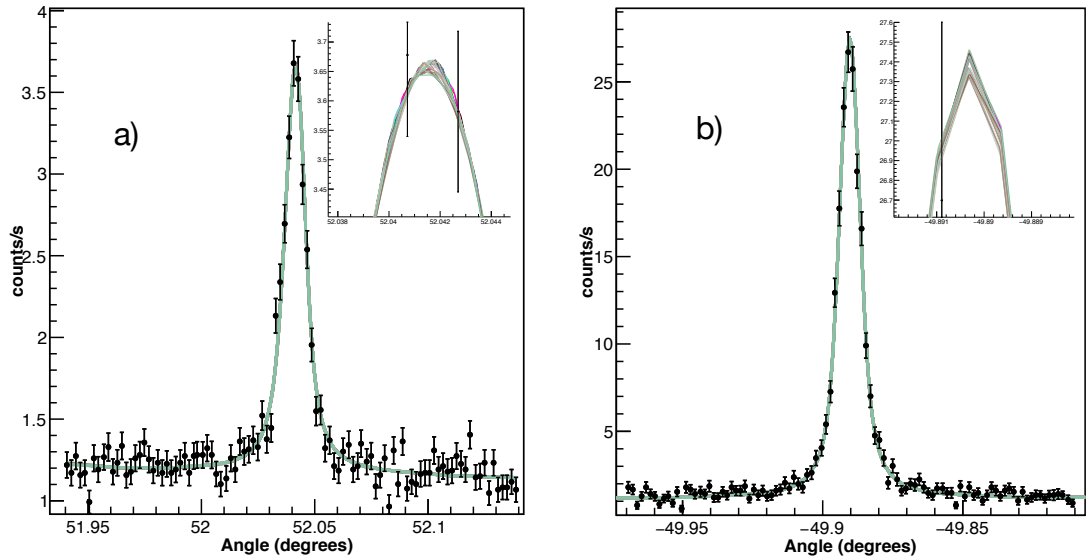

Figure 2.3 – Example of 5 different temperatures T_l at 6 different energies E_k simulated spectra fitted to both experimental non-dispersive (a) and dispersive (b) spectrum of the He-like Ar $1s\,2s\,^1P_1 \rightarrow 1s^2\,^1S_0$ transition. Zoom in of the peak in both spectrum in order to notice the different colored lines correspondent to each interpolated function.

$$\Delta\theta^{n,k,l}_{\text{Exp.–Simul.}} = (\theta^{n}_{\text{Exp.DM}} - \theta^{n}_{\text{Exp.NDM}}) - (\theta^{n}_{\text{Simul.DM}} - \theta^{n}_{\text{Simul.NDM}}) \tag{2.9}$$

and the experimental value, having been obtained in the step above. This offset should be 0 if the energy and temperature used in the simulation were identical to the experimental conditions;

- As the steps above are done automatically in a loop for each pair of parallel and antiparallel experimental spectra, some checks have to be done in the process for the goodness-of-a-fit of each fit. One of this checks can be seen of Fig. 2.4 where the χ^2_r is calculated and plotted for each fit performed on Fig. 2.3. As it can be seen, the χ^2_r value almost does not change for each fit from the simulations for both the dispersive and non-dispersive modes;

- Fit the bidimensional function

$$\Delta\theta_{\text{Exp.–Simul.}}(E,T) = p + qE + rE^2 + sET + uT + vT^2, \tag{2.10}$$

where p, q, r, s, u and v are adjustable parameters, to the set of points $\left[E_k, T_l, \Delta\theta^{k,l}_{\text{Exp.–Simul.}}\right]$ obtained from the fits with interpolated functions from the simulations spectra to the experimental dispersive and non-dispersive

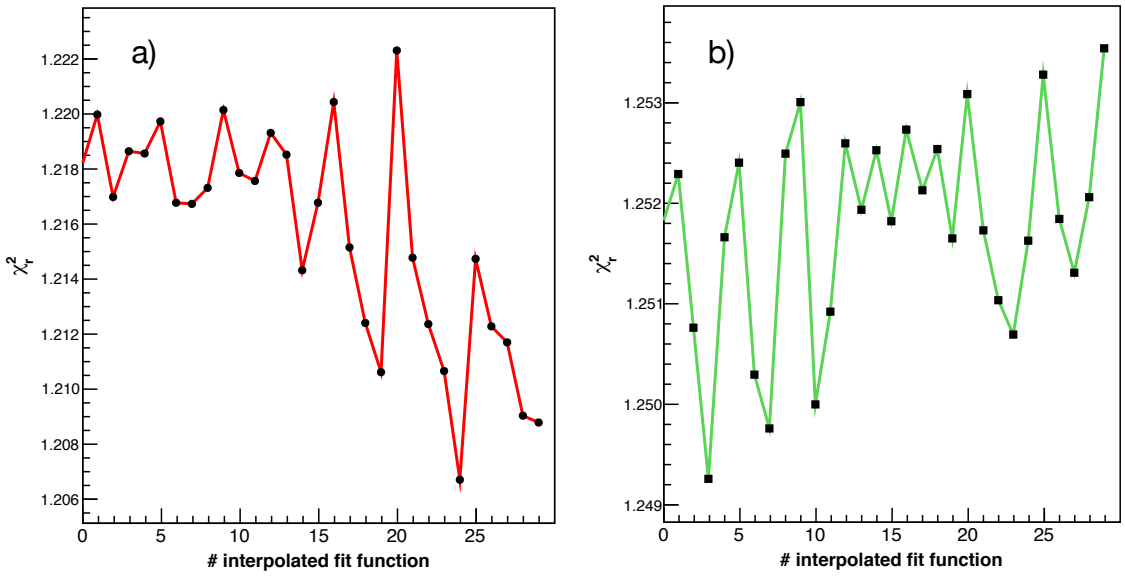

Figure 2.4 – χ^2_r value as function of the fit number of each simulated spectrum of both dispersive (a) and non-dispersive modes for the fits shown on Fig. 2.3.

spectrum. Figure 2.5 shows an example of the fit with the bidimensional function to the set of data, with the offset $\Delta\theta^{n,k,l}_{\text{Exp.–Simul.}}$ obtained from the fits of Fig. 2.3. The error bar at each point of Fig. 2.5 is calculated from the quadratic sum of the standard errors $\delta\theta$ of the offset θ fit parameter from the dispersive and non-dispersive spectrum:

$$\delta\Delta\theta^{k,l}_{\text{Exp.–Simul.}} = \sqrt{(\delta\theta^{k,l}_{\text{Exp.–Simul.DM}})^2 + (\delta\theta^{k,l}_{\text{Exp.–Simul.NDM}})^2};$$

- The experimental line energy $E^n_{\text{Exp.}}$ for spectrum pair number n, is the energy such that $\Delta\theta_{\text{Exp.–Simul.}}(E^n_{\text{Exp.}}, T_{\text{Exp.}}) = 0$ where $T_{\text{Exp.}}$, stands for the average measured temperature on the second crystal;

- As for obtain the natural width, the value for the energy for each pair of dispersive and non-dispersive spectrum is plotted and a weighted average is calculated in order to obtain the final value of the experimental energy. The results of the transitions under study are presented on Chapter 4. The statistical error bar $\delta E^n_{\text{Exp.}}$ of each energy point $E^n_{\text{Exp.}}$, which is the weight factor for the calculated average, is obtain from

$$\delta E^n_{\text{Exp.}} = \pm\sqrt{\mathbf{c}.[C].\mathbf{c}}, \tag{2.11}$$

where $[C]$ is the covariance matrix of the fit and $\mathbf{c}$ is the vector of the fit parameters first order derivatives. From Eq. (2.11) we get the 68% (1σ) confidence interval for each energy point $E^n_{\text{Exp.}}$, assuming that the probability

distribution of the parameter is Gaussian. A weighted standard deviation from all values is also obtained. At the end, the final uncertainty is the quadratic combination of the instrumental uncertainty, which will be discussed on Chapter 3, and the statistical error obtained from the weighted standard deviation;

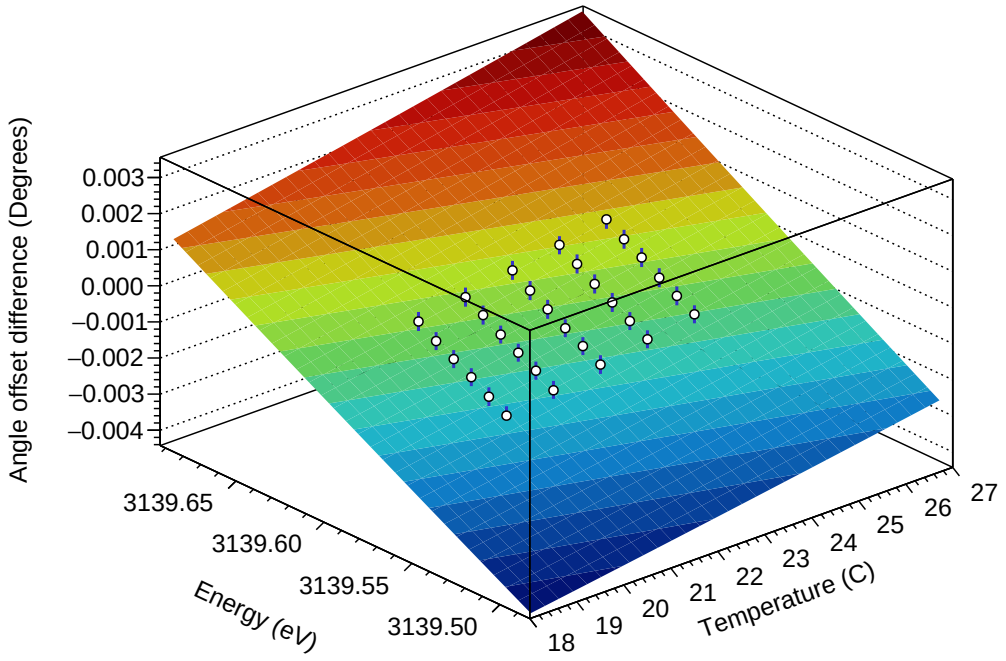

Figure 2.5 – Example of the fit with the bidimensional function (Eq. (2.10)) to the set of data $\left[E_k, T_l, \Delta\theta^{k,l}_{\text{Exp.–Simul.}}\right]$, with the offset $\Delta\theta^{n,k,l}_{\text{Exp.–Simul.}}$ obtained from the fits of Fig. 2.3. The error bar at each point is calculated from the quadratic sum of the standard errors $\delta\theta$ of the offset θ fit parameter from the dispersive and non-dispersive spectrum.

- To check the result, the pairs $E^n_{\text{Exp.}}, T^n_{\text{Exp.}}$ are also plotted and are fitted with $E_0 + bT^m$, for $m = 1, 2$, to check that there is no residual temperature dependence.

- As a last check, we also use the line energy such that $\Delta\theta_{\text{Exp.–Simul.}}(E^n_{\text{Exp.}}, T_{\text{Ref.}}) = 0$, ($T_{\text{Ref.}} = 22.5\,^\circ$ C). This leads to a temperature-dependent energy. We then fit a straight line to the line energy, as a function of the second crystal temperature, and extrapolated to $T = 22.5\,^\circ$ C. Both methods lead to very close values, well within the uncertainties.

Chapter 3

Study of systematic errors and error budget

In this Chapter, the systematic uncertainties in the measurements using the DCS are discussed. This uncertainties can be divided in 3 main classes. The first class is related to all uncertainties coming from the instrument itself, its alignment and the uncertainties from the all measuring instruments (*e.g.*, encoders, thermistors) that compose the spectrometer. Other class of uncertainties can be grouped as the uncertainties related with the diffraction of the x rays in the crystals, the knowledge of the diffraction profile and the polarization of the x rays. The third class of uncertainties is related with the uncertainties of the fundamental constants (*e.g.*, conversion factor from wavelength to energy) and the crystal proprieties as the uncertainty in the crystals lattice value. Some of uncertainties from the first group, uncertainties related with the alignment and geometry of the spectrometer, can be evaluated with the help of the developed simulation code, since it has implemented the DCS geometry.

3.1 Crystals Verticality

As discussed in Chapter 1, the crystals must be parallel for a correct measurement, a small vertical angle in the crystal is translated to a shift in the antiparallel peak, which will lead to an incorrect Bragg angle measurement and will ultimately end in an incorrect energy measurement. To evaluate the spectrometer vertical alignment, the vertical angle of each support as a function of the rotation angle

of each support has been measured for several table positions. In Fig. 3.1 a plot of the measured vertical angle as a function of the crystal support rotation angle for each crystal support is presented for the table in the nominal "0" position (see Figs. 1.12 and 1.14). The measurements have been performed for a full turn of the support (2π) using the Wyler Zerotronic sensor connected to the Wyler Clino 2000 tilt-meter with a precision of a few seconds of arc. The Zerotronic sensor is placed on the back of the crystals supports, by 3 equidistant screws forming a triangular shape, in a perpendicular position in respect to the support vertical axis. The vertical angle is evaluated in steps of 10°. In order to get the tilt angle of each support, a fit of the form of

$$f(\theta) = a\sin(\theta + \phi) + b, \tag{3.1}$$

being a, b and ϕ adjustable fit parameters. From the fit, the tilt angle corresponding to the amplitude a of the Eq. (3.1) is obtained for each support for a specific table position, being in this case, *i.e.*, with the table in the nominal position, $\approx 0.063°$ for the first crystal support and $\approx 0.058°$ for the first crystal support.

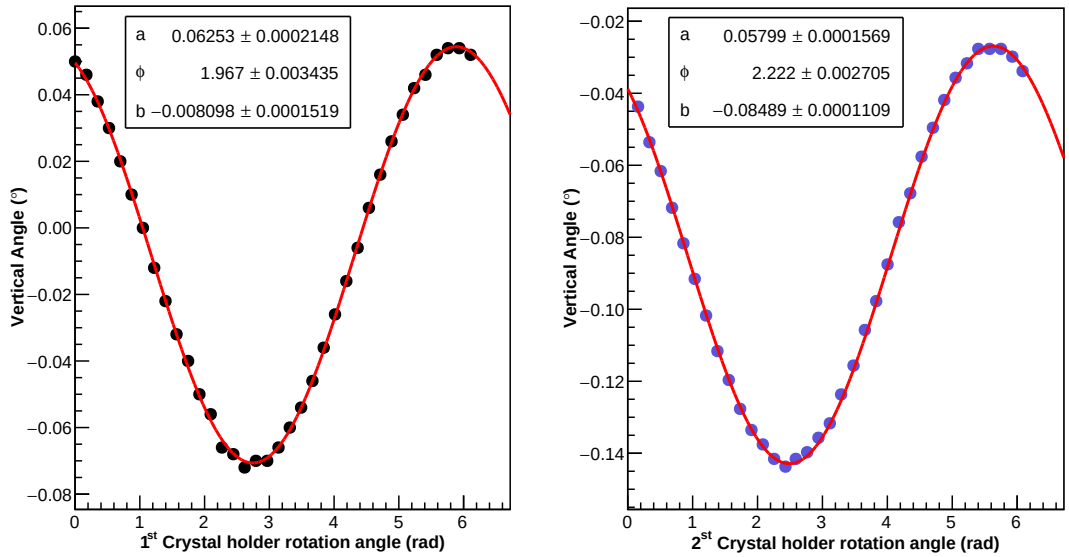

Figure 3.1 – Measurement of the crystals supports vertical tilt measured with the Zerotronic sensor as a function of the crystals supports horizontal angles. Plot on the left (black dots) corresponding to the first crystal support and plot on the right (blue dotes) corresponding to the second crystal support. A fit of the form of Eq. (3.1) is performed in both plots (red full curve), being the correspondent optimized fit coefficients present in the plot together with they respective standard errors. The measurement has been performed for four different table positions.

The fit coefficient b gives us the constant angle between the screwed Zerotronic

sensor and the crystal support while the ϕ the phase difference. From the comparison between the ϕ coefficient of fits performed to each support measurement, we can see that the tilt in both supports have similar direction, having similar values for the phase ϕ. This can be seen also by Fig. 3.2 in which the measured values of the vertical angle of each crystal are presented by a polar plot. The position of the circumference is similar for the measurements in both supports.

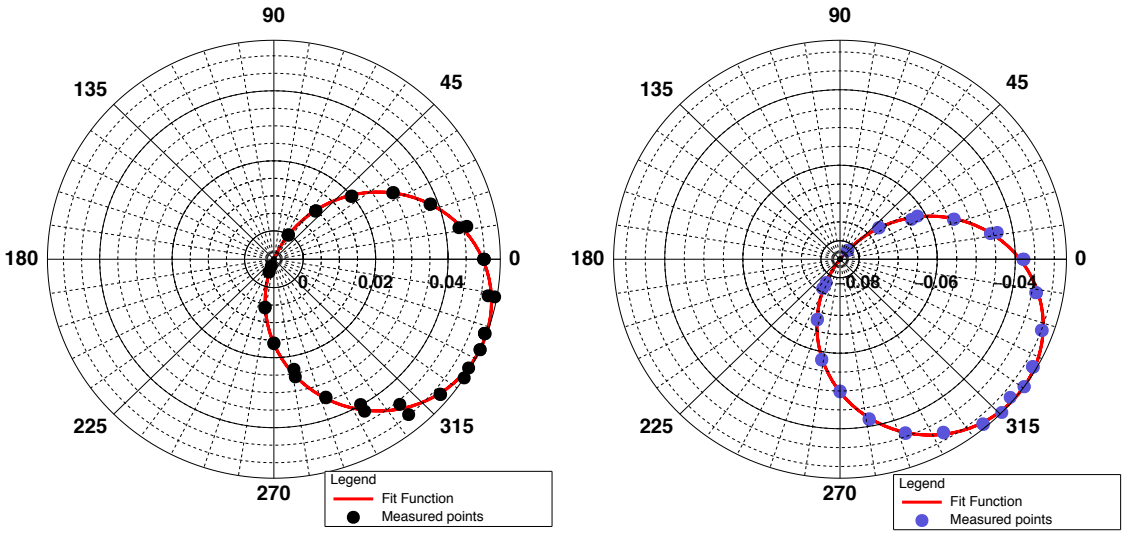

Figure 3.2 – Polar plot of the vertical tilt measured the Zerotronic sensor as a function of the crystals supports horizontal angle correspondent to the data of Fig 3.1, being the left plot (black dotes) corresponding to the first crystal support and the plot on the right (blue dots) corresponding to the second crystal support. The fit function from Eq. (3.1) is also plotted.

As mentioned, the crystals supports tilt measurements have been performed for four different table positions: in the nominal "0" position, at 79.493° (corresponding to $2\theta_{\text{Bragg}}$ of the $1s\,2s^2\,2p\,^1P_1 \rightarrow 1s^2\,2s^2\,^1S_0$ transition in Be-like argon from Ref. [231]), at 120° and at 140°. The measurement in different table positions of the crystal supports tilt gives us a measure of the table horizontality. For a completely horizontal table, the crystals supports tilt should not change for any given table position. Yet, as it can be seen from Fig. 3.3, in which the parameters of the fit function from Eq.3.1 as a function of the table angle is presented, the phase parameter ϕ (in radians) changes as $\approx -0.017\theta_{\text{Table}}$ for the first crystal support and $\approx -0.026\theta_{\text{Table}}$ for the second. Although the tilt angle of the supports (parameter a) changes just by a little for both cases, the phase difference along the measurements for different table angles shows that another contribution from the table position is contributing for the tilt. This is corrected through the adjustment of the screws system in the special metallic track on which the table rotates. The

parameter b does not changes with the table angle since the measurements have been done continuously for each crystal support without removing the Zerotronic sensor between measurements.

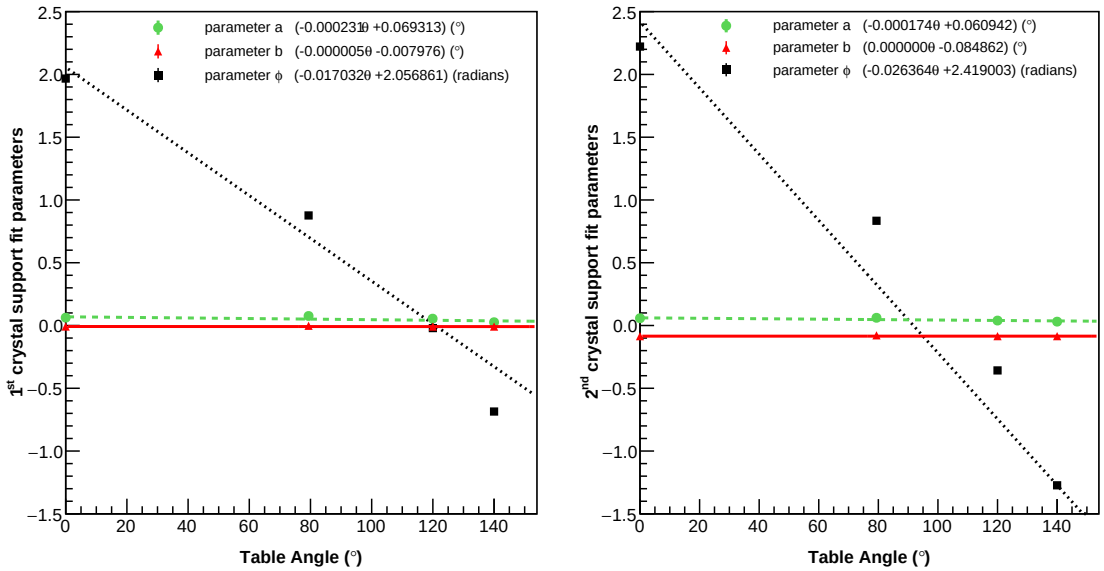

Figure 3.3 – Best fit coefficients for fits performed to the verticality of the crystals supports (see Fig. 3.1) as a function of the table angle for both supports, left plot corresponding to the measurements on the first crystal support and the right plot corresponding to the measurements on the second crystal support). The measurements have been performed at four different table positions: at 0°, 79.493°, 120° and 140°. A linear fit is performed at each fit coefficient and its equation is also presented in the legend of each plot.

Based on simulations, a systematic study on the influence of the crystals tilt in the measured energy has been performed. Several simulations have been computed considering the energy of the $1s\,2p\,^1P_1 \rightarrow 1s^2\,^1S_0$ transition in He-like argon from Ref. [125] for the generation of the x rays. For each simulation, a vertical angle of $-0.04° \leq \delta\theta_{v(1,2)} \leq 0.04°$ for each crystal has been selected for a fixed temperature of 22.5°C. The relative energy difference in ppm between the output analysis of the simulation, performed by obtaining the Bragg angle with Eq. (1.2) from the difference of the dispersive and non-dispersive spectra by fitting the spectra with Voigt profiles and corrected just for the index of refraction of the crystals, and the simulated energy has been evaluated for the dataset of $[\delta\theta_{v1}, \delta\theta_{v2}]$. In Fig. 3.4 is shown the results of the effect of a existing vertical angle in the crystals for the analysis of the energy from the spectra. As it can be seen from the plot of Fig .3.4, a vertical angle of 0.04° on both crystals in the same direction is enough for having a analyzed energy difference from spectra higher than 1.4 ppm, which can be quite dramatic in measurements that are intended to be of high-precision.

This effect is corrected by measuring the vertical angle of both crystals when the spectrometer is in measuring position. The vertical angle is measured with the Zerotronic sensor and corrected with the help of the micrometric screw and flexure installed on the each crystal support (see Fig. 1.10).

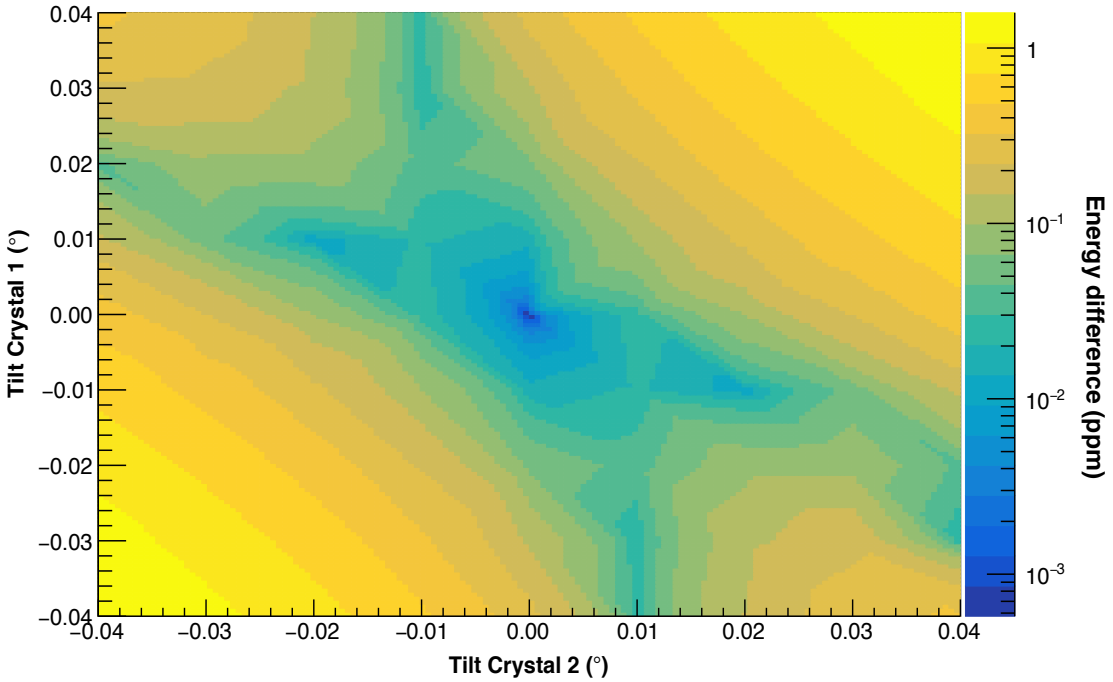

Figure 3.4 – Plot of the energy difference (ppm) as a function of an angle tilt of the first and second crystal supports evaluated from simulations. The simulations have been performed for the line energy of 3139.5821 eV corresponding to the $1s\,2p\,^1P_1 \rightarrow 1s^2\,^1S_0$ transition in He-like argon from Ref. [125].

Although the observed tilt in the crystals support is always present, its effect on the second crystal angular scan when performing a measurement can be neglected when aligned, since the maximum angular range for the scan is typically 0.2° given a maximum tilt angle of 0.0001°, as it can be deduced from Fig. 3.1 and Eq. (3.1). This maximum tilt angle is translated in an energy relative difference of less than 0.001 ppm, corresponding to less than 3.1×10^{-6} eV energy difference for the simulated $1s\,2p\,^1P_1 \rightarrow 1s^2\,^1S_0$ transition energy in He-like argon of Fig. 3.4, being completely negligible to the final error budget of the measurements. Although the vertical tilt in each crystal can be corrected at a given table position, each time the table is moved, the tilt in each crystal has to be evaluated and corrected. An online system to automatically correct the tilt, *i.e.*, correcting the crystals vertical alignment while performing a measurement scan is foreseen. A description of this and others foreseen future updates on the spectrometer is given on Section 3.4.

3.2 Temperature

Although being the accuracy of the Pt100 thermistor of 0.1 °C, the final value of 0.5 °C for the temperature uncertainty is considered for the final error budget of the measurement. As discussed by *Guerra* [190] and *Amaro* [149], a temperature miscalibration has been founded, related with the bad thermal contact under vacuum between the copper heater and the crystal (see Fig. 1.10), being the heat conduction the main reason for the miscalibration. Figure 3.5 shows a measurement of the temperature with one sensor in tightly pressed against the front surface of the crystal (red line of Fig. 3.5) and other between the heater and the back of the crystal ((blue line of Fig. 3.5)).

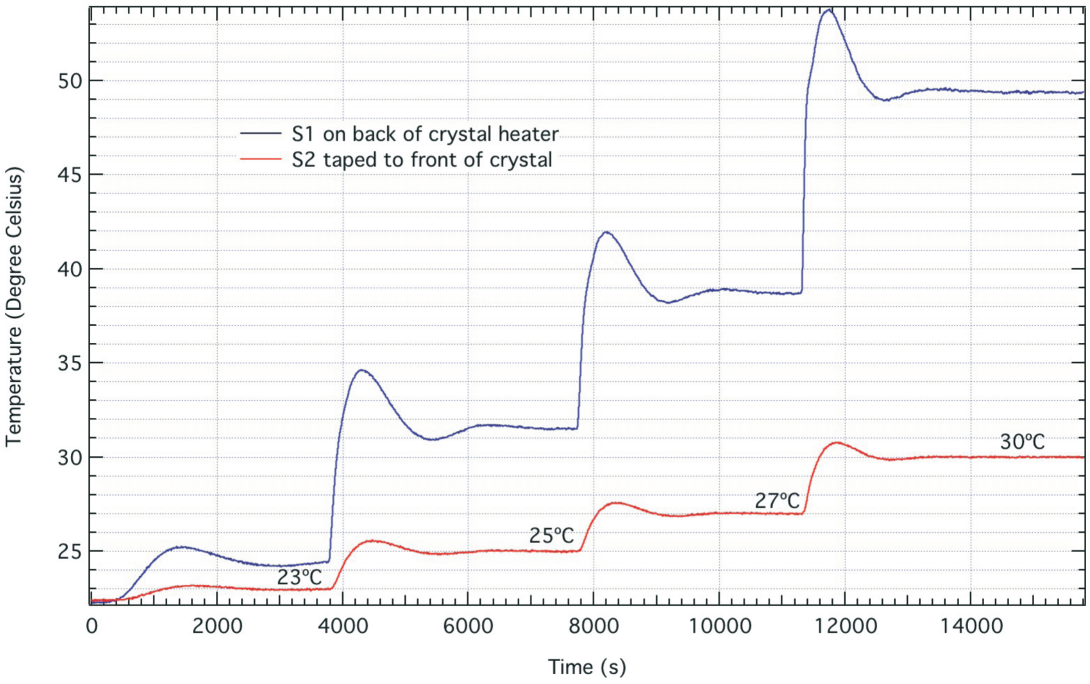

Figure 3.5 – Front-to-back measured crystal temperatures. The blue line corresponds to a temperature measurement at the crystal heater, while the red line corresponds to the temperature at the crystal surface. The measurement was performed in order to do two or three degrees steps at the crystal surface in each hour. Figure and caption taken from Ref. [190].

As one can see, the bad heat conduction to the front surface of the crystal is the main reason for the temperature miscalibration. A calibration from the front-to-back temperature difference has been performed and the recorded temperature for each scan has been modified accordingly. The value of 0.5 °C for the temperature uncertainty is used to compensate this effect.

An update of the DCS, related with the temperature measurement at front surface of the detector, is foreseen and it will be presented on Section 3.4.

3.3 Total Error Budget

Several other studies based on simulations of possible systematic errors related to the alignment and geometry on the DCS measurements as well as diffraction profile uncertainties have been performed by *Amaro* [141, 149]. In these studies, geometrical and diffraction profile uncertainties have been evaluated using simulations. The studied geometrical uncertainties are related to the vertical alignment of the crystals, the accuracy in the alignment procedure described in Section 1.4, and the alignment of the input collimators of the DCS. Both geometrical uncertainties studies lead to a final value of 0.0002 eV of each misalignment contribution. These geometrical contributions have been considered in the final value of the energy uncertainty of the measured transitions of this work. Besides these two geometrical contributions to the final error budget, it has been shown that in a ECRIS, the position of HCI may change depending on its operation conditions [232], which may contribute to the final energy uncertainty. The plasma geometry depends, among other smaller effects, on the magnetic field configuration, the microwave frequency and power and the polarization electrode bias. To estimate a possible effect to the total uncertainty budget, a study based on simulations has been performed in Reference [141]. Two simulations, considering the production of the x rays by two different plasma diameters, a 12 mm (diameter of the collimator) and a 6 mm plasma diameters, have been performed. A difference of 1.3 meV has been obtained from the simulations, which is used as a largely overestimated uncertainty for this effect. Other sources of geometrical errors from a possible small curvature of the crystals, due to the tightening of the crystals on the supports and a possible horizontal or vertical crystal translation, have been also evaluated in these studies. While a small curvature has an effect in the shape of the non-dispersive spectrum, a vertical or horizontal translation of the crystal has shown no considerable effect. The curvature of the crystal is avoid by using nylon screws just to brought it to contact, holding the crystal against the reference surface of the support without bending it.

Besides the uncertainties sources due to geometrical effects and misalignments, the diffraction profiles uncertainties have also been estimated using simulations. Two effects have been studied: the unknown polarization of the x rays from the ECRIS plasma and the utilization of different form factors in the calculation in the

diffraction curve. Two simulations have been performed, one with a diffraction profile considering just the σ polarization and other considering unpolarized ($\sigma + \pi$) radiation. The founded maximum difference from the simulations was 1 meV, which is considered as uncertainty due to the possible presence of polarized x rays. Although the consideration of this uncertainty, the agreement between experimental spectra and simulation containing unpolarized x rays was founded to be excellent. By comparing simulations using different form factors, taken from References [233–237], in the calculation of the diffraction curve by XOP and with the diffraction curve calculated by the X0h, a 2 meV for the diffraction profile uncertainty has been obtained [141], which has been added to the final uncertainty budget.

In Table 3.1 are given the instrumental uncertainties, the uncertainties related with diffraction of the x rays and the uncertainties related with fundamental constants. As it can be seen, the instrumental error budget is dominated by the uncertainty of the crystal temperature measurements. As discussed, the stabilization of the temperature at the front surface of the crystals while performing a angle scan under vacuum is difficult due to the inefficient thermal contact under vacuum between the copper heater and the crystal. This effect has lead to the increase of the temperature uncertainty for a higher value than the uncertainty in the temperature measurements by the thermistors, which has been assumed to be much worse than its calibration.

Table 3.1 – Total error budget from the instrumental contributions, x-ray diffraction and fundamental constants.

Contribution:	Value (eV)
Crystal tilts (± 0.01°) for each crystal)	0.0002
Vertical misalignment of collimators (1 mm)	0.0002
X-ray source size (6 mm to 12 mm)	0.0013
Form factors	0.0020
X-ray polarization	0.0014
Angle encoder error	0.0036
Lattice spacing error	0.00012
Index of refraction	0.0016
Coefficient of thermal expansion	0.00019
X-ray polarization	0.00100
Energy-wavelength correction	0.000078
Temperature (0.5 °C)	0.0040
Total (quadratic sum)	0.0063

The second largest contribution for the total instrumental uncertainty is related with the precision of the angular encoders. At the measured x-ray energies ($\approx$ 3.1 keV) using the Si_{111} crystals, the dispersion is such that an uncertainty of 0.2 arc s of accuracy in the angle measurement is translated in 3.6 meV.

The third largest contribution to the final error budget comes from the fact that there are no accurate measurements of the index of refraction of Si at these energies. In order to get an uncertainty for the index of refraction, we calculate the maximum energy deviation obtained by using different values of the index of refraction in Eq. (2.1). We use as index of refraction values the XOP value and the values from References [238, 239]. The obtained maximum deviation of the final energy by using different values for the index of refraction for the energy region around 3.1 keV is 1.6 meV which is used as the uncertainty value for the index of refraction.

3.4 Future updates on the DCS setup

Considering all the instrumental contributions for the final uncertainty in the DCS measurements, one can see that the temperature uncertainty is dominating the error budget, giving already a relative contribution of 1.3 ppm for the final uncertainty for the x-ray energies discussed in this work. One foreseen update to the Paris DCS, which would considerable reduce this uncertainty, is the replacement of thermistors by infra-red thermometer for high-precision non-contact temperature measurements. The implementation of a sensor of this kind would not only reduce the uncertainty contribution of the temperature measurements of the crystals but would also improve the stabilization of the crystals temperature during an experiment. The major concern of using thermistors for the temperature measurement is that they are contact sensors which are measuring the temperature on the back of the crystals, between the crystal and the copper heater used to stabilize the temperature. Yet, as discussed, the heat conduction under vacuum from the back to the front surface of the crystal has been experimentally observed as inefficient. With the implementation of the infra-red thermometers, this problem would no longer play an important role since the temperature would be measured contactless at the front surface of the crystals, allowing a more reliable temperature measurement and stabilization along the experiment.

Another update is foreseen and its implementation has already started. As discussed, the vertical alignment is very import for a accurate transition energy measurement. Although the correction of the vertical axis is possible and very

precise with the implementation of the new laser system (see Fig. 1.12(a)) for a given table position, when changing the table angle to measure another transition, the alignment procedure described on Section 1.4 has to be repeated to avoid vertical misalignments. To prevent this and to monitor and correct the alignment while recording data, an online alignment system, which makes use of the already implemented laser bench system, is under development. The principal idea is to have implemented in the crystal supports two different planes in the same vertical reference plane, one x-ray plane for the x rays diffraction, with the crystals installed, and an optical plane for the laser reflection with implemented optics (polarizers or mirrors). Figure 3.6 illustrates the design of the new supports with the implementation of the two planes. Besides the two planes, the design of the supports have been also though to have implemented a miniature, with a linear encoder stepping piezo drive actuator on the supports base. The implementation of this drive will allow to change the vertical axis of the reference vertical plane which will be controlled over a single computer interface.

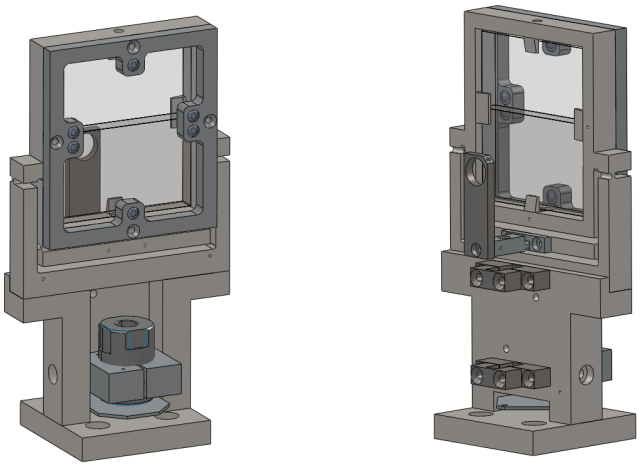

Figure 3.6 – Illustration of the new foreseen DCS crystal supports design with two different planes, an optical plane with polarizers and a x-ray plane with the crystals in the same vertical plane.

In Fig 3.7 a schematic drawing of the online alignment system is shown. Using the flat mirrors in the laser bench, the laser beam can be aligned with the source axis and a reference cross of the SIMPA axis is installed in the bench. With the spectrometer aligned, by controlling the vertical axis with the piezo stepping motors one can match the reference outgoing laser beam spot with the reflected laser beam spot in the camera. When both laser spots, outgoing and reflected,

are concentric, the crystals vertical axes are parallel. The laser beam enters the spectrometer through a non-reflective blind flange which allows the light to go through without reflection while keeping the primary vacuum in the spectrometer chamber. It is intended to develop a software (Labview) to control automatically the piezo motors by reading the camera output. This update to the apparatus will avoid uncontrolled systematic errors due to the vertical misalignment while scanning the second crystal and will also allow to change the table position without the need of breaking the chamber vacuum and to repeat the alignment procedure. The final estimated uncertainty for the online alignment system apparatus is 2.06×10^{-06} degrees, evaluated using the optical design program ZEMAX.

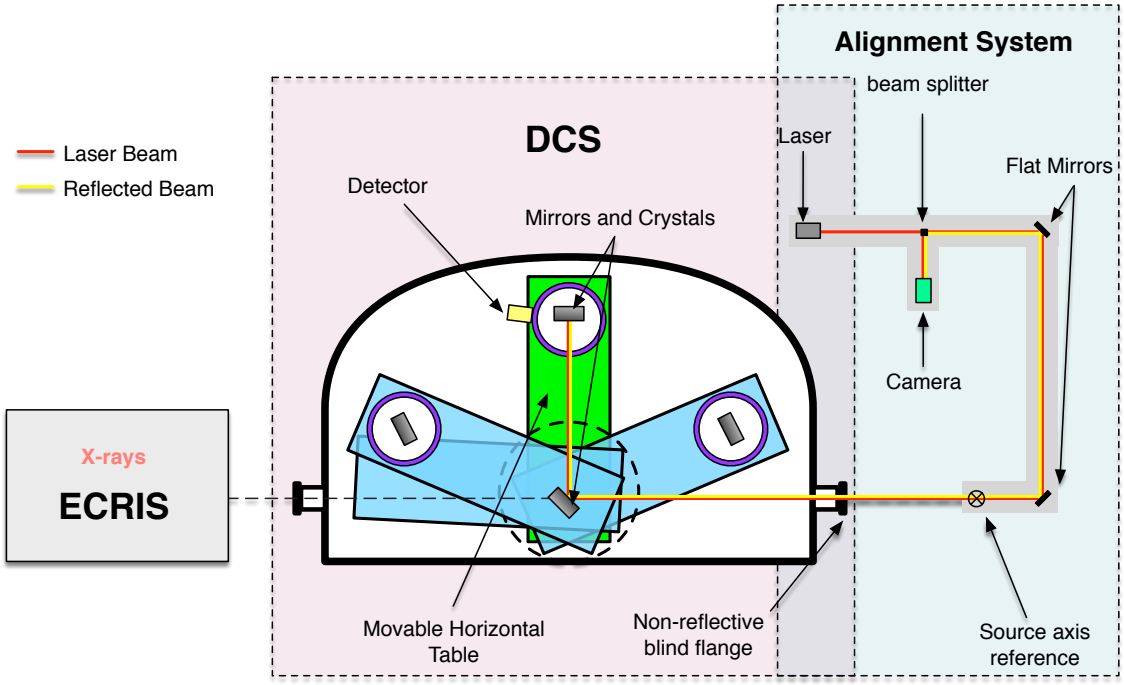

Figure 3.7 – Schematic illustration of the laser system to the online crystal tilt correction.

Chapter 4

Experimental Results on the Double Crystal Spectrometer

Four argon transitions from $n = 2 \rightarrow n = 1$ have been measured, the $1s\,2p\,^1P_1 \rightarrow 1s^2\,^1S_0$ in He-like argon, the $1s\,2s^2\,2p\,^1P_1 \rightarrow 1s^2\,2s^2\,^1S_0$ Be-like argon and the $1s\,2s\,2p\,^2P_J \rightarrow 1s^2\,2s\,^2S_{1/2}$ Li-like argon doublet. In this Chapter the experimental results of the transitions natural width and absolute value of the energy is presented. A complete comparison with available experimental results and theory to each measured transition with the DCS is discussed. For the case of the He-like systems, a systematic and very detailed study of all available experimental data compared with the most accurate BSQED theory of Ref. [125], for evaluation of a possible discrepancy between experiment and theory, is also presented and discussed.

4.1 The $1s\,2p\,^1P_1 \rightarrow 1s^2\,^1S_0$ transition in He-like argon

The $1s\,2p\,^1P_1 \rightarrow 1s^2\,^1S_0$ transition observed in this work, results from the excitation of the $1s^2\,^1S_0$ ground sate in the ECRIS plasma. It is the weakest line measured in this work. In Fig. 4.1 is shown the obtained value for the natural width from the data analysis method described on Section 2.2.1, for each recorded dispersive spectrum. The weighted average (red full curve) and respective $\pm\sigma$ (dashed blue and green curves) is are also presented in Fig 4.1.

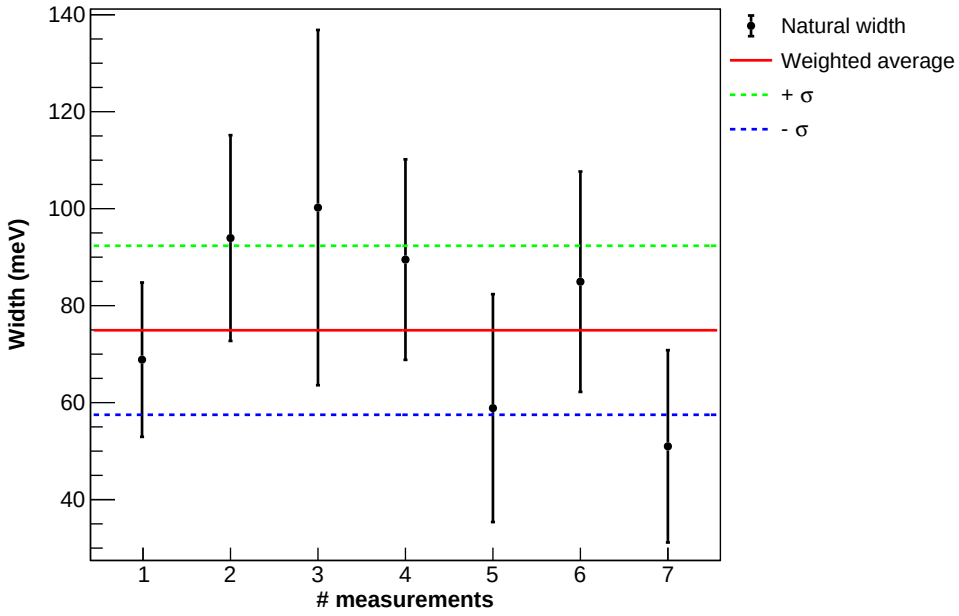

Figure 4.1 – Natural width values of all spectra recorded during the experiment of the $1s\,2p\,^1P_1 \rightarrow 1s^2\,^1S_0$ He-like argon transition. The weighted average and the confidence interval of 68%, evaluated with Eq. (2.8), are also shown.

The obtained experimental result is compared with available theoretical predictions in Table 4.1. There are several possible E1 radiative transitions originating from the 1s2p1P1 level, yet, because of the large energy difference the $1s\,2p\,^1P_1$ level width is strongly dominated by the $1s\,2p\,^1P_1 \rightarrow 1s^2\,^1S_0$ transition. The $n = 2 \rightarrow n = 1$ has been calculated using Multiconfiguration Dirac-Fock (MCDF) with the 2016 version of the general relativistic MCDF code (MCDFGME), developed by *Desclaux* and *Indelicato* [240–243], Drake's unified method [244], with Relativistic Configuration Interaction (RCI) and QED [245]. The agreement between all theoretical values and our measurement is always well within the experimental error bar.

Table 4.1 – Comparison of the measured natural line width values for the $1s\,2p\,^1P_1 \rightarrow 1s^2\,^1S_0$ transition in He-like Ar with computed ones. All values are given in meV, and estimated uncertainties are shown in parentheses.

Transition	Experiment	Theory	Reference
$1s\,2p\,^1P_1 \rightarrow 1s^2\,^1S_0$	75 (17)	70.43	Johnson *et al.*(1995) [245]
		70.4778 (25)	Machado *et al.*(2017) [246]
		70.49 (14)	Drake (1979) [244]

In Fig 4.2, the transition energy values obtained from the successive measured

pairs of dispersive and non-dispersive spectra, for the $1s\,2p\,^1P_1 \rightarrow 1s^2\,^1S_0$ He-like transition, following the method described on Section 2.2.2 is presented. Its average mean, obtained considering just the uncertainty in the fit for the peak position, is represented by the red full curve, the statistical uncertainty is represented by the pink shaded area and the $\pm\sigma$ is represented by the dashed blue and green lines. Error bars in each point correspond to the quadratic sum of the peak fitting uncertainty with the uncertainties from Table 3.1, which have random fluctuations only, *i.e.*, the angle measurement and the temperature correction.

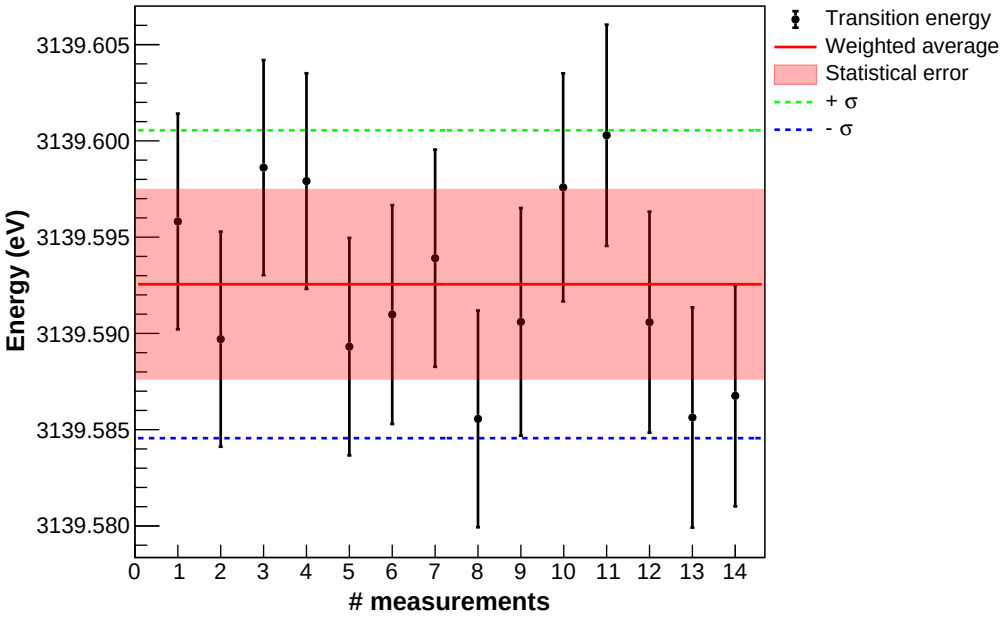

Figure 4.2 – He-like argon $1s\,2p\,^1P_1 \rightarrow 1s^2\,^1S_0$ transition energy values of the different pair of dispersive and non-dispersive spectra recorded during the experiment. Error bars correspond to statistical uncertainty obtained from Eq. (2.11) quadratically combined with the uncertainties in the temperature and angle measurement. Red full curve corresponds to the weighted average mean, obtained considering only the statistical uncertainty in each point. The pink shaded area corresponds to the statistical uncertainty and the dashed blue and green lines ($\pm\sigma$) represent the total uncertainty obtained by the quadratically combination of the statistical uncertainty and all the contributions given on Table 3.1. Every pair of points correspond to one-day data taking.

The obtained value with respective calculated uncertainty together with all known theoretical and experimental values are presented in Table 4.2. The final experimental accuracy is the combination of the instrumental contribution (see Table 3.1) with the statistical contribution, being the final value 2.5 ppm. The value is in agreement with the preliminary results given in Refs. [191, 193]

using the same experimental setup but using Voigt profiles to analyze the data, obtaining the Bragg angle from the dispersive and non-dispersive peaks position. Table 4.2 shows the measured value of the He-like argon $1s\,2p\,^1P_1 \rightarrow 1s^2\,^1S_0$ transition energy combined with the most precise experiments and advanced theoretical results. The agreement with the measured value with the two reference-free results [8, 135] and with the recoil ion experiment of *Deslattes et al.* [133] is well within combined uncertainties. Compared with theory, with *Artemyev et al.* [125], the calculation performed with effective self-energy operators [246] and the most recent and advance calculations, our result is also well within combined error bars.

Table 4.2 – Comparison of our He-like argon $1s\,2p\,^1P_1 \rightarrow 1s^2\,^1S_0$ transition experimental energy with previous experimental and theoretical values. All energies are given in eV, and estimated uncertainties are shown in parentheses.

Energy	Reference	Exp. Method
	Experiment	
3139.5927 (50) (63) (80)	This Work (stat.) (sys.) (tot.)	ECRIS
3139.567 (11)	Schlesser *et al.*(2013) [138]	ECRIS
3139.581 (5)	Kubiček *et al.*(2012) [135]	EBIT
3139.583 (63)	Bruhns *et al.*(2007) [8]	EBIT
3139.552 (37)	Deslattes *et al.*(1984) [133]	Recoil ions
3139.60 (25)	Briand *et al.*(1983) [129]	Beam-foil
3140.1 (7)	Dohmann *et al.*(1979) [128]	Beam-foil
3138.9 (9)	Neupert *et al.*(1971) [247]	Solar emission
	Theory	
3139.584 (6)	Machado *et al.*(2017) [246]	
3139.5821 (4)	Artemyev *et al.*(2005) [125]	
3139.582	Plante *et al.*(1994) [248]	
3139.617	Cheng *et al.*(1994) [249]	
3139.576	Drake (1988) [250]	
3139.649	Indelicato *et al.*(1987) [242]	
3139.56	Safronova (1981) [251]	
3140.15	Johnson *et al.*(1976) [252]	
3140.46	Gabriel (1972) [253]	

4.1.1 Comparison between measurements and theory for the He-like isoelectronic sequence

Many measurements have been performed of $n = 2 \rightarrow n = 1$ for He-like systems.

Table 4.3 summarizes all available $n = 2 \rightarrow n = 1$ transition energies in He-like ions experimental reference-free measurements, as the one presented in this work, and measurements calibrated against x-ray standards or transitions in H-like ions. *Chantler et al.*has ignited a controversy by the analysis of the He-like x-ray data [10, 12, 112] claiming a discrepancy between the experimental data and the theoretical prediction of *Artemyev et al.* [125]. Moreover, it has been claimed that the founded deviation scales as $\approx Z^3$ which could provide insight into the *proton size puzzle*, the Rydberg and fine-structure constants, or missing three-body BSQED terms.

Triggered by this controversy, *Beiersdorfer* and *Brown* have measured the w, x, y, and z transitions, labels introduced by *Gabriel* [253] corresponding respectively to $1s\,2p\,^1P_1$, $1s\,2p\,^3P_2$, $1s\,2p\,^3P_1$ and $1s\,2p\,^3S_1$ to the $1s^2\,^1S_0$ ground state, in He-like Cu. A reasonable agreement of their experimental results with the predictions of *Drake's* [250] and *Artemyev et al.* [125] has been observed and they were also falling well outside the proposed trending of Z^3 by *Chantler et al.*. Also triggered by this controversy, a detailed and systematic analyzes of available data in the He-like isoelectronic sequence is presented, adding our $1s\,2p\,^1P_1 \rightarrow 1s^2\,^1S_0$ experimental result to the available data. The difference between available data shown in Table 4.3 and *Artemyev et al.*theoretical values are plotted in Fig. 4.3, being the error bar at each point the provided uncertainty of the measurement quadratically summed with the provided estimated uncertainty from the calculations. To the plotted data, several weighted fits of the form aZ^n for $n = 0, 1, 2, 3$ have been done. The $\pm 1\sigma$ error bands of each performed fit are also presented in the plot showing that there no significant difference between theory and experiment.

In order to reinforce this statement, a more detailed significance analysis has been performed. The analysis has been performed by fitting functions of the form $f(Z) = aZ^n$, $0 \leq n \leq 12$, for steps of $n = 0.2$ considering three datasets, which are subsets of the data presented on Table 4.3. One of the datasets contains only the w-lines, another contains all w, x, y and z transitions and the other is similar with the latter but the values of this work, *Kubiček et al.* [14] and *Amaro et al.* [9] which have been removed. The value of the reduced χ^2 (χ^2_r) has been evaluated at each fit for each considered dataset and plotted in Fig 4.4 as a function n. As it can be noticed in the plot of Fig. 4.4, the χ^2_r increases as a function of n for the

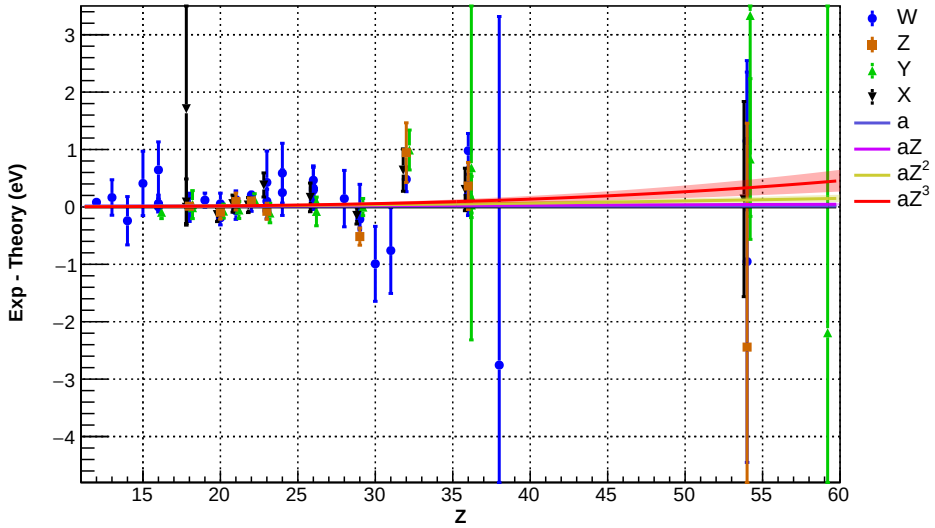

a) $11 \leq Z \leq 60$-range.

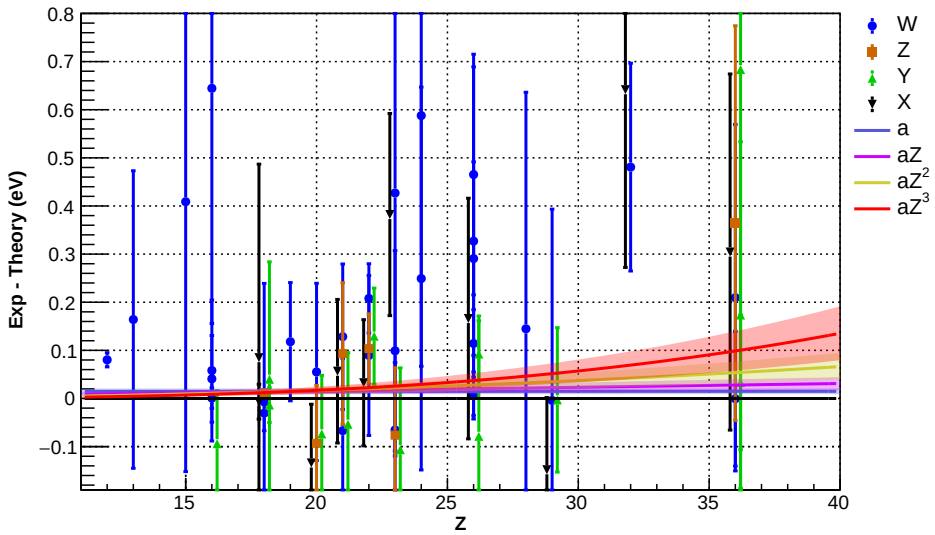

b) Zoom on the $11 \leq Z \leq 40$-range, and small energy differences.

Figure 4.3 – Comparison between the theoretical values by *Artemyev et al.* [125] and experimental data for $n = 2 \rightarrow n = 1$ transition in He-like ions presented in Tables 4.3 for $12 \leq Z \leq 54$. The error bar at each point is the provided uncertainty of the measurement quadratically summed with the provided estimated uncertainty from the calculations. The continuous lines represent the weighted fit with a, aZ, aZ^2 and aZ^3 functions, and the shaded area the $\pm 1\sigma$ bands, representing the 68% confidence interval from the fit. The deviation is always lower than $\pm 2\sigma$ and thus is not significant. From this we cannot conclude in favor of a systematic Z dependent deviation. Some plotted values for the same Z have been shifted in Z, for illustration purposes only, so one can identify the different plotted values.

Table 4.3 – Summary of all measured in $n = 2 \rightarrow n = 1$ transition energies in He-like ions $7 \leq Z \leq 92$. The theoretical values are from Ref. [125], which are available for $Z \geq 12$. The experimental values are either reference-free measurements (RF) or measurements calibrated against standard reference x-ray transitions, or hydrogen-like transitions (SR).

	$1s2p\,^1P_1 \rightarrow 1s^2\,^1S_0$ (w)			$1s2p\,^3P_2 \rightarrow 1s^2\,^1S_0$ (x)			$1s2p\,^3P_1 \rightarrow 1s^2\,^1S_0$ (y)			$1s2s\,^3S_1 \rightarrow 1s^2\,^1S_0$ (z)				
Z	Exp. (eV)	Err.	Theory	Exp. (eV)	Err.	Theory	Exp. (eV)	Err.	Theory	Exp. (eV)	Err.	Theory	Method	Ref.
7	430.6870	0.0030											SR	[254]
8	573.949	0.011											SR	[254]
11	1126.72	0.31											SR	[127]
12	1352.329	0.015	1352.2483			1343.5417			1343.0988			1331.1118	SR	[127]
13	1598.46	0.31	1598.2914			1588.7611			1588.1254			1574.9799	SR	[127]
14	1864.76	0.42	1865.0014			1854.6679			1853.7804			1839.4495	SR	[127]
15	2152.84	0.56	2152.4310			2141.3188			2140.1082			2124.5619	SR	[127]
16	2461.27	0.49	2460.6292			2448.7628			2447.1439			2430.3512	SR	[127]
16	2460.69	0.15	2460.6292			2448.7628			2447.1439			2430.3512	SR	[255]
16	2460.630	0.021	2460.6292			2448.7628			2447.1439			2430.3512	RF	[14]
16	2460.670	0.090	2460.6292			2448.7628	2447.05	0.11	2447.1439			2430.3512	SR	[256]
18			3139.5821			3126.2896			3123.5344	3104.1605	0.0077	3104.1483	RF	[9]
18			3139.5821	3128	2	3126.2896			3123.5344			3104.1483	SR	[257]
18	3139.5927	0.0080	3139.5821			3126.2896			3123.5344			3104.1483	RF	this work
18	3139.5810	0.0092	3139.5821			3126.2896			3123.5344			3104.1483	RF	[14]
18	3139.552	0.037	3139.5821	3126.283	0.036	3126.2896	3123.521	0.036	3123.5344			3104.1483	SR	[133]
18	3139.57	0.25	3139.5821	3126.37	0.40	3126.2896	3123.57	0.24	3123.5344			3104.1483	SR	[129]
19	3510.58	0.12	3510.4616			3496.4937			3492.9736			3472.2417	SR	[258]
20	3902.43	0.18	3902.3777			3887.7607			3883.3169			3861.2059	SR	[255]
20	3902.19	0.12	3902.3777	3887.63	0.12	3887.7607	3883.24	0.12	3883.3169	3861.11	0.12	3861.2059	SR	[259]
21	4315.54	0.15	4315.4124			4300.1720			4294.6220			4271.0997	SR	[258]
21	4315.35	0.15	4315.4124	4300.23	0.15	4300.1720	4294.57	0.15	4294.6220	4271.19	0.15	4271.0997	SR	[260]
22	4749.73	0.17	4749.6441			4733.8008			4726.9373			4701.9746	SR	[258]
22	4749.852	0.072	4749.6441	4733.83	0.13	4733.8008	4727.07	0.10	4726.9373	4702.078	0.072	4701.9746	SR	[13]
23	5205.59	0.55	5205.1653			5188.7378			5180.3264			5153.8962	SR	[255]
23	5205.26	0.21	5205.1653			5188.7378			5180.3264			5153.8962	SR	[258]
23	5205.10	0.14	5205.1653	5189.120	0.210	5188.7378	5180.22	0.17	5180.3264	5153.82	0.14	5153.8962	SR	[261]
24	5682.66	0.52	5682.0684			5665.0715			5654.8491			5626.9276	SR	[255]

Table 4.3 – Summary of all measured in $n = 2 \rightarrow n = 1$ transition energies in He-like ions $7 \leq Z \leq 92$. The theoretical values are from Ref. [125], which are available for $Z \geq 12$. The experimental values are either reference-free measurements (RF) or measurements calibrated against standard reference x-ray transitions, or hydrogen-like transitions (SR). (continued)

	$1s2p\,^1P_1 \rightarrow 1s^2\,^1S_0$ (w)			$1s2p\,^3P_2 \rightarrow 1s^2\,^1S_0$ (x)			$1s2p\,^3P_1 \rightarrow 1s^2\,^1S_0$ (y)			$1s2s\,^3S_1 \rightarrow 1s^2\,^1S_0$ (z)				
Z	Exp. (eV)	Err.	Theory	Exp. (eV)	Err.	Theory	Exp. (eV)	Err.	Theory	Exp. (eV)	Err.	Theory	Method	Ref.
24	5682.32	0.40	5682.0684			5665.0715			5654.8491			5626.9276	SR	[258]
26	6700.76	0.36	6700.4347			6682.3339			6667.5786			6636.6126	SR	[255]
26	6700.73	0.20	6700.4347			6682.3339			6667.5786			6636.6126	SR	[258]
26	6700.441	0.049	6700.4347			6682.3339			6667.5786			6636.6126	RF	[14]
26	6700.90	0.25	6700.4347	6682.50	0.25	6682.3339	6667.50	0.25	6667.5786			6636.6126	SR	[262]
26	6700.549	0.070	6700.4347			6682.3339	6667.671	0.069	6667.5786			6636.6126	RF	[11]
27	7245.88	0.64	7242.1133			7223.4718			7205.9299			7173.4164	SR	[255]
28	7805.75	0.49	7805.6053			7786.4246			7765.7048			7731.6307	SR	[255]
29	8391.03	0.40	8391.0349			8371.3181			8346.9929			8311.3467	SR	[255]
29	8390.82	0.15	8391.0349	8371.17	0.15	8371.3181	8346.99	0.15	8346.9929	8310.83	0.15	8311.3467	SR	[15]
30	8997.53	0.65	8998.5238			8978.2677			8949.8740			8912.6466	SR	[255]
31	9627.45	0.75	9628.2072			9607.4099			9574.4461			9535.6292	SR	[255]
32	10280.70	0.22	10280.2175	10259.52	0.37	10258.8739	10221.79	0.35	10220.7996	10181.33	0.52	10180.3868	SR	[263]
36	13115.45	0.30	13114.4705			13090.8657	13026.8	3.0	13026.1165			12979.2656	SR	[264]
36	13114.68	0.36	13114.4705	13091.17	0.37	13090.8657	13026.29	0.36	13026.1165	12979.63	0.41	12979.2656	SR	[265]
36	13114.47	0.14	13114.4705			13090.8657	13026.15	0.14	13026.1165			12979.2656	RF	[16]
38	14666.8	6.1	14669.5399			14644.7518			14562.2995			14512.1996	SR	[255]
39	15475.6	2.9	15482.1565			15456.7619			15364.1984			15312.4664	SR	[255]
54	30629.1	3.5	30630.0512			30594.3635	30209.6	3.5	30206.2652			30129.1420	SR	[266]
54	30619.9	4.0	30630.0512			30594.3635	30210.5	4.5	30206.2652	30126.70	3.90	30129.1420	SR	[267]
54	30631.2	1.2	30630.0512	30594.50	1.70	30594.3635	30207.1	1.4	30206.2652			30129.1420	SR	[139]
59			37003.7270			36964.0900	36389.1	6.8	36391.2920			36305.1570	SR	[268]
92	100626	35	100610.89			100537.18			96169.63			96027.15	SR	[269]
92	100598	107	100610.89			100537.18			96169.63			96027.15	SR	[270]

three considered datasets, although in two of the subsets there is a local weak minimum.

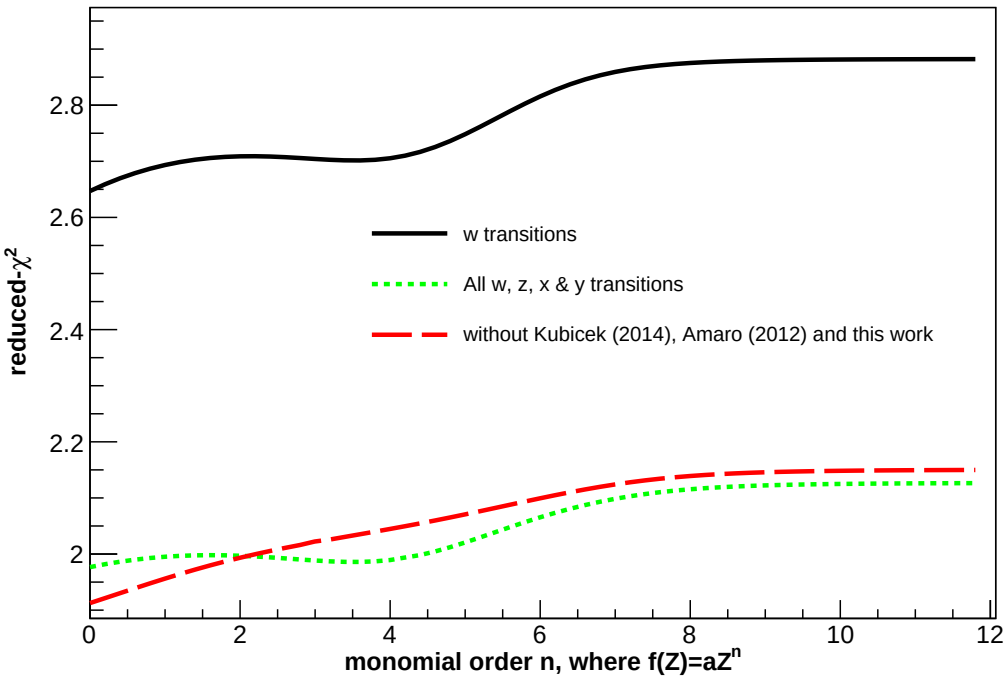

Figure 4.4 – Values of χ^2_r as a function of n, when fitting aZ^n, for $0 \leq n \leq 12$, to the experiment-theory differences from Table 4.3. Dotted line: χ^2_r fitting all 4 w, x, y, z transitions energies differences with theory. Dotted line: χ^2_r fitting only the $1s\,2p\,^1P_1 \rightarrow 1s^2\,^1S_0$ (w) values. Dashed line: fit to all transitions values, removing the reference-free values from this work and from Refs. [9, 14].

From the same fits performed to construct Fig. 4.4, the uncertainty of the fit coefficient a in standard-error units as a function of n for all three datasets has been evaluated and plotted in Fig. 4.5. The figure shows that the maximum deviation from zero is obtained for the three datasets when considering the fit function aZ^0. It can be notice that the deviation of the fit coefficient tends to zero with increasing value of n while χ^2_r increases. Yet, when considering all experimental values presented in Table 4.3 or considering the subset of the w-lines, there is a local maximum for these two datasets. For all experimental data the local maximum happens at $n \approx 3.6$ with a coefficient significance of 3.5 standard errors, while for the w-lines the local maximum is at approximately for the same n ($n \approx 3.6$) has a deviation of 3 standard errors from zero. Although the presence of this local maximum for different monomial orders of n, the maximum deviation from zero of the fit parameter is at $n = 0$ as well as the minimum χ^2_r value. This leads to the

conclusion that the $f(Z) = aZ^0$ is the most probable model to describe the data when considering a power law dependence with Z.

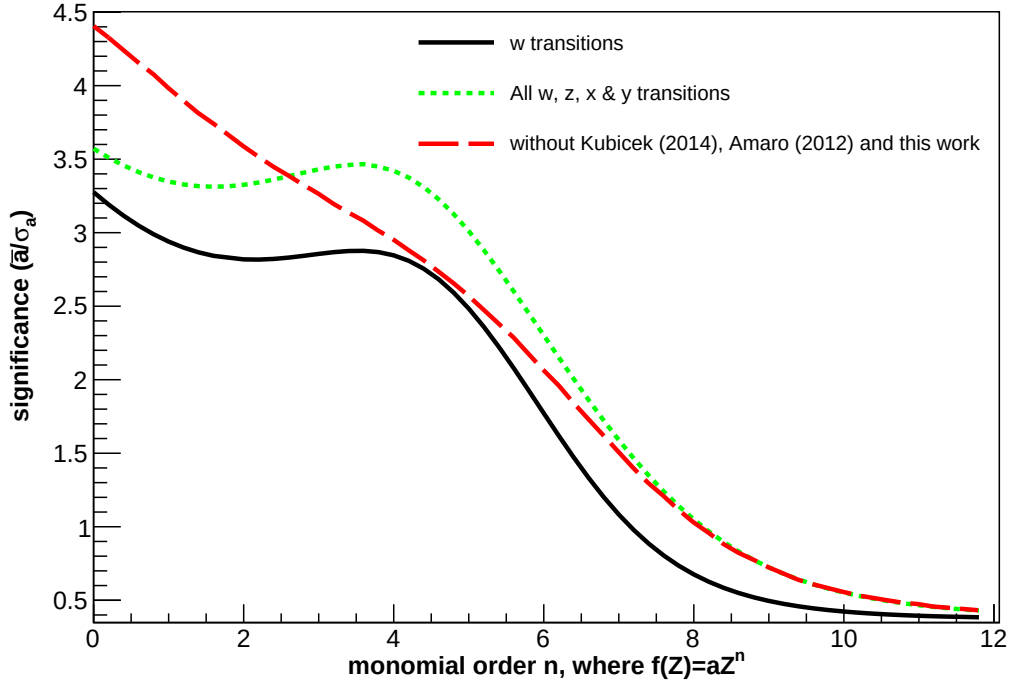

Figure 4.5 – Values of the significance of the fit coefficient a in standard-error units as a function of n when fitting aZ^n to the experiment-theory differences from Table 4.3. The three considered datasets are the same as Fig. 4.4.

To sustain this conclusion, a χ^2 goodness-of-a-fit test has been also performed. Figure 4.6 shows the result probability (p-value) of the χ^2 cumulative distribution function (upper tail) as a function of n, for the given degrees of freedom and the minimum χ^2 value of each performed fit. It can be noticed that the highest p-value for the three considered datasets is for $n = 0$, and, as before, one can see a local maximum when considering all experimental results from Table 4.3 or just the w-lines for the same n value as from the Fig.4.5. Considering the standard significance level of 0.05 to evaluate the acceptance or rejection of the null hypotheses, and since the highest p-value is $\approx 1.5 \times 10^{-6}$ for the three considered datasets, the null hypotheses (that the data can be described by the aZ^n function) cannot be accepted. Therefore, we conclude that we cannot claim that there is a Z dependence of the form $f(Z) = aZ^n$ for any given n with $0 \leq n \leq 12$.

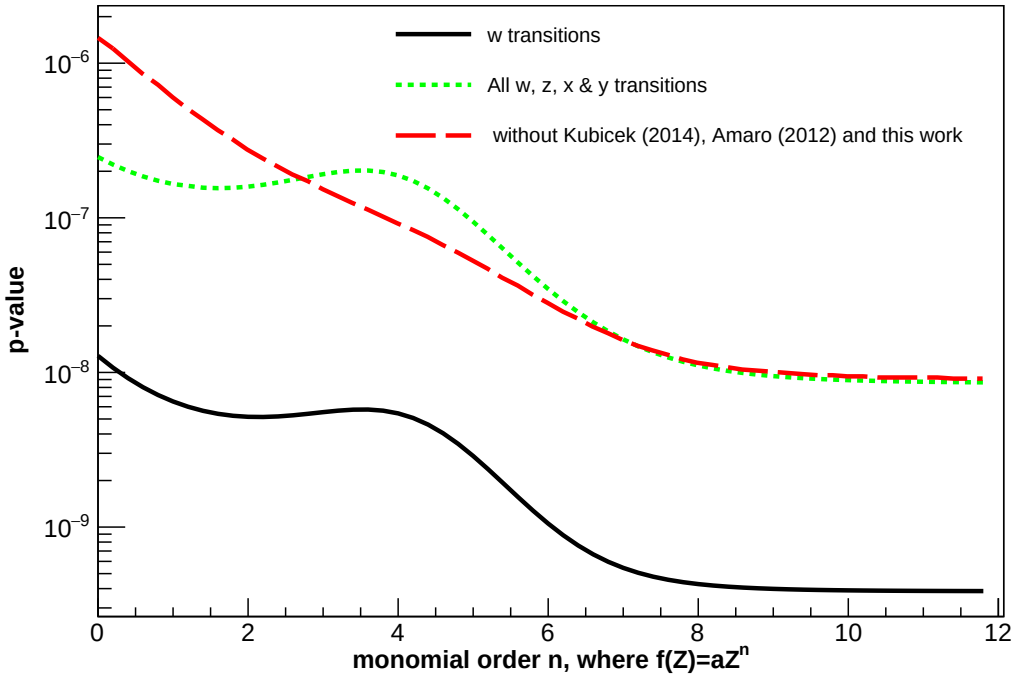

Figure 4.6 – p-value as a function of n when fitting aZ^n to the experiment-theory differences from Table 4.3. The three considered datasets are the same as Fig. 4.4.

4.2 The $1s\,2s^2\,2p\,^1P_1 \rightarrow 1s^2\,2s^2\,^1S_0$ transition in Be-like argon

The Be-like excited level, $1s\,2s^2\,2p\,^1P_1$, is mostly produced by ionization of the ground state of boron-like argon, which is a well-populated charge-state. The $1s\,2s^2\,2p\,^1P_1 \rightarrow 1s^2\,2s^2\,^1S_0$ line is the most intense we observed. Measurements of this line are scarce, some measurements are relative measurements using tokamaks, where the Be-like $1s^2\,2s\,2p\,^1P_1 \rightarrow 1s^2\,2s^2\,^1S_0$ line appears as a satellite line for He-like $n = 2 \rightarrow n = 1$ transitions. The $1s\,2p\,^1P_1 \rightarrow 1s^2\,^1S_0$ line is often used as calibration, as in the measurements at TFR for Ar [271] and Ni [272, 273]. These measurements, being relative measurements which use the theoretical calculation for the energy of the He-like $1s\,2p\,^1P_1 \rightarrow 1s^2\,^1S_0$ line, they must be re-calibrated using the most advanced and recent calculations. Besides the relative measurements, several other observations of this Be-like line have been observed, yet no energy has been reported (*e.g.* Ref. [274]) or the experimental accuracy is not completely documented ([259, 260, 275]). Measurements in vanadium [136] and iron [137], or terrestrial and astrophysics plasma applications, are also known using EBITs. From the ECRIS side, there have been also relative measurements

of the $1s\,2s^2\,2p\,^1P_1 \rightarrow 1s^2\,2s^2\,^1S_0$ line sulfur, argon and chlorine [138], using the theoretical value for the energy of the relativistic M1 transition $1s\,2s\,^3S_1 \rightarrow 1s^2\,^1S_0$ as reference.

The width of the $1s\,2s^2\,2p\,^1P_1$, in contrast with the He-like $1s\,2p\,^1P_1$, has both radiative and non-radiative (Auger) contributions. Yet, the radiative part is also strongly dominated by the $1s\,2s^2\,2p\,^1P_1 \rightarrow 1s^2\,2s^2\,^1S_0$ transition.

The experimentally obtained natural width of the Be-like argon $1s\,2s^2\,2p\,^1P_1 \rightarrow 1s^2\,2s^2\,^1S_0$ transition by the analysis method described in Section 2.2.1, for each recorded dispersive spectrum is presented on Fig 4.7. The weighted average (red full curve) and the $\pm 1\sigma$ (dashed blue and green curves) are also plotted in the figure.

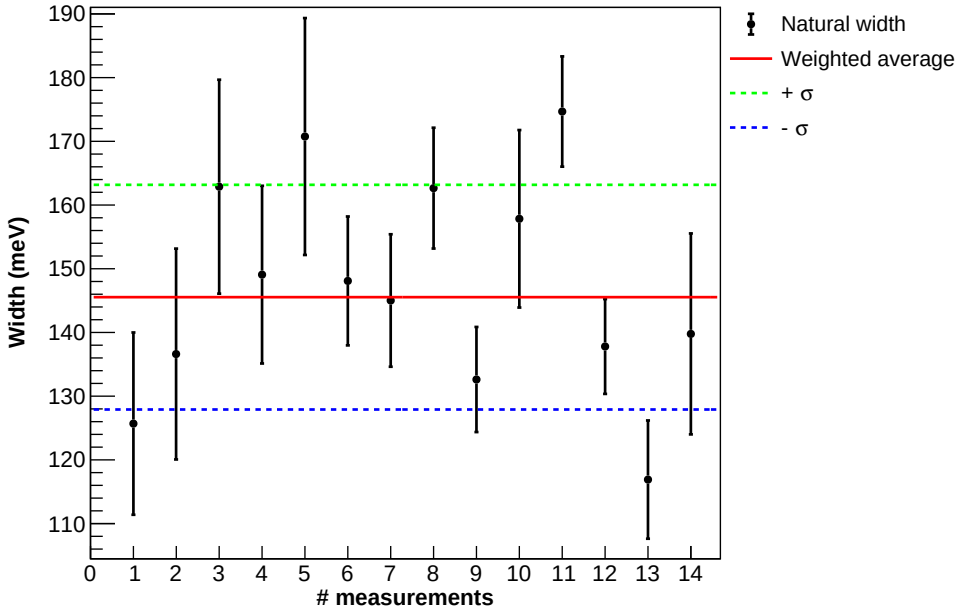

Figure 4.7 – Natural width values of all spectra recorded during the experiment of the $1s\,2s^2\,2p\,^1P_1 \rightarrow 1s^2\,2s^2\,^1S_0$ Be-like argon transition. The weighted average and the confidence interval of 68%, evaluated with Eq. (2.8), are also shown.

Our experimental result for the natural transition width compared with several available theoretical calculations are presented on Table 4.4. As it can be seen from the table, the agreement of our experimental value for the natural width of the $1s\,2s^2\,2p\,^1P_1 \rightarrow 1s^2\,2s^2\,^1S_0$ transition is within combined experimental and theoretical uncertainties.

In Fig. 4.8 the experimental energy value of the $1s\,2s^2\,2p\,^1P_1 \rightarrow 1s^2\,2s^2\,^1S_0$ for each pair of recorded dispersive and non-dispersive spectrum is presented. Each pair of points in the plot corresponds to one-day data taking. The weighted

Table 4.4 – Comparison of the measured natural line width values for the $1s\,2s^2\,2p\,^1P_1 \rightarrow 1s^2\,2s^2\,^1S_0$ transition in Be-like Ar with computed values. All values are given in meV, and estimated uncertainties are shown in parentheses.

Transition	Experiment	Theory	Reference
$1s\,2s^2\,2p\,^1P_1 \rightarrow 1s^2\,2s^2\,^1S_0$	146 (18)	126.9	Machado *et al.*(2017) [246]
		106.1 (25)	Safranova *et al.*(1979) [276]
		146.8 (14)	Chen (1985) [277]
		150.9 (14)	Costa (2001) [206]

average (full red curve), the statistical uncertainty (pink shaded area) and the $\pm 1\sigma$ (dashed blue and green curves) corresponding to the 68% confidence interval are also represented in the plot of Fig. 4.8.

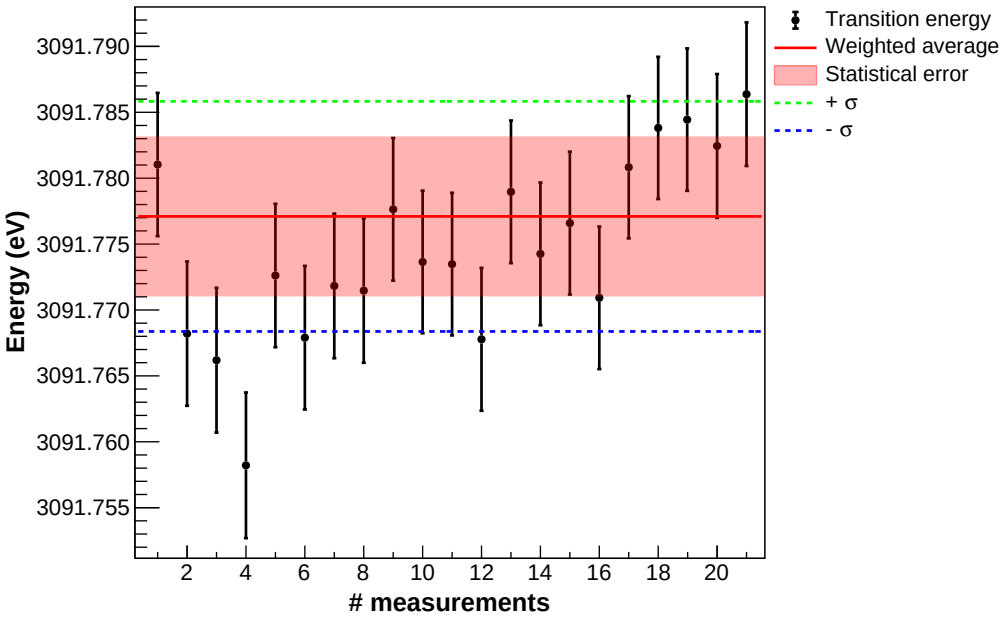

Figure 4.8 – Be-like argon $1s\,2s^2\,2p\,^1P_1 \rightarrow 1s^2\,2s^2\,^1S_0$ transition energy values of the different pair of dispersive and non-dispersive spectra recorded during the experiment. Error bars correspond to statistical uncertainty obtained from Eq. (2.11) quadratically combined with the uncertainties in the temperature and angle measurement. Full red curve corresponds to the weighted average mean, obtained considering only the statistical uncertainty in each point. The pink shaded area corresponds to the statistical uncertainty and the dashed blue and green lines ($\pm\sigma$) represent the total uncertainty obtained by the quadratically combination of the statistical uncertainty and all the contributions given on Table 3.1. Every pair of points correspond to one-day data taking.

The weighted average of the data presented in Fig 4.8, together with its final uncertainty calculated by the quadratic sum of the statistical confidence interval

corresponding to 68% with the instrumental uncertainty, is compared in Table 4.5 with the available relative experimental measurement of *Schlesser et al.* [138] and the available theoretical predictions. Our reference-free measurement has been performed with a total uncertainty of 2.8 ppm. The difference between our measurement and the calculation of *Yerokhin et al.* [231] given with a relative accuracy of 11×10^{-6} is only 9.7×10^{-6}. The difference to the MCDF calculation done within our group, using effective operators self-energy screening is 2.3×10^{-6}, using the Welton method [246] it is 3.6×10^{-6}. The difference between the present reference-free measurement and the relative measurement presented in Ref. [138], calibrated against the theoretical value of the $1s\,2s\,^3S_1 \rightarrow 1s^2\,^1S_0$ transition energy of Ref.[125] is only 0.4×10^{-6}. All recent measurement and calculation are thus forming a very coherent set of data.

Table 4.5 – Comparison between experimental and theoretical Be-like argon $1s\,2s^2\,2p\,^1P_1 \rightarrow 1s^2\,2s^2\,^1S_0$ transition energies. All energies are given in eV and estimated uncertainties are shown in parentheses.

Energy	Reference
	Experiment
3091.7771 (61) (63) (87)	This Work (stat.) (sys.) (tot.)
3091.776 (3)	Schlesser *et al.*(2013) [138]
	Theory
3091.7729 (77)	Machado *et al.*(2017) [246]
3091.749 (34)	Yerokhin *et al.*(2015) [231]
3088.958	Natarajan (2003) [278]
3091.95	Costa et al. (2001) [206]
3092.157	Safronova and Shlyaptseva (1996) [279]
3090.64	Chen and Crasemann (1987) [280]
3090.66	Chen (1985) [277]
3092.18	Safronova and Lisina (1979) [276]
3092.18	Boiko et al. (1978) [281]

One feature that can be notice in the scattered profile of the data points of the Be-like $1s\,2s^2\,2p\,^1P_1 \rightarrow 1s^2\,2s^2\,^1S_0$ line energy present on Fig 4.8 is the apparent linear trend of the energy value as a function of time. In order to investigate a possible temperature drift or residual dependence with temperature, in Fig. 4.9 the values of energy for each pair of dispersive and non-dispersive spectra as function of time together with the energy values as function of measured value of the second crystal temperature in dispersive mode, are presented. As it can be

seen from the plot, the time trend seems to be strictly random since we cannot correlate it with the second crystal temperature and everything else during the experiment as kept stable at the same conditions for each dispersive spectrum recorded.

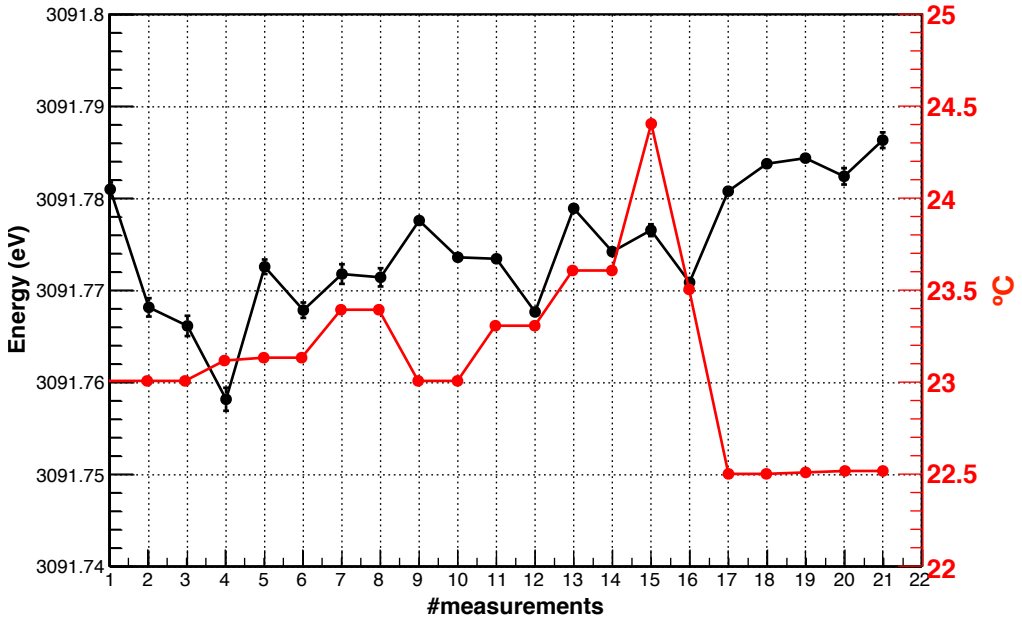

Figure 4.9 – Values of energy for each pair of dispersive and non-dispersive spectra of the Be-like $1s\,2s^2\,2p\,^1P_1 \rightarrow 1s^2\,2s^2\,^1S_0$ line as a function of time (a.u.) (black dots and black line) and the average temperature of the second crystal of each dispersive spectrum used to calculate each energy value as a function of time (a.u.) (red dots and red line).

4.2.1 Comparison between available measurements and theory for the Be-like isoelectronic sequence

The energy of the Be-like $1s\,2s^2\,2p\,^1P_1 \rightarrow 1s^2\,2s^2\,^1S_0$ transitions has not been extensively studied. As mentioned, it was measured relative to either theoretical value in S, Cl and Ar [138], Sc [260], Fe [282, 283], Ni [273] and Pr [268] or to K-edges in Fe [11]. The width and Auger rate for this transition have also been measured in Fe [11, 284], with the combined use of synchrotron radiation and ion production with an EBIT. In Fig. 4.10, we present a comparison between theory and experiment, and between different calculations for the $1s\,2s^2\,2p\,^1P_1 \rightarrow 1s^2\,2s^2\,^1S_0$ line energy, for $10 \leq Z \leq 29$. Since there is no recent calculation covering all elements for which there is an experimental, we use as reference the old calculation from Ref. [285], which does not include accurate QED corrections.

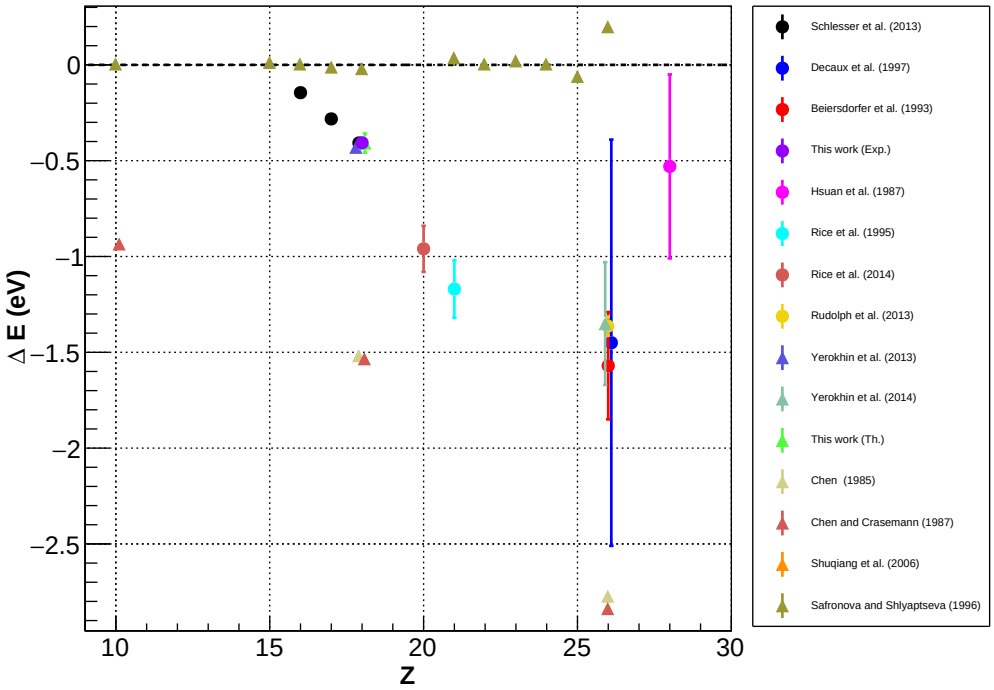

Figure 4.10 – Comparison between experimental and theoretical values for the $1s\,2s^2\,2p\,^1P_1 \rightarrow 1s^2\,2s^2\,^1S_0$ transition energies, as a function of Z. Round dots represents experimental results and triangular ones theoretical results. All values are compared to the energies in Ref. [285]. Experimental results references: Schlesser *et al.*(2013) [138], Beiersdorfer *et al.*(1993) [282], Decaux *et al.*. (1997) [283], Rudolph *et al.*(2013) [11], Hsuan *et al.*(1987) [273], Rice *et al.*(1995) [260], Rice *et al.*(2014) [259]. Theoretical results references: Yerokhin *et al.*(2015) [231], Yerokhin *et al.*(2014) [286], Chen and Crasemann (1987) [280], Chen (1985) [287], Safronova and Shlyaptseva (1996) [279]. For the same Z, some values have been shifted in Z so one can notice the different points. The value of Shuqiang *et al.*(2006) [288] for $Z = 29$ is out of the selected energy range difference.

4.2.2 Analysis of small peak structure near the $1s\,2s^2\,2p\,^1P_1 \rightarrow 1s^2\,2s^2\,^1S_0$ line

In the analysis process of the dispersive spectra of the $1s\,2s^2\,2p\,^1P_1 \rightarrow 1s^2\,2s^2\,^1S_0$ Be-like line, a suggestion of a peak is visible in all recorded dispersive spectrum. Figure 4.11 shows an example of a dispersive spectrum of the $1s\,2s^2\,2p\,^1P_1 \rightarrow 1s^2\,2s^2\,^1S_0$ transition. As it can be seen, a small peak, purple shadowed, around 49.82° is noticeable. The peak has been fitted with a simulation performed with the experimentally obtained energy and natural width, interpolated using splines and using 4 adjustable fit coefficients as in Eq. (2.4). At the bottom of the dispersive spectrum, the fit residuals are shown. This small peak has a contribution of

several radiative transitions in Ar^{14+} and Ar^{13+}.

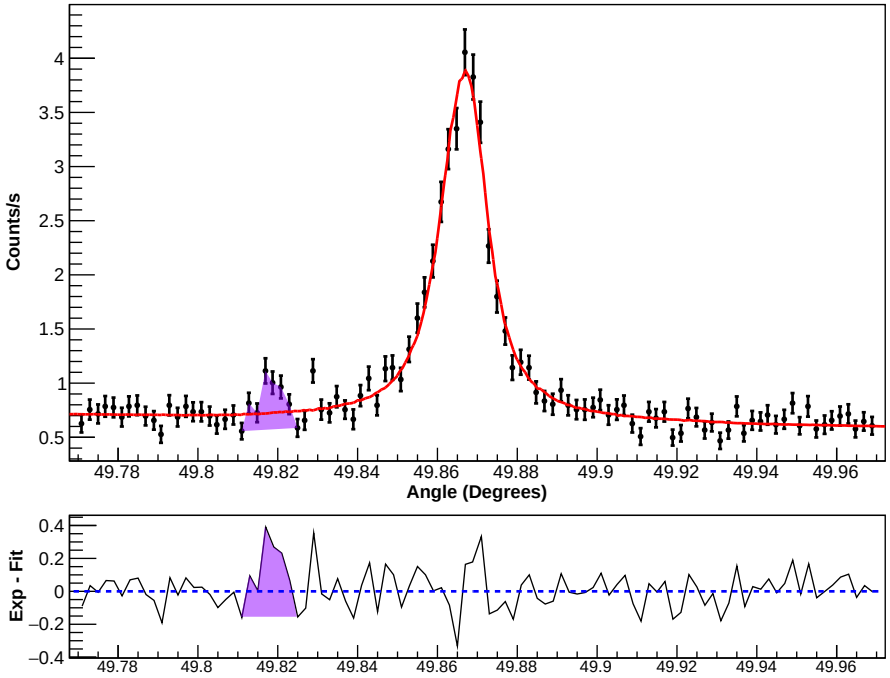

Figure 4.11 – Example of a dispersive spectrum of the $1s\,2s^2\,2p\,^1P_1 \rightarrow 1s^2\,2s^2\,^1S_0$ transition. The red full curve is the fit from simulation performed with the obtained energy and natural width. The purple shadow area highlights the observed small peak and at the bottom the fit residuals are shown.

Even though the peak is clearly noticeable in almost all recorded spectra (see Appendix B to see more examples), its complicated structure and low intensity makes it impossible to analyze, given in some dispersive spectra, numerical problems when performing the fit. Yet, it does not have any contribution to the $1s\,2s^2\,2p\,^1P_1 \rightarrow 1s^2\,2s^2\,^1S_0$ Be-like line analysis, being the evaluated χ^2_r for the case when fitting both peaks (when possible) or just the large one, significantly the same.

4.3 The $1s\,2s\,2p\,^2P_J \rightarrow 1s^2\,2s\,^2S_{1/2}$, $J = 1/2, 3/2$ Li-like argon doublet

For the argon Li-like $1s\,2s\,2p\,^2P_J \rightarrow 1s^2\,2s\,^2S_{1/2}$ doublet transition, the data analysis has been performed following a similar method than the one described on Chapter 2. Yet, in this case we have measured two lines simultaneously in the same spectra that are not completely resolved, each line has a contribution from

the other which modifies the data analysis method to obtain the experimental line widths.

4.3.1 Data analysis of the Li-like argon double

The analysis has been performed with the following procedure:

- As for the single line case in the dispersive spectrum, perform a set of simulation with theoretical energies E_0, with $\Gamma_G^{\text{Exp.}} = 80.5(46)$ meV as the Gaussian broadening experimentally obtained in [9] and with Lorentzian widths Γ_L ranging from 0 meV to 400 meV. A set of 25 simulation has been performed for crystals temperature of $T_{\text{Ref.}} = 22.5$ °C;
- Interpolate the spectra from the simulation using splines to obtain a set of parametrized, continuous functions $S_{E_0,\Gamma_L^i,\Gamma_G^{Exp.},T_{Exp.}}(\theta-\theta_0)$;
- Fit each experimental dispersive spectrum with all the possible combinations of two from the above interpolated functions

$$\begin{aligned} I(\theta-\theta_0^1,\theta-\theta_0^2,I_{\max}^1,I_{\max}^2,a^1,a^2,b^1,b^2) = I_{\max}^1 S_{E_0,\Gamma_L^1,\Gamma_G^{\text{Exp.}},T_{\text{Exp.}}}(\theta-\theta_0^1) \\ + I_{\max}^2 S_{E_0,\Gamma_L^2,\Gamma_G^{\text{Exp.}},T_{\text{Exp.}}}(\theta-\theta_0^2) + a + b\theta, \end{aligned} \tag{4.1}$$

  being the upper scripts 1 and 2 corresponding to the two lines in the spectra, $I_{\max}^1$ and $I_{\max}^2$ the lines intensity, θ the crystal angle, θ_0^1 and θ_0^2 the offset coefficient between the experimental spectrum and the simulated one for each line, a the background intensity and b the background slope. The combination of the different simulated Lorentzian widths results in a total of 625 fits at each experimental dispersive spectra. An example of a fitted spectrum with the combination of all the different Lorentzian widths can be seen in Fig. 4.12;
- At each fit, the χ^2 is evaluated. The bidimensional function

$$\chi^2(\Gamma_L^1,\Gamma_L^2) = a + b\Gamma_L^1 + c\Gamma_L^2 + d\Gamma_L^1\Gamma_L^2 + e(\Gamma_L^1)^2 + f(\Gamma_L^2) + g(\Gamma_L^1)^3 + h(\Gamma_L^2)^3 \tag{4.2}$$

  is fitted to the set of points $[\chi^2,\Gamma_L^1,\Gamma_L^2]$, where a,b,c,d,e,f,g and h are adjustable parameters to the set of points obtained. In Fig. 4.13 is presented an example of the bidimensional fit to the set of points $[\chi^2,\Gamma_L^1,\Gamma_L^2]$ for one spectrum;

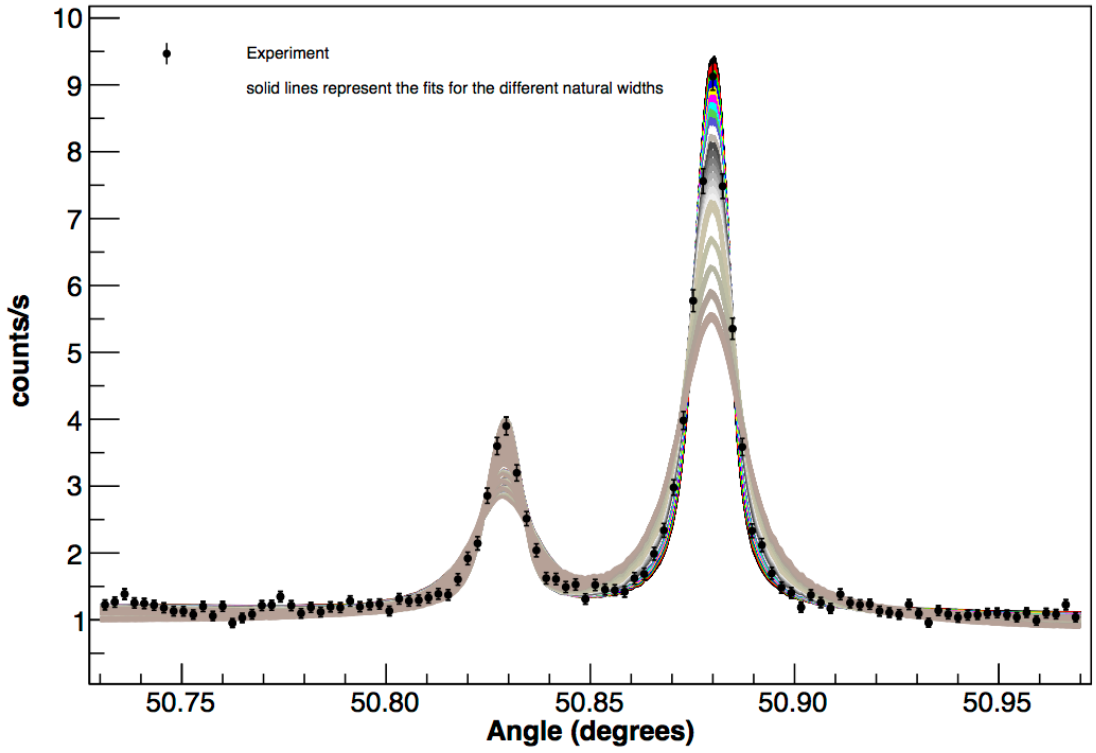

Figure 4.12 – Fit example to a dispersive spectrum of the Li-like argon $1s\,2s\,2p\,^2P_J \rightarrow 1s^2\,2s\,^2S_{1/2}$, $J = 1/2, 3/2$ transitions by interpolated simulations spectra with Eq. (4.1) for a set of Lorentzian widths. The colored curves are the combination of 25 different simulated dispersive spectra with Lorentzian widths ranging from $\Gamma_L = 0$ mev to $\Gamma_L = 400$ mev, being 625 (25×25) the total number of fits to each experimental dispersive spectrum. The error bar in each point is the $\sqrt{n}/t$, being n the number of counts and t the time spent in the bin.

- From the bidimensional fit function, get the minimum value to find the best pair of widths $[\Gamma^1_{L,\text{opt.}}, \Gamma^2_{L,\text{opt.}}]$ for the $1s\,2s\,2p\,^2P_J \rightarrow 1s^2\,2s\,^2S_{1/2}$ doublet;

- Get the 68% error bars, $\delta\Gamma^1_{L\text{opt.}}$ and $\delta\Gamma^2_{L\text{opt.}}$, for each obtained natural width (Γ^1_L, Γ^2_L), by finding the values for which [229]

$$\chi^2\left(\Gamma^{1,2}_{L\text{opt.}} \pm \delta\Gamma^{1,2}_{L\text{opt.}}\right) = \chi^2\left(\Gamma^{1,2}_{L\text{opt.}}\right) + 1. \tag{4.3}$$

  In Fig. 4.14 the confidence intervals represented by the colored contours are shown for the χ^2 grid presented in Fig 4.13. Each different colored contour represents the $n\sigma$ confidence intervals, for $n = 1, 2, 3, \cdots$. The individual 1σ confidence interval for each variable ($\delta\Gamma^1_{L\text{opt.}}$ and $\delta\Gamma^2_{L\text{opt.}}$) is represented by the interval between the $\Delta\chi^2 = 1$ lines, which in Fig. 4.14 are illustrated by the white lines.

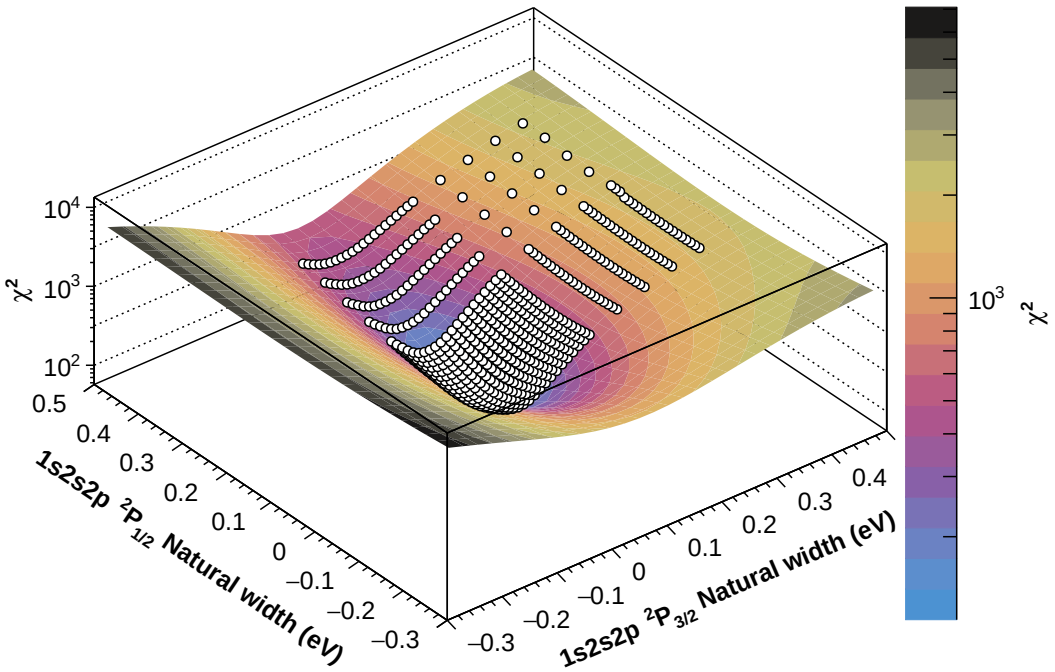

Figure 4.13 – Fit to the set of point $[\chi^2, \Gamma_L^1, \Gamma_L^2]$ using Eq. (4.2). The χ^2 values are obtained from the fits shown on Fig. 4.12 for the respective combination of Lorentzian widths $[\Gamma_L^1, \Gamma_L^2]$. From the optimized fit function by χ^2 minimization the pair of optimum Lorentzian widths $[\Gamma_L^1, \Gamma_L^2]$ is obtained by getting the minimum of the function. The z coordinate (χ^2) is shown in log scale. In this example, the minimum $\chi^2 = 101.26$ has been obtained corresponding to a reduced $\chi_r^2 = 1.08$, being 94 the total number of degrees of freedom (100 points minus 6 free fit coefficients).

- At the end, a weighted average is performed to the set of $(\Gamma_{L\,\text{opt.}}^1)$ and $(\Gamma_{L\,\text{opt.}}^2)$, a pair of widths for each recorded spectrum, with the respective error bar. The mean value and the $\pm\sigma$ interval for the pair of widths of the $1s\,2s\,2p\,^2P_J \rightarrow 1s^2\,2s\,^2S_{1/2}$ doublet is presented on Fig. 4.15.

As for the energy analysis, the method is similar to the one described in Section 2.2.2. The difference compared with that description are the interpolated functions (constructed by the simulation output), which are fit to experimental spectra. For the non-dispersive spectrum there is no difference, since we only have one peak for both transitions. Yet, since the dispersive spectra has two peaks, corresponding to each line of the doublet transition, after obtaining the natural widths of each transition the constructed fit function by splines interpolation from the simulations are, in this case, defined by Eq. (4.1).

A set of 5 different energies with an energy difference separated by $\Delta E =$

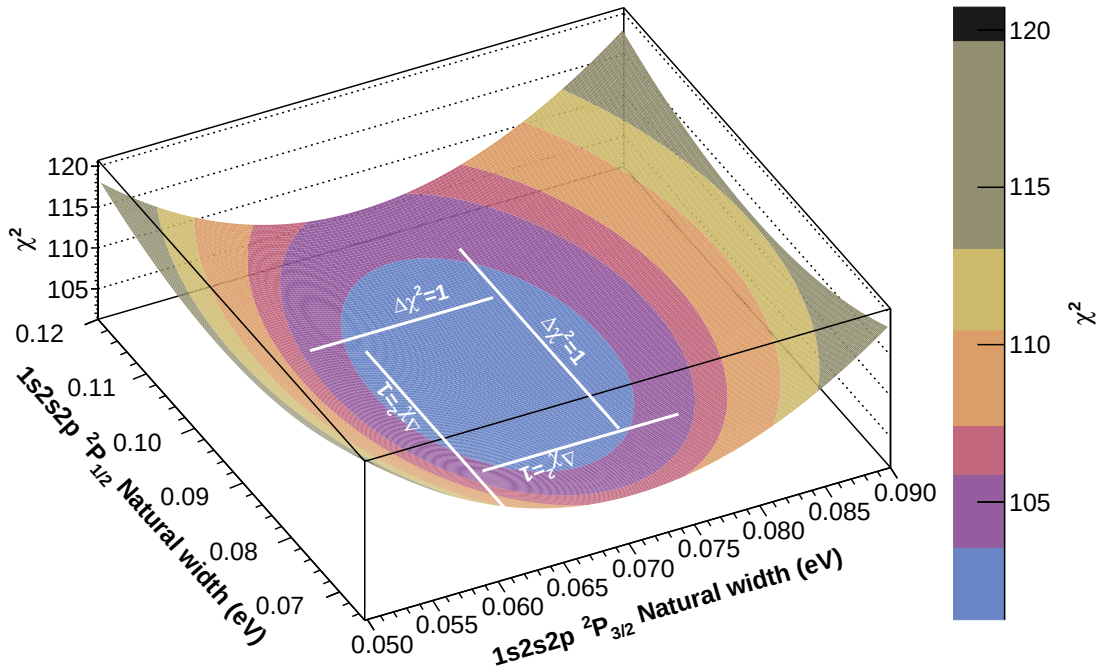

Figure 4.14 – Best fit to the set of point $[\chi^2, \Gamma_L^1, \Gamma_L^2]$ from a χ^2 minimization using the fit function given in Eq. (4.2). The colored contours represent the $n\sigma$ confidence intervals around the minimum χ^2 value, for $n = 1, 2, 3, \cdots$. The interval given by Eq. (4.3), from where the 68% confidence interval is obtained for each natural width, is shown in the plot by the $\Delta\chi^2 = 1$ white lines.

0.01 eV has been simulated for 10 different temperatures ranging from 20 °C to 30 °C for each line. From the fits to the parallel and antiparallel peaks, the offset parameters θ_0^1 and θ_0^2 are obtained. The difference between the dispersive and non-dispersive offset difference from experimental spectra and simulation are obtained from Eq. (2.9) for each transition of the Li-like argon double. For each peak a bidimensional function of the form of Eq. (2.10) is fitted to the set of points $\left[E_k, T_l, \Delta\theta^{k,l}_{\text{Exp.–Simul.}}\right]$, where E_k and T_l are the simulated energies and temperatures, respectively. An example of the bidimensional fit function for each Li-like transition is presented on Fig. 4.16.

From the two bidimensional fit functions, the experimental line energy $E^n_{\text{Exp.}}$ for spectrum pair number n, is obtained by $\Delta\theta_{\text{Exp.–Simul.}}(E^n_{\text{Exp.}}, T_{\text{Exp.}}) = 0$, where $T_{\text{Exp.}}$ stands for the average measured temperature on the second crystal. When all experimental energy values for each pair of dispersive and non-dispersive spectra are obtained, an weighted average is performed and the final value of the energy is obtained with the respective statistical uncertainty. The values obtained for each pair of dispersive and non-dispersive spectra for both Li-like lines are

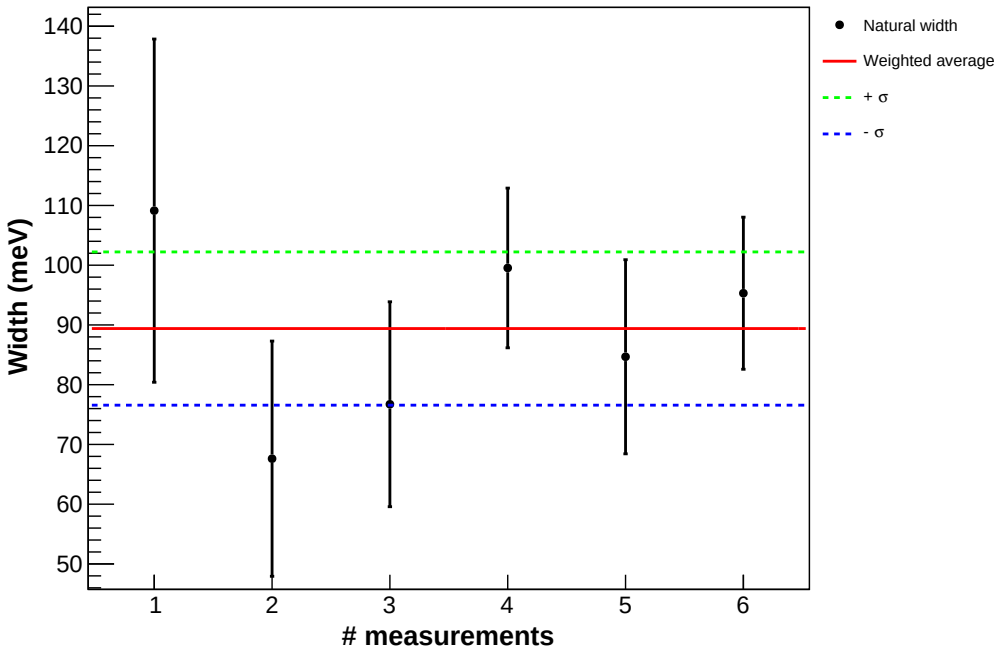

a) $1s\,2s\,2p\,^2P_{1/2} \rightarrow 1s^2\,2s\,^2S_{1/2}$

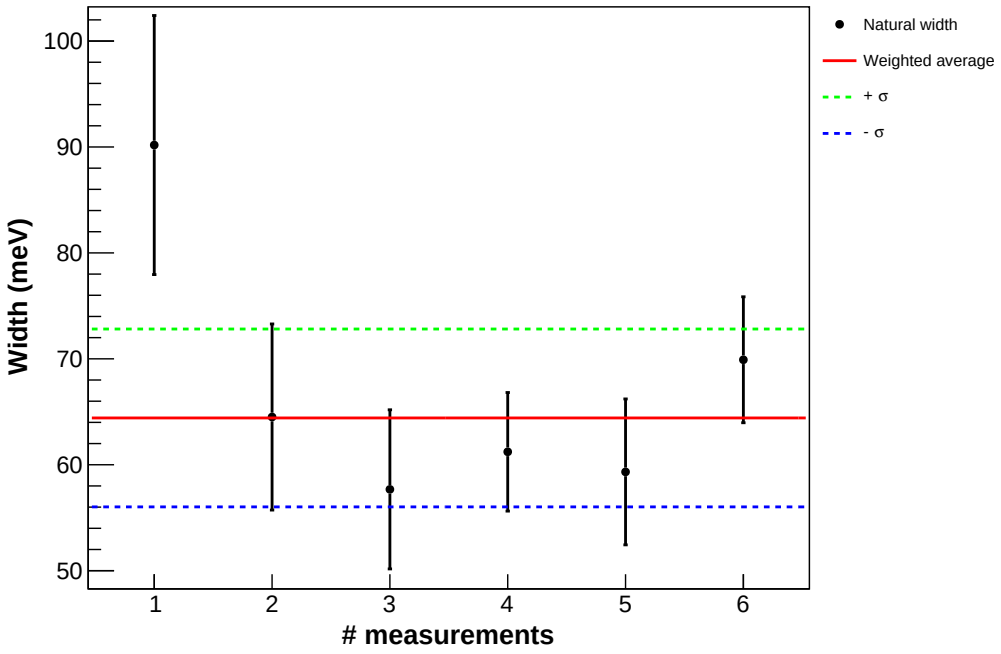

b) $1s\,2s\,2p\,^2P_{3/2} \rightarrow 1s^2\,2s\,^2S_{1/2}$

Figure 4.15 – Natural width values of all spectra recorded during the experiment of the $1s\,2s\,2p\,^2P_J \rightarrow 1s^2\,2s\,^2S_{1/2}$, $J = 1/2, 3/2$ Li-like argon transition. The weighted average and the confidence interval of 68%, evaluated with Eq. (2.8), are also shown.

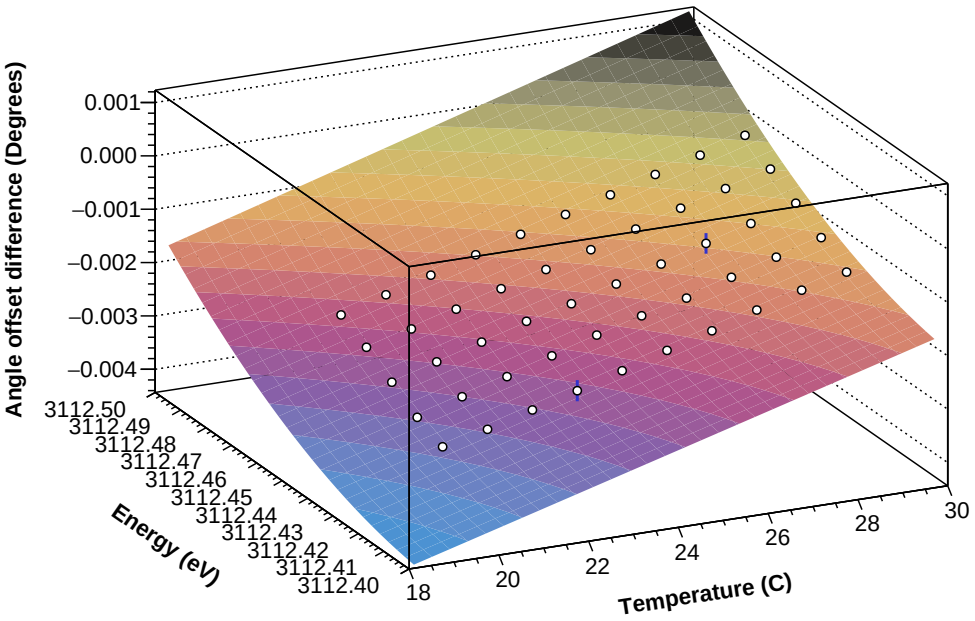

a) $1s\,2s\,2p\,^2P_{1/2} \rightarrow 1s^2\,2s\,^2S_{1/2}$

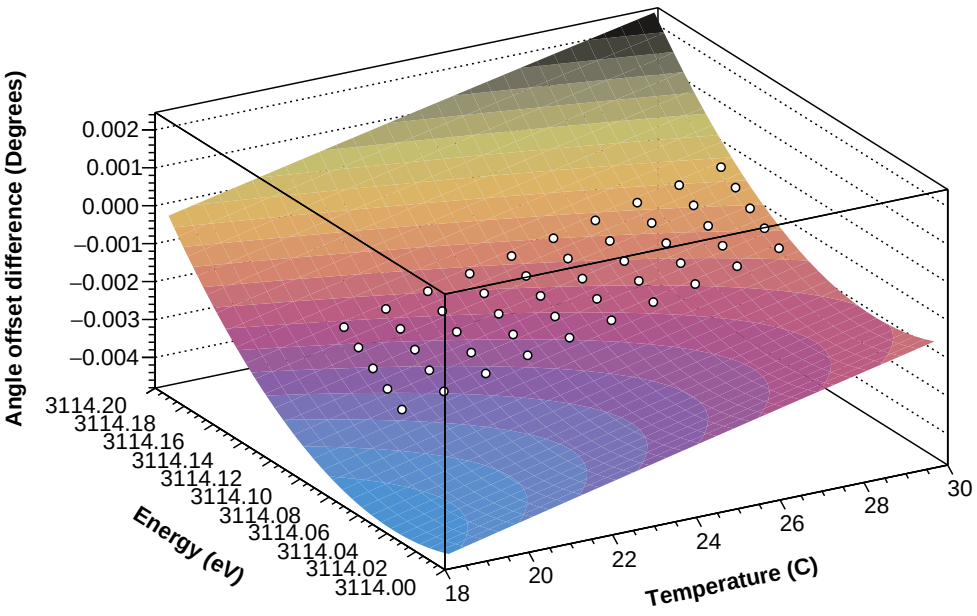

b) $1s\,2s\,2p\,^2P_{3/2} \rightarrow 1s^2\,2s\,^2S_{1/2}$

Figure 4.16 – Example of the fit with the bidimensional function (Eq. (2.10)) to the set of data $\left[E_k, T_l, \Delta\theta^{k,l}_{\text{Exp.–Simul.}}\right]$ for the two measured Li-like transitions, with the offset $\Delta\theta^{n,k,l}_{\text{Exp.–Simul.}}$ obtained by fitting both dispersive and non-dispersive spectra. The error bar at each point is calculated from the quadratic sum of the standard errors $\delta\theta$ of the offset θ fit parameter from the dispersive and non-dispersive spectra.

presented in Fig. 4.17. The weighted average value is represented by the full red line and the dashed red and blue lines represent the $+\sigma$ and $-\sigma$, respectively. The error bar at each point is obtained from Eq. (2.11), which corresponds to the statistical uncertainty of obtaining the energy value from the bidimensional fit function of Fig. 4.16 quadratically combined with the uncertainties due to the temperature and angle measurement. Every pair of points on both plots of Fig. 4.17 corresponds to one-day data taking.

4.3.2 Results and discussion

Both $1s\,2s\,2p\,^2P_J$, $J = 1/2$, $3/2$ have radiative and non-radiative (Auger) contributions to the level width. The available calculations, our experimental result from the weighted average from Fig. 4.15 and a MCDF calculation performed within the group for the pair of widths are compared in Table 4.6. As it can be seen, our experimental result is in agreement with the available calculation within combined experimental and theoretical uncertainties. Yet, one can notice that almost all calculations, with the exception of Costa *et al.*(2001) [206], attributes a larger width to $J = 3/2$ level, which is in disagreement from what we have found experimentally.

Table 4.6 – Comparison between experimental and theoretical Li-like argon $1s\,2s\,2p\,^2P_J$, $J = 1/2$, $3/2$ level width. All energies are given in meV.

Transition	Experiment	Theory	Reference
$1s\,2s\,2p\,^2P_{1/2} \rightarrow 1s^2\,2s\,^2S_{1/2}$	89.4 (12.8)	62.61	Machado *et al.*(2018) [289]
		77.80	Costa *et al.*(2001) [206]
		68.59	Nilsen (1988) [290]
		65.56	Vainshtein and Safronova [291]
$1s\,2s\,2p\,^2P_{3/2} \rightarrow 1s^2\,2s\,^2S_{1/2}$	64.4 (8.4)	65.07	Machado *et al.*(2018) [289]
		72.15	Costa *et al.*(2001) [206]
		69.70	Nilsen (1988) [290]
		67.36	Vainshtein and Safronova [291]

Li-like ions are among the simplest many-electron systems representing a very attractive object for the *ab initio* theoretical descriptions. For comparison with the most advanced and accurate BSQED theories, high-precision experimental results are necessary which can also provide new benchmark energies for the calculation of missing theoretical contributions, such as Auger shifts or electronic correlations.

There are three available experimental energy values for the Li-like $1s\,2s\,2p\,^2P_J \rightarrow 1s^2\,2s\,^2S_{1/2}$, $J = 1/2$, $3/2$ transition doublet in argon, which are either calibrated

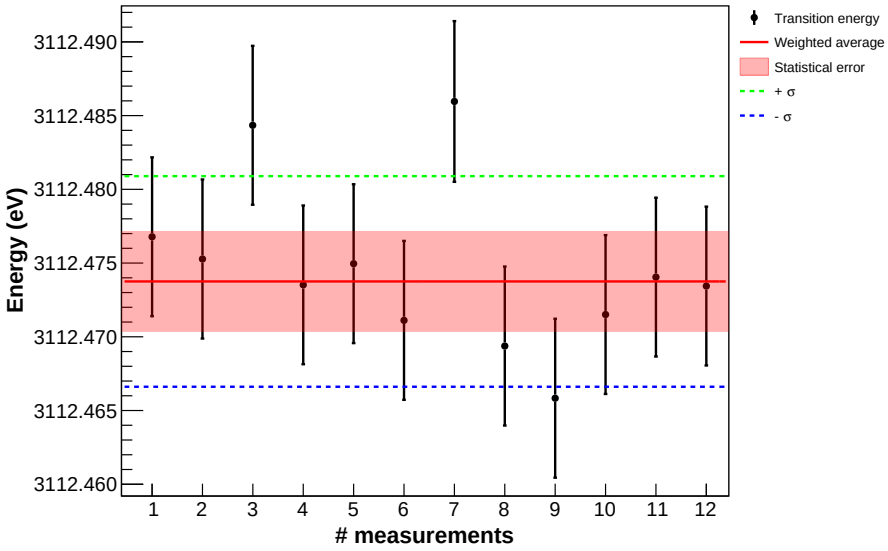

a) $1s\,2s\,2p\,^2P_{1/2} \rightarrow 1s^2\,2s\,^2S_{1/2}$

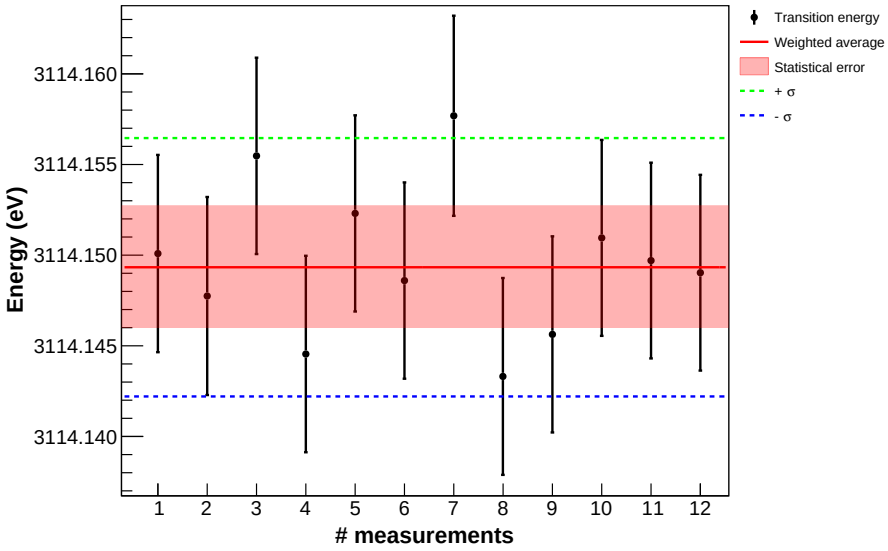

b) $1s\,2s\,2p\,^2P_{3/2} \rightarrow 1s^2\,2s\,^2S_{1/2}$

Figure 4.17 – Li-like argon $1s\,2s\,2p\,^2P_J \rightarrow 1s^2\,2s\,^2S_{1/2}$, $J = 1/2, 3/2$ doublet transition energy values of the different pair of dispersive and non-dispersive spectra recorded during the experiment. Error bars correspond to statistical uncertainty obtained from Eq. (4.3) quadratically combined with the uncertainties in the temperature and angle measurement. Red full curve corresponds to the weighted average mean, obtained considering only the statistical uncertainty in each point. The pink shaded area corresponds to the statistical uncertainty and the dashed blue and green lines ($\pm\sigma$) represent the total uncertainty obtained by the quadratically combination of the statistical uncertainty and all the contributions given on Table 3.1. Every pair of points correspond to one-day data taking.

using theoretical values or standard reference x-ray lines. It has been measured in ions produced by an ECRIS with a single spherically bent crystal spectrometer [138], which has been then calibrated against the M1 transition value from Ref. [125], from ions produced in the Oxford EBIT using a crystal spectrometer in the Johann geometry [292] and by ions produced in tokamak plasma measured with a bent-crystal spectrometer [271]. The experimental results of this work for the Li-like $1s\,2s\,2p\,^2P_J \rightarrow 1s^2\,2s\,^2S_{1/2}$, $J = 1/2, 3/2$ transition doublet are the first reference-free measurement of these lines. The obtained experimental results for the two Li-like lines with the respective 68% of the statistical confidence interval quadratically summed with the instrumental uncertainty, are presented together with the all known experimental and theoretical values in Table 4.7.

The experimental relative total uncertainty of the measured $1s\,2s\,2p\,^2P_J \rightarrow 1s^2\,2s\,^2S_{1/2}$, $J = 1/2, 3/2$, energy transition of our measurements is 2.3 ppm for both transitions. Comparing with the theory of *Yerokhin and Surzykhov* [293] we find a very good agreement of our results. The relative difference from our values is 2.4×10^{-6} for the transition initial state with $J = 3/2$, while for $J = 1/2$ our value is 8.7×10^{-7}. Yet, when compared with the experimental value of *Schlesser et al.* [138], given with a relative uncertainty of 0.6 ppm, we find a much higher relative difference, being 7.3×10^{-6} for $J = 1/2$ and 8.8×10^{-6} for $J = 3/2$. Besides this discrepancy, considering that the experimental results of *Schlesser et al.* [138] were given with a relative accuracy of just 0.6 ppm, our value is in agreement with previous experimental results and with old and recent calculation within combined experimental and theoretical uncertainties.

In addition to the natural width and energy of each transition, in this measurement, since both peaks have been measured in the same spectrum, the ratio between the intensities of the two lines can also be obtained. This will give us an experimental result of the ratio between the fluorescence yields of the two transitions.

With the obtained natural widths and energy of the two transitions, two simulations (one for each line) have been performed with high statistics to fit the spectra with the function from Eq. (4.1). From the fit to the experimental dispersive spectrum, the optimized adjustable coefficients of the fit function were obtained from a χ^2 minimization. With these obtained coefficients, the integral of each individual peak I_1 and I_2 has been numerically obtained by

Table 4.7 – Comparison between experimental and theoretical Li-like argon $1s\,2s\,2p\,^2P_J \rightarrow 1s^2\,2s\,^2S_{1/2}$, $J = 1/2$, 3/2 transition energies. All energies are given in eV.

Energy	Reference
	$\mathbf{1s\,2s\,2p\,^2P_{1/2} \rightarrow 1s^2\,2s\,^2S_{1/2}}$
	Experiment
3112.4737 (72)	This Work
3112.451 (2)	Schlesser *et al.*(2013) [138]
3112.405 (78)	Tarbutt *et al.*(2001) [292]
3112.626 (156)	T.F.R. group *et al.*[271]
	Theory
3112.402	(MCDF)
3112.471	Yerokhin and Surzykhov (2012) [293]
3112.52	Safronova and Safronova (2004) [294]
3118.04	Whiteford *et al.*(2002) [295]
3112.40	Costa *et al.*(2001) [206]
3110.74	Nilsen (1988) [290]
3113.07	Vainshtein and Safronova (1978) [291]
	$\mathbf{1s\,2s\,2p\,^2P_{3/2} \rightarrow 1s^2\,2s\,^2S_{1/2}}$
	Experiment
3114.1493 (71)	This Work
3114.122 (2)	Schlesser *et al.*(2013) [138]
3114.132 (78)	Tarbutt *et al.*(2001) [292]
3114.190 (78)	T.F.R. group *et al.*[271]
	Theory
3114.101	(MCDF)
3114.1418 (45)	Yerokhin and Surzykhov (2012) [293]
3114.16	Safronova and Safronova (2004) [294]
3119.69	Whiteford *et al.*(2002) [295]
3114.15	Costa *et al.*(2001) [206]
3112.44	Nilsen (1988) [290]
3114.71	Vainshtein and Safronova (1978) [291]

$$
\begin{aligned}
I_1 &= \int_{\theta_i}^{\theta_f} I^1_{\max} S^1_{E_{\text{Exp.}},\Gamma_L^{\text{Exp.}},\Gamma_G^{\text{Exp.}},T_{Exp.}}(\theta-\theta_0^1)d\theta \\
I_2 &= \int_{\theta_i}^{\theta_f} I^2_{\max} S^2_{E_{\text{Exp.}},\Gamma_L^{\text{Exp.}},\Gamma_G^{\text{Exp.}},T_{Exp.}}(\theta-\theta_0^2)d\theta,
\end{aligned}
\tag{4.4}
$$

where θ_i and θ_f are the angular range of the experimental dispersive spectrum and S^1 and S^2 the interpolated simulated dispersive spectra of each transition performed with the experimentally obtained energy ($E_{\text{Exp.}}$) and natural width ($\Gamma_L^{\text{Exp.}}$) and the gaussian width from Reference [9]. As a check, the numerical integration of the total fit function from Eq. (4.1) to the spectrum, with it's background removed, has been also performed and its result compared with the sum of the individuals integrals of Eq. (4.4). The numerical integrals have been calculated with the data analysis framework ROOT CERN [80–82] through the MathMore library. This library uses the integration algorithms of GSL [228], which reimplements the algorithms used in the QUADPACK [296], a numerical integration package written in Fortran. In Fig. 4.18 an example of the numerical integration to a dispersive spectra of the Li-like doublet transition in argon is presented. The total integral fit is represented by the black full curve and the respective integral is represented by the shadowed white area with the wave like texture. The individual peak fits are represented by the red ($J = 1/2$) and green ($J = 3/2$) full curves, being its respective integrals the shadowed area with the same color. The background has been removed from the integrals and the obtained values for the integrals are presented in the legend with the respective estimated error. The estimated error in the integration is due to the uncertainties of each adjustable coefficient of the fit function optimized by the χ^2 minimization.

The integration of each peak area has been performed to all recorded dispersive spectra. The ratio between the $1s\,2s\,2p\,^2P_{1/2} \rightarrow 1s^2\,2s\,^2S_{1/2}$ and $1s\,2s\,2p\,^2P_{3/2} \rightarrow 1s^2\,2s\,^2S_{1/2}$ transitions peak intensities is presented in Fig. 4.19 for all recorded dispersive spectra. The weighted average value is represented by the red full line and the $\pm\sigma$ are represented by the green and blue dashed lines. The final obtained value for the ratio between the two transitions is 0.358(13). The error bar in each point of Fig. 4.19 corresponds to the contribution of the uncertainty in the numerical integration of each peak.

As discussed by *Guerra* in Reference [204], in a DCS the number of x rays of a given line reaching the detector do not depend only on the balance between the feeding mechanisms and the radiative transitions of the ion species, but also on the geometrical settings of the DCS, the shape of the collimator and the angle

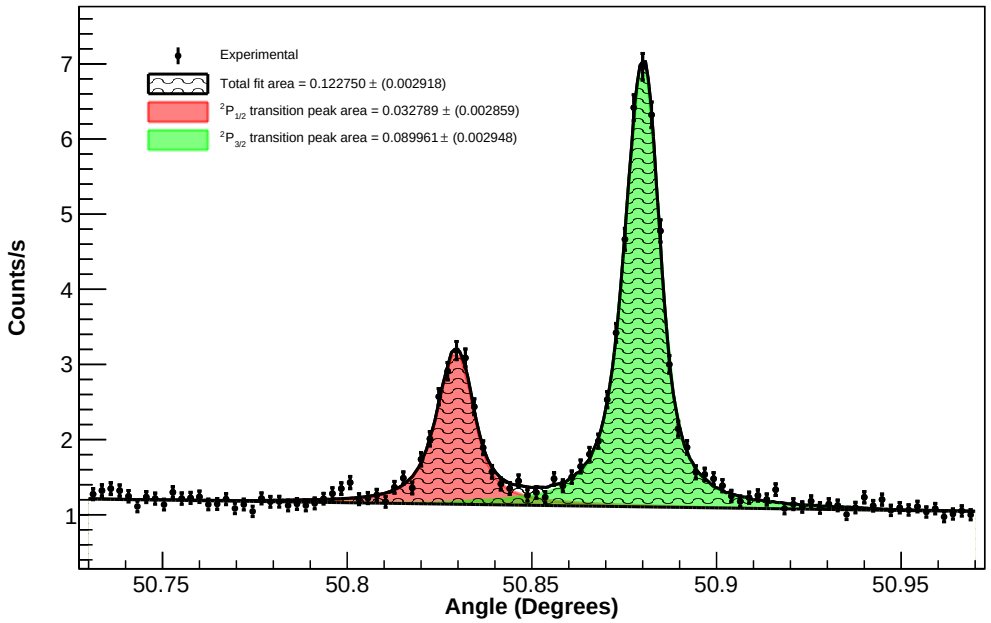

Figure 4.18 – Integral example of the Li-like argon $1s\,2s\,2p\,^2P_J \rightarrow 1s^2\,2s\,^2S_{1/2}$, $J = 1/2, 3/2$ doublet transition dispersive spectrum. The black full curve represents the total fit to the spectrum from Eq. (4.1) with its respective integral represented by the shadowed white area with the wave like texture. Red ($J = 1/2$) and green ($J = 3/2$) full curves represents the individual fits to each peak being the individual integrals represented by the shadowed area with the same color. The obtained values for the integrals are presented in the legend with the respective estimated error.

acceptance of the first Bragg crystal. From a study based on simulation for the energy region of 3087-3120 eV, a hyperbolic expression that relates the normalized intensity of a line in this energy region as a function of the second crystal angle (simulated energy) was found to be the best fit to the simulations intensities [204]

$$I(E) = 1.04815 - 6.27647 \times 10^{-5} \times \sqrt{|588509 + 690026(E - 3103.89)^2|}. \qquad (4.5)$$

This study has been performed for the same DCS experimental geometry as the one of this work. From the expression of Eq. (4.5), the ratio of the normalize intensity for the Li-like doublet lines obtained above has been calculated in order to obtain the final ratio of the peaks intensity considering the geometry of the spectrometer. By inserting the experimental values of the energy from Table 4.7 in Eq. (4.5), the obtained ratio is

$$\frac{I_{E_{J=1/2}}}{I_{E_{J=3/2}}} = 1.1091, \qquad (4.6)$$

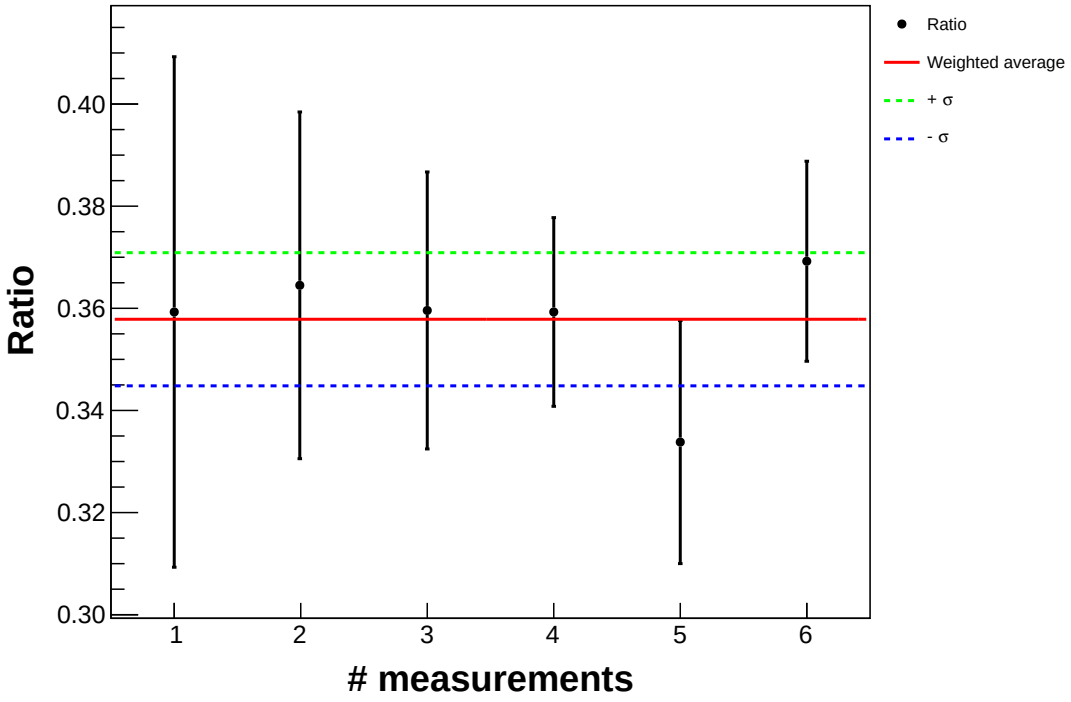

Figure 4.19 – Ratio between the $1s\,2s\,2p\,^2P_{1/2} \rightarrow 1s^2\,2s\,^2S_{1/2}$ and $1s\,2s\,2p\,^2P_{3/2} \rightarrow 1s^2\,2s\,^2S_{1/2}$ transitions peak intensities for all recorded dispersive spectra. The weighted average value is represented by the red full line and the $\pm\sigma$ are represented by the green and blue dashed lines. The error bar at each point corresponds to the contribution of the uncertainty in the numerical integration of each peak.

which multiplied by the above obtained ratio between the integral peaks gives the final number of 0.397(14). This number can now be compared with the ratio between calculated fluorescence yields of the two transitions.

The $1s2s2p$ configuration in Ar^{15+} is mostly created by the excitation of the ground state configuration $1s^2\,2s$ but can also be feed from double KL ionization of the Ar^{13+} ion ground configuration [208]. Being two transitions of the same charge state of argon in the same configuration, and assuming that the population of each level (with a given J value) in the final configuration is statistical, the ratio of the two relative intensities is given by

$$\frac{I_{J=1/2}}{I_{J=3/2}} = \frac{Ty_{J=1/2}}{Ty_{J=3/2}} \cdot \frac{g_{J=1/2}}{g_{J=3/2}}, \tag{4.7}$$

being Ty the radiative transition yield and g the statistical weight of each level J given by the states degeneracy $2J+1$. For the radiative transitions yield Ty values taken from Reference [206], the obtained ratio between the intensities of the two transitions was found to be 0.401, which is in perfect agreement with the

obtained experimental value, within experimental uncertainty.

4.3.3 Comparison between available measurements and theory for the Li-like isoelectronic sequence

As well as for the already discussed, $1s\,2s^2\,2p\,^1P_1 \rightarrow 1s^2\,2s^2\,^1S_0$ Be-like and the $1s\,2p\,^1P_1 \rightarrow 1s^2\,^1S_0$ He-like argon transitions, a survey of available experimental data for all Z and its comparison with theory has been carried out. Our results are the only existent reference-free measurements of the $1s\,2s\,2p\,^2P_J \rightarrow 1s^2\,2s\,^2S_{1/2}$, $J = 1/2$, 3/2 doublet transitions. All the other available experimental values are either calibrated using x-ray reference standards lines or theoretical values. There are available data of spectral lines in laser plasmas of Na, Mg, Al, Si, P, S, Cl, K, Ca, Ti, and V ions (Z = 11 -23) [297], on Ar [292] and V [136] from ions produced in EBIT's, on Fe from the PETRA III synchrotron photon source, on Ca [259] and on Ar, Sc, V, Cr and Mn [271, 275] from ions produced in Tokamaks. As for ions produced in an ECRIS, there are results on Ar and S measured with a single spherically bent crystal spectrometer [138] calibrated with the calculation of the M1 transition value from Ref. [125]. All the available data is presented on Table 4.8 together with our value and the calculation of *Yerokhin* and *Surzykhov* [293] for the available Z values. For the referenced non reference-free measurements, the values have been corrected using the He-like transition energies from Ref. [125] when a different calibration had been used.

In Fig. 4.20, the difference from the experimental values of Table 4.8 and a Dirac-Fock calculation performed within the group is plotted. The difference from the available elements of the calculation of Ref. [293] and the Dirac-Fock calculation are also plotted as the red dashed full curve, being the Dirac-Fock values used as baseline. As can be seen, for the available Z, the experimental values are in agreement with the calculation of *Yerokhin* and *Surzykhov*, from where we cannot notice any discrepancy between theory and experiment. As mentioned, our values (green triangles) are in perfect agreement with the calculation of *Yerokhin* and *Surzykhov* as it can also be concluded from the plot. Yet, for $Z = 25$ the energy values of the $1s\,2s\,2p\,^2P_{1/2} \rightarrow 1s^2\,2s\,^2S_{1/2}$ transition from *Yerokhin* and *Surzykhov* and Dirac-Fock calculation disagrees in about 6 eV and for $Z = 23$ of the $1s\,2s\,2p\,^2P_{3/2} \rightarrow 1s^2\,2s\,^2S_{1/2}$ transition a difference of about 1.8 eV has also been found. This two values were removed from the plots of Fig. 4.20 since they are completely off the trend of the calculated values from *Yerokhin* and *Surzykhov*.

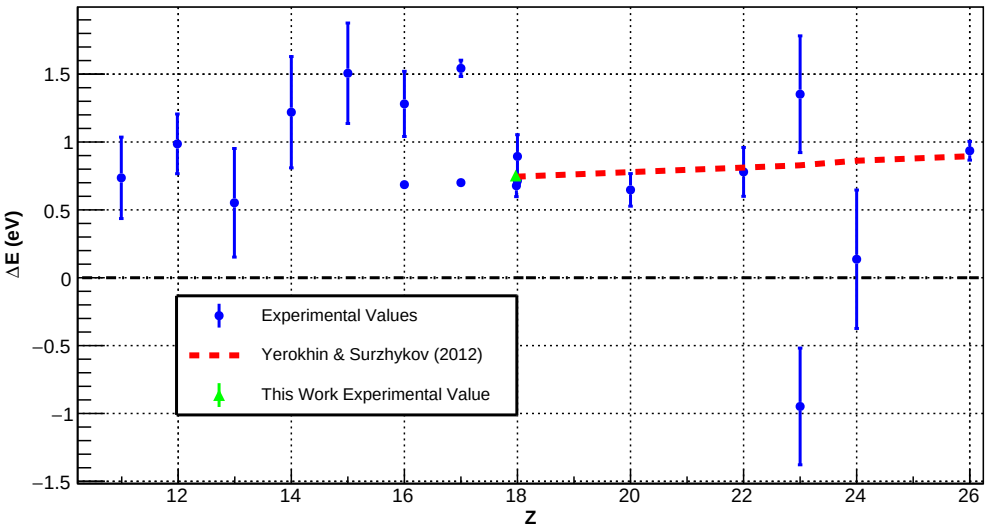

a) $1s\,2s\,2p\,^2P_{1/2} \rightarrow 1s^2\,2s\,^2S_{1/2}$

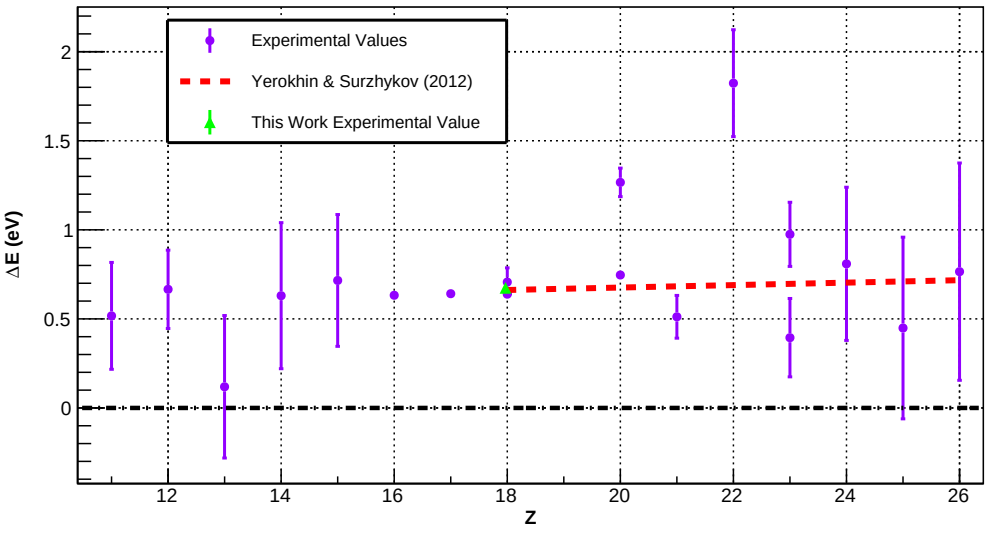

b) $1s\,2s\,2p\,^2P_{3/2} \rightarrow 1s^2\,2s\,^2S_{1/2}$

Figure 4.20 – Comparison between experimental energies values from Table 4.8 and a Dirac-Fock calculation, used as baseline. The difference between the Theoretical values from Ref. [293] and the Dirac-Fock value is also plotted for elements where it is available ($18 \leq Z \leq 36$).

Table 4.8 – Comparison between experimental and theoretical transition energies as a function of Z. All energies are given in eV. Theoretical values are from Ref. [293]. RF: reference-free, SR: calibration using standard reference x-ray lines, RT: calibration using theoretical values. These values have been corrected using He-like transition energies [125].

Z	$1s\,2s\,2p\,^2P_{1/2} \rightarrow 1s^2\,2s\,^2S_{1/2}$				$1s\,2s\,2p\,^2P_{3/2} \rightarrow 1s^2\,2s\,^2S_{1/2}$					
	Exp.	Error	Theory	Error	Exp.	Error	Theory	Error	Calib.	Reference
11	1111.47	0.30			1111.47	0.30			SR	Aglitski *et al.*(1974) [297]
12	1335.58	0.22			1335.58	0.22			SR	Aglitski *et al.*(1974) [297]
13	1579.62	0.40			1579.62	0.40			SR	Aglitski *et al.*(1974) [297]
14	1845.39	0.41			1845.39	0.41			SR	Aglitski *et al.*(1974) [297]
15	2131.45	0.37			2131.45	0.37			SR	Aglitski *et al.*(1974) [297]
16	2437.115	0.005			2438.106	0.003			RT	Schlesser *et al.*(2013) [138]
16	2437.71	0.24							SR	Aglitski *et al.*(1974) [297]
17	2764.378	0.005			2765.678	0.003			RT	Schlesser *et al.*(2013) [138]
17	2765.22	0.06							SR	Aglitski *et al.*(1974) [297]
18	3112.471	0.007	3112.471	0.012	3114.152	0.0069	3114.1417	0.0055	RF	This work
18	3112.451	0.002	3112.471	0.012	3114.122	0.002	3114.1417	0.0055	RT	Schlesser *et al.*(2013) [138]
18	3112.405	0.078	3112.471	0.012	3114.132	0.078	3114.1417	0.0055	SR	Tarbutt *et al.*(2001) [292]
18	3112.63	0.16	3112.471	0.012	3114.190	0.078	3114.1417	0.0055	RT	T.F.R. group *et al.*(1985) [271]
20			3871.242	0.013	3874.540		3873.9457	0.0061	SR	Suleiman *et al.*(1994) [298]
20	3871.12	0.12	3871.242	0.013	3874.02	0.12	3873.9457	0.0061		Rice *et al.*(2014) [259]
21	4285.28	0.30	4282.058	0.013	4285.28	0.30	4285.4456	0.0074	RT	T.F.R. group *et al.*(2005) [275]
22	4713.87	0.18	4713.895	0.016	4719.25	0.18	4718.1102	0.0072	RT	Bitter *et al.*. (1985). [272]
23	5167.35	0.43	5166.811	0.019	5172.31	0.22	5173.1364	0.0065		Beiersdorfer *et al.*(1991) [136]
23	5165.05	0.43	5166.811	0.019	5171.73	0.43	5173.1364	0.0065	RT	T.F.R. group *et al.*(1985) [275]

Table 4.8 – Comparison between experimental and theoretical transition energies as a function of Z. All energies are given in eV. Theoretical values are from Ref. [293]. RF: reference-free, SR: calibration using standard reference x-ray lines, RT: calibration using theoretical values. These values have been corrected using He-like transition energies [125]. (continued)

Z	$1s\,2s\,2p\,^2P_{1/2} \rightarrow 1s^2\,2s\,^2S_{1/2}$				$1s\,2s\,2p\,^2P_{3/2} \rightarrow 1s^2\,2s\,^2S_{1/2}$					
	Exp.	Error	Theory	Error	Exp.	Error	Theory	Error	Calib.	Reference
24	5640.19	0.51	5640.899	0.021	5647.39	0.51	5647.2787	0.0077	RT	T.F.R. group *et al.*(1985) [275]
25			6136.194	0.021	6143.71	0.61	6143.9664	0.0091	RT	T.F.R. group *et al.*(1985) [275]
26	6652.826	0.069	6652.776	0.025	6662.240	0.069	6662.1887	0.0107	SR	Rudolph *et al.*2013 [11]

4.4 The B-like argon transitions experiment

Recently, an experimental campaign has been put forward aiming the measurement of B-like argon transitions with the DCS from an argon plasma produced in the SIMPA ECRIS. Figure 4.21 shows an example of such obtained dispersive spectra. The spectra has been recorded with the spectrometer table aligned to the $1s\,2s^2\,2p\,^1P_1 \rightarrow 1s^2\,2s^2\,^1S_0$ transition energy in Be-like argon. The spectrum of Fig 4.21 has been recorded during 26587 seconds with a total number of counts of about 2.1×10^5 for an angular scan range of the second crystal of 0.4°.

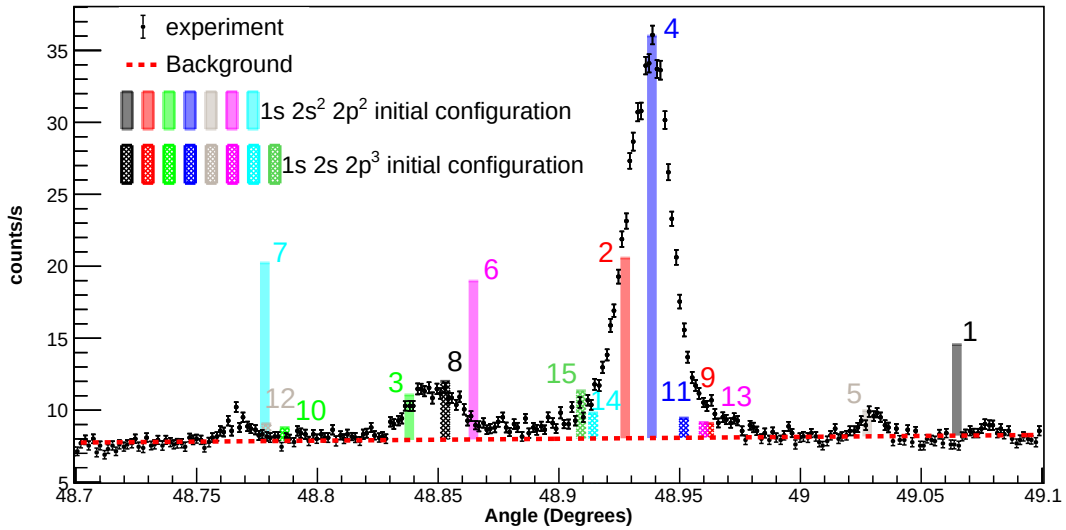

Figure 4.21 – Dispersive spectrum of a few B-like transitions in argon. The data has been recorded during 26587 seconds with a total number of counts of about 2.1×10^5 for an angular scan range of the second crystal of 0.4°. Several peaks can be seen. The lines listed on Table 4.9 from Reference [206] are represented by the several colored bars. The height of each bar represents the fluorescence yield of each transition considering the statistical weight of each level J. The most intense line (line 4 in Table 4.9), with the ion in the $1s\,2s^2\,2p^2$ initial configuration, has been used for normalization by taking the value of the highest peak and its fluorescence yield as a normalization factor. For the lines with $1s\,2s\,2p^3$ initial configuration, the second most intense peak amplitude has been taken as a normalization with the line 8 fluorescence yield for all transitions resulting from the $1s\,2s\,2p^3$ initial configuration. The angle of each bar has been calculated by taking the most intense line as a reference at the highest counts/s value of the spectrum. The angular offset of all represent lines has been calculated by taking line 4 as a reference. The background (represented by the dashed red line) has been obtained by fitting a linear function to the points out of the range of all visible peaks. The identification, the analysis of the energy and natural width of the transitions contributing to the spectrum is ongoing.

Several peaks can be seen in the spectrum of Fig 4.21, from either individual transitions or a combination of different x-ray transitions with close energy that cannot be resolved by the DCS. The colored bars represent the Ar^{13+} transitions from the $1s\,2s^2\,2p^2$ and $1s\,2s\,2p^3$ initial configurations listed on Table 4.9. Although the $1s\,2s^2\,2p^2$ configuration can be populated by excitation mechanisms, it is mostly created by the ionization of the Ar^{12+} ground state configuration, being thus a more populated configuration than the $1s\,2s\,2p^3$ that is created by excitation processes. Therefore, the lines listed on Table 4.9, which have been taken from Reference [206], although having an energy corresponding to the right angular range of the spectra, they have been selected considering a fluorescence yield higher than 10^{-2} for the $1s\,2s^2\,2p^2$ initial configuration and higher than 10^{-1} for the $1s\,2s\,2p^3$ initial configuration. The labeled lines on Fig 4.21 correspond to the labeled line numbers in Table 4.9. The height of each bar represents the fluorescence yield of each transition, for which, a normalization by corresponding the highest value of the spectrum to the transition with highest fluorescence yield of the $1s\,2s^2\,2p^2$ initial configuration (line 4) has been performed. For the lines resulting from the Ar^{13+} charge state in the $1s\,2s\,2p^3$ configuration, the second most intense peak amplitude value has been considered for the normalization, assuming that line 8 is the line corresponding to its maximum value. The angular position of each peak has been calculated by taking the line 4 as reference corresponding the angle with the highest intensity value in the spectrum to its energy.

The recorded B-like Ar spectra is composed by several different transitions that might be contributing to all observed peaks, which will probably limit the energy and natural width experimental accuracy. The identification, the analysis of the energy and natural width of the transitions contributing to the experimental spectra is ongoing.

Table 4.9 – Transition energy in eV and radiative transition yield (RT Yield) values from Reference [206] for the Ar^{13+} charge state in the $1s\,2s^2\,2p^2$ and $1s\,2s\,2p^3$ initial configurations with transition energies corresponding to the angular range of the spectrum of Fig. 4.21. The listed transitions have been selected considering a radiative transition yield higher than 10^{-2} for the ion in the $1s\,2s^2\,2p^2$ initial configuration and higher than 10^{-1} for the ion in the $1s\,2s\,2p^3$ initial configuration.

Line number	Initial level		Final level		Transition energy [eV]	RT Yield
1	$1s\,2s^2\,2p^2$	$^2S_{1/2}$	$1s^2\,2s^2\,2p$	$^2P_{3/2}$	3069.60	0.184
2		$^2P_{1/2}$		$^2P_{1/2}$	3065.24	0.364
3		$^2P_{1/2}$		$^2P_{3/2}$	3062.41	0.091
4		$^2P_{3/2}$		$^2P_{3/2}$	3065.59	0.406
5		$^2P_{3/2}$		$^2P_{1/2}$	3068.42	0.026
6		$^2D_{3/2}$		$^2P_{1/2}$	3063.25	0.160
7		$^2D_{5/2}$		$^2P_{3/2}$	3060.52	0.120
8	$1s\,2s\,2p^3$	$^2P_{3/2}$	$1s^2\,2s\,2p^2$	$^2P_{3/2}$	3062.88	0.413
9		$^2P^{(1)}_{1/2}$		$^2D_{3/2}$	3066.34	0.201
10		$^2P^{(2)}_{1/2}$		$^2P_{1/2}$	3060.78	0.186
11		$^2P^{(1)}_{3/2}$		$^2D_{5/2}$	3066.01	0.139
12		$^2P^{(2)}_{3/2}$		$^2P_{3/2}$	3060.54	0.121
13		$^4P_{1/2}$		$^4P_{3/2}$	3066.27	0.214
14		$^4P_{3/2}$		$^4P_{5/2}$	3064.82	0.180
15		$^4P_{5/2}$		$^4P_{5/2}$	3064.66	0.225

Chapter 5

Conclusion

In this work, four different x-ray lines transition energies and widths in highly-charged argon have been measured using a double-crystal spectrometer from ions produced in a ECRIS. The $1s\,2s^2\,2p\,^1P_1 \rightarrow 1s^2\,2s^2\,^1S_0$ transition in Be-like argon and the $1s\,2s\,2p\,^2P_J \rightarrow 1s^2\,2s\,^2S_{1/2}$, $J = 1/2, 3/2$ Li-like argon doublet transition are the first reference-free measurements performed in an ion with more than two-electrons. With the dedicated x-ray tracing simulation code that includes the physical characteristics and geometry of both the source and the spectrometer, it has been proved that besides obtaining the transition energy with high-precision the natural width can also be obtained by measuring a transition where the natural width can be neglected when compared to the intrinsic resolution of the apparatus and the plasma temperature. Both transition energies and level widths are in agreement with theory within the error bars and with the more recent measurements.

For all measured transitions in this work, a survey of available experimental data has been performed and compared with the most recent and advanced calculations. For all cases, we did not find a deviation between theory and experiment. Especially, for the He-like isoelectronic sequence, the performed detailed statistical analysis, when taking into account the recent high-precision, reference-free measurements in He-like argon, we have shown that there is no significant Z-dependent deviation between the most advanced theory and experiment.

The transition energies have been measured with a relative uncertainty better than 3 ppm. This small relative uncertainty, allows the use of this narrow transitions as x-ray standards that can be used to calibrate instruments in this energy

range.

The ratio between the relative intensities of the $1s\,2s\,2p\,^2P_J \rightarrow 1s^2\,2s\,^2S_{1/2}$, $J = 1/2, 3/2$ Li-like argon doublet transition has been experimentally obtained. The result has been compared with calculated radiative transition yields from literature. A perfect agreement has been found between our experimental value for the relative intensities ratio and the one obtained with the calculated fluorescence yields from literature.

The recent experiment on B-like argon x-ray transitions has been very successful. Yet, the dispersive spectra contributions of several radiative transitions on B-like Ar, that might not be completely resolved by the spectrometer, will limit the energy and natural width experimental accuracy. The identification, analysis of the energies and natural widths of the measured transitions is ongoing and the results are expected soon.

With the foreseen updates on the apparatus, specially the stabilization and measurement of the crystal temperature, energy measurements with an accuracy below 1 ppm will be possible. This will improve our understanding and can provide tests of higher-order QED-corrections in middle Z elements. It will also provide new an more accurate x-ray standards based on narrow transitions of highly charged ions.

The method presented here will be extended to other charge-states and nearby elements in the near future.

Bibliography

[1] A. Matveev, C. G. Parthey, K. Predehl, J. Alnis, A. Beyer, R. Holzwarth, T. Udem, T. Wilken, N. Kolachevsky, M. Abgrall, et al., "Precision Measurement of the Hydrogen 1 S- 2 S Frequency via a 920-km Fiber Link," *Physical Review Letters* **2013**, *110*, 230801.

[2] C. G. Parthey, A. Matveev, J. Alnis, B. Bernhardt, A. Beyer, R. Holzwarth, A. Maistrou, R. Pohl, K. Predehl, T. Udem, et al., "Improved measurement of the hydrogen 1 s–2 s transition frequency," *Physical review letters* **2011**, *107*, 203001.

[3] B De Beauvoir, C. Schwob, O Acef, L Jozefowski, L Hilico, F Nez, L Julien, A Clairon, F Biraben, "Metrology of the hydrogen and deuterium atoms: determination of the Rydberg constant and Lamb shifts," *The European Physical Journal D-Atomic Molecular Optical and Plasma Physics* **2000**, *12*, 61–93.

[4] D. Z. Kandula, C. Gohle, T. J. Pinkert, W. Ubachs, K. S. Eikema, "Extreme ultraviolet frequency comb metrology," *Physical review letters* **2010**, *105*, 063001.

[5] J. Borbely, M. George, L. Lombardi, M Weel, D. Fitzakerley, E. Hessels, "Separated oscillatory-field microwave measurement of the 2 P 3 1–2 P 3 2 fine-structure interval of atomic helium," *Physical Review A* **2009**, *79*, 060503.

[6] M. Smiciklas, D. Shiner, "Determination of the fine structure constant using helium fine structure," *Physical review letters* **2010**, *105*, 123001.

[7] K. Pachucki, V. A. Yerokhin, "Fine structure of heliumlike ions and determination of the fine structure constant," *Physical review letters* **2010**, *104*, 070403.

[8] H Bruhns, J Braun, K Kubiček, J. C. López-Urrutia, J Ullrich, "Testing QED screening and two-loop contributions with He-like ions," *Physical review letters* **2007**, *99*, 113001.

[9] P. Amaro, S. Schlesser, M. Guerra, E.-O. Le Bigot, J.-M. Isac, P. Travers, J. P. Santos, C. I. Szabo, A. Gumberidze, P. Indelicato, "Absolute Measurement of the Relativistic Magnetic Dipole Transition Energy in Heliumlike Argon," *Physical Review Letters* **2012**, *109*, 043005.

[10] C. T. Chantler et al., "Testing Three-Body Quantum Electrodynamics with Trapped Ti20+Ions: Evidence for a Z-dependent Divergence Between Experiment and Calculation," *Physical Review Letters* **2012**, *109*, 153001.

[11] J. K. Rudolph et al., "X-Ray Resonant Photoexcitation: Linewidths and Energies of K alpha Transitions in Highly Charged Fe Ions," *Physical Review Letters* **2013**, *111*, 103002.

[12] C. T. Chantler, A. T. Payne, J. D. Gillaspy, L. T. Hudson, L. F. Smale, A Henins, J. A. Kimpton, E Takacs, "X-ray measurements in helium-like atoms increased discrepancy between experiment and theoretical QED," *New Journal of Physics* **2014**, *16*, 123037.

[13] A. Payne, C. Chantler, M. Kinnane, J. Gillaspy, L. Hudson, L. Smale, A Henins, J. Kimpton, E Takacs, "Helium-like titanium x-ray spectrum as a probe of QED computation," *Journal of Physics B: Atomic Molecular and Optical Physics* **2014**, *47*, 185001.

[14] K Kubiček, P. H. Mokler, V Mäckel, J Ullrich, J. R. C. López-Urrutia, "Transition energy measurements in hydrogenlike and heliumlike ions strongly supporting bound-state QED calculations," *Physical Review A* **2014**, *90*, 032508.

[15] P. Beiersdorfer, G. V. Brown, "Experimental study of the x-ray transitions in the heliumlike isoelectronic sequence: Updated results," *Physical Review A* **2015**, *91*, 53.

[16] S. W. Epp et al., "Single-photon excitation of Kαin heliumlike Kr34+: Results supporting quantum electrodynamics predictions," *Physical Review A* **2015**, *92*, 020502.

[17] S. Sturm, A. Wagner, B. Schabinger, J. Zatorski, Z. Harman, W. Quint, G. Werth, C. H. Keitel, K. Blaum, "g Factor of Hydrogenlike Si 13+ 28," *Physical review letters* **2011**, *107*, 023002.

[18] A Wagner, S Sturm, F Köhler, D. A. Glazov, A. V. Volotka, G Plunien, W Quint, G Werth, V. M. Shabaev, K Blaum, "g Factor of Lithiumlike Silicon $^{28}Si^{11+}$," *Physical Review Letters* **2013**, *110*, 033003.

[19] S Sturm, F Köhler, J Zatorski, A Wagner, Z Harman, G Werth, W Quint, C. H. Keitel, K Blaum, "High-precision measurement of the atomic mass of the electron," *Nature* **2014**, 1–4.

[20] F. Köhler, S. Sturm, A. Kracke, G. Werth, W. Quint, K. Blaum, "The electron mass from g-factor measurements on hydrogen-like carbon 12C5+," *Journal of Physics B: Atomic Molecular and Optical Physics* **2015**, *48*, 144032.

[21] J. Ullmann, Z. Andelkovic, A. Dax, W. Geithner, C. Geppert, C. Gorges, M. Hammen, V. Hannen, S. Kaufmann, K. König, et al., "An improved value for the hyperfine splitting of hydrogen-like 209Bi82+," *Journal of Physics B: Atomic Molecular and Optical Physics* **2015**, *48*, 144022.

[22] J. Marques, P Indelicato, F Parente, J. Sampaio, J. Santos, "Ground-state Landé g factors for selected ions along the boron isoelectronic sequence," *Physical Review A* **2016**, *94*, 042504.

[23] V. Yerokhin, E Berseneva, Z Harman, I. Tupitsyn, C. Keitel, "Weighted difference of g factors of light Li-like and H-like ions for an improved determination of the fine-structure constant," *Physical Review A* **2016**, *94*, 022502.

[24] P Beiersdorfer, A. L. Osterheld, J. H. Scofield, J. R. Crespo López-Urrutia, K Widmann, "Measurement of QED and Hyperfine Splitting in the 2s1/2-2p3/2X-ray transition in Li-like209Bi80+," *Physical Review Letters* **1998**, *80*, 3022–3025.

[25] P Seelig, S Borneis, A Dax, T Engel, S Faber, M Gerlach, C Holbrow, G Huber, T Kühl, D Marx, et al., "Ground State Hyperfine Splitting of Hydrogenlike 207 Pb 8 1+ by Laser Excitation of a Bunched Ion Beam in the GSI Experimental Storage Ring," *Physical review letters* **1998**, *81*, 4824.

[26] S Boucard, P. Indelicato, "Relativistic many-body and QED effects on the hyperfine structure of lithium-like ions," *The European Physical Journal D* **2000**, *8*, 59.

[27] P. Beiersdorfer, S. B. Utter, K. L. Wong, J. R. C. López-Urrutia, J. A. Britten, H. Chen, C. L. Harris, R. S. Thoe, D. B. Thorn, E. Träbert, et al., "Hyperfine structure of hydrogenlike thallium isotopes," *Physical Review A* **2001**, *64*, 032506.

[28] V. Yerokhin, V. Shabaev, "One-loop self-energy correction to the 1 s and 2 s hyperfine splitting in H-like systems," *Physical Review A* **2001**, *64*, 012506.

[29] V. M. Shabaev, A. N. Artemyev, V. A. Yerokhin, O. M. Zherebtsov, G Soff, "Towards a Test of QED in Investigations of the Hyperfine Splitting in Heavy Ions," *Physical Review Letters* **2001**, *86*, 3959–3962.

[30] A. V. Volotka, D. A. Glazov, O. V. Andreev, V. M. Shabaev, I. I. Tupitsyn, G Plunien, "Test of Many-Electron QED Effects in the Hyperfine Splitting of Heavy High-Z Ions," *Physical Review Letters* **2012**, *108*, 073001.

[31] O. Andreev, D. Glazov, A. Volotka, V. Shabaev, G Plunien, "Evaluation of the screened vacuum-polarization corrections to the hyperfine splitting of Li-like bismuth," *Physical Review A* **2012**, *85*, 022510.

[32] W. Nörtershäuser, M. Lochmann, R. Jöhren, C. Geppert, Z. Andelkovic, D. Anielski, B. Botermann, M. Bussmann, A. Dax, N. Frömmgen, et al., "First observation of the ground-state hyperfine transition in 209Bi80+," *Physica Scripta* **2013**, *2013*, 014016.

[33] M. Lochmann et al., "Observation of the hyperfine transition in lithium-like bismuth," *Physical Review A* **2014**, *90*, 030501.

[34] P Beiersdorfer, E Träbert, G. V. Brown, J Clementson, D. B. Thorn, M. H. Chen, K. T. Cheng, J Sapirstein, "Hyperfine Splitting of the 2s1/2and 2p1/2Levels in Li- and Be-like Ions of Pr59141," *Physical Review Letters* **2014**, *112*, 233003.

[35] J Vollbrecht, Z Andelkovic, A Dax, W Geithner, C Geppert, C Gorges, M Hammen, V Hannen, S Kaufmann, K König, et al. in Journal of Physics: Conference Series, *Vol. 583*, IOP Publishing, **2015**, p. 012002.

[36] J. Ullmann, Z. Andelkovic, C. Brandau, A. Dax, W. Geithner, C. Geppert, C. Gorges, M. Hammen, V. Hannen, S. Kaufmann, et al., "High precision hyperfine measurements in Bismuth challenge bound-state strong-field QED," *Nature Communications* **2017**, *8*.

[37] R. Pohl et al., "The size of the proton," *Nature* **2010**, *466*, 213–216.

[38] A Antognini et al., "Proton Structure from the Measurement of 2S-2P Transition Frequencies of Muonic Hydrogen," *Science* **2013**, *339*, 417–420.

[39] P. J. Mohr, B. N. Taylor, D. B. Newell, "CODATA recommended values of the fundamental physical constants: 2010 a," *Journal of Physical and Chemical Reference Data* **2012**, *84*, 1527.

[40] R. Pohl, others, "Laser spectroscopy of muonic deuterium," *Science* **2016**, *353*, 669–673.

[41] A. Beyer et al., "The Rydberg Constant and Proton Size from Atomic Hydrogen," *Science* **2017**, *358*, 79–85.

[42] V. Shabaev, A. Artemyev, V. Yerokhin, O. Zherebtsov, G Soff, "Towards a test of QED in investigations of the hyperfine splitting in heavy ions," *Physical review letters* **2001**, *86*, 3959.

[43] J. Ullmann, Z. Andelkovic, C. Brandau, A. Dax, W. Geithner, C. Geppert, C. Gorges, M. Hammen, V. Hannen, S. Kaufmann, et al., "High precision hyperfine measurements in Bismuth challenge bound-state strong-field QED," *Nature Communications* **2017**, *8*.

[44] M. Herrmann, M Haas, U. D. Jentschura, F. Kottmann, D. Leibfried, G. Saathoff, C. Gohle, A. Ozawa, V. Batteiger, S. Knünz, et al., "Feasibility of coherent xuv spectroscopy on the 1 S- 2 S transition in singly ionized helium," *Physical Review A* **2009**, *79*, 052505.

[45] W. E. Lamb Jr, R. C. Retherford, "Fine structure of the hydrogen atom by a microwave method," *Physical Review* **1947**, *72*, 241.

[46] P Kusch, H. Foley, "The magnetic moment of the electron," *Physical Review* **1948**, *74*, 250.

[47] I. Sick, "Problems with proton radii," *Progress in Particle and Nuclear Physics* **2012**, *67*, 473–478.

[48] A Antognini, K Schuhmann, F. Amaro, P Amaro, M Abdou-Ahmed, F Biraben, T.-L. Chen, D. Covita, A. Dax, M. Diepold, et al. in EPJ Web of Conferences, *Vol. 113*, EDP Sciences, **2016**, p. 01006.

[49] C. E. Carlson, "The proton radius puzzle," *Progress in Particle and Nuclear Physics* **2015**, *82*, 59–77.

[50] T. Nebel, F. Amaro, A Antognini, F Biraben, J. Cardoso, D. Covita, A Dax, L. Fernandes, A. Gouvea, T Graf, et al., "The Lamb-shift experiment in muonic helium," *Hyperfine interactions* **2012**, *212*, 195–201.

[51] A. Antognini, F. Biraben, J. Cardoso, D. Covita, A. Dax, L. Fernandes, A. Gouvea, T. Graf, T. W. Hänsch, M Hildebrandt, et al., "Illuminating the proton radius conundrum: the μHe+ Lamb shift This paper was presented at the International Conference on Precision Physics of Simple Atomic Systems, held at École de Physique, les Houches, France, 30 May–4 June, 2010.," *Canadian Journal of Physics* **2011**, *89*, 47–57.

[52] E. Kemble, R. Present, "On the breakdown of the Coulomb law for the Hydrogen atom," *Physical Review* **1933**, *44*, 1031.

[53] E. Uehling, "Polarization effects in the positron theory," *Physical Review* **1935**, *48*, 55.

[54] H. A. Bethe, "The electromagnetic shift of energy levels," *Physical Review* **1947**, *72*, 339.

[55] B. Franke, J. J. Krauth, A. Antognini, M. Diepold, F. Kottmann, R. Pohl, "Theory of the n= 2 levels in muonic helium-3 ions," *arXiv preprint arXiv:1705.00352* **2017**.

[56] M. Diepold, J. J. Krauth, B. Franke, A. Antognini, F. Kottmann, R. Pohl, "Theory of the Lamb shift and fine structure in μ 4He+," *arXiv preprint arXiv:1606.0523* **2016**.

[57] S. G. Karshenboim, V. G. Ivanov, E. Y. Korzinin, "Relativistic recoil corrections to the electron-vacuum-polarization contribution in light muonic atoms," *Physical Review A* **2012**, *85*, 032509.

[58] A. Krutov, A. Martynenko, G. Martynenko, R. Faustov, "Theory of the Lamb shift in muonic helium ions," *Journal of Experimental and Theoretical Physics* **2015**, *120*, 73–90.

[59] E. Borie, "Lamb shift in light muonic atoms," *arXiv 1103.1772v7* **2014**.

[60] U. D. Jentschura, B. J. Wundt, "Semi-analytic approach to higher-order corrections in simple muonic bound systems: Vacuum polarization, self-energy and radiative-recoil," *The European Physical Journal D* **2011**, *65*, 357–366.

[61] E. Y. Korzinin, V. G. Ivanov, S. G. Karshenboim, "α 2 (Z α) 4 m contributions to the Lamb shift and the fine structure in light muonic atoms," *Physical Review D* **2013**, *88*, 125019.

[62] S. G. Karshenboim, E. Y. Korzinin, V. Ivanov, V. Shelyuto, "Contribution of light-by-light scattering to energy levels of light muonic atoms," *JETP letters* **2010**, *92*, 8–14.

[63] C. Ji, N. N. Dinur, S. Bacca, N. Barnea, "Nuclear polarization effects in muonic atoms," *Few-Body Systems* **2014**, *55*, 917–921.

[64] C. Ji, N. N. Dinur, S. Bacca, N. Barnea, "Nuclear Polarization Corrections to the μ He+ 4 Lamb Shift," *Physical review letters* **2013**, *111*, 143402.

[65] K. Pachucki, "Theory of the Lamb shift in muonic hydrogen," *Physical Review A* **1996**, *53*, 2092.

[66] G Reifenröther, E Klempt, R. Landua, "Cascade of muonic helium atoms," *Physics Letters B* **1987**, *191*, 15–20.

[67] H. Von Arb, F Dittus, H Heeb, H Hofer, F Kottmann, S Niggli, R Schaeren, D Taqqu, J Unternährer, P Egelhof, "Measurement of the lifetime and quenching rate of metastable 2S muonic helium ions," *Physics Letters B* **1984**, *136*, 232–236.

[68] R Bacher, "Decay rates of the metastable states of one-electron atoms and of the 2S-states of muonic atoms," *Zeitschrift für Physik A Hadrons and Nuclei* **1984**, *315*, 135–136.

[69] M Olivo, E Mariani, J. Sherman, "The PSI 870 keV high intensity Cockcroft–Walton preinjector," *Review of scientific instruments* **1992**, *63*, 2714–2716.

[70] P DeCecco, P Hauser, D Horváth, F Kottmann, L. Simons, D Taqqu, "A new method to produce a negative muon beam of keV energies," *Nuclear Instruments and Methods in Physics Research Section A: Accelerators Spectrometers Detectors and Associated Equipment* **1997**, *394*, 287–294.

[71] M Mühlbauer, H Daniel, F. Hartmann, P Hauser, F Kottmann, C Petitjean, W Schott, D Taqqu, P Wojciechowski, "Frictional cooling: Experimental results," *Hyperfine Interactions* **1999**, *119*, 305–310.

[72] J. Vogelsang, M. Diepold, A. Antognini, A. Dax, J. Götzfried, T. W. Hänsch, F. Kottmann, J. J. Krauth, Y.-W. Liu, T. Nebel, et al., "Multipass laser cavity for efficient transverse illumination of an elongated volume," *Optics express* **2014**, *22*, 13050–13062.

[73] L. Fernandes, F. Amaro, A Antognini, J. Cardoso, C. Conde, O. Huot, P. E. Knowles, F Kottmann, J. Lopes, L. Ludhova, et al., "Characterization of large area avalanche photodiodes in X-ray and VUV-light detection," *Journal of Instrumentation* **2007**, *2*, P08005.

[74] A. Gouvêa, Doctoral dissertation, Faculty of Sciences and Technology of the University of Coimbra, **2015**.

[75] A. Antognini, K. Schuhmann, F. D. Amaro, F. Biraben, A. Dax, A. Giesen, T. Graf, T. W. Hansch, P. Indelicato, L. Julien, et al., "Thin-disk Yb: YAG oscillator-amplifier laser, ASE, and effective Yb: YAG lifetime," *IEEE Journal of Quantum Electronics* **2009**, *45*, 993–1005.

[76] K. Schuhmann, A. Antognini, K. Kirch, T. Graf, M. A. Ahmed, A. Voss, B. Weichelt in Advanced Solid State Lasers, Optical Society of America, **2013**, ATu3A–46.

[77] T. Nebel, Doctoral dissertation, Ludwig–Maximilians–University Munich, **2010**.

[78] S Ritt, P Amaudruz, et al. in Proc. IEEE 10th Real Time Conf. **1997**, pp. 309–312.

[79] S. Ritt, P.-A. Amaudruz, "MIDAS-Maximum Integrated Data Acquisition System," *Paul Scherrer Institut and TRIUMF http://midas. triumf. ca* **2001**.

[80] R. Brun, F. Rademakers, "ROOT—an object oriented data analysis framework," *Nuclear Instruments and Methods in Physics Research Section A: Accelerators Spectrometers Detectors and Associated Equipment* **1997**, *389*, 81–86.

[81] I. Antcheva, M. Ballintijn, B. Bellenot, M. Biskup, R. Brun, N. Buncic, P. Canal, D. Casadei, O. Couet, V. Fine, et al., "ROOT—A C++ framework for petabyte data storage, statistical analysis and visualization," *Computer Physics Communications* **2009**, *180*, 2499–2512.

[82] I. Antcheva, M. Ballintijn, B. Bellenot, M. Biskup, R. Brun, N. Buncic, P. Canal, D. Casadei, O. Couet, V. Fine, et al., "ROOT—A C++ framework for petabyte data storage, statistical analysis and visualization," *Computer Physics Communications* **2011**, *182*, 1384–1385.

[83] A. Baron, S. Ruby, "Time resolved detection of X-rays using large area avalanche photodiodes," *Nuclear Instruments and Methods in Physics Research Section A: Accelerators Spectrometers Detectors and Associated Equipment* **1994**, *343*, 517–526.

[84] M. Diepold et al., "Improved x-ray detection and particle identification with avalanche photodiodes," *Review of Scientific Instruments* **2015**, *86*, 053102.

[85] M. Diepold, Doctoral dissertation, Ludwig–Maximilians–University Munich, **2015**.

[86] J. Krauth, Doctoral dissertation, Ludwig–Maximilians–University Munich, **2017**.

[87] P. Amaro et al., "Quantum interference effects in laser spectroscopy of muonic hydrogen, deuterium, and helium-3," *Physical Review A* **2015**, *92*, 022514.

[88] R. C. Brown, S. Wu, J. Porto, C. J. Sansonetti, C. Simien, S. M. Brewer, J. N. Tan, J. Gillaspy, "Quantum interference and light polarization effects in unresolvable atomic lines: Application to a precise measurement of the 6, 7 Li D 2 lines," *Physical Review A* **2013**, *87*, 032504.

[89] A. Antognini, Doctoral dissertation, Ludwig–Maximilians–University Munich, **2005**.

[90] G. Y. Korenman, V. Pomerantsev, V. Popov, "Collisional shift and broadening of the 2 p-2 s spectral lines in muonic helium ions," *Physical Review A* **2013**, *88*, 032503.

[91] R. Loudon, *The quantum theory of light*, OUP Oxford, **2000**.

[92] I. Sick, "Precise root-mean-square radius of He 4," *Physical Review C* **2008**, *77*, 041302.

[93] I. Sick, "Elastic electron scattering from light nuclei," *Progress in Particle and Nuclear Physics* **2001**, *47*, 245–318.

[94] R. D. Deslattes, E. G. Kessler Jr, P. Indelicato, L De Billy, E Lindroth, J Anton, "X-ray transition energies: new approach to a comprehensive evaluation," *Reviews of Modern Physics* **2003**, *75*, 35.

[95] R. Deslattes, P. Cowan, R. LaVilla, K Dyall in AIP Conference Proceedings, *Vol. 94*, AIP, **1982**, pp. 100–104.

[96] R. Deslattes, R. LaVilla, P. Cowan, A Henins, "Threshold studies of a multivacancy process in the K β region of argon," *Physical Review A* **1983**, *27*, 923.

[97] M Deutsch, O Gang, K Hämäläinen, C. Kao, "Onset and Near Threshold Evolution of the Cu K α X-Ray Satellites," *Physical review letters* **1996**, *76*, 2424.

[98] M Deutsch, G Hölzer, J Härtwig, J Wolf, M Fritsch, E Förster, "Kα and Kβ x-ray emission spectra of copper," *Physical Review A* **1995**, *51*, 283.

[99] M. Deutsch, E. Förster, G. Hölzer, J. Härtwig, K Hämäläinen, C.-C. Kao, S Huotari, R Diamant, "X-ray spectrometry of copper: new results on an old subject," *Journal of research of the National Institute of Standards and Technology* **2004**, *109*, 75.

[100] G Hölzer, M Fritsch, M Deutsch, J Härtwig, E Förster, "K α 1, 2 and K β 1, 3 x-ray emission lines of the 3 d transition metals," *Physical Review A* **1997**, *56*, 4554.

[101] D. F. Anagnostopoulos, D Gotta, P Indelicato, L. M. Simons, "Low-Energy X-Ray Standards from Hydrogenlike Pionic Atoms," *Physical Review Letters* **2003**, *91*, 79.

[102] D. F. Anagnostopoulos et al., "On the characterisation of a Bragg spectrometer with X-rays from an ECR source," *Nuclear Instruments and Methods in Physics Research Section A: Accelerators Spectrometers Detectors and Associated Equipment* **2005**, *545*, 217–224.

[103] D. F. Anagnostopoulos et al., "Highly charged ions in exotic atoms research at PSI," *Nuclear Instruments and Methods in Physics Research Section B: Beam Interactions with Materials and Atoms* **2003**, *205*, 9–14.

[104] G Douysset, H Khodja, A Girard, J. Briand, "Highly charged ion densities and ion confinement properties in an electron-cyclotron-resonance ion source," *Physical Review E* **2000**, *61*, 3015.

[105] P. Indelicato, E.-O. Le Bigot, M. Trassinelli, D. Gotta, M. Hennebach, N. Nelms, C. David, L. M. Simons, "Characterization of a charge-coupled device array for Bragg spectroscopy," *Review of scientific instruments* **2006**, *77*, 043107.

[106] P Indelicato et al., "Highly charged ion X-rays from Electron–Cyclotron Resonance Ion Sources," *Nuclear Instruments and Methods in Physics Research Section A: Accelerators Spectrometers Detectors and Associated Equipment* **2007**, *580*, 8–13.

[107] E. Le Bigot, S. Boucard, D. Covita, D. Gotta, A Gruber, A. Hirtl, H Fuhrmann, P. Indelicato, J. dos Santos, S Schlesser, et al., "High-precision x-ray spectroscopy in few-electron ions," *Physica Scripta* **2009**, *2009*, 014015.

[108] M. C. Martins, J. P. Marques, A. M. Costa, J. P. Santos, F. Parente, S. Schlesser, E.-O. Le Bigot, P. Indelicato, "Production and decay of sulfur excited species in an electron-cyclotron-resonance ion-source plasma," *Physical Review A* **2009**, *80*, 032501.

[109] J. P. Santos, M. C. MARTINS, A. M. COSTA, P Indelicato, F PARENTE, "X-ray spectra emitted by Cl14+ ions in ECRIS plasmas," *Vacuum* **2008**, *82*, 1522–1524.

[110] J. P. Santos, A. M. COSTA, J. P. Marques, M. C. MARTINS, P Indelicato, F PARENTE, "X-ray-spectroscopy analysis of electron-cyclotron-resonance ion-source plasmas," *Physical Review A* **2010**, *82*, 062516.

[111] J. P. Santos, M. C. MARTINS, A. M. COSTA, J. P. Marques, P Indelicato, F PARENTE, "Production and decay of chlorine ion excited species in an electron cyclotron resonance ion source plasma," *Physica Scripta* **2011**, *T144*, 014005.

[112] C. Chantler, J. Kimpton, "Recent developments in X-ray tests of quantum electrodynamics This paper was presented at the International Conference on Precision Physics of Simple Atomic Systems, held at University of Windsor, Windsor, Ontario, Canada on 21–26 July 2008.," *Canadian Journal of Physics* **2009**, *87*, 763–772.

[113] G. Plunien, B. Müller, W. Greiner, G. Soff, "Nuclear polarization in heavy atoms and superheavy quasiatoms," *Physical Review A* **1991**, *43*, 5853.

[114] G. Plunien, G. Soff, "Nuclear-polarization contribution to the Lamb shift in actinide nuclei," *Physical Review A* **1995**, *51*, 1119.

[115] G. Plunien, G. Soff, "Erratum: Nuclear-polarization contribution to the Lamb shift in actinide nuclei," *Physical Review A* **1996**, *53*, 4614.

[116] T Beier, P. Mohr, H Persson, G Soff, "Influence of nuclear size on QED corrections in hydrogenlike heavy ions," *Physical Review A* **1998**, *58*, 954.

[117] K. Eikema, W Ubachs, W Vassen, W Hogervorst, "Precision Measurements in Helium at 58 nm: Ground State Lamb Shift and the 1 1 S-2 1 P Transition Isotope Shift," *Physical review letters* **1996**, *76*, 1216.

[118] K. Eikema, W Ubachs, W Vassen, W Hogervorst, "Lamb shift measurement in the 1 t 1 S ground state of helium," *Physical Review A* **1997**, *55*, 1866.

[119] D. Z. Kandula, C. Gohle, T. J. Pinkert, W. Ubachs, K. S. Eikema, "XUV frequency-comb metrology on the ground state of helium," *Physical Review A* **2011**, *84*, 062512.

[120] K. Pachucki, "Effective Hamiltonian approach to the bound state: energy of helium-states in the order," *Journal of Physics B: Atomic Molecular and Optical Physics* **1998**, *31*, 2489.

[121] K. Pachucki, "Quantum electrodynamics effects on singlet S-states of helium of order," *Journal of Physics B: Atomic Molecular and Optical Physics* **1998**, *31*, 3547.

[122] K. Pachucki, "α 4 R corrections to singlet states of helium," *Physical Review A* **2006**, *74*, 022512.

[123] K. Pachucki, "Helium energy levels including m α 6 corrections," *Physical Review A* **2006**, *74*, 062510.

[124] V. A. Yerokhin, K. Pachucki, "Theoretical energies of low-lying states of light helium-like ions," *Physical Review A* **2010**, *81*, 022507.

[125] A. N. Artemyev, V. M. Shabaev, V. A. Yerokhin, G Plunien, G Soff, "QED calculation of the n=1and n=2energy levels in He-like ions," *Physical Review A* **2005**, *71*, 062104.

[126] I Angeli, K. Marinova, "Table of experimental nuclear ground state charge radii: An update," *Atomic Data and Nuclear Data Tables* **2013**, *99*, 69–95.

[127] E. Aglitskii, V. Boiko, S. Zakharov, S. A. Pikuz, A. Y. Faenov, "Observation in laser plasmas and identification of dielectron satellites of spectral lines of hydrogen-and helium-like ions of elements in the Na–V range," *Soviet Journal of Quantum Electronics* **1974**, *4*, 500.

[128] H. Dohmann, R Mann, "Measurement of the lifetime of the 3 P 2 and 4 P 5/2 states in Ar 16+ and Ar 15+," *Zeitschrift für Physik A Hadrons and Nuclei* **1979**, *291*, 15–22.

[129] J. Briand, J. Mosse, P Indelicato, P Chevallier, D Girard-Vernhet, A Chetioui, M. Ramos, J. Desclaux, "Spectroscopy of hydrogenlike and heliumlike argon," *Physical Review A* **1983**, *28*, 1413.

[130] T. Stöhlker, P. Mokler, K Beckert, F Bosch, H Eickhoff, B Franzke, H Geissel, M Jung, T Kandler, O Klepper, et al., "X-ray emission from very-heavy H-and He-like ions in collisions with gaseous and solid targets," *Nuclear Instruments and Methods in Physics Research Section B: Beam Interactions with Materials and Atoms* **1994**, *87*, 64–69.

[131] T. Stöhlker, P. Mokler, F Bosch, R. Dunford, F Franzke, O Klepper, C Kozhuharov, T Ludziejewski, F Nolden, H Reich, et al., "1 s Lamb Shift in Hydrogenlike Uranium Measured on Cooled, Decelerated Ion Beams," *Physical review letters* **2000**, *85*, 3109.

[132] A. Gumberidze, T. Stöhlker, D Banaś, K Beckert, P Beller, H. Beyer, F Bosch, S Hagmann, C Kozhuharov, D Liesen, et al., "Quantum electrodynamics in strong electric fields: the ground-state lamb shift in hydrogenlike uranium," *Physical review letters* **2005**, *94*, 223001.

[133] R. Deslattes, H. Beyer, F Folkmann, "Precision X-ray wavelength measurements in helium-like argon recoil ions," *Journal of Physics B: Atomic and Molecular Physics* **1984**, *17*, L689.

[134] H. Beyer, P Indelicato, K. Finlayson, D Liesen, R. Deslattes, "Measurement of the 1s Lamb shift in hydrogenlike nickel," *Physical Review A* **1991**, *43*, 223.

[135] K Kubiček, J Braun, H Bruhns, J. R. Crespo López-Urrutia, P. H. Mokler, J Ullrich, "High-precision laser-assisted absolute determination of x-ray diffraction angles," *Review of Scientific Instruments* **2012**, *83*, 013102.

[136] P Beiersdorfer, M. Chen, R. Marrs, M. Schneider, R. Walling, "Dielectronic satellite spectrum of heliumlike vanadium," *Physical Review A* **1991**, *44*, 396.

[137] P Beiersdorfer, T Phillips, V. Jacobs, K. Hill, M Bitter, S Von Goeler, S. Kahn, "High-resolution measurements, line identification, and spectral modeling of K-alpha transitions in Fe XVIII-Fe XXV," *The Astrophysical Journal* **1993**, *409*, 846–859.

[138] S Schlesser et al., "High-accuracy x-ray line standards in the 3-keV region," *Physical Review A* **2013**, *88*, 022503.

[139] D. B. Thorn, M. F. Gu, G. V. Brown, P. Beiersdorfer, F. S. Porter, C. A. Kilbourne, R. L. Kelley, "Precision measurement of the K-shell spectrum from highly charged xenon with an array of x-ray calorimeters," *Physical review letters* **2009**, *103*, 163001.

[140] R. D. Deslattes, "Single Axis, Two Crystal X-Ray Instrument," *Review of Scientific instruments* **1967**, *38*, 815–820.

[141] P Amaro et al., "A vacuum double-crystal spectrometer for reference-free X-ray spectroscopy of highly charged ions," *Radiation Physics and Chemistry* **2014**, *98*, 132–149.

[142] D. Camarillo-Ravelo, V. Kaftandjian, P. Duvauchelle, "Accurate standard-based quantification of X-ray fluorescence data using metal-contaminated plant tissue," *X-Ray Spectrometry* **2010**, *39*, 391–398.

[143] S. C.P.-L. Santos, M. E. Cruz, A. M. Barroso, C. P. Fonseca, M. Guerra, M. L. Carvalho, J. P. Santos, "Elemental characterization of plants and soils in Panasqueira tungsten mining region," *Journal of soils and sediments* **2014**, *14*, 778–784.

[144] C. S. Schnohr, M. C. Ridgway, *Introduction to X-Ray Absorption Spectroscopy*, Springer, **2015**, pp. 1–26.

[145] D. Guimarães, M. L. Carvalho, V. Geraldes, I. Rocha, L. C. Alves, J. P. Santos, "Lead in liver and kidney of exposed rats: Aging accumulation study," *Journal of Trace Elements in Medicine and Biology* **2012**, *26*, 285–290.

[146] E. Bulbul, M. Markevitch, A. Foster, R. K. Smith, M. Loewenstein, S. W. Randall, "Detection of an unidentified emission line in the stacked X-ray spectrum of galaxy clusters," *The Astrophysical Journal* **2014**, *789*, 13.

[147] A. Boyarsky, O. Ruchayskiy, D. Iakubovskyi, J. Franse, "Unidentified line in X-ray spectra of the Andromeda galaxy and Perseus galaxy cluster," *Physical Review Letters* **2014**, *113*, 251301.

[148] C. Shah, S. Dobrodey, S. Bernitt, R. Steinbrügge, J. R. C. López-Urrutia, L. Gu, J. Kaastra, "LABORATORY MEASUREMENTS COMPELLINGLY SUPPORT A CHARGE-EXCHANGE MECHANISM FOR THE "DARK MATTER" 3.5 keV X-Ray LINE," *The Astrophysical Journal* **2016**, *833*, 52.

[149] P Amaro, Doctoral dissertation, New University of Lisbon, University Pierre, and Marie Currie, **2012**.

[150] W. C. Röntgen, "On a new kind of rays," *Science* **1896**, *3*, 227–231.

[151] C. G. Barkla, "Ionisation by Röntgen Rays," *Nature* **1909**, *80*, 187–187.

[152] C. G.B. M. D.Sc., "XXXIX. The spectra of the fluorescent Röntgen radiations," *Philosophical Magazine* **1911**, *22*, 396–412.

[153] W Friedrich, P Knipping, M. Laue, "Interference phenomena with Röntgen rays," *Sitzber. Math-phys. Kl. bayer. Akad. Wiss. Manche* **1912**, *22*, 303.

[154] W. L. Bragg, "The specular reflection of X-rays," *Nature* **1912**, *90*, 410.

[155] W. Bragg, "Bakerian lecture: X-rays and crystal structure," *Philosophical Transactions of the Royal Society of London. Series A Containing Papers of a Mathematical or Physical Character* **1915**, *215*, 253–274.

[156] A. Compton, "The reflection coefficient of monochromatic X-rays from rock salt and calcite," *Phys. Rev* **1917**, *10*, 95.

[157] W. L. Bragg, R. W. James, C. Bosanquet, "XXIX. The intensity of reflexion of X-rays by rock-salt," *The London Edinburgh and Dublin Philosophical Magazine and Journal of Science* **1921**, *41*, 309–337.

[158] E. Wagner, H Kulenkampff, "Die Intensität der Reflexion von Röntgenstrahlen verschiedener Wellenlänge an Kalkspat und Steinsalz," *Annalen der Physik* **1922**, *373*, 369–413.

[159] B. Davis, W. Stempel, "An experimental study of the reflection of X-rays from calcite," *Physical Review* **1921**, *17*, 608.

[160] B. Davis, H. Purks, "Measurement of the Mo. K doublet distances by means of the double X-ray spectrometer," *Proceedings of the National Academy of Sciences* **1927**, *13*, 419–422.

[161] B. Davis, H. Purks, "Additional lines in the K series of molybdenum and the natural breadth of spectral lines," *Proceedings of the National Academy of Sciences* **1928**, *14*, 172–178.

[162] S. K. Allison, "The Natural Widths of the K α X-Ray Doublet from 26FE to 47AG," *Physical Review* **1933**, *44*, 63.

[163] S. K. Allison, J. H. Williams, "The Resolving Power of Calcite for X-Rays and the Natural Widths of the Molybdenum K α Doublet," *Physical Review* **1930**, *35*, 1476.

[164] J. H. Williams, "A correction to wave-length measurements with the double-crystal spectrometer," *Physical Review* **1932**, *40*, 636.

[165] J. Bearden, "Absolute wave-lengths of the copper and chromium K-series," *Physical Review* **1931**, *37*, 1210.

[166] J. Bearden, "Status of X-ray wavelengths in minutes of the new haven meeting, June 23–25, 1932," *Phys. Rev* **1932**, *41*, 399.

[167] J. Bearden, "The grating constant of calcite crystals," *Physical Review* **1931**, *38*, 2089.

[168] A. H. Compton, "A PRECISION X-RAY SPECTROMETER AND THE WAVE LENGTH OF Mo Kα1," *Review of Scientific Instruments* **1931**, *2*, 365–376.

[169] J. Williams, S. Allison, "Design of a Double X-ray Spectrometer," *JOSA* **1929**, *18*, 473–478.

[170] M. Schwarzschild, "Theory of the double X-ray spectrometer," *Physical Review* **1928**, *32*, 162.

[171] R. James, G Bell, "THE OPTICAL PRINCIPLES," *G. Bell and sons Ltd London* **1948**.

[172] U Bonse, M Hart, "An X-ray interferometer," *Applied Physics Letters* **1965**, *6*, 155–156.

[173] R. D. Deslattes, A. Henins, "X-ray to visible wavelength ratios," *Physical Review Letters* **1973**, *31*, 972.

[174] L. Ferroglio, G. Mana, E. Massa, "Si lattice parameter measurement by centimeter x-ray interferometry," *Optics express* **2008**, *16*, 16877–16888.

[175] E Massa, G Mana, U Kuetgens, "Comparison of the INRIM and PTB lattice-spacing standards," *Metrologia* **2009**, *46*, 249.

[176] E Massa, G Mana, U Kuetgens, L. Ferroglio, "Measurement of the lattice parameter of a silicon crystal," *New Journal of Physics* **2009**, *11*, 053013.

[177] J Schweppe, R. Deslattes, T Mooney, C. Powell, "Accurate measurement of Mg and Al Kα1, 2 X-ray energy profiles," *Journal of electron spectroscopy and related phenomena* **1994**, *67*, 463–478.

[178] E. Kessler Jr, R. Deslattes, D Girard, W Schwitz, L Jacobs, O Renner, "Mid-to-high-Z precision x-ray measurements," *Physical Review A* **1982**, *26*, 2696.

[179] J Consolino, R Geller, C Lerot in 1st Int'l. Conf. on Ion Sources (Saclay), **1969**, p. 537.

[180] H Postma, "Multiply charged heavy ions produced by energetic plasmas," *Physics Letters A* **1970**, *31*, 196–197.

[181] P Apard, S Bliman, R Geller, B Jacquot, C Jacquot in 2nd Int'l. Conf. on Ion Sources (Wien), **1971**, p. 632.

[182] G Melin et al., "Status of development of ECR ion sources at Grenoble (invited)," *Review of Scientific Instruments* **1994**, *65*, 1051–1056.

[183] R Geller, "Electron cyclotron resonance sources: Historical review and future prospects (invited)," *Review of Scientific Instruments* **1998**, *69*, 1302.

[184] A. G. Drentje, "Review of the Eleventh International Workshop on ECR ion sources (invited)," *Review of Scientific Instruments* **1994**, *65*, 1045–1050.

[185] C. M. Lyneis, T. A. Antaya, "ERC sources for the production of highly charged ions (invited)," *Review of Scientific Instruments* **1990**, *61*, 221–224.

[186] R Geller, "ECRIS: The Electron Cyclotron Resonance Ion Sources," *Annual Review of Nuclear and Particle Science* **1990**, *40*, 15–43.

[187] C Bieth, J. L. Bouly, J. C. Curdy, S Kantas, P Sortais, P Sole, J. L. Vieux-Rochaz, "Electron cyclotron resonance ion source for high currents of mono- and multicharged ion and general purpose unlimited lifetime application on implantation devices," *Review of Scientific Instruments* **2000**, *71*, 899–901.

[188] A Gumberidze et al., "Electronic temperatures, densities, and plasma x-ray emission of a 14.5 GHz electron-cyclotron resonance ion source," *Review of Scientific Instruments* **2010**, *81*, 033303.

[189] A Gumberidze, D Attia, C. I. Szabo, P Indelicato, A Vallette, S Carmo, "Trapping of highly charged ions with an electrostatic ion trap," *Journal of Physics: Conference Series* **2009**, *163*, 012110.

[190] M. Guerra, Doctoral dissertation, New University of Lisbon, **2013**.

[191] C. I. Szabo, P Amaro, M Guerra, J. P. Santos, A Gumberidze, J Attard, P Indelicato, "Ion temperature and x-ray line width measurements of highly charged argon ions in an ECR ion source," *Physica Scripta* **2013**, *T156*, 014077.

[192] C. I. Szabo, P. Indelicato, E.-O. LeBigot, A. Vallette, P. Amaro, M. Guerra, A. Gumberidze in THE 17TH INTERNATIONAL CONFERENCE ON ATOMIC PROCESSES IN PLASMAS (ICAPIP), AIP, pp. 236–239.

[193] C. I. Szabo, P. Amaro, M. Guerra, S. Schlesser, A. Gumberidze, J. P. Santos, P. Indelicato in APPLICATION OF ACCELERATORS IN RESEARCH AND INDUSTRY: Twenty-Second International Conference, AIP, **2013**, pp. 68–72.

[194] M Trassinelli et al., "Suppression of the thermal hysteresis in magnetocaloric MnAs thin film by highly charged ion bombardment," *Applied Physics Letters* **2014**, *104*, 081906.

[195] M Trassinelli et al., "Magnetic properties of MnAs thin films irradiated with highly charged ions," *Nuclear Inst. and Methods in Physics Research B* **2013**, *317*, 154–158.

[196] M Trassinelli et al., "Low energy Ne ion beam induced-modifications of magnetic properties in MnAs thin films," *Journal of Physics: Condensed Matter* **2016**, *29*, 055001.

[197] J Machado, C. I. Szabo, J. P., Santos, P Amaro, M Guerra, A Gumberidze, B Guojie, J. M. Isac, P Indelicato, "High-precision measurements of n = 2 $\rightarrow$ n = 1 transition energies and level widths in He- and Be-like Argon Ions," *submitted* **2017**.

[198] H. F. Beyer, H. J. Kluge, V. P. Shevelko, X-Ray Radiation of Highly Charged Ions, Springer Berlin Heidelberg, Berlin, Heidelberg, **1997**.

[199] J Arianer, R Geller, "The Advanced Positive Heavy Ion Sources," *Annual Review of Nuclear and Particle Science* **1981**, *31*, 19–51.

[200] D Leitner, C. Lyneis, S. Abbott, D Collins, R. Dwinell, M. Galloway, M Leitner, D. Todd, "Next generation ECR ion sources: First results of the superconducting 28GHz ECRIS–VENUS," *Nuclear Instruments and Methods in Physics Research Section B: Beam Interactions with Materials and Atoms* **2005**, *235*, 486–493.

[201] S Gammino, G Ciavola, L Celona, D Hitz, A Girard, G Melin, "Operation of the SERSE superconducting electron cyclotron resonance ion source at 28 GHz," *Review of Scientific Instruments* **2001**, *72*, 4090–4097.

[202] S Biri, L Simons, D Hitz, "Electron cyclotron resonance ion trap: A hybrid magnetic system with very high mirror ratio for highly charged ion production and trapping," *Review of Scientific Instruments* **2000**, *71*, 1116–1118.

[203] I. H. Hutchinson, "Principles of plasma diagnostics," *Plasma Physics and Controlled Fusion* **2002**, *44*, 2603.

[204] M Guerra, P Amaro, C. I. Szabo, A Gumberidze, P Indelicato, J. P. Santos, "Analysis of the charge state distribution in an ECRIS Ar plasma using high-resolution x-ray spectra," *Journal of Physics B: Atomic Molecular and Optical Physics* **2013**, *46*, 065701.

[205] J. P. Santos, A. M. COSTA, J. P. Marques, M. C. MARTINS, P Indelicato, F PARENTE, "X-ray-spectroscopy analysis of electron-cyclotron-resonance ion-source plasmas," *Physical Review A* **2010**, *82*, 062516.

[206] A. M. COSTA, M. C. MARTINS, F PARENTE, J. P. Santos, P Indelicato, "Dirac-Fock transition energies and radiative and radiationless transition probabilities for Ar9+ to Ar16+ ion levels with K-shell holes," *Atomic Data and Nuclear Data Tables* **2001**, *79*, 223–239.

[207] M. C. MARTINS, J. P. Marques, A. M. COSTA, J. P. Santos, F PARENTE, S Schlesser, E. O. Le Bigot, P Indelicato, "Production and decay of sulfur excited species in an electron-cyclotron-resonance ion-source plasma," *Physical Review A* **2009**, *80*, 032501.

[208] M. C. MARTINS, A. M. COSTA, J. P. Santos, P Indelicato, F PARENTE, "Interpretation of x-ray spectra emitted by Ar ions in an electron-cyclotron resonance ion source," *Journal of Physics B: Atomic Molecular and Optical Physics* **2001**, *34*, 533–543.

[209] S. Schlesser, Doctoral dissertation, **2009**.

[210] H Fujimoto, A Waseda, X. Zhang, "Homogeneity characterization of lattice spacing of silicon single crystals by a self-referenced lattice comparator," *Metrologia* **2011**, *48*, S55.

[211] B. Andreas, Y Azuma, G Bartl, P Becker, H Bettin, M Borys, I Busch, M Gray, P Fuchs, K Fujii, et al., "Determination of the Avogadro Constant by Counting the Atoms in a Si 28 Crystal," *Physical review letters* **2011**, *106*, 030801.

[212] K. Fujii, A. Waseda, N. Kuramoto, S. Mizushima, P. Becker, H. Bettin, A. Nicolaus, U. Kuetgens, S. Valkiers, P. Taylor, et al., "Present state of the Avogadro constant determination from silicon crystals with natural isotopic compositions," *IEEE transactions on instrumentation and measurement* **2005**, *54*, 854–859.

[213] E. G. Kessler, S. M. Owens, A. Henins, R. D. Deslattes, "Silicon lattice comparisons related to the Avogadro project: uniformity of new material and surface preparation effects," *IEEE Transactions on Instrumentation and Measurement* **1999**, *48*, 221–224.

[214] E Massa, G Mana, L Ferroglio, E. Kessler, D Schiel, S Zakel, "The lattice parameter of the 28Si spheres in the determination of the Avogadro constant," *Metrologia* **2011**, *48*, S44.

[215] R Schödel, M Matus, R. Yang, F. Pollinger, K. Meiners-Hagen, M. Krystek, J. Tan, H. Bosse, "Recent developments in traceable dimensional measurements," *Measurement Science and Technology* **2015**, *26*, 80401–80401.

[216] H. McSkimin, "Measurement of elastic constants at low temperatures by means of ultrasonic waves–data for silicon and germanium single crystals, and for fused silica," *Journal of applied physics* **1953**, *24*, 988–997.

[217] M. S. Del Rio, R. J. Dejus in SPIE proceedings, *Vol. 3448*, **1998**, pp. 340–345.

[218] M. S. del Río, R. J. Dejus in AIP Conference Proceedings, *Vol. 705*, AIP, **2004**, pp. 784–787.

[219] M. S. del Rio, R. J. Dejus in Proc. SPIE, *Vol. 5536*, **2004**, pp. 171–174.

[220] W. H. Zachariasen, *Theory of X-ray Diffraction in Crystals*, Courier Corporation, **2004**.

[221] E. Gullikson, E Gramsch, M Szawlowski, "Large-area avalanche photodiodes for the detection of soft x rays," *Applied optics* **1995**, *34*, 4662–4668.

[222] J. Pansart, "Avalanche photodiodes for particle detection," *Nuclear Instruments and Methods in Physics Research Section A: Accelerators Spectrometers Detectors and Associated Equipment* **1997**, *387*, 186–193.

[223] L. M. P. Fernandes, J. A. M. Lopes, J. M. F. dos Santos, C. A. N. Conde, "Application of large-area avalanche photodiodes to energy-dispersive x-ray fluorescence analysis," *X-Ray Spectrom.* **2001**, *30*, 164–169.

[224] J. M. Paros, W Weinstein, *How to design flexure hinges*, Int. J. Machine Design, **1965**.

[225] J. Bearden, J. Thomsen, "The double-crystal X-ray spectrometer: corrections, errors, and alignment procedure," *Journal of Applied Crystallography* **1971**, *4*, 130–138.

[226] O. Lugovskaya, S. Stepanov, "Calculation of the polarizabilities of crystals for diffraction of x-ray on the continuous spectrum at wavelengths of 0.1-10 Å," *Soviet physics. Crystallography* **1991**, *36*, 478–481.

[227] J. J. Moré in *Numerical analysis*, Springer, **1978**, pp. 105–116.

[228] B. Gough, *GNU scientific library reference manual*, Network Theory Ltd., **2009**.

[229] W. H. Press, *Numerical recipes 3rd edition: The art of scientific computing*, Cambridge university press, **2007**.

[230] S Wolfram, "Mathematica Version 11.0," *Champaign: Wolfram Research Inc* **2016**.

[231] V. A. Yerokhin, A Surzhykov, S Fritzsche, "Relativistic configuration-interaction calculation of K α transition energies in beryllium-like argon," *Physica Scripta* **2015**, *90*, 054003.

[232] S Biri, A Valek, T Suta, E Takacs, C. Szabó, L. T. Hudson, B Radics, J Imrek, B Juhász, J Pálinkás, "Imaging of ECR plasmas with a pinhole x-ray camera," *Review of Scientific Instruments* **2004**, *75*, 1420–1422.

[233] D Waasmaier, A Kirfel, "New analytical scattering-factor functions for free atoms and ions," *Acta Cryst (1995). A51 416-431 [doi:10.1107/S0108767394013292]* **1995**, 1–16.

[234] L. Kissel, "RTAB: the Rayleigh scattering database," *Radiation Physics and Chemistry* **2000**, *59*, 185–200.

[235] B. L. Henke, E. M. Gullikson, J. C. Davis, "X-Ray Interactions: Photoabsorption, Scattering, Transmission, and Reflection at E = 50-30,000 eV, Z = 1-92," *Atomic Data and Nuclear Data Tables* **1993**, *54*, 181–342.

[236] C. T. Chantler, "Detailed Tabulation of Atomic Form Factors, Photoelectric Absorption and Scattering Cross Section, and Mass Attenuation Coefficients in the Vicinity of Absorption Edges in the Soft X-Ray (Z=30–36, Z=60–89, E=0.1 keV–10 keV), Addressing Convergence Issues of Earlier Work," *Journal of Physical and Chemical Reference Data* **2000**, *29*, 597–1056.

[237] C. T. Chantler, "Theoretical Form Factor, Attenuation, and Scattering Tabulation for Z=1–92 from E=1–10 eV to E=0.4–1.0 MeV," *Journal of Physical and Chemical Reference Data* **1995**, *24*, 71–643.

[238] B. L. Henke, E. M. Gullikson, J. C. Davis, "X-ray interactions: photoabsorption, scattering, transmission, and reflection at E= 50-30,000 eV, Z= 1-92," *Atomic data and nuclear data tables* **1993**, *54*, 181–342.

[239] S Brennan, P. Cowan, "A suite of programs for calculating x-ray absorption, reflection, and diffraction performance for a variety of materials at arbitrary wavelengths," *Review of scientific instruments* **1992**, *63*, 850–853.

[240] J. P. Desclaux, "A Multiconfiguration Relativistic Dirac-Fock Program," *Comp. Phys. Commun.* **1975**, *9*, 31–45.

[241] P Indelicato, J. P. Desclaux, "Multiconfiguration Dirac-Fock Calculations of Transition Energies with Qed Corrections in Three-Electron Ions," *Physical Review A* **1990**, *42*, 5139–5149.

[242] P Indelicato, O Gorceix, J. P. Desclaux, "MCDF studies of two electron ions II: Radiative corrections and comparison with experiment.," *Journal of Physics B: Atomic Molecular and Optical Physics* **1987**, *20*, 651–663.

[243] P Indelicato, J. P. Desclaux, *Mcdfgme, a multiconfiguration dirac fock and general matrix elements program (release 2005)*, URL http://dirac. spectro. jussieu. fr/mcdf, **2005**.

[244] G. W. F. Drake, "Unified relativistic theory for 1s2p 3P1-1s2 1S0 and 1s2p 3P1-1s2 1S0 frequencies and transition rates in heliumlike ions," *Physical Review A* **1979**, *19*, 1387–1397.

[245] W. R. Johnson, D. R. Plante, J Sapirstein in *Advances in Atomic, Molecular and Optical Physics*, (Eds.: B Bederson, H Walters), Addison-Wesley, New York, **1995**, pp. 255–329.

[246] J. Machado, C. I. Szabo, J. P. Santos, P. Amaro, M. Guerra, A. Gumberidze, G. Bian, J. M. Isac, P. Indelicato, "High-precision measurements of $n = 2 \rightarrow n = 1$ transition energies and level widths in He- and Be-like Argon Ions," *Submitted* **2017**.

[247] W. M. Neupert, "Satellite lines in the solar x-ray spectrum," *Solar Physics* **1971**, *18*, 474–488.

[248] D. Plante, W. Johnson, J Sapirstein, "Relativistic all-order many-body calculations of the n= 1 and n= 2 states of heliumlike ions," *Physical Review A* **1994**, *49*, 3519.

[249] K. T. Cheng, M. H. Chen, W. R. Johnson, J Sapirstein, "Relativistic configuration-interaction calculations for the ground state and n=2 singlet states of heliumlike ions," *Physical Review A* **1994**, *50*, 247–255.

[250] G. W. Drake, "Theoretical energies for the n= 1 and 2 states of the helium isoelectronic sequence up to Z= 100," *Canadian Journal of Physics* **1988**, *66*, 586–611.

[251] U. I. Safronova, "Relativistic and Radiative Effects in He-like Ions," *Physica Scripta* **1981**, *23*, 241–248.

[252] W. Johnson, J Sapirstein, "Relativistic many-body perturbation theory applied to n= 2 triplet states of heliumlike ions," *Physical Review A* **1992**, *46*, R2197.

[253] A. H. Gabriel, "Dielectronic Satellite Spectra for Highly-Charged Helium-Like Ion Lines," *Monthly Notices of the Royal Astronomical Society* **1972**, *160*, 99–119.

[254] L Engstrom, U Litzen, "High-precision wavelength measurements of the 1s 2 1 S-1snp 1 P resonance lines in He-like nitrogen and oxygen," *Journal of Physics B: Atomic Molecular and Optical Physics* **1995**, *28*, 2565–2574.

[255] E. Aglitsky, P. Antsiferov, S. Mandelstam, A. Panin, U. Safronova, S. Ulitin, L. Vainshtein, "Comparison of calculated and measured wavelengths of resonance transitions in He-like ions for Z= 16-39," *Physica scripta* **1988**, *38*, 136.

[256] L Schleinkofer, F Bell, H. D. Betz, G Trolman, J Rothermel, "Precision Wavelength Determination of 2 1P1-1 1S0 and 2 3P1-1 1S0 transitions in heliumlike sulfur," *Physica Scripta* **1982**, *25*, 917–923.

[257] H. D. Dohmann, D Liesen, H Pfeng, "High resolution spectroscopy of prompt and metastable decaying levels in highly ionized argon, especially of the metastable³P₂-state of Ar¹⁶⁺ and the⁴P_{5/2}-state of Ar<sup>15+</sup&gt," *Zeitschrift für Physik A Hadrons and Nuclei* **1978**, *285*, 171–176.

[258] P Beiersdorfer, M Bitter, S von Goeler, K. W. Will, "Experimental study of the x-ray transitions in the heliumlike isoelectronic sequence," *Physical Review A* **1989**, *40*, 150–157.

[259] J. E. Rice et al., "X-ray observations of Ca 19 + , Ca 18 + and satellites from Alcator C-Mod tokamak plasmas," *Journal of Physics B: Atomic Molecular and Optical Physics* **2014**, *47*, 075701.

[260] J. E. Rice, M. A. Graf, J. L. Terry, E. S. Marmar, K Giesing, F Bombarda, "X-ray observations of helium-like scandium from the Alcator C-Mod tokamak," *Journal of Physics B: Atomic Molecular and Optical Physics* **1995**, *28*, 893–905.

[261] C. T. Chantler, D Paterson, L. T. Hudson, F. G. Serpa, J. D. Gillaspy, E Takacs, "Absolute measurement of the resonance lines in heliumlike vanadium on an electron-beam ion trap," *Physical Review A* **2000**, *62*, 042501–1–13.

[262] J. P. Briand, M Tavernier, R Marrus, J. P. Desclaux, "High-precision spectroscopic study of heliumlike iron," *Physical Review A* **1984**, *29*, 3143–3149.

[263] S MacLaren, P Beiersdorfer, D. A. Vogel, D Knapp, R. E. Marrs, K Wong, R Zasadzinski, "Precision measurement of Ka transitions in heliumlike Ge30+," *Physical Review A* **1992**, *45*, 329–332.

[264] P Indelicato, M Tavernier, J. P. Briand, D Liesen, "Experimental study of relativistic correlations and QED effects in Heliumlike Krypton ions.," *Zeitschrift für Physik D* **1986**, *2*, 249–250.

[265] K Widmann, P Beiersdorfer, V Decaux, M Bitter, "Measurements of the $K\alpha$ transition energies of heliumlike krypton," *Physical Review A* **1996**, *53*, 2200–2205.

[266] J. P. Briand, P Indelicato, A Simionovici, V San Vicente, D Liesen, D Dietrich, "Spectroscopic study of hydrogenlike and heliumlike xenon ions.," *Europhysics Letters* **1989**, *9*, 225–230.

[267] K. Widmann, P. Beiersdorfer, G. V. Brown, J. R. C. López-Urrutia, A. L. Osterheld, K. J. Reed, J. H. Scofield, S. B. Utter in AIP Conference Proceedings, *Vol. 506*, AIP, **2000**, pp. 444–466.

[268] D. B. Thorn, G. V. Brown, J. H. T. Clementson, H Chen, M Chen, P Beiersdorfer, K. R. Boyce, C. A. Kilbourne, F. S. Porter, R. L. Kelley, "High-resolution spectroscopy of K-shell praseodymium with a high-energy microcalorimeter," *Canadian Journal of Physics* **2008**, *86*, 241–244.

[269] J. P. Briand, P Chevallier, P Indelicato, D Dietrich, K Ziock, "Observation and Measurement of n=2⟶n=1 Transitions of Hydrogenlike and Heliumlike Uranium," *Physical Review Letters* **1990**, *65*, 2761–2764.

[270] J. H. Lupton, D. D. Dietrich, C. J. Hailey, R. E. Stewart, K. P. Ziock, "Measurements of the ground-state Lamb shift and electron-correlation effects in hydrogenlike and heliumlike uranium," *Physical Review A* **1994**, *50*, 2150.

[271] T. F. R. Group, F Bombarda, F Bely-Dubau, P Faucher, M Cornille, J Dubau, M Loulergue, "Dielectronic satellite spectrum of heliumlike argon: A contribution to the physics of highly charged ions and plasma impurity transport," *Physical Review A* **1985**, *32*, 2374–2383.

[272] M Bitter et al., "Satellite spectra for heliumlike titanium. II," *Physical Review A* **1985**, *32*, 3011–3029.

[273] H Hsuan et al., "Satellite spectra of heliumlike nickel," *Physical Review A* **1987**, *35*, 4280–4285.

[274] J. E. Rice, M. L. Reinke, J. M. A. Ashbourn, C Gao, M Bitter, L Delgado-Aparicio, K Hill, N. T. Howard, J. W. Hughes, U. I. Safronova, "X-ray observations of medium Z H- and He-like ions with satellites from C-Mod tokamak plasmas," *Journal of Physics B: Atomic Molecular and Optical Physics* **2015**, *48*, 144013.

[275] T. F. R. Group, M Cornille, J Dubau, M Loulergue, "Charge-dependent wavelength shifts and line intensities in the dielectronic satellite spectrum of heliumlike ions," *Physical Review A* **1985**, *32*, 3000–3004.

[276] U. Safronova, T. Lisina, "Atomic constants of autoionization states of ions with Z= 6, 8, 10–42 in the Be isoelectronic sequence," *Atomic Data and Nuclear Data Tables* **1979**, *24*, 49–93.

[277] M. H. Chen, "Relativistic Auger and x-ray emission of the 1s 2l (2l')m configurations of Be-like ions," *Physical Review A* **1985**, *31*, 1449–1457.

[278] L Natarajan, "Relativistic configuration interaction calculations on the Kα x-ray satellites of argon," *Journal of Physics B: Atomic Molecular and Optical Physics* **2003**, *36*, 105.

[279] U. I. Safronova, A. S. Shlyaptseva, "Inner-shell excitation energy and autoionization rates for Li-, Be-, B-like ions with Z = 6–54," *Physica Scripta* **1996**, *54*, 254–270.

[280] M. H. Chen, B Crasemann, "Dielectronic satellite spectra of Li-like ions," *At. Data Nucl. Data Tab.* **1987**, *37*, 419–439.

[281] V. A. Boiko, A. Y. Chugunov, T. G. Ivanova, A. Y. Faenov, I. V. Holin, S. A. Pikuz, A. M. Urnov, L. A. Vainshtein, U. I. Safronova, "He-like ion resonance-line satellites radiated from Be-like ions," *Monthly Notices of the Royal Astronomical Society* **1978**, *185*, 305–324.

[282] P Beiersdorfer, T Phillips, V. L. Jacobs, K. W. Hill, M Bitter, S von Goeler, S. M. Kahn, "High-resolution measurements, line identification, and spectral modeling of K-alpha transitions in Fe XVIII-Fe XXV," *The Astrophysical Journal* **1993**, *409*, 846.

[283] V Decaux, P Beiersdorfer, S. M. Kahn, V. L. Jacobs, "High-Resolution Measurement of the Kα Spectrum of Fe XXV-XVIII: New Spectral Diagnostics of Nonequilibrium Astrophysical Plasmas," *The Astrophysical Journal* **1997**, *482*, 1076–1084.

[284] R Steinbrügge et al., "Absolute measurement of radiative and Auger rates of K-shell-vacancy states in highly charged Fe ions," *Physical Review A* **2015**, *91*, 032502.

[285] U. I. Safronova, T. G. Lisina, "Atomic constants of autoionization states of ions with Z = 6, 8, 10-42 in the Be isoelectronic sequence," *At. Data Nucl. Data Tables* **1979**, *24*, 49–93.

[286] V. A. Yerokhin, A Surzhykov, S Fritzsche, "Relativistic configuration-interaction calculation of K? transition energies in berylliumlike iron," *Physical Review A* **2014**, *90*, 022509.

[287] M. H. Chen, "Relativistic Auger and x-ray emission of the 1s 2l (2l')m configurations of Be-like ions," *Physical Review A* **1985**, *31*, 1449–1457.

[288] S Shuqiang, P Feng, J Gang, "Properties of the Kα and Kβ x-ray transitions in CuXX through CuXXVIII," *Journal of Physics B: Atomic Molecular and Optical Physics* **2006**, *39*, 2087–2093.

[289] J. Machado, C. I. Szabo, J. P. Santos, P. Amaro, M. Guerra, A. Gumberidze, G. Bian, J. M. Isac, P. Indelicato, "High-precision measurements transition energies and level widths of the $1s\,2s\,2p\,^2P_J$, $J = 1/2, 3/2$ doublet in Li-like Argon Ions," *In Preparation* **2018**.

[290] J. Nilsen, "Dielectronic Satellite Spectra for Helium-Like Ions," *At. Data Nucl. Data Tab.* **1988**, *38*, 339–379.

[291] L. A. Vainshtein, U. I. Safronova, "Wavelengths and Transition Probabilities of Satellites to Resonance Lines of H- and He-Like Ions," *At. Data Nucl. Data Tab.* **1978**, *21*, 49–68.

[292] M. R. Tarbutt, R Barnsley, N. J. Peacock, J. D. Silver, "Wavelength Measurements of the Satellite Transitions to the N = 2 Resonance Lines of Helium-Like Argon," *Journal of Physics B: Atomic Molecular and Optical Physics* **2001**, *34*, 3979–3991.

[293] V. A. Yerokhin, A Surzhykov, "Relativistic Configuration-Interaction Calculation of Energy Levels of Core-Excited States in Lithiumlike Ions: Argon through Krypton," *Physical Review A* **2012**, *86*, 042507.

[294] U. I. Safronova, M. S. Safronova, "Relativistic many-body calculations of E1, E2, M1, and M2 transitions rates for the 1 s 2 l ´ 2 l ´ ´ - 1 s 2 2 l lines in Li-like ions," *Molecular Physics* **2004**, *102*, 1331–1344.

[295] A. D. Whiteford, N. R. Badnell, C. P. Ballance, S. D. Loch, M. G. O'Mullane, H. P. Summers, "Excitation of Ar 15+ and Fe 23+ for Diagnostic Application to Fusion and Astrophysical Plasmas," *Journal of Physics B: Atomic Molecular and Optical Physics* **2002**, *35*, 3729–3740.

[296] R. Piessens, E. de Doncker-Kapenga, C. W. Überhuber, D. K. Kahaner, *Quadpack: a subroutine package for automatic integration*, *Vol. 1*, Springer Science & Business Media, **2012**.

[297] E. V. Aglitskii, V. A. Boiko, S. M. Zakharov, S. A. Pikuz, A. Y. Faenov, "Observation in laser plasmas and identification of dielectron satellites of spectral lines of hydrogen- and helium-like ions of elements in the Na–V range," *Soviet Journal of Quantum Electronics* **1974**, *4*, 500–513.

[298] J Suleiman, H. Berry, R. Dunford, R. Deslattes, P. Indelicato, "Observations of doubly excited states in lithiumlike calcium," *Physical Review A* **1994**, *49*, 156.

[299] A. Martynenko, "Lamb shift in the muonic helium ion," *Physical Review A* **2007**, *76*, 012505.

[300] I. Sick, "Precise root-mean-square radius of He 4," *Physical Review C* **2008**, *77*, 041302.

[301] E Borie, "Lamb shift in muonic 3 He," *Zeitschrift für Physik A Hadrons and Nuclei* **1980**, *297*, 17–18.

[302] P Mueller, I. Sulai, A. Villari, J. Alcantara-Nunez, R Alves-Condé, K Bailey, G. Drake, M Dubois, C Eléon, G Gaubert, et al., "Nuclear Charge Radius of He 8," *Physical review letters* **2007**, *99*, 252501.

Appendix A

The Lamb Shift transitions of the muonic helium-3 and helium-4 ions

Table A.1 – $2S-2P$ transition properties for $\mu^4\mathrm{He}^+$ and $\mu^3\mathrm{He}^+$. Listed are the energy difference, wavelength, sub-level population ν, transition matrix element and laser fluence required to saturate the transition F_{sat}. The transition at 1108 nm cannot be accessed with a Ti:sapphire laser. The energy differences and wavelengths for the $\mu^4\mathrm{He}^+$ transitions have been taken from [299] and adjusted to the most recent value of the nuclear radius $r_{^4He} = 1.681(4)$ fm [300]. The $\mu^3\mathrm{He}^+$ transition energies have been taken from [301] and adjusted to a ^{3}He nuclear value of $r_{^3He} = 1.971(4)$ fm (deduced from $r_{^4He}$ and the recent measurement of the isotope shift [302]).

Isotope	Transition	ΔE [meV]	λ [nm]	Pop. (ν)	M [a_u^2]	F_{sat} [J/cm^2]
$\mu^4\mathrm{He}^+$	$2S_{1/2} - 2P_{3/2}$	1526	812	1	6	1.1
$\mu^4\mathrm{He}^+$	$2S_{1/2} - 2P_{1/2}$	1380	898	1	3	2.2
$\mu^3\mathrm{He}^+$	$2S^{F=0}_{1/2} - 2P^{F=1}_{1/2}$	1119	1108	1/4	3	2.1
$\mu^3\mathrm{He}^+$	$2S^{F=0}_{1/2} - 2P^{F=1}_{3/2}$	1294	958	1/4	6	1.1
$\mu^3\mathrm{He}^+$	$2S^{F=1}_{1/2} - 2P^{F=1}_{1/2}$	1286	964	3/4	2	3.2
$\mu^3\mathrm{He}^+$	$2S^{F=1}_{1/2} - 2P^{F=0}_{1/2}$	1344	923	3/4	1	6.4
$\mu^3\mathrm{He}^+$	$2S^{F=1}_{1/2} - 2P^{F=2}_{3/2}$	1436	863	3/4	5	1.3
$\mu^3\mathrm{He}^+$	$2S^{F=1}_{1/2} - 2P^{F=1}_{3/2}$	1461	849	3/4	1	6.4

Appendix

B

Example of Be-like $1s\,2s^2\,2p\,^1P_1 \rightarrow 1s^2\,2s^2\,^1S_0$ transition dispersive spectra

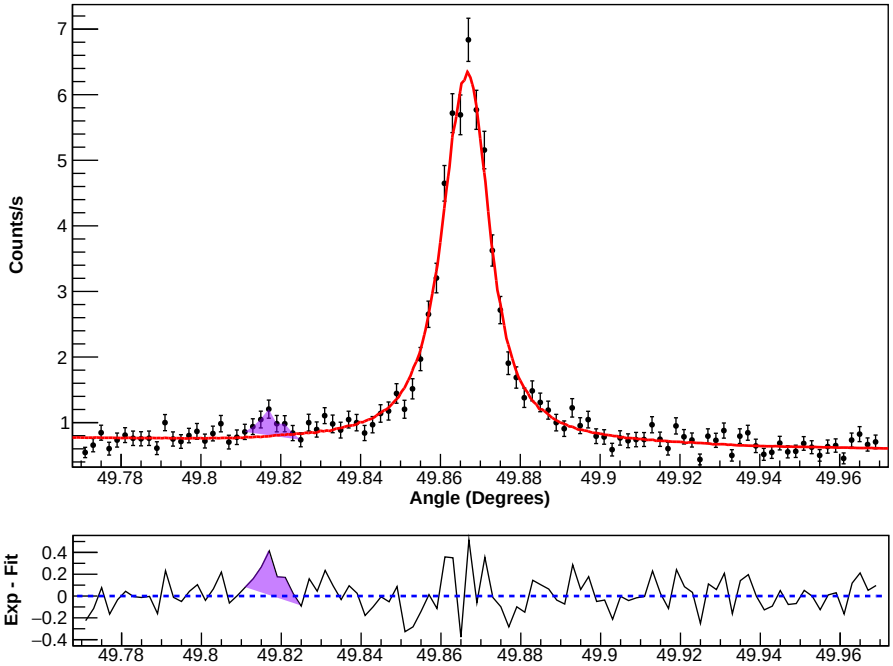

Figure B.1 – Example of a dispersive spectrum of the $1s\,2s^2\,2p\,^1P_1 \rightarrow 1s^2\,2s^2\,^1S_0$ transition. The red full curve is the fit from simulation performed with the obtained energy and natural width. The purple shadow area highlights the observed small peak and at the bottom the fit residuals are shown.

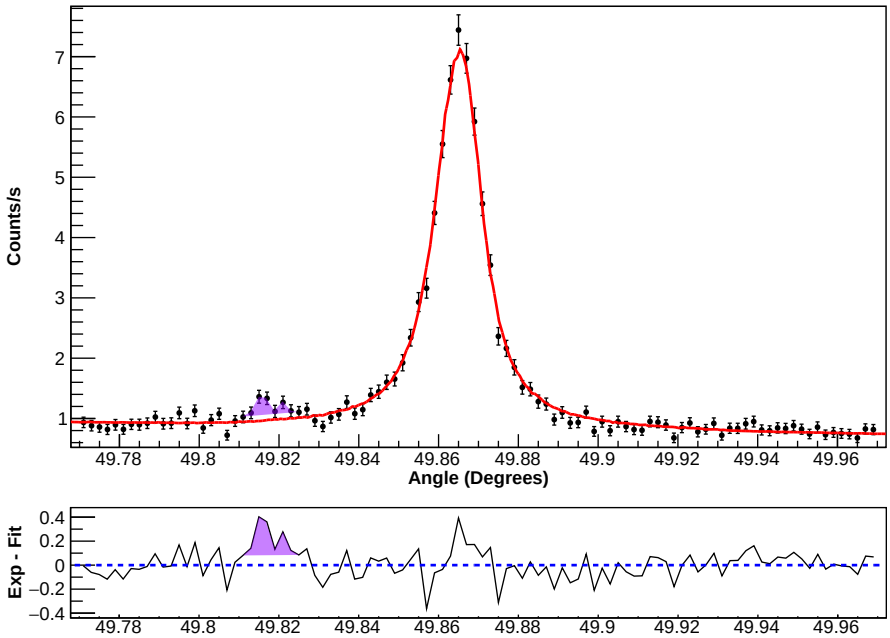

Figure B.2 – Example of a dispersive spectrum of the $1s\,2s^2\,2p\,^1P_1 \rightarrow 1s^2\,2s^2\,^1S_0$ transition. The red full curve is the fit from simulation performed with the obtained energy and natural width. The purple shadow area highlights the observed small peak and at the bottom the fit residuals are shown.

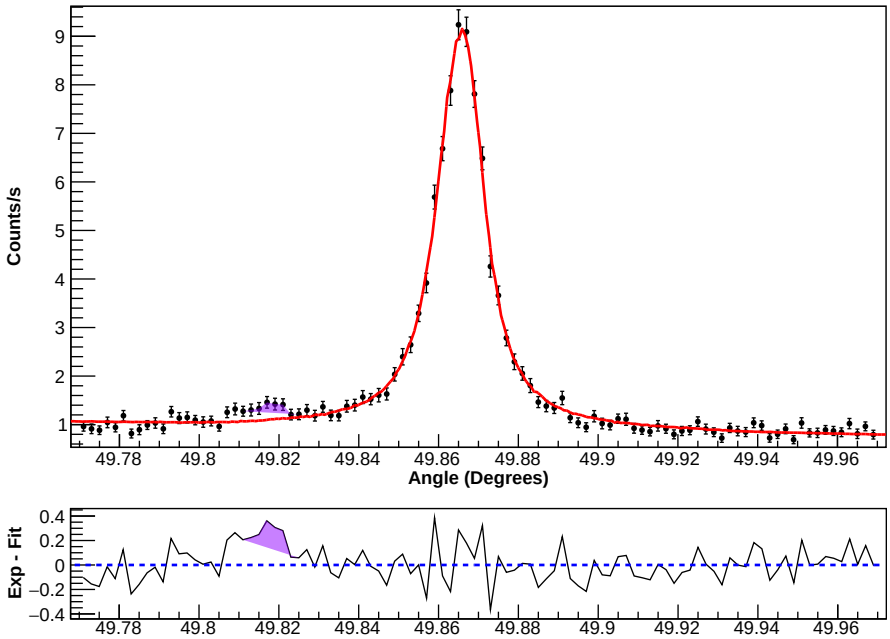

Figure B.3 – Example of a dispersive spectrum of the $1s\,2s^2\,2p\,^1P_1 \rightarrow 1s^2\,2s^2\,^1S_0$ transition. The red full curve is the fit from simulation performed with the obtained energy and natural width. The purple shadow area highlights the observed small peak and at the bottom the fit residuals are shown.

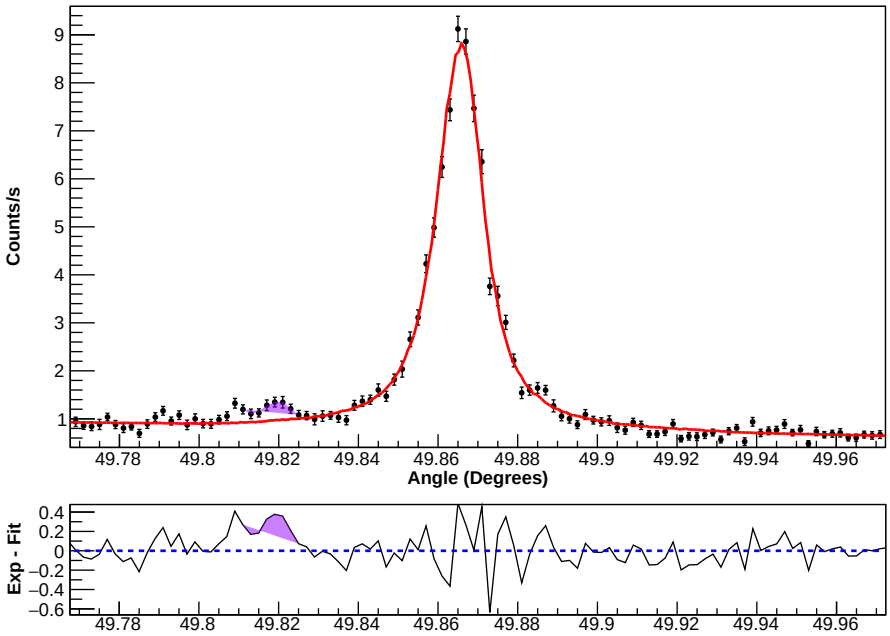

Figure B.4 – Example of a dispersive spectrum of the $1s\,2s^2\,2p\,^1P_1 \rightarrow 1s^2\,2s^2\,^1S_0$ transition. The red full curve is the fit from simulation performed with the obtained energy and natural width. The purple shadow area highlights the observed small peak and at the bottom the fit residuals are shown.